Nuclear magnetic resonance insights into membrane and cellular systems

Inaugural dissertation

for the attainment of the title of doctor
in the Faculty of Mathematics and Natural Sciences

at the Heinrich Heine University Düsseldorf

presented by

Thibault Viennet

from Clermont-Ferrand (France)

Düsseldorf, March 2017

from the institute for Physical Biology

at the Heinrich Heine University Düsseldorf

Published by permission of the
Faculty of Mathematics and Natural Sciences at

Heinrich Heine University Düsseldorf

Supervisor: Dr. Manuel Etzkorn

Co-supervisor: Prof. Dr. Lutz Schmitt

Date of the oral examination: 18.05.2017

Eidesstattliche Versicherung

Ich versichere an Eides Statt, dass die Dissertation von mir selbständig und ohne unzulässige fremde Hilfe unter Beachtung der Grundsätze zur Sicherung guter wissenschaftlicher Praxis an der Heinrich-Heine Universität Düsseldorf erstellt worden ist.
Ich versichere, dass die eingereichte schriftliche Fassung der auf dem beigefügten Medium gespeicherten Fassung entspricht.

I declare under oath that I have complied my dissertation independently and without any undue assistance by third parties under consideration of the „Principles for the Safeguarding of Good Scientific Practices at Heinrich Heine University Düsseldorf".

Düsseldorf, den 02.03.2017

CHAPTER I – ABSTRACT CONTRIBUTIONS ACKNOWLEDGEMENTS

Abstract

Structural biology has benefited in the past years from both the improvement in biochemical procedures (protein expression, purification and modification, membrane protein refolding systems, etc.) and the development of powerful and complementary biophysical techniques allowing to study structures, dynamics and interactions. Certain particularly relevant biological systems, however, still remain difficult to study, including dynamics in big biomolecules, structure of membrane proteins, and structural information of proteins in their native environments. For this reason, further improvements in both biochemical and biophysical techniques still need to be implemented.

One of these techniques, nuclear magnetic resonance (NMR) has a high potential and applicability in the study of structure, dynamics and interactions of biomolecules. Nevertheless it also faces limitations, some of which we propose to tackle in this work. This includes a new way of acquiring solution NMR data in a more time efficient manner (Chapter IV), allowing to get additional, complementary, information during the acquisition of conventional experiments. Moreover, in Chapter V we introduce specific hyperpolarization using dynamic nuclear polarization (DNP) NMR in order to specifically detect a target protein in its cell lysate. This overcomes the need for sample purification and drastically reduces the amount of protein needed.

Furthermore, sample preparation is critical in all NMR studies, and gets particularly challenging in the case of membrane proteins. Suitable membrane mimicking systems have still to be implemented, with the difficulty of being suitable for the chosen NMR method while providing a native environment for the target protein. In particular, lipid bilayer nanodiscs appear as an interesting alternative to conventional membrane mimetics. We review the biochemistry and the NMR applications of nanodiscs in Chapter III, and show initial results towards better understanding of their arrangement and behavior. We apply this methodology to the study of the membrane protein Barttin, an ion channel regulator, and compare the results with more conventional detergent micelles in Chapter VII. Moreover, nanodiscs allowed us to characterize the membrane association mechanisms of the Parkinson's disease relevant protein α-Synuclein and their effect on fibril formation in Chapter VI.

Ultimately, we bring together the nanodisc system and the specific hyperpolarization of targeted DNP with the aim of developing a universal platform for the study of membrane proteins by magic angle spinning solid-state NMR. One advantage of this platform could be the characterization of low-populated states in membrane-associated systems.

Zusammenfassung

Die Strukturbiologie hat in den letzten Jahren große Fortschritte in der (Weiter)Entwicklung sowohl biochemischer Verfahren, als auch komplementärer biophysikalischer Methoden zur Untersuchung der Struktur, Dynamik und Interaktion von Biomolekülen gemacht. Dennoch bleiben einige Systeme, wie z.B. Membranproteine und Protein in ihrer zellulären Umgebung, immer noch schwer zugänglich. Daher sind weitere Fortschritte in biochemischen und biophysikalischen Techniken in diesen Bereichen immer noch äußerst wichtig.

Die Kernmagnetische-Resonanzspektroskopie (NMR) bietet generell ein großes Potential für die Untersuchung der Struktur, Dynamik und Interaktionen von Proteinen. Es existieren jedoch auch deutliche Limitierungen der Technik. In dieser Arbeit widmen wir uns einigen dieser Limitierungen sowie Möglichkeiten diese zu überwinden. Ein Beispiel hierfür ist die von uns entwickelte effizientere Aufnahme von Lösungs-NMR Spektren, welche einen höheren Informationsgehalt der Messdaten ermöglicht (s. Kapitel IV). Zusätzlich führen wir selektive Hyperpolarisation mittels dynamischer Kernpolarisation (DNP) ein (s. Kapitel V). Dieses Verfahren ermöglicht die spezifische Detektion eines Zielproteins direkt in Zelllysaten und beseitigt weitestgehend die Notwendigkeit der Proteinaufreinigung.

Generell stellt die Probenpräparation ein zentrales Element für NMR Untersuchungen da. Diese kann jedoch, insbesondere für Membranproteine, zu einer großen Herausforderung werden, da geeignete membranmimetische Umgebungen verwendet werden müssen, welche auf der einen Seite zugänglich für die verwendeten NMR Methoden sein sollen und auf der anderen Seite eine möglichst native Umgebung für das Zielprotein darstellen sollen. In diesem Zusammenhang bieten sogenannte Nanodiscs, bestehend aus einer Lipiddoppelschicht, eine interessante Alternative gegenüber anderen konventionellen Membranmimetica. Kapitel III dieser Arbeit gibt eine Übersicht über die Biochemie sowie NMR Anwendungen von Nanodiscs und gibt Anhaltspunkt für ein besseres Verständnis der Anordnung und des Verhaltens dieses Systems. Kapitel VII zeigt eine Anwendung der Nanodisctechnologie, sowie einen Vergleich mit eher konventionellen Detergenzmizellen, für die Untersuchung des Membranproteins Barttin, welches als Regulator verschiedener Ionenkanälen fungiert. Des Weiteren konnten wir mittels Nanodiscs die Membraninteraktion des Parkinsons assoziierten Proteins α-Synuclein und deren Effekt auf die krankheitsrelevante Fibrillenausbildung charakterisieren (Kapitel VI).

Abschließend kombinieren wir die Potentiale des Nanodiscsystems und der spezifische Hyperpolarisation, um eine allgemein verwendbare Plattform zur Untersuchung von Membranproteinen mittels DNP-Festkörper-NMR zu entwickeln, welche u.a. die Möglichkeit eröffnen sollte niedrig besetzte Zustände in Membransystemen besser zu untersuchen.

Table of contents

List of figures, tables and equations

Figures

Tables

Equations

List of symbols, abbreviations and acronyms

Entries appear by order of appearance in the dissertation. Names of chemicals and proteins which were not widely used in this work are not included here but defined in the text.

NMR – nuclear magnetic resonance
DNA – deoxyribonucleic acid
RNA – ribonucleic acid
EM – electron microscopy
DNP – dynamic nuclear polarization
MAS – magic angle spinning
I – spin quantum number (S for electron)
m_I – magnetic quantum number (m_S for electron)
ω – frequency (ω_0 – Larmor frequency)
γ – spin gyromagnetic ratio
B_0 – external magnetic field
μ – magnetic moment
N – population of a given spin state
k_B – Boltzmann constant
δ – chemical shift (also homogenous line broadening in electron paramagnetic resonance)
FID – free induction decay
T_1 – longitudinal relaxation specific time
T_2 – transverse relaxation specific time
J – scalar coupling constant
D – dipolar coupling constant
μ_0 – vacuum permeability
$\hbar$ – Dirac constant (reduced Planck constant)
INEPT – insensitive nuclei enhanced by polarization transfer
NOE – nuclear Overhauser effect
W_0 – cross relaxation rate constant
τ_c – correlation specific time
COSY – correlation spectroscopy
TOCSY – total correlation spectroscopy
NOESY – nuclear Overhauser effect spectroscopy
FLOPSY – flip-flop spectroscopy
HSQC – heteronuclear single quantum correlation
RDC – residual dipolar coupling
TROSY – transverse relaxation optimized spectroscopy
DD – dipole-dipole interaction tensor
CSA – chemical shift anisotropy
EPR – electron paramagnetic resonance
PRE – paramagnetic relaxation enhancement
μ_B – Bohr magneton
Γ_1 – longitudinal paramagnetic relaxation enhancement
Γ_2 – transverse paramagnetic relaxation enhancement
PCS – pseudo contact shift
CP – cross polarization
PDSD – proton driven spin diffusion
Δ – inhomogeneous line broadening (electron paramagnetic resonance)
ε – dynamic nuclear polarization enhancement factor
ASR – absolute sensitivity ratio
$T_{1\rho}$ – specific relaxation time under spin-lock conditions
CFE – cell free expression
CMC – critical micelle concentration
GPCR – G-protein coupled receptor
ND – nanodisc
MSP – membrane scaffold protein
Bcl-x_L – B-cell lymphoma extra-large
OmpX – outer membrane protein X
ApoA1 – apolipoprotein A-I
HDL – high density lipoprotein
αS – α-Synuclein
NAC – non amyloid-β component
SEC – size exclusion chromatography
DLS – dynamic light scattering
bR – bacteriorhodopsin
IMAC – immobilized metal affinity chromatography
PAGE – polyacrylamide gel electrophoresis
UTOPIA – unified time optimized interleaved acquisition
MD – molecular dynamics
τ_{DNP} – dynamic nuclear polarization build-up specific time
SUV – small unilamellar vesicle
BLI – bio-layer interferometry
CD – circular dichroism

Contributions

- Chapter III: The power, pitfalls and potential of the nanodisc system for NMR-based studies
  - Contribution 40% (shared first author)
  - Compiled literature and wrote parts of the manuscript about "History and background", "Structure of nanodiscs" and "Working with nanodiscs". Prepared samples and acquired data from figures 3D,E and 5D. Contributed to review manuscript.

- Chapter IV: UTOPIA NMR, activating unexploited magnetization using interleaved low-gamma detection
  - Contribution 15% (second author)
  - Prepared one sample. Participated in some measurements. Contributed to review manuscript.

- Chapter V: Selective protein hyperpolarization in cell lysates using targeted dynamic nuclear polarization
  - Contribution 70% (first author)
  - Prepared samples. Carried out, processed and interpreted all measurements (excluding peptide and radical synthesis). Contributed to writing and reviewing the manuscript.

- Chapter VI: Modulation of structural and kinetic determinants of α-synuclein aggregation by stable, planar lipid bilayer nanodiscs
  - Contribution 70% (first author)
  - Prepared all nanodiscs used. Carried out all NMR, BLI and SEC measurements. Contributed to process and interpret all data. Wrote the manuscript.

- Chapter VII: Reconstitution and NMR characterization of an ion-channel regulator protein in detergents and bilayer nanodiscs
  - Contribution 60% (first author)
  - Participated in all sample preparations and biochemical assays. Carried out NMR measurements. Participated in data processing and interpretation. Wrote the manuscript.

List of related publications

- Viegas A.*, **Viennet T.*** and Etzkorn M. The power, pitfalls and potential of the nanodisc system for NMR-based studies. *Biol. Chem.* 397 (12), 1335-1354 (**2016**). DOI: 10.1515/hsz-2016-0224
  *these authors contributed equally

- Viegas A., **Viennet T.**, Yu T.-Y., Schumann F., Bermel W., Wagner G.and Etzkorn M. UTOPIA NMR: activating unexploited magnetization using interleaved low-gamma detection. *J. Biomol. NMR.* 64 (1), 9-15 (**2016**). DOI: 10.1007/s10858-015-0008-7

- **Viennet T.**, Viegas A., Kuepper A., Arens S., Gelev V., Petrov O., Grossmann T. N., Heise H. and Etzkorn M. Selective protein hyperpolarization in cell lysates using targeted dynamic nuclear polarization. *Angew. Chem. Int. Ed. Engl.* 55 (36), 10746-10750 (**2016**). DOI: 10.1002/anie.201603205

- **Viennet T.**, Woerdehoff M. M., Shaykhalishahi H., Uluca B., Heise H., Buell A. K., Hoyer W. and Etzkorn M. Modulation of structural and kinetic determinants of α-synuclein aggregation by stable, planar lipid bilayer nanodiscs. *In preparation.*

- Uluca B., Shaykhalishahi H., Petrovic D., **Viennet T.**, Gönülalan A., Etzkorn M., Hoyer W. and Heise H. Conformational ensembles of (intrinsically disordered) proteins studied by dynamic nuclear polarization nuclear magnetic resonance. *In preparation.*

- Schriek S., Viegas A., **Viennet T.** and Etzkorn M. Melanocortin signaling: modulation through membrane and calcium interactions. *In preparation.*

- **Viennet T.**, Bungert-Pluemke S., Elter S., Viegas A., Fahlke C. and Etzkorn M. Reconstitution and nuclear magnetic resonance characterization of an ion-channel regulator protein in detergents and bilayer nanodiscs. *In preparation.*

Acknowledgements

The work presented here was done in a highly collaborative environment at both the Institut für Physikalische Biologie, Heinrich-Heine-Universität Düsseldorf and the Institute of Complex Systems, Forschungszentrum Jülich. Far from being one person's achievement it was only made possible by the involvement of many. I am grateful to Prof. Dr. Dieter Willbod for having provided the suitable scientific environment in both institutes for this to happen.

For the same reason, I would like to thank my main supervisor Dr. Manuel Etzkorn for being so accessible and helpful and for having built such a good collaborative environments in his group. All members of the group were part of this success as well: Dr. Aldino Viegas, Sabine Schriek, Shantha Elter, Marcel Falke, Jan Borgräffe, Laetitia Heid, Carla Schenk, Maria Dahlhaus, Aldo Vacco, Kübra Bilici and Mojtaba Oraki.

I would like to acknowledge all collaborators who contributed to the different parts of the work. Dr. Tsyr-Yan Yu and Prof. Gerhard Wagner from Harvard Medical School, Dr. Franck Schumann and Dr. Wolfgang Bermel from Bruker Biopsin contributed to the development of UTOPIA NMR. Arne Küpper and Dr. Tom Grossmann from the Chemical Genomic Center of the Max-Planck-Society as well as Prof. Vladimir Gelev and Prof. Ognyan Petrov from the University of Sofia were key in the success of the implementation of targeted DNP. Dr. Stefanie Bungert-Plümke and Prof. Dr. Christoph Fahlke are central in the Barttin project.

Moreover, all people who contributed to the work from inside the Institute walls are gratefully acknowledged as well: Dr. Aldino Viegas, Sabine Schriek, Shantha Elter, Laetitia Heid, Michael Wördehoff, Hamed Shaykhalishahi, Dr. Wolfgang Hoyer, Prof. Dr. Alexander Büll, Boran Uluca, Prof. Dr. Henrike Heise and of course Dr. Manuel Etzkorn.

Finally, I want to personally thank a number of persons without whom my own scientific knowledge as well as skills and ideas wouldn't be what they are now. Dr. Aldino Viegas taught me and worked with me on a day-to-day basis in, I think, the most fruitful way. Dr. Fabien Aussenac and Prof. Dr. Henrike Heise also contributed to my NMR and DNP knowledge and skills through our many conversations. I want to thank Dr. Céline Galvagnion for fruitful discussions as well. I am very grateful to Prof. Dr. Alexander Büll for having the patience to explain new techniques and concepts to me and for fascinating discussions.

Last, but not least, if some people should not be forgotten here they are my supervisors: Prof. Dr. Lutz Schmitt, Prof. Dr. Henrike Heise and especially my main supervisor Dr. Manuel Etzkorn. Firstly for giving me the chance to work in his group and on many different topics according to my own interests and motivations, secondly for being always accessible, always helpful, and always willing to have long and crazy scientific discussions. His involvement and guidance truly has lead both me and my work to the success we have now.

CHAPTER II – GENERAL INTRODUCTION

Structural biology is the field of natural science investigating the atomic structures of biomolecules (proteins, DNA, RNA, etc.). Notably, this not only involves structures themselves but also dynamic processes as well as interactions between biomolecules or e.g. between proteins and membranes. The aim is to understand the physiology of natural events (normal as well abnormal or disease relevant) at a molecular level. Several techniques have proven to be efficient in the structure elucidation of biomolecules, e.g. X-ray crystallography [1] which by far has led to the highest number of solved structures (around 90% of PDB deposited structures in 2015) but also cryo-electron microscopy [2]. Nevertheless, these techniques still struggle with some limitations. For X-ray crystallography, the difficulty in getting some biomolecules in a crystalline state impairs certain studies. As for electron microscopy, it is subject to a size limitation, which so far has been pushed to around 130 kDa with resolution of 3.5 Å [3]. Hence, all techniques have their own intrinsic limitations and have to be seen as complementary. Another paradigm in structural biology is the lack of data on biomolecules in their native environments. This is critical because the structure, dynamics and behavior of e.g. proteins does not only rely on their primary sequence but also depends on the environmental conditions [4], largely different from native ones in most *in vitro* studies. Structural biology would then need to be equipped with a technique able to solve structure and dynamics of biomolecules in their natural environments.

Nuclear Magnetic Resonance (NMR) has the intrinsic potential to solve this problem since it doesn't in principle require "non-natural" treatment of the samples. The technique has however its own limitations, i.e. an intrinsic low sensitivity leading to the need for NMR-active isotope enrichment, impairment by traces of isotope-labeled impurities leading to the need of extensive purification and size limitation of solution NMR which becomes inefficient for slow tumbling particles (size limitation of approximately 25 kDa for regular solution NMR [5]). The usage of more advanced NMR methodologies (see below) now allows access to bigger systems with solution NMR. The biggest proteins studied so far are up to 1 MDa in molecular weight [6]. Another possibility is to turn to solid-state NMR which is not impaired by any size limitation, and renders the usage of Dynamic Nuclear Polarization (DNP, a way to enhance sensitivity) possible. The fundamental principle of NMR will be explained in this general introduction with a focus on advanced techniques. The work presented here includes further advances in solution NMR (see Chapter IV) and DNP-solid state NMR (Chapter V).

Proteins are ubiquitous in the physiology of all species, their functional and structural study is of primary importance for the understanding of metabolism and disease mechanisms. Important targets are membrane proteins that control cell trafficking and cascade responses, and as such are the most relevant pharmaceutics targets (they represent 30% of the coding genome but 60% of the market drug targets [7, 8]). Nevertheless, their lack of solubility in the absence of membranes and the difficulty in producing them from conventional bacterial culture also makes them very challenging systems. The development of membrane mimetic systems that are, on the one hand suitable for NMR investigation, and on the other hand providing a close-to-native environment, is therefore a requirement. In this work, we mostly used phospholipid bilayer nanodiscs as a membrane mimetic. A review of the nanodisc system (see Chapter III) as well as new development (Chapter VIII) and application (Chapter VI and Chapter VII) are presented. The presence of lipids of defined compositions is needed for function of most membrane proteins. Such lipid bilayer systems, however, are very complex and their behavior is not fully understood to date. Therefore, membrane proteins in their membrane mimicking environments represent a big challenge in NMR structural studies and the primary objective of my work is to tackle this challenge using different, yet complementary techniques.

Nuclear Magnetic Resonance (NMR)

This section provides fundamental comprehension of nuclear magnetic resonance (NMR) spectroscopy. This shall be the basis for understanding key methodologies pushing the potential of NMR for the study of challenging systems (in the next section, see below). The goal is not to review the knowledge on NMR or to get deep insights into the understanding of the phenomenon, this would be out of the scope of this work.

Nuclear magnetic resonance is defined as the absorption of radio-frequencies by nuclei in the presence of an external magnetic field. This property is based on the fundamental physical concept of spin, dictating how a given nucleus will react in those conditions. This spin is characterized by a spin quantum number (I), which can take any value higher or equal to zero by increment of ½. Nuclei having a non-zero spin are NMR active and those with I=0 are invisible because they do not react to the external magnetic field (see Table 1).

$I = 0$	$I = n \cdot 1/2$	$I = n$
^{12}C, ^{16}O, …	^{1}H, ^{13}C, ^{15}N, ^{19}F, ^{31}P, …	^{2}H, ^{14}N, …
NMR inactive	NMR active	NMR active + higher order processes

Table 1. List of common nuclei in biomolecules in respect to their spin quantum number and NMR activity

In biomolecular NMR spectroscopy, NMR-active isotopes of natural nuclei are observed, preferentially with I=1/2 in order to simplify their behavior (the properties of higher order isotopes will not be presented here, from now on only spin ½ nuclei will be considered). This is the case in particular for ^{1}H, ^{13}C and ^{15}N. Nevertheless, the natural abundance of ^{1}H (over ^{2}H and ^{3}H) is 99.99%, making hydrogen a sensitive NMR probe, while those of ^{13}C and ^{15}N are only 1.07% and 0.37%, respectively, making them poor probes. This is why biomolecules usually need to be produced isotopically enriched in order to maximize the sensitivity on different types of atoms.

Zeeman effect

The presence of a nuclear spin by itself (in the void) has no effect at all, it is only when submitted to an external magnetic field that the physical behavior is revealed. In NMR spectroscopy the external magnetic field (B_0) originates from the magnet inside which the measurement takes place. In this case, the nucleus of spin quantum number I is allowed to adopt a fixed number of quantized energy levels. These energy levels are defined by the quantum number m_I which can adopt $2I+1$ values from $-I$ to I. In the case of a nucleus of spin ½, two energy levels corresponding to -½ and +½ are possible. This effect is called Zeeman splitting (also see Figure 1).

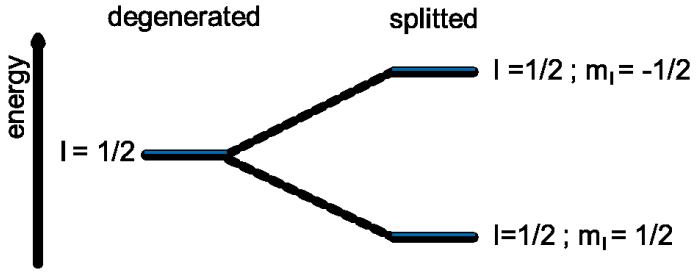

Figure 1. Energy diagram showing Zeeman degeneracy (left, absence of B_0) or splitting (right, presence of B_0) of a ½ spin nucleus

Larmor effect

The quantum probability of a given nuclear spin to adopt one of these two energy levels creates a magnetic moment (μ) that can be seen as a small magnet. It will eventually align with the external magnetic field B_0 (equilibrating the probability of being in one or the other energy level). As spins normally have an initial orientation in respect to B_0, this creates a spin angular momentum that forces the spin to precess around B_0 (rather than settle down in a direction either parallel or anti-parallel to B_0). This occurs at a specific frequency named Larmor frequency, which is given by $\omega_0 = \frac{-\gamma \cdot B_0}{2\pi}$. The Larmor frequency depends on the value of the external magnetic field as well as on a nucleus-specific parameter γ, the gyromagnetic ratio.

Note that Larmor frequency directly correlates with B_0 (defined in Tesla) for a given nucleus type, for that reason NMR spectroscopists usually define the external magnetic fields used by spectrometers on the ^{1}H Larmor frequency scale (see Table 2).

^{1}H ω_0 (MHz)	B_0 (T)
400	9.4
600	14.1
700	16.5
800	18.8
1000	23.5

Table 2. Correlation between field values of usual NMR spectrometers and ^{1}H Larmor frequencies

Boltzmann effect

The probabilistic approach derived from quantum mechanics can also be translated to an ensemble statistical view on all the spins of the same type present in a given sample. In this case the two splitted energy levels are populated according to Boltzmann law, where the energy difference between the two levels is proportional to the Larmor frequency according to the Planck formula (see Figure 2).

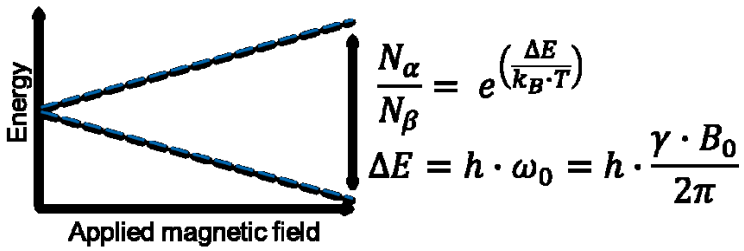

Figure 2. Energy diagram for ½ spin nuclei and dependence of the Zeeman splitting on the external magnetic field with the respective equations for the resulting populations in NMR conditions and their energy difference

The macroscopic nuclear polarization corresponds to the difference in population between the two states (usually named α and β) and depends on the temperature, the external magnetic field and the gyromagnetic ratio of the given nucleus type. In general, in order to maximize sensitivity, one would prefer lower temperatures (this would be true in a static case), high magnetic fields (up to 23.5T available nowadays on the market) and high γ. Here again ^{1}H is the most sensitive nucleus type, 4-fold higher than ^{13}C and 10-fold than ^{15}N (see Table 3).

Species	Gyromagnetic ratio ($C.kg^{-1}$) [$Hz.T^{-1}$]
^{15}N	$-2.71 \cdot 10^{7}$
^{13}C	$6.73 \cdot 10^{7}$
^{1}H	$2.68 \cdot 10^{8}$

Table 3. Gyromagnetic ratios of the most commonly used nuclei in biomolecular NMR

Chemical shift

It is then trivial that any nucleus of the same type (same γ) in the same conditions would precess at the same frequency (its Larmor frequency). Nevertheless, the observed resonance frequency not only depends on the gyromagnetic ratio γ and on the external magnetic field B_0, but also on the surrounding molecular chemical environment. This happens because the electrons that surround the nucleus create their own magnetic fields (local magnetic fields, B_{loc}) which create a microenvironment around the nucleus with an effective magnetic field B_{eff}. These different chemical environments lead to different precession frequencies (ω_{eff}), which can be referenced against the Larmor frequency on a "chemical shift" (δ) scale as follow:

Equation 1. Definition of chemical shift from the effective magnetic field received by a nucleus (ω_{ref} is the resonant frequency of a reference compound, δ is defined in parts per million, ppm).

The advantage of using chemical shifts scale rather than resonant frequencies relies on the fact that chemical shifts do not depend on B_0. Thus, comparison of data acquired in different spectrometers, operating at different magnetic fields is made easier.

NMR signal

The aim of NMR spectroscopy is to detect the precession frequency of a given nucleus in its environment. This can be done using the inducted electric current in a coil placed in the plane orthogonal to the axis of B_0 (usually called the xy plane and the z axis, respectively) because the precession creates an oscillation which period is proportional to the effective frequency of the nucleus. In order to maximize sensitivity (because the normal deviation from z into the xy plane of spins is extremely low) the system is in practice shifted in the xy plane by a resonant pulse from a coil orthogonal to z, this is a 90° pulse experiment (see Figure 3).

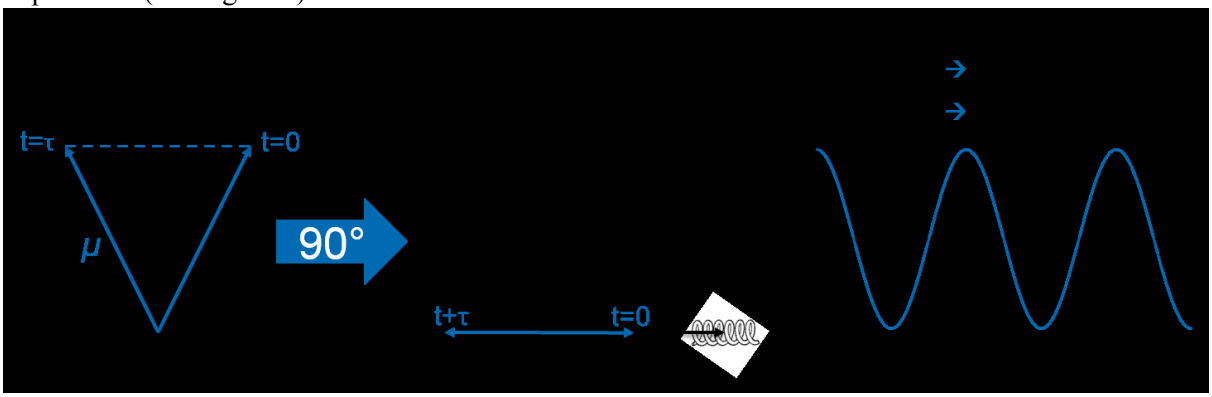

Figure 3. General scheme and result in the time domain for an ideal 90° NMR experiment (μ being the magnetic moment)

As many more than one nucleus of a given effective precession frequency is present in biomolecular samples, the obtained time domain curves are complicated modulations of all the sinusoidal oscillations. In order to simplify the problem and access the information (the frequencies or chemical shifts) a Fourier transform is applied shifting from time to frequency domain and providing one Dirac signal per perfect sinusoidal oscillation (see Figure 4).

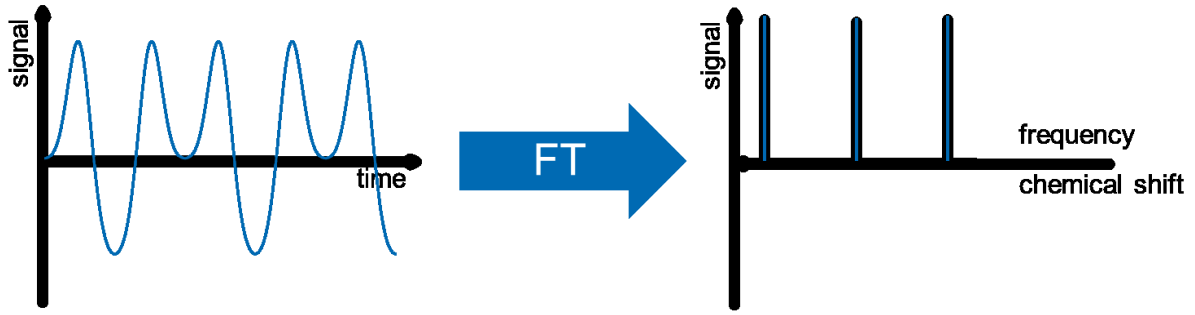

Figure 4. Fourier transform of an ideal system of three spins of different chemical shifts

Spin relaxation

The 90° experiment uses a pulse tuned to be resonant with the Larmor frequency of the target spins, but this is just a perturbation of the system, meaning that it brings the macroscopic net magnetization in the xy plane but does not hold it there. The spins eventually go back to their ground position along the z axis because that is the state where they are at their ground energy levels (i.e. to the Boltzmann distribution between energy levels). This process is called relaxation.

So over the time of a FID, net magnetization in xy decreases while net magnetization along z builds up again (see Figure 5). Importantly however, these two processes depend on different phenomena and do not happen at the same rate.

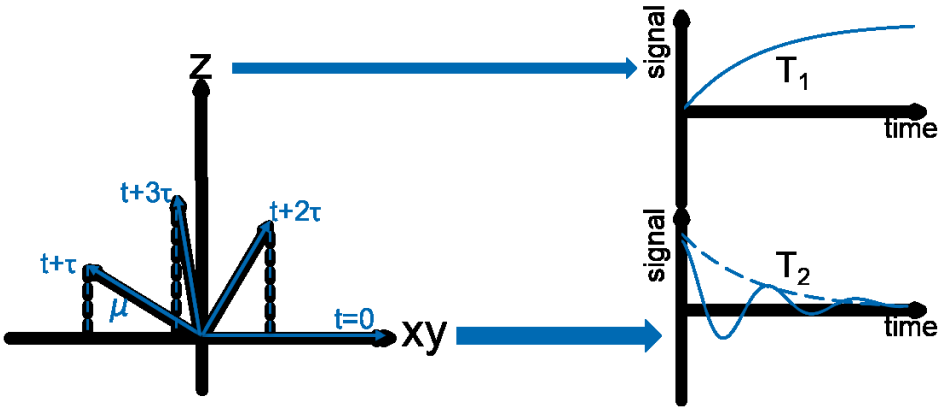

Figure 5. General scheme of longitudinal and transverse spin relaxation processes

The build-up of magnetization along z is due to the so-called longitudinal or spin-lattice relaxation at a specific time T_1. As discussed before, the reason is simply that spins get back to their ground energy levels, in which the thermal equilibrium is respected. T_1 relaxation depends primarily on the field strength, the gyromagnetic ratio and the temperature. It is very critical for the sensitivity of NMR experiments because one usually would repeat the same experiment several times in order to sum signal over the noise. Nevertheless the system has to reach thermal equilibrium between each accumulation in order to maximize the intrinsic sensitivity of each experiment. Thus both the number of scans and the so-called recycle delay (the time spent waiting for T_1 relaxation between each scans) modulate the absolute signal-to-noise level. The theoretical recycle delay for optimal signal-to-noise per time unit is $1.26 \cdot T_1$ [9].

The absolute sensitivity of NMR measurements depends on the concentration of spins (need to have concentrated samples), the number of accumulation (signal-to-noise scales with the square root of this number) as well as the gyromagnetic ratio (^{1}H being most sensitive) and the T_1 relaxation time of the observed nuclei. The need of long recycle delays (in order to ensure the best signal-to-noise), which are in the order of seconds, leads to the fact that most of the time spent in an NMR experiment is actually "lost" just waiting for equilibration of the system. Interestingly, one can make use of this waiting time to perform NMR experiments detected on other nuclei types, meaning that one or more experiments can be acquired in the meantime (see Chapter IV for more details).

The decrease of magnetization in xy is due to the so-called transverse or spin-spin relaxation phenomenon at a specific time T_2. This phenomenon can be seen as a dephasing process. Indeed, all the observed spins should precess in phase at time zero (after the 90° pulse) but they are all submitted to anisotropic interactions and random events (collisions, diffusion, etc.) and thus dephase over time. This leads to a gradual reduction of the net macroscopic magnetization (pictured as the sum of the projection of the spin magnetization in the xy plane). T_2 relaxation depends, on a trivial way, on the number of spins involved, the temperature and the tumbling rate of particles. Because of this relaxation phenomenon, the signal detected in the xy plane both oscillates and becomes lower over time. This is called the free induction decay (FID).

The resolution of NMR signals directly depends on T_2 since the Fourier transform of a FID gives a Lorentzian signal, which width is inversely proportional to the life time of the detected oscillations (see Figure 6), this is called homogenous line broadening (also see below). The lack of resolution due to short T_2 relaxations in big particles, e.g. big proteins or membrane proteins associated to their membrane mimetic, is the main reason for the size limitation in solution NMR.

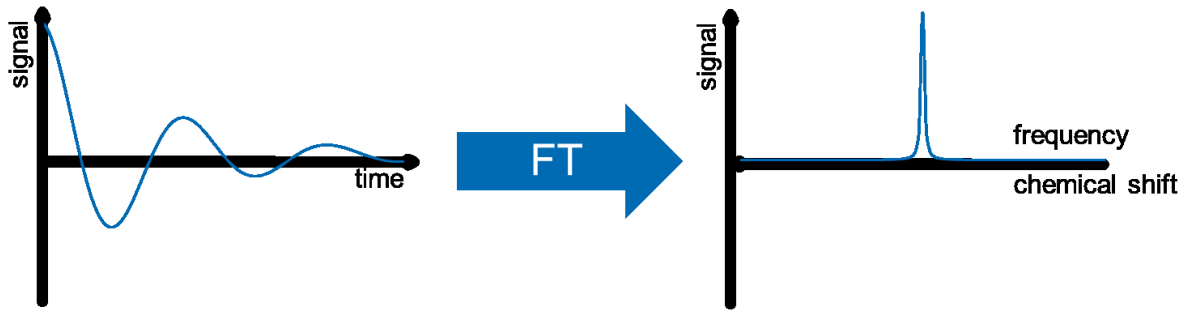

Figure 6. Fourier transform of a single-spin free induction decay signal

Spin coupling

Two covalently bound atoms share a molecular orbital, i.e. their bonding electrons are delocalized and usually create an anisotropic probability ensemble. These electrons are charged particles and thus have the ability to induce magnetic fields upon movement, which is why the shape of molecular orbitals affects the NMR properties of both nuclei involved in the bond. Modification of the nuclei's magnetic environment leads to modification of their resonant frequencies and additionally creates more energy levels accessible to nuclear spins. This is called scalar coupling, usually termed *J*, and *J*-splitting (see Figure 7).

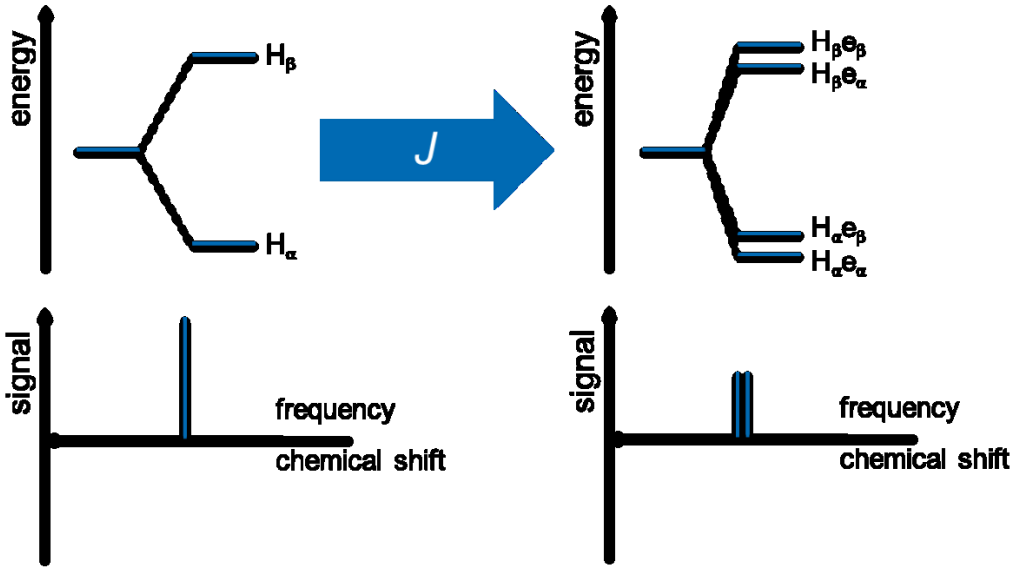

Figure 7. Energy diagrams (top) and ideal Fourier transform signals for a spin ½ nucleus submitted (right) or not (left) to scalar coupling from a neighbor nucleus

The multiplicity and magnitude of *J*-couplings depend very accurately on the number of coupled (i.e. neighboring through chemical bonds) nuclei, the number and nature of chemical bonds between them and the dihedral angles between the bonds according to Karplus law [10]. *J*-couplings are of primary importance for correlation, assignment and secondary structure information in biomolecules.

Furthermore, as previously said, all nuclei behave as small magnets, thus modulating the effective magnetic field received by their neighbors. In the same fashion as for scalar coupling this creates more energy levels accessible to a given nucleus and leads to splitting and shifting of the chemical shifts. This type of coupling is called dipolar and termed *D*. Dipolar couplings do not rely on chemical bonds but take place through space. Their magnitudes depend on the gyromagnetic ratios of the coupled spins as well as the inverse cube of the distance between and are given by $D_{12} = \frac{\mu_0 \hbar}{4\pi} \frac{\gamma_1 \gamma_2}{{r_{12}}^3}$, where μ_0 is the vacuum permeability and $\hbar$ the Planck constant divided by 2π.

As dipolar couplings directly report on the distance between two nuclei they give access to restraints due to the tertiary structure of biomolecules.

Even though *J* or *D* coupling constants contain very useful information, as far as biomolecular samples are concerned they usually are not desirable. Indeed, such samples contain a very high number of spins and extremely dense coupling network, this would make the spectra too complex to be analyzed. That is why most of the routine experiments contain decoupling sequences during acquisition or evolving of nuclei in order to obtain one single averaged signal per spin.

Spin polarization transfer

The coupling phenomena presented before not only allow the gain of useful information but also can be used to transfer magnetization from one spin to another.

The Insensitive Nuclei Enhanced by Polarization Transfer (INEPT) [11] experiment relies on the energy conservative mixing between two *J*-coupled spins leading to an exchange in magnetization from the most sensitive nucleus I (e.g. ^{1}H) to the least sensitive nucleus X (e.g. ^{13}C or ^{15}N). After a 90° pulse on I creating the transverse magnetization ($I_\alpha \rightarrow I_\beta$), an evolution period optimized to $1/(2 \cdot J_{IX})$ is left where the energy conservative flip-flop zero quantum mixing can take place ($I_\beta X_\alpha \rightarrow I_\alpha X_\beta$). In the

middle of the evolution period a simultaneous 180° pulse on both I and X is applied in order to remove chemical shift evolution without removing the coupling. Finally a 90° pulse on X is applied in order to bring magnetization back in the xy plane and pursue detection. Note that efficient INEPT needs a certain amount of dynamics or fast tumbling, because then T_2 relaxation is long enough to allow efficient transfer.

The Nuclear Overhauser Effect (NOE) [12] on the contrary makes use of the dipolar coupling between two nuclei in order to transfer magnetization via a cross-relaxation mechanism [13, 14]. After a 90° pulse on a nucleus A ($A_\alpha \rightarrow A_\beta$), a delay is set during which A relaxes to its ground state in the coupled two-spin system where zero quantum flip-flop cross-relaxation is allowed ($A_\beta B_\alpha \rightarrow A_\alpha B_\beta$). NOE relies on T_1 relaxation processes and as such is generally less efficient than INEPT for magnetization transfer, and impeded if the tumbling happens near to the Larmor frequency. NOE, on the contrary of INEPT, is dipolar based and thus relaxation rates scale with the product of the dipolar coupling constants on both nuclei, meaning that it is inversely proportional to the sixth power of the distance between them, limiting the transfer to rather short distances (up to 6 Å roughly). For large molecules which have slow tumbling times τ_c the rate is predominantly given by:

$$W_0 = \frac{2\tau_c}{r^6(1 + (\omega_A - \omega_B)^2{\tau_c}^2)}$$

Equation 2. Rate constant for dipolar based cross-relaxation between two coupled spins

Routine biomolecular solution NMR experiments

Homonuclear experiments

Following the previous section (see above) we can explain the basic two-dimensional (2D) NMR experiments based on homonuclear polarization transfer and couplings. Correlation Spectroscopy (COSY) [15] correlates *J*-coupled spins of the same type using energy conservative mixing during a simple evolution period and can be tuned to allow correlation of nuclei separated by 2 to 4 chemical bonds.

Total Correlation Spectroscopy (TOCSY) [16] however does not rely on energy conservative processes but uses a series of pulses allowing to force magnetization transfer through the *J*-couplings. This allows correlation of nuclei separated from much more than 4 chemical bonds but is done in an unspecific way (with series of pulses covering the resonant range of expected *J*-coupling magnitudes) and therefore is not quantitative.

Finally, Nuclear Overhauser Effect Spectroscopy (NOESY) transfers magnetization from one spin to another of the same type through space in an unspecific fashion using the NOE effect. In addition to all the neighboring nuclei also linked by chemical bonds, NOESY detects through-space correlations which are critical for structural restraints [17].

Figure 8 shows a comparison between these three experiments for a peptide.

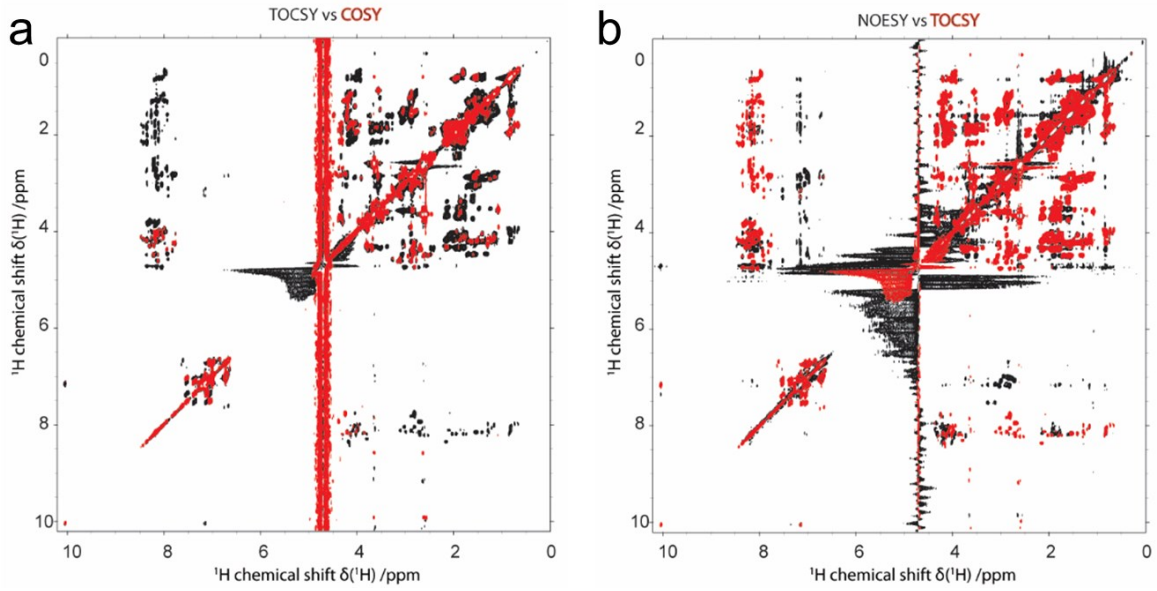

Figure 8. **a)** Overlay of TOCSY (black) and COSY (red) and **(b)** overlay of NOESY (black) and TOCSY (red) for a 40 residue peptide ACTH39C. The different ^{1}H correlation types leading to increasing number of cross-peaks is visible.

While most of the time ^{1}H-^{1}H experiment are used in order to optimize sensitivity, it can also be interesting to use other type of nuclei like ^{13}C, which, despite its lower γ, also has longer T_2 relaxation times and as such can provide better resolution. In this respect, Flip-Flop Spectroscopy (FLOPSY) [18], which is very similar to TOCSY with a large bandwidth isotropic mixing can be used to correlate *J*-coupled ^{13}C. In proteins, some specific regions displaying Cα-Cβ correlations of certain amino acid types are present, as well as cross-peaks between all the consecutive carbons of their side chains (see Figure 9, also see Chapter IV).

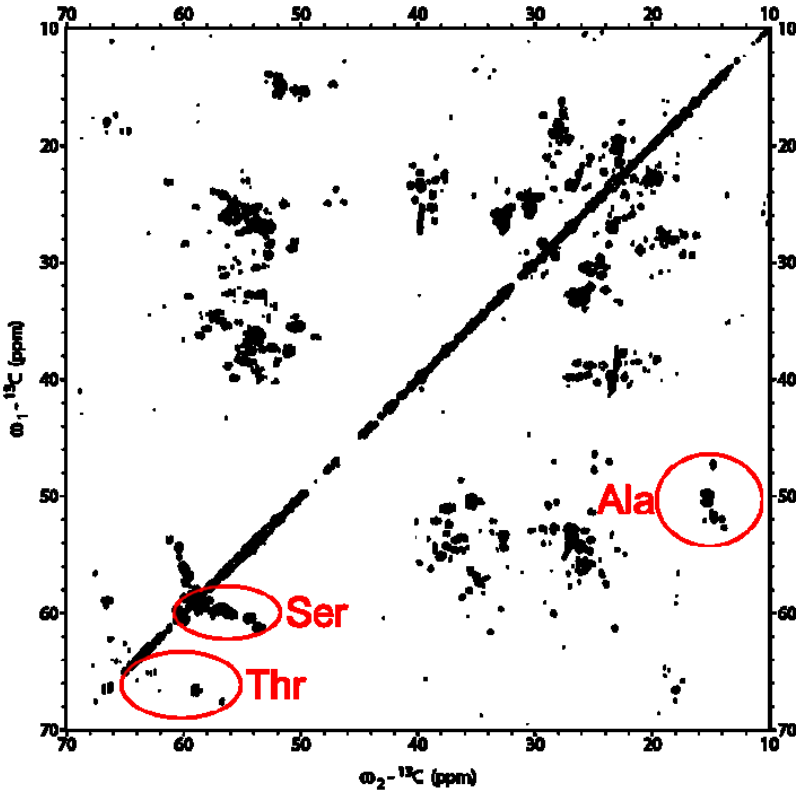

Figure 9. ^{13}C-FLOPSY spectrum of the 21 kDa Bcl-x$_L$ protein. The spectral regions exhibiting isolated amino-acid type signals are indicated.

Heteronuclear experiments

The most used and one of the most useful NMR experiments, as far as proteins are concerned, is the Heteronuclear Single Quantum Correlation (HSQC) [19]. It correlates, for instance, ^{1}H and ^{15}N using an INEPT transfer thus providing one peak per amide group, i.e. per amino acid (if glutamine, asparagine and tryptophan side chains are excluded, as well as proline which does not have an amide group). The pattern obtained is very specific for each protein and can be used as a "fingerprint". Despite different spectra would be required to identify each of the peaks in a ^{15}N-HSQC spectrum, some amide groups have very specific chemical shifts and can be easily identified (see Figure 10).

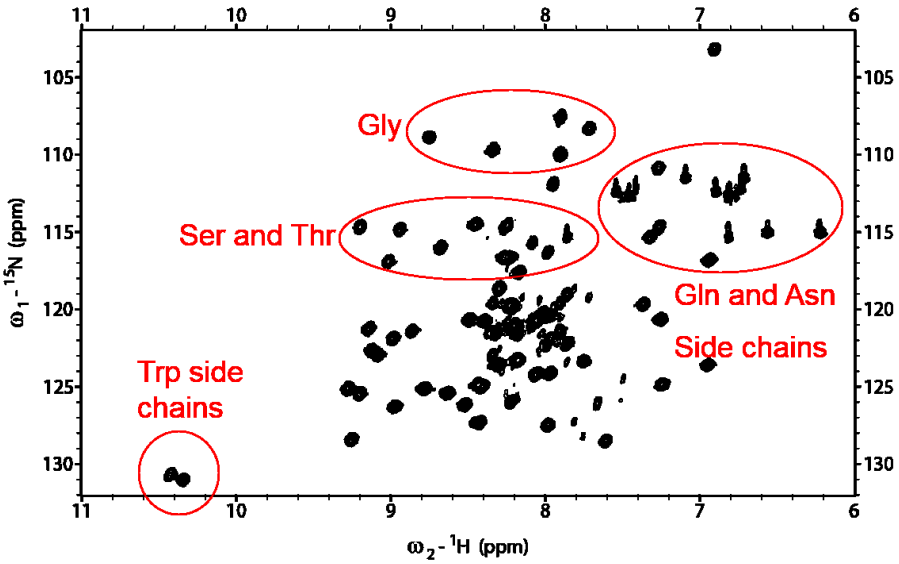

Figure 10. ^{15}N-HSQC spectrum of the 10 kDa GB1 protein. Spectral regions exhibiting isolated amino-acid type signals are indicated.

Interestingly, also the distribution of amide-^{1}H chemical shifts reports on the torsion angles in a protein. One can visualize the predominant secondary structures from the HSQC pattern (see Figure 11).

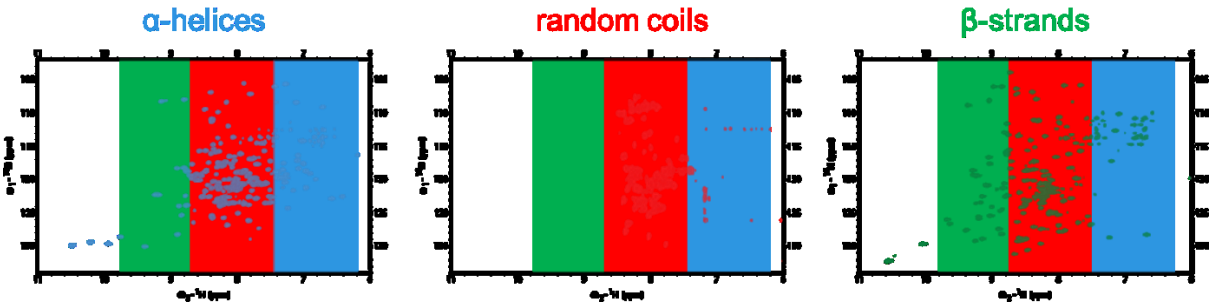

Figure 11. ^{15}N-HSQC spectra of three proteins containing very different secondary structure elements. Bcl-x_L (right) is very predominantly α-helical, bacterioopsin (bO, middle) in SDS largely unstructured and OmpX in DPC micelles is a folded β-barrel. The typical ^{1}H spectral regions of each secondary structure element are shown.

The HSQC experiment can be reversed in order to detect ^{15}N instead of the usual ^{1}H if resolution is preferred over sensitivity [20]. Correlation between ^{1}H and ^{13}C can also be established and are very useful in the assignment of side chain ^{1}H in proteins, which are good reporters for structure determination from their tertiary contacts.

Finally, other types of heteronuclear experiments can be designed, for example the CO-N [21] experiment correlating carbonyl ^{13}C to amide ^{15}N and providing sequential contacts in proteins with good resolution due to ^{13}C detection (see Chapter IV).

Protein backbone assignment

The first step in protein structural studies using NMR is always to measure a HSQC spectrum and to assign all the peaks to their respective amino acid in the primary sequence of the protein. This is usually conducted using a set of triple-resonance 3D experiments. All of these use INEPT type magnetization transfers in order to correlate the following nuclei (by order of sensitivity):

- HNCO [22] – correlates amide ^{1}H and ^{15}N with carbonyl ^{13}C of the previous residue in the sequence in one dimension each, provides one 3D cross-peak per sequential link.
- HNCa [22] – correlates amide ^{1}H and ^{15}N with ^{13}Cα of the same and the previous residue in the sequence, provides two sets of 3D cross-peaks, one per residue and one per sequential link.
- HN(Ca)CO [23] – correlates amide ^{1}H and ^{15}N with carbonyl ^{13}C of the same and the previous residue in the sequence, provides two sets of 3D cross-peaks, one per residue and one per sequential link.
- HN(CO)Ca [24] – correlates amide ^{1}H and ^{15}N with ^{13}Cα of the previous residue in the sequence, provides one 3D cross-peak per sequential link.
- HNCaCb [25] – correlates amide ^{1}H and ^{15}N with ^{13}Cα and ^{13}Cβ of the same and the previous residue in the sequence, provides four sets of 3D cross-peaks, one per residue and one per sequential link for both Cα and Cβ with opposed phases. It can also be tuned to bring full magnetization to the Cβ if a HNCa is already available.
- HN(CO)CaCb [25] – correlates amide ^{1}H and ^{15}N with ^{13}Cα and ^{13}Cβ of the previous residue in the sequence, provides two sets of 3D cross-peaks, one per residue for both Cα and Cβ with opposed phases. It can also be tuned to bring full magnetization to the Cβ if a HN(CO)Ca is already available.

Pushing up the size limitation of NMR

As it was already discussed before, solution NMR has an intrinsic size limitation estimated to be around 25 kDa for regular solution NMR experiments presented above [5]. This is largely due to the fast relaxation rates found for bigger particles, especially T_2 which predominantly scales with the tumbling rate. Homogenous line broadening takes place until the intensity of NMR signals obtained falls beyond the detection limit. At this step it is worth mentioning that the density (also leading to reduced T_2) and high number (crowding of the spectra) of spins involved is also a problem, but the latter can largely be overcome by the usage of higher order multi-dimensional NMR experiments [26].

A number of approaches have been developed in the last 20 years to overcome this issue [27]. One relies on the sample preparation and aims at diluting the ^1H spins in the sample in order to obtain a weaker dipolar coupling network and to lengthen T_2 of the residual ^1H. This can be achieved by expression of proteins in D_2O based media and partial or full back-exchange of the labile ^2H to ^1H (mostly amide protons) and is called triple labeling (when ^{13}C and ^{15}N are also enriched) [28]. Usage of new structural restraints (other than NOE) which are less sensitive to relaxation is also possible, for instance by Residual Dipolar Couplings (RDC) [29] or Paramagnetic Relaxation Enhancement (PRE) (see below). Finally, focus can be put on nuclei which have intrinsic dynamics allowing more resolved spectra, like in the case of the rotation of methyl groups. Specific isotope labeling of methyl groups [30] together with suitable methyl-directed NMR experiments [31] so far allowed NMR studies of proteins with a size up to 1 MDa [6]. In the rest of this section will be presented three of this alternatives in more details.

Transverse Relaxation Optimized Spectroscopy (TROSY)

As explained above (see NMR section), T_2 relaxation is a dephasing mechanism of spins of the same type over time. Several factors can lead to this, e.g. diffusion of spins, differential coupling events, differential evolution of spins or random spin collisions. This is a big issue in large molecules because the number of spins and couplings is large, therefore it is more likely that they evolve in different ways. Actually in these systems two of these mechanisms are predominant:

- Dipole-Dipole (*DD*) interactions i.e. the dipolar couplings of a given nucleus with all of its neighbors. This is particularly true for ^1H which have high density and high *D* magnitudes.
- Chemical Shift Anisotropy (CSA) i.e. the fact that a single nucleus receives different effective magnetic fields because its electronic environment is not isotropic (also see *J*-coupling) and adopts different orientations in respect to B_0.

In a non-decoupled ^{15}N-HSQC spectrum, each ^1H-^{15}N correlation appears as four peaks because the average signal is spitted in both the ^1H dimension and the ^{15}N dimension due to $^1J_{HN}$ coupling. Nevertheless, the four components of this multiplet are not submitted to the same relaxation rates, thus showing different intensities. Indeed the four single quantum transitions detected ($H_\alpha N_\alpha \rightarrow H_\alpha N_\beta$ / $H_\alpha N_\beta \rightarrow H_\beta N_\beta$ / $H_\alpha N_\alpha \rightarrow H_\alpha N_\beta$ / $H_\beta N_\alpha \rightarrow H_\beta N_\beta$) have different magnitudes or populations. Interestingly it is possible to modulate these transitions in order to reach conditions where *DD* and CSA contributions to the relaxation cancel each other out through destructive interferences of their oscillations, leaving only the component of slowest relaxation. This transition also yields the smallest line width and highest intensity.

Selection of this transition is achieved by the mean of phase cycling, i.e. pulsing and acquiring with radio-frequency coils placed on different axis in order to average the signal coming from the short-lived transitions over space (out of phase over the whole cycle) while the signal coming from the long-lived transition is summed (in phase over the cycle) [32].

Notably, by selecting one out of the four components of the multiplet, TROSY also gets a four-fold lower intrinsic sensitivity as compared to normal HSQC. The intensity of the obtained signal however is higher due to the reduced line broadening and therefore makes it a very useful tool for large molecules. This is especially true for perdeuterated proteins, which have a reduced ^{1}H-^{1}H dipolar network, and for high magnetic fields because CSA contribution is higher, bringing *DD* close to CSA (the optimal field to obtain reduced line-width in both ^{1}H and ^{15}N dimensions is predicted to be between 1200 and 1500 MHz) [33]. Furthermore, TROSY can be adapted to ^{15}N-detected instead of ^{1}H-detected HSQC, making use of the lower *DD* experienced by low-γ nuclei in order to reach CSA matching condition without the need for additional labeling (perdeuteration) and yielding similar sensitivity under certain conditions [20].

The TROSY effect can also be included in any INEPT based experiment, especially the triple resonance sequences for protein backbone assignment presented above [34]. This was a critical step in the investigation of large molecules by NMR and pushed the size limitation to several hundreds of kDa for proteins without the need for special treatment or labeling schemes.

A very similar approach has been developed as well using the interference between auto- and cross-correlated ^{1}H-^{1}H relaxations in order to select the sharpest signal in methyl groups of big molecules [31]. The so-called methyl-TROSY effect, together with specific methyl labeling so far has been the most efficient way to get useful data out of biomolecules and complexes up to 1 MDa.

Paramagnetic Relaxation Enhancement (PRE)

Another step towards solving structures of large biomolecules by NMR is to find suitable ways of getting structural restraints. In that respect, ^{1}H NOE-based methods are the canonical route but due the intrinsic efficiency of NOE magnetization transfer, the range of distance accessible remains limited (≤6 Å) which might be insufficient for large proteins and impeded by the high level of crowding in ^{1}H-^{1}H correlation spectra.

As explained in the dedicated section (see above), the efficiency of NOE transfers depend both on the net spin magnetization of the nuclei (thus of their gyromagnetic ratios) and of the cross-relaxation rate W_0. For this reason, the mechanism would be more effective with very high-γ and fast relaxing spins, which is the case for paramagnetic species. Paramagnetic species (arising from unpaired electrons found in conduction bands of metals and radical compounds) are attracted to external magnetic fields and thus have positive magnetic susceptibility. This means they are magnetically active but their properties differ from diamagnetic nuclei discussed so far, basically the probability exchange between energy states α and β upon absorption of resonant frequencies is reversed (α → β instead of β → α). The formalism used is also slightly different, with spin quantum numbers named *S* and m_S (instead of *I* and m_I) and magnetic moments being defined as $\mu = m_s \cdot \mu_B \cdot g_e$ with μ_B a fundamental constant, the Bohr magneton, and g_e the Landé g-factor which value is closed to 2.0023 for free electrons (instead of $\mu = m_I \cdot \gamma \cdot \hbar$). Apart from the sign of the transitions and the formalism, free electrons have a spin quantum number of 1/2 and basic NMR theory can be directly translated. Moreover a "gyromagnetic ratio" can be defined as:

$$\gamma_e = \frac{g_e \cdot \mu_B}{\hbar}$$

Interestingly, free electron have a very high gyromagnetic ratio and very fast relaxation (see Table 4). These free electrons are usually not naturally present in proteins (except for metalloproteins and proteins containing some cofactors) and as such need to be introduced, generally under the form of nitroxide radicals like S-(1-oxyl-2,2,5,5-tetramethyl-2,5-dihydro-1H-pyrrol-3-yl)methyl methanesulfonothioate (MTSL) [35] containing a thiol or maleimide chemical group that can be

conjugated to cysteine residues, either naturally present or introduced as well via mutagenesis. This is called site-directed spin labeling [36].

Species	Gyromagnetic ratio (C.kg^{-1}) [Hz.T^{-1}]	Typical T_2 or T_{1e} (ms)
^{13}C	$6.73 \cdot 10^7$	4
^{1}H	$2.68 \cdot 10^8$	1
e^-	$1.76 \cdot 10^{11}$	0.1

Table 4. Gyromagnetic ratios and PRE relevant relaxation specific times, i.e. nuclear T_2 or electron T_1, for ^1H, ^{13}C and electron. The values are typical for nuclei in large proteins or for unpaired electron in nitroxide radicals.

The aforementioned properties of free electrons lead to similar event of the NOE between dipolar coupled nucleus and electron, i.e. spin cross-relaxation [14], in this case, Paramagnetic Relaxation Enhancement (PRE). The rate W_0 is predominantly governed by the correlation time τ_c, which on the contrary of nucleus-nucleus (NOE) case, depends mostly on the electron spin relaxation time T_{1e} because it is much shorter than the tumbling or nuclei correlation times. The Solomon-Bloembergen equations are directly derived from the expression of W_0 allow to calculate the difference between nuclei T_1 and T_2 in the presence of paramagnetic cross-relaxation [14, 37]:

$$\Gamma_1 = \frac{2}{15} \cdot \left(\frac{\mu_0}{4\pi}\right)^2 \cdot \frac{{\gamma_I}^2 {g_e}^2 {\mu_B}^2 S(S+1)}{r^6} \cdot \left(\frac{\tau_c}{1+(\omega_I-\omega_e)^2{\tau_c}^2} + \frac{3\tau_c}{1+{\omega_I}^2{\tau_c}^2} + \frac{6\tau_c}{1+(\omega_I+\omega_e)^2{\tau_c}^2}\right)$$

$$\Gamma_2 = \frac{1}{15} \cdot \left(\frac{\mu_0}{4\pi}\right)^2 \cdot \frac{{\gamma_I}^2 {g_e}^2 {\mu_B}^2 S(S+1)}{r^6} \cdot \left(4\tau_c + \frac{\tau_c}{1+(\omega_I-\omega_e)^2{\tau_c}^2} + \frac{3\tau_c}{1+{\omega_I}^2{\tau_c}^2} + \frac{6\tau_c}{1+(\omega_I+\omega_e)^2{\tau_c}^2} + \frac{6\tau_c}{1+{\omega_e}^2{\tau_c}^2}\right)$$

Equation 3. Longitudinal and transverse PRE rates is a system of one electron-one nucleus submitted to correlation under the specific time τ_c. Γ represents the difference between the specific relaxation time with and without presence of paramagnetic agent (e.g. T_2(no MTSL) – T_2(MTSL)).

The correlation time $\tau_c = ({\tau_e}^{-1} + {\tau_m}^{-1} + {\tau_r}^{-1})^{-1}$ is calculated out of the respective contributions from the electron relaxation (largely T_{1e}), the chemical exchange and the tumbling but the two last contribution can be neglected in the case of large proteins and nitroxide radicals.

As a result, the predominant effect will be faster T_2 relaxation of the nucleus detected in NMR, leading to homogenous line broadening phenomenon in a distance dependent manner. As for the NOE, it is inversely proportional the sixth power of the distance but with a much longer accessible range, up to roughly 25 Å [38]. The PRE can be measured by mean of intensity comparison between the signals of a same nucleus in the presence and absence of free electron [39] and transferred to distance restraints for structure calculations [40]. This has been applied successfully to large proteins [41] but is not straightforward since the flexibility of nitroxide spin-labels is high and leads to consequent space sampling of the free electron, more advanced approaches using prediction of these movements [42] or more rigid spin-labels [43] are still under development.

Not only site-directed spin labeling PRE can be useful in the study of proteins but also so-called solvent PRE in which the paramagnetic species is randomly distributed in solution. In the latter case, only residues being accessible to solvent will be affected by the PRE and as such it is very relevant for i.e. topology of membrane proteins [44] or interfaces of large complexes [45]. Spin probes directed to the inside of membranes can also be designed [46] and used as a complement for membrane proteins topology studies [47].

Notably under some circumstances not only T_2 but also T_1 of nuclei can be reduced via PRE, this is the case usually when metal-based spin probes are used such as Cu^{2+} or Fe^{3+} [48]. This phenomenon is particularly useful in order to be able to reduce the recycle delays of NMR experiments [49], at the conditions of not having too much homogenous line broadening from the T_2 contribution, thus impeding the resolution. Application of this phenomenon using Cu-EDTA however pushed the accessible range of sample concentration to the nanomolar scale, using recycle delays as short as 0.2s for a small protein [50].

Finally, it is notable that PRE is not the only effect arising from the presence of paramagnetic species and other phenomenon can be useful as well, like Residual Dipolar Couplings (RDC) coming from partial alignment of paramagnets with B_0 [38] or Pseudo-Contact Shifts (PCS) coming from the high CSA interaction of a nucleus with the anisotropic tensor of a paramagnet. This is usually not relevant for nitroxide spin-labels which exhibit isotropic tensors but becomes significant for lanthanide-based probes like Dy^{3+} or Tb^{3+}. It presents two advantages: the CSA on the contrary of *DD* scales with the inverse power of three with the distance, thus allowing to push the limit of restraints to roughly 40 Å and it has an anisotropic behavior, meaning that orientation information in respect to the paramagnet can be extracted as well [51].

Magic Angle Spinning (MAS) solid-state NMR

A way of overcoming the size limitation in NMR is to measure samples in the solid-state, where spins intrinsically have longer relaxation times because the inexistent tumbling does not interfere with relaxation mechanisms. Nevertheless, in that case no averaging of spin orientations in respect to B_0 takes place (again because of the inexistent tumbling) meaning that each spin contributing to the same signal is likely to have slightly different effective precession frequency and chemical shift, and as such exhibit a large and anisotropic distribution named the powder pattern. This large distribution of chemical shifts drastically impedes the resolution of solid-state spectra in the static case.

Note that the latter is true for the two components of spin relaxation CSA and *DD* (same as in the solution case), different orientations of detected spins and of their dipolar-coupled neighbors leading to modulations of the transitions and different chemical shifts. Interestingly both this terms in the spin system tensor contain at the first order the same dependence on the angle θ between the spin tensor and the external magnetic field: $3(\cos\theta)^2 - 1$. Therefore, these first order contributions to CSA and *DD* are averaged if the sample spins around an axis tilted by 54.74° from B_0 (called the magic angle) [52]. Nevertheless, while CSA is efficiently averaged by the magic angle, *DD* still contains a significant higher order inhomogeneity, part of which can be suppressed by the mean of making the sample spin around the axis of the magic angle [53]. If the spinning speed is high enough in magnitude to interfere with *DD* relaxation, sharp lines can be obtained, this is usually done in the range of 8 to 115 kHz and provides spectra of very good quality at very high spinning speed, even for ^{1}H-detection when the *DD* is very high [54].

In solid-state NMR, INEPT-based magnetization transfers which require a sufficient amount of flexibility are usually not efficient. Cross-Polarization (CP) [55] is a way to exchange magnetization from one spin to another in rigid systems. The principle is based on "spin-locking" both nuclei in the tilted frame (magic angle axis) by a pulse which keeps magnetization trapped in the new orientation. The result is a new rotation movement around the new axis, called nutation (by opposition of precession around B_0). This nutation frequency ω_1 depends on the gyromagnetic ratio of the nucleus and on the amplitude of the spin-lock pulse. Under spin-lock nuclei thus also exhibit splitting of their energy levels but with a much lower amplitude than Zeeman splitting. It is then possible to match the nutation frequencies of both nuclei at a resonant condition where dipolar cross-relaxation is allowed in an energy conservative manner: $\omega_{1A} \pm \omega_{1B} = n \cdot \omega_r$ where $n = \pm 1,2$ and ω_r is the MAS frequency [56].

Solid-state NMR usually prefers to make use of ^{13}C detection because they exhibit weaker *DD* than ^{1}H and thus have longer lived FID and better resolution. The Proton Driven Spin Diffusion (PDSD) [57] makes use of the different dipolar behaviors of ^{1}H and ^{13}C. After an initial use of ^{1}H-^{13}C CP, evolution of ^{13}C magnetization happens under ^{1}H decoupling (this preserves resolution in the indirect dimension), then ^{13}C magnetization is stored along the z-axis and decoupling is switched off in order to leave ^{1}H-^{1}H spin diffusion in the strong *DD* network happening and thus exchanging magnetization between ^{13}C exhibiting coupling to the ^{1}H dipolar network. Finally ^{13}C is detected under ^{1}H decoupling again in order to preserve resolution in the direct dimension. That way, use is made of the intrinsic resolution of ^{13}C and of the efficient magnetization transfer allowed by strong couplings between ^{1}H spins. This experiment couples ^{13}C with all its neighbors in protonated samples and is the most widely used experiment in MAS-NMR. In that respect it can be compared to the HSQC spectrum in solution, acting as a “fingerprint” spectrum for proteins.

Enhancing NMR sensitivity using Dynamic Nuclear Polarization

NMR is intrinsically limited due to the low sensitivity (low γ-ratio) of the observed nuclei. This fact leads to the need for pure, highly concentrated and isotopically enriched samples. Together with the measurement time and the cost of instrumentation it makes NMR a costly technique. It is especially true for challenging samples (e.g. membrane proteins, big complexes, toxic proteins), for which expression, purification, and/or the need of refolding is most of the time difficult and yields low amounts of sample.

Overcoming this issue, i.e. increasing sensitivity in NMR experiments can be done through different means: (i) optimization of sample preparation (discussed in the dedicated section below), (ii) optimization of NMR pulse sequences (discussed in the "key NMR and DNP features" section below) (iii) improvement of the hardware in terms of magnetic field (the higher B_0 and the higher the magnetization of spins) and electronics (more efficient micro-coils, etc.), (iv) lower temperatures leading to higher magnetization and more efficient electronics, and (v) use of spin-alignment transfer strategies [58]. The latter makes use of electrons, which have much higher magnetic susceptibility, in a similar manner as in PRE. Magnetization is transferred from electrons to nuclei in a way leading to hyperpolarization of the nuclei. Nevertheless it requires use of paramagnets, special compounds containing either long-lived triplet states of chemical bonds (para-hydrogen), light-induced exited states of coupled electrons (optical pumping) or unpaired electrons in metal conduction bands, complexes or radicals.

In this work the last case was used, i.e. magnetization transfer from unpaired electrons to nuclei, also called Dynamic Nuclear Polarization (DNP) [59]. The phenomenon was first proposed theoretically by Albert Overhauser in 1953 [12, 60] and proved experimentally by Carver and Slichter three years later in metals [61]. Nevertheless, it was more than 40 years later that the concept could be successfully applied to biomolecules in solution due to the work of Griffin and coworkers [62-66]. This section aims at presenting the mechanisms and the biomolecular applications of DNP.

General concept and experimental setup

The general concept of DNP is the transfer of magnetization from electrons to nuclei by cross-relaxation phenomena, in a similar fashion as in the NOE experiment (discussed in the sections dedicated to NOE and PRE above) [13]. The rate and thus efficiency of cross-relaxation is given by:
$W_0 = \frac{2\tau_c}{r^6(1+(\omega_A-\omega_B)^2\tau_c{}^2)}$ with $\tau_c = (\tau_e{}^{-1} + \tau_m{}^{-1} + \tau_r{}^{-1})^{-1}$ (also see Equation 2)
where τ_c is the correlation specific time of the system, τ_e its contribution from electron relaxation, τ_m from chemical exchange and τ_r from molecular tumbling.

In an ideal case with a cross-relaxation rate efficiency of 100%, the exchange in magnetization between electrons and nuclei should be proportional to the ratio of their energy population differences and thus to their gyromagnetic ratios (see section dedicated to PRE above for definition of the electron gyromagnetic ratio). Therefore the theoretical maximum enhancement or increase in nucleus magnetization is γ_e/γ_H=657 for ^{1}H and γ_e/γ_C=2615 for ^{13}C.

In reality two modes are possible, either τ_r dominates τ_c if the tumbling rate is fast (small molecules, high temperatures) or the contribution of the electron relaxation τ_e is dominant (big molecules, low temperatures leading to lower τ_r and longer τ_e). In the first case, the cross-relaxation is rather inefficient. In the second case, however, it gets very efficient at very low temperatures because T_{1e} gets short enough, dominating τ_c and increasing the cross-relaxation rate. Different mechanisms are possible to achieve this but in general, because of the higher population difference and higher relaxation rates of electrons, the allowed cross-relaxation transition would exchange magnetization from the nuclei

to the electrons. In order to get exchange in the other way, saturation of the electron resonant transition is needed [67]. Electrons however have much higher Larmor frequencies, not in the radio-frequency range but in the microwave range, which cannot be implemented using the standard NMR probe coils [59].

This has three implications: (i) for efficient DNP the samples have to be cooled down to very low temperatures (usually around 100 K), (ii) frozen samples do not tumble and thus use of solid-state NMR is required (together with MAS, CP, see above) and (iii) microwave irradiation has to reach the sample [68]. That is why the experimental setup for DNP is more complex than a regular NMR spectrometer. In addition to a wide-bore solid-state spectrometer (magnet, console, and computer), a cooling unit with cold transfer line to the probe, a microwave source with wave-guide to the probe and a suitable probe handling MAS, cooling and microwave irradiation of the sample have to be installed [69].

In practice the sample is cooled down to approximately 100 K in order to get decent DNP efficiency (enhancement factor on nuclei). This is achieved by precooling and pressurizing nitrogen gas before use for holding the sample in the probe (bearing), making it spin (drive) and keeping it cold (VT or variable temperature). These three gas lines are cooled in a chamber filled with liquid nitrogen. The temperatures used can be pushed down by the use of liquid helium exhibiting lower temperature and higher fluidity to about 25 K but this remains very costly and is not of common use [70].

The microwave irradiation used to saturate the electron spin transition has to be resonant with the electron Larmor frequency and thus tuned to the external magnetic field of the NMR spectrometer (see Table 5). For this, a gyrotron containing another magnet and an electronic tube through which a flow of electrons travel is used. The electron beam starts rotating when submitted to the magnetic field and thus produces resonant microwaves [71]. The microwaves are then guided to the probe in a corrugated waveguide and into the sample [72]. Efficient penetration of microwaves into the sample is actually thought to be one of the main limiting factors in DNP enhancement so far (see "key NMR and DNP features" section below). In order to maximize the number of electrons submitted to the microwave irradiation, sapphire rotors are usually preferred over conventional zirconium oxide ones for their better penetration.

B_0 (T)	^1H ω_0 (MHz)	e^- ω_0 (GHz)
9.4	400	260
14.1	600	395
18.8	800	527

Table 5. ^1H and electron Larmor frequencies corresponding to the three commercially available DNP spectrometers field strengths.

DNP mechanisms

The following section provides a summary of the different specific DNP mechanisms available [73] with a focus on the optimal B_0 field, microwave irradiation and radicals. These characteristics are summarized in Table 6. The different mechanisms are presented in historical order, which happens to correspond as well as to the number of electrons involved.

Mechanism	Condition	Field dependence	Microwave requirement	Radical design
Overhauser effect	$\omega_{MW}=\omega_e$	Scales with B_0	Low power	Narrow lines Short T_{1e}
Solid effect	$\omega_n<\delta,\Delta$ $\omega_{MW}=\omega_e\pm\omega_n$	Scales with B_0^{-2}	High power	Narrow lines
Cross effect	$\delta<\omega_n<\Delta$ $\omega_{e1}-\omega_{e2}=\omega_n$	Scales with B_0^{-1}	$\omega_{MW}=\omega_e$ Low power	Broad line biradical with fixed d_{ee} and θ_{ee}
Thermal mixing	$\omega_n<\delta$	Scales with B_0^{-1}	$\omega_{MW}=\omega_e$ Low power	Broad line High concentration or D_{ee}

Table 6. Summary of DNP mechanisms' characteristics (ω_{MW}, frequency of microwave irradiation; ω_e, electron Larmor frequency; ω_n, nuclear Larmor frequency; δ, electron transition homogenous line broadening; Δ, electron transition inhomogeneous line broadening; d_{ee}, electron-electron distance; θ_{ee}, electron-electron angle, D_{ee}, electron-electron dipolar coupling magnitude)

Overhauser effect

The first DNP mechanism was described by Overhauser in 1953 [12] and experimentally proved by Carver and Slichter [61]. In a system of two coupled spins (in that case a hyperfine electron-nucleus coupling) direct cross-relaxation through ($e_\alpha I_\beta \rightarrow e_\beta I_\alpha$) or double-quantum ($e_\beta I_\beta \rightarrow e_\alpha I_\alpha$) transitions is ideally possible [12]. In that case however the probability of such a transition is thermodynamically unlikely (so-called forbidden transitions). When the electron transition resonance is saturated by microwave irradiation, however, this becomes more likely as compared with the electron single-quantum transition though.

Notably, as the Overhauser effect directly relies on the relaxation rates of the two-spin system, it works better if temperature, fluidity, external magnetic field, etc. are high. So far Overhauser DNP was mainly used in solution, where is becomes rather efficient at high fields (e.g. from nitroxides to water) [74]. Recently, solid-state DNP research has also focused on this mechanism. Because of the very different properties as compared to the other DNP mechanisms conventionally used, it could be a way to overcome the field and resolution barrier faced so far (see below) [75].

Microwave power has to be tuned to the electron Larmor frequency and the power does not need to be particularly high because the electron single quantum transition is thermodynamically favorable, as such Overhauser effect conditions are rather easy to achieve at high fields.

In terms of radical design, the electron resonance properties are not very critical but narrow lines are preferred because they are easier to saturate with the available microwave sources. As such, carboxides are a good alternative to nitroxides. Optimization of electron relaxation properties is very important, in nitroxides the hyperfine coupling with ^{14}N plays an important role, in carboxides delocalization of the unpaired electron over several carbon atoms is a good way to enhance electron relaxation, like in 1,3-bis(diphenylene)-2-phenylallyl (BDPA) [76].

Solid effect

The solid effect has been more widely applied so far. It was discovered in 1957 by Jeffries [77], which is a one electron to one nucleus magnetization transfer mechanism. In a similar way as for the Overhauser effect, it directly relies on direct zero- ($e_\alpha I_\beta \rightarrow e_\beta I_\alpha$) or double-quantum ($e_\beta I_\beta \rightarrow e_\alpha I_\alpha$) flip-flop magnetization exchange based on cross-relaxation. Here the mechanism relies on dipolar coupled

electron-nuclear two-spin rigid system. Because solid effect directly relies on Larmor frequencies of the two elements of the system, it scales with the inverse square of the field. While these transitions are forbidden, they can be forced by microwave irradiation. Nevertheless, this is a time-independent effect which requires high microwave power to compensate for the unfavorable energy exchange [78, 79].

It can thus be directly understood that the optimal microwave condition for solid effect DNP to achieve maximal positive enhancement is the sum between electron and nucleus Larmor frequencies (double quantum condition). A precise tuning and high power of microwave irradiation is required, which is currently rather difficult to achieve with gyrotrons for high fields.

In order to achieve maximum enhancement factors, either zero- or double-quantum transition have to be implemented. In electron system containing large homogenous or inhomogeneous broadening, selection of one of these is practically difficult to achieve and thus the two transfer conditions tend to cancel each other. Indeed radicals with very narrow lines such as trityl based carboxides [76] are preferred. Nevertheless nuclear Larmor frequency has to stay much lower than electron broadening in order to keep efficient microwave saturation of the transitions ($\omega_n<\delta,\Delta$).

Cross effect

The third DNP mechanism, proposed in 1967 by Hwang and Hill [80] and proved right away [81] is the so-called cross effect. Cross effect, on the contrary of the two previous mechanisms, is a two electrons-one nucleus process. When the difference (or the sum) in Larmor frequencies between two dipolar coupled electrons corresponds to the nuclear Larmor frequency ($\omega_{e1}-\omega_{e2}=\omega_n$ or $\omega_{e1}+\omega_{e2}=\omega_n$) the allowed electron single quantum transitions are degenerate with forbidden zero- or double-quantum transitions of the three spin system ($e_{1\alpha}e_{2\alpha}I_\beta=e_{1\alpha}e_{2\beta}I_\alpha$; $e_{1\alpha}e_{2\beta}I_\beta=e_{1\beta}e_{2\alpha}I_\alpha$ and $e_{1\beta}e_{2\alpha}I_\beta=e_{1\beta}e_{2\beta}I_\alpha$). The energy diagram of such a system is exemplified below (see Figure 12). In this case three spin magnetization exchange through energy-conservative flip-flop transition is possible [82-84].

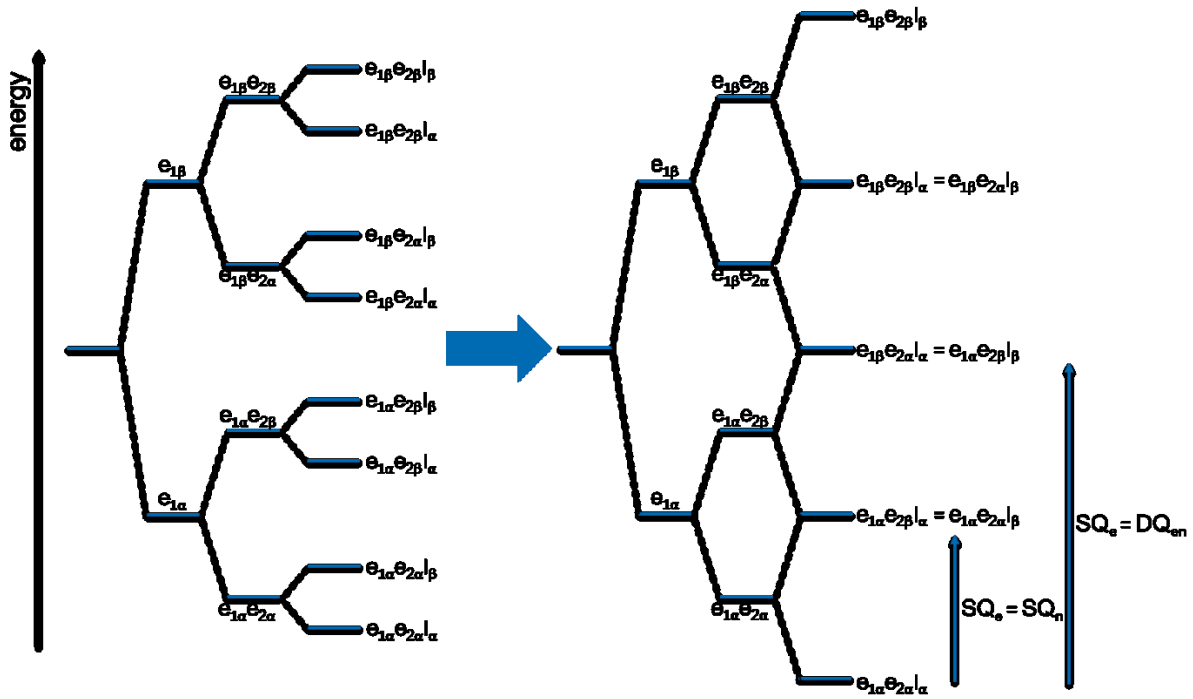

Figure 12. Energy diagram of a dipolar coupled three-spin electron-electron-nucleus system out of (left) and in the Cross effect condition (right). Examples of degenerated transitions are shown.

As magnetization transfer in this case happens through the mean of allowed single quantum electron transitions, the microwave irradiation does not have to be very high. It has however to be tuned

to the resonant frequency in order to achieve sizeable enhancements because the probability of having couple of electrons with the right orientation is rather low (this is compensated by MAS level crossings, see below).

The radicals for cross effect DNP represent the main limiting factor and have to be designed carefully. Biradicals with defined electron-electron dipolar coupling magnitude (distance and tensor orientation) as well as relaxation properties (longer T_{1e}) are preferred. They also need to have large inhomogeneous electron transition broadening (larger than the nuclear Larmor frequency at least) in order to achieve cross effect condition [85]. For this reason, enhancement scales with the inverse of the field (because of reduced homogeneous line broadening). Nevertheless, homogeneous line broadening has to be lower than nuclear Larmor frequency because spectral overlap leads to destructive interferences of enhancements like in the Solid effect case. Condition is therefore: $\delta<\omega_n<\Delta$. See below for more details on cross effect radicals.

Thermal mixing

Thermal mixing is a thermodynamic description of DNP from a high number of electron spins to one nucleus. This mechanism is likely to be dominant at limited fields, very low temperatures (typically under 10 K) and high electron density because the dipolar network among electron spins has to be very efficient. The mechanism was proposed in 1968 [86] and relies on thermal contact between the nuclear Zeeman system and the electron dipolar broadening system. For this reason it requires homogenous, dipolar-broadened electron transitions. This is found for instance in nitroxides containing one electron (TEMPO-like) at rather high concentrations, when electron-electron cross-relaxations are very efficient and make the inhomogenously broadened electron transition virtually homogenous over time [87]. In the likely case where the electron transition homogenous broadening δ is higher than the nuclear Larmor frequency ($\delta>\omega_n$), three spin flip-flop energy conservative processes are possible from the electron coupling bath to the nuclei in a similar manner as in the cross effect. The latter also implies that the enhancement factor scales with the inverse of the external magnetic field [88].

Microwave irradiation here serves as a mean to provide a non-equilibrium magnetization gradient across the broadened electron transition in a first step, which will relax through the three-spin energy exchange process. As such, off-resonant electron Larmor irradiation is needed, preferably near to the center of the broadened transition where the greatest density of spin packets resides.

Radicals have to be optimized for having either a large homogenous broadening (which is very unlikely at high fields) of electron transition or an efficient dipolar cross-relaxation across large inhomogeneous broadening as discussed above. In practice, high concentrations of nitroxides are used.

DNP under Magic Angle Spinning

All the aforementioned mechanisms give a theoretical framework for understanding DNP processes. They are however experimentally valid only in static cases which is not relevant for bio-applications because magic angle spinning is used. Under MAS all the energy levels are mixed and their values change according to the angle between the external magnetic field and the spin tensor over a rotor period. Thus static conditions are not valid anymore.

We will consider the solid and cross effect cases which are most widely used in solid-state DNP. In these two mechanisms, some precise resonance conditions have to be achieved, in MAS-driven DNP they are attained as a rotor event rather than during the whole experiment time. These events constitute energy level crossings or anti-crossings. If spinning speed if sufficient, these crossings are adiabatic and thus can lead to magnetization exchange without disturbing the global energy state of the system.

Different rotor events contribute to the build-up of magnetization. The relevant ones are: (i) electron Larmor events when microwave irradiation reaches the single quantum coherence of the electron ($e_\alpha \rightarrow e_\beta$ or $e_\beta \rightarrow e_\alpha$), (ii) nucleus Larmor event when microwave irradiation reaches the single quantum coherence of the nucleus ($I_\alpha \rightarrow I_\beta$ or $I_\beta \rightarrow I_\alpha$) and (iii) solid effect event when microwave irradiation reaches the zero- or double-quantum coherence of the coupled system ($e_\alpha I_\beta \rightarrow e_\beta I_\alpha$ or $e_\beta I_\beta \rightarrow e_\alpha I_\alpha$) or cross effect event when nuclear system and two-electron system reach resonance ($e_\beta e_\alpha I_\beta \rightarrow e_\alpha e_\beta I_\alpha$ or $e_\alpha e_\beta I_\beta \rightarrow e_\beta e_\alpha I_\alpha$ and $e_\beta e_\alpha I_\alpha \rightarrow e_\alpha e_\beta I_\beta$ or $e_\alpha e_\beta I_\alpha \rightarrow e_\beta e_\alpha I_\beta$). All these events are likely to happen during a rotation period leading to, respectively, electron spin saturation, nuclear spin saturation and electron-to-nucleus magnetization exchange (or the other way around, so-called depolarization, see below). Together with electron and nucleus relaxation processes, their probability and efficiency define the enhancement obtained on nuclei [89-91].

In fact, the presence of MAS-driven mechanisms of DNP is the reason why the enhancements obtained experimentally are rather robust against the microwave tuning, the cross effect condition, etc. [92] Nevertheless, complete theoretical understanding and proper simulations are still deficient, rendering some predictions difficult. For instance, the field dependence of cross effect DNP under MAS (also discussed below) is not fully understood yet [93].

Other considerations in cross effect DNP

This section's goal is to underline some key features of cross effect DNP and sample preparation of biomolecules for cross effect DNP measurements, which is the mechanism used in the present work (see Chapter V and Chapter VI).

Development and choice of the radical

As pointed out above, the choice of the unpaired electron source, i.e. radicals in the case of most bio-applications of DNP, is critical. Especially in the case of cross effect DNP where two electrons with precise characteristics are required. In the early days of DNP nitroxide monoradicals like (2,2,6,6-tétraméthylpipéridin-1-yl)oxy (TEMPO) were used. Nevertheless high concentrations were required because the average electron-electron distance has to be lowered in order to achieve electron-electron dipolar coupling [94]. Soon, more robust biradicals that can be used at lower concentrations and still maintain sizable cross effect DNP were developed. Besides, lower concentrations also lead to lower signal quenching (T_2 PRE, see above) because distances between electrons and target molecules are on average lower. Originally, simple chemical ligation of two TEMPO moieties through polyethylene glycol (PEG) of different length was used, the so-called BTnE series [85]. Careful investigation of the series as well as theoretical description of those [67] lead to the following conclusions: (i) use of nitroxides is favorable because the ^{14}N hyperfine coupling lead to large anisotropic broadening, (ii) electron-electron distance is critical for optimal dipolar coupling (BT2E with a distance of approximately 12.8 Å lead to the best results), (iii) orientation of the two anisotropic electron tensors is also important, with the best results achieved at approximately 90° (more rigid linkers were developed for 1-(TEMPO-4-oxy)-3-(TEMPO-4-amino)propan-2-ol (TOTAPOL) [95] and bis-TEMPO-bisketal (bTbK) [96]) and (iv) longer electron relaxation times (T_{1e}) provide better enhancement factors. Removal of relaxation sink acting methyl-groups in TEMPO for more bulky or deuterated groups is a possible solution for the latter. In that respect, deuterated versions of TOTAPOL and bTbK were developed [97, 98] as well as bTbK with hydropyran groups (bTbK-py or SPIROPOL) [99] and TOTAPOL with the same substituent named AMUPol [100]. The latter is currently the best performing biradical still soluble and as such applicable to the study of biomolecules. Derivatives of bTbK with very bulky groups were developed as well but are not soluble. Nevertheless, they have shown the best enhancements so far with the best performing one being TEKPol2 [101].

Other approaches in the field of radical development are also under consideration. One of those is to improve cross effect DNP using two radicals or a biradical containing two electrons of very different

properties, namely a nitroxide of broad transition and a carboxide of very sharp transition in the hope of getting the best of the two mechanisms (easy electron saturation by microwaves and easy reaching of cross effect conditions). This has been proven to work [102] and is promising also in the scope of the two mechanisms solid effect and cross effect contributing simultaneously to the enhancements (see below) [91, 93, 103]. Another way is to use unpaired electrons from metals in metallo-organic complexes such as Mn^{2+} or Gd^{3+}. The understanding of such electron spin behavior is more complex because they exhibit higher spin quantum numbers *S* (5/2 and 7/2, respectively). This has been proven to work as well and is under further development [92, 104].

Choice of the external magnetic field

Three types of DNP spectrometers, with different external magnetic fields, are currently commercially available (see Table 5) [69]. With the exception of the Overhauser effect, DNP usually becomes less efficient with increasing magnetic fields because of the lower broadening of electron transitions. In the case of biomolecular applications spectrometers are tuned to the Cross effect and the same mechanism under MAS is thought to be predominant. The field dependence has however been measured to be more dramatic than the predicted B_0^{-1} for cross effect (between B_0^{-1} and B_0^{-2}) [93], it is very likely that both cross effect and solid effect contribute with significant levels to the observed enhancements [103].

Of course, higher magnetic fields also exhibit the advantage of providing longer relaxation times for both electron and nuclei. While the first can partly overcome loss of enhancement for some radical designs or using Overhauser DNP (see below), the second is critical because DNP generally suffers from a lack of resolution. This loss of resolution impedes most of NMR applications (such as single amino-acid assignment in proteins) and comes from two factors: (i) nuclear inhomogeneous line broadening due to freezing out of different conformations [105] and (ii) homogeneous line broadening (T_2 reduction) due to lower temperature and also in some cases to PRE from the electron [106]. Going to higher fields can reduce the homogeneous contribution to an insignificant level and as such, good resolutions are observed at high fields in systems that are not affected by inhomogeneous line broadening (microcrystals, very rigid proteins or complexes) [107-109].

Sample preparation

Sample preparation is a critical step in DNP, especially in the case of biomolecules. First the choice of the radical used according to the underlying DNP mechanism, as discussed above, but also its concentration and behavior are to be taken into account. Optimizing concentration of radical is an interplay between providing enough source of polarization in the sample (to attain sizeable enhancement) and keeping the average electron-to-target molecule distance as low as possible (to reduce the PRE) [110]. While 10 to 20 mM TOTAPOL are conventionally used, for better performing radicals such as AMUPol as low as 2.5 mM has been shown to provide a good compromise. Additionally, statistical distribution of radicals throughout the sample is not always obtained, especially in the case were detergents or lipids are involved. For instance, TOTAPOL has been shown to be rather hydrophobic and thus is prone to aggregation [108]. Besides, it interacts with amyloid fibrils [111] and other proteins with lower affinity [112] or membranes and detergents [113], providing much higher local concentrations for membrane proteins and sometimes impeding their investigation under DNP. Note that the effect can be reversed for soluble proteins, encapsulating TOTAPOL into detergent micelles and thus creating a barrier between radical and target proteins [114].

Secondly, very low temperatures (usually in the order of 100 K), way below the protein phase transitions (200-230 K), are used and as such water ice crystals formation has to be avoided. Protection of the sample by high content of cryoprotectant such as dimethylsulfoxyd (DMSO) or glycerol in order to form a robust glassy matrix is proved very efficient [94]. Glassy matrix formation also has the

property of avoiding radical clustering and thus achieving optimal polarization distribution [108]. In some cases, such as loss of crystallinity and thus of resolution in some samples, a matrix-free approach might be preferred but careful handling of the freezing procedure [105] and radical distribution, e.g. via the use of gluing agents like trehalose providing high local concentration and sufficient barrier against PRE can be used [115, 116]. Another approach is to use *in situ* sedimentation during MAS of both protein and radical in order to mimic a glassy behavior [112].

Lastly, it is very unlikely that all electron transitions are irradiated by microwaves during an experiment. In fact, only a small fraction is irradiated and thus polarization distribution and related enhancement factors can be rather poor [103]. Therefore another mechanism of magnetization relay throughout the sample is needed, and the most efficient is ^{1}H-^{1}H spin diffusion in a sufficiently tight coupled ^{1}H network [117]. Here also, optimization of ^{1}H density is not so straightforward because an interplay between efficient magnetization distribution to the largest number of targets and intact electron resonance properties has to be found [118]. For all the aforementioned reasons, conventional studies of biomolecules under DNP are made using so-called "DNP juice" containing 60% glycerol and 10% ^{1}H (60% glycerol-d_8, 30% $^{2}H_2O$, 10% $^{1}H_2O$) [94].

As described above, the relaxation rates of both electrons and nuclei are very critical in DNP. Removal of relaxation sinks such as methyl groups (exhibiting fast dynamics even at very low temperatures) in both the radicals and the target [98, 119] via e.g. deuteration usually yields better enhancements. Moreover, the presence of dissolved molecular oxygen is known to enhance relaxation processes and as such is detrimental. Better DNP enhancement can generally be obtained by reducing the amount of oxygen in the sample using several freeze-thaw cycles before injecting in the spectrometer [87, 120].

Key NMR and DNP features

Efforts in DNP usually aim at optimizing the enhancement factor, called ε, which is defined as the ratio of NMR intensity of the detected nucleus with and without microwave irradiation. It is however not the only relevant factor since other processes take place when performing DNP-MAS-NMR. Instead, an absolute sensitivity ratio (ASR) can be defined [121], taking into account: (i) the DNP enhancement factor ε, (ii) the sensitivity gain due to lower temperatures via increased Boltzmann magnetization, (iii) the gain in signal per unit time due to decreased T_1 from PRE [122], (iv) the reduction of signal due to decreased T_2 from PRE (signal bleaching) [106], (v) the better signal-to-noise due to better performing electronics at low temperatures and (vi) the specific features due to the pulse sequence used.

While signal bleaching arising from homogeneous line broadening of observed nuclei upon T_2 PRE is a well-known phenomenon [48] and is present both with or without the presence of microwave irradiation, another process can lead to misinterpretation of DNP enhancement factors: the so-called depolarization effect [123-125]. Under MAS and without microwave irradiation, some of the described energy level anticrossings still happen, namely electron Larmor, nucleus Larmor and Cross effect events (see above). Without microwaves to drive electron magnetization to saturation, they actually act as a sink, thus reducing nuclear magnetization. This is why intensity of microwave-off spectra is usually measured to lower values, and, as such, leads to higher measured ε. The right reference for DNP enhancement factor measurement should be a sample prepared without radicals (keeping in mind that radicals do have other effects included in the definition of ASR). Nonetheless, comparison between DNP performances is usually done using ε.

The pulse sequences chosen and especially the types of magnetization transfers are also of importance. For example, use of ^{1}H-^{13}C instead of direct ^{13}C 90° pulsing has been shown to provide better signal despite the higher enhancements theoretically obtainable for ^{13}C (up to 2615) [126]. This is partly due to much better distribution of polarization through ^{1}H-^{1}H dipolar network (see above) but

also to the fact that DNP setups are equipped with a gyrotron tuned to electrons-^{1}H Cross effect condition using TOTAPOL or AMUPol and not to electrons-^{13}C condition. Higher order processes are also relevant when considering more the canonical three-spin model of DNP, for instance heteronuclear four-spin ($e^{-}/e^{-}/^{1}H/^{13}C$) cross effect conditions ($\omega_{e1}-\omega_{e2}=\omega_{H}\pm\omega_{C}$) [127] and enhanced heteronuclear cross relaxation [128] have been observed leading to positive or negative additional ^{13}C hyperpolarization. Our understanding of "real" DNP, i.e. taking into account all factors and spins present in a real sample, is still very poor because of the lack of theoretical models and realistic simulation procedures.

Another factor which has been shown to be extremely critical in order to achieve DNP enhancement factors close the theoretical maxima is how microwave can penetrate the sample and efficiently irradiate and saturate electron spins. Efficient saturation has been discussed before but efficient penetration and diffusion into the sample is limiting. The use of sapphire rotors instead of conventional solid-state NMR zirconium oxide rotors helps since they exhibit better microwave penetration. Moreover introducing diamagnetic particles able to relay microwaves efficiently inside the sample (e.g. NaCl or KBr crystals) has provided so far the best enhancements factors observed (515 on ^{1}H using TEKPol in TCE) [120].

New features and perspectives

One of the limitations of DNP so far has been the loss of enhancement when increasing external magnetic fields. Nevertheless, recent development of cross effect radicals with more robust relaxation properties (TEKPol series) [101] and design of Overhauser methodologies applicable to MAS-NMR [74] enabled DNP studies up to 800 MHz ^{1}H with good resolution and fair enhancement factors.

When reaching the possibilities described above, one main issue remains, i.e. the inhomogeneous line broadening of samples at very low temperatures with different conformations frozen out [105, 108]. The resulting lack of resolution [129, 130] is not very dependent on the field strength and as such can mainly be overcome by increasing temperatures. This is of course possible but usually dramatic for the enhancement because electron longitudinal relaxation times falls beyond the lower limit for efficient DNP. Use of matrices exhibiting smoother glass transitions such as *ortho*-terphenyl (OTP) and robust radicals such as TEKPol is possible [131] ($\varepsilon\leq80$ on ^{1}H) but not applicable for biomolecules. Very recently, enhancements up to 15 at 200 K have been reported on biomolecules in conventional conditions using AMUPol and CD_3-TOTAPOL (note however that it is reported to be very sample-dependent) [132].

While conventionally radicals are dissolved in the sample to obtain a statistical distribution, and homogenous hyperpolarization throughout the sample, other approaches using localized [133-136], covalently-bonded [137-140] or targeted [141, 142] radicals are also possible. This presents several advantages such as better handling of PRE effects and access to specific information and is an interesting approach for the study of proteins in their native environments (see Chapter V).

For a long time the idea of using pulsed microwave irradiation instead of continuous wave in DNP has been around [73] but its implementation has been impeded by the design of high frequency microwave sources. Nevertheless some significant advantages could be obtained. For instance, very short hyperpolarization build-up times using electron spin-lock $T_{1\rho}$ build-up in the order of ns instead of the conventional T_1 build-up of approximately a second have been successfully carried out at 0.34 T (NOVEL experiment) [143]. Implementation of this at high fields is still not possible but this would open the frontiers of DNP to implementation of electron in the pulse sequences.

Biomolecular applications of DNP

In addition to beautiful applications in the field of material sciences and catalysis [144, 145], DNP has been applied to numerous types of biomolecules including soluble, membrane and fibrillar proteins as well as nucleotides, e.g. reviewed in [146, 147]. In general, DNP studies have been employed in two respects: (i) study of low temperature dynamics in proteins making use of the required temperatures [148] applicable to flexible or intrinsically disordered proteins (see Chapter VI) and (ii) study of very rigid molecules in which inhomogeneous line broadening is not such an issue [109]. Here, the focus will be put on three main strengths of DNP, i.e. the study of big complexes, low populated states and proteins in their native environments.

General overview

One of the main areas of application for solid-state NMR is the structural study of amyloid fibrils which are relevant species of fibrillated proteins or peptides in different classes of degenerative diseases, and DNP also has participated in the field. After prove of feasibility on the core peptide of the yeast prion Sup35 GNNQQNY [107, 149], several studies have followed including the SH3 domain of the PI3 kinase [150], a segment of the transthyretin (TTR) protein [151] and the Alzheimer relevant peptide Aβ1-40 [152]. DNP allowed to get an increased number of intermolecular contact or torsion angles in fibrils using mixed labeling schemes, and to probe transient, metastable, species throughout the fibrillation pathway at temperature lower than 30 K.

Another area of research benefiting from DNP is the structural study of nucleotide arrangements. Unusual DNA structures inside the virion of the Pf1 bacteriophage have been resolved [153] as well as intra-complex conformational states of the full-length hammerhead ribozyme HHRz [154].

Nevertheless, it is probably the field of membrane proteins which benefitted the most from DNP developments. The first big application was the observation of Lysine side chain chemical shift perturbations of the Schiff base during the photo-cycle of bacteriorhodopsin (bR) [66, 155, 156]. In general proteins of the rhodopsin class have been the most studied because they exhibit higher rigidity as compared to most of the other membrane proteins, especially G-protein coupled receptors (GPCR). The protein proteorhodopsin (PR) has been investigated in membranes, with successful structural characterization of the retinal structure in different color-tuned mutants [157] and monomer-to-monomer restraints in PR pentamers using mixed ^{13}C- and ^{15}N-labeling schemes [158]. Using the same approach, retinal-to-protein correlations have been elucidated in the optogenetic-relevant channelrhodospin-2 (ChR2) [159]. Note that localized DNP methodology was also applied to the sensory rhodopsin (ASR) [139] as well as to the potassium channel KcsA [137]. A similar method based on reconstitution of a Cross effect biradical upon dimerization of two mono-radical conjugated monomers allowed to follow dimerization of gramicidin A in membranes [140]. Finally, use of DNP in orientated membrane MAS-NMR on model transmembrane peptide hΦ17W opened the way to use of residual dipolar couplings in DNP structural studies of membrane proteins [160].

Big complexes

DNP-MAS-NMR overcomes some of the challenges related to big proteins and big biomolecular complexes (size-limitation, need for high amounts of product, etc.). The first application of DNP on such a sample was shown on an entire 800 kDa ribosome [161], and then mainly applied to the protein complexes forming bacterial secretion needles. Differential rigidities in the protein MxiH were investigated in reconstituted type 3 needles [162] and even study of type 4 needle core complexes in entire bacteria has been successfully demonstrated [163]. This area has been pushed by the high overall rigidity and homogeneity of such complexes leading to fair resolution even at low temperatures

[109]. Recently other applications have been shown, e.g. detection of isolated conformers of the CA capsid protein in HIV-1 capsids [164] and region-specific dynamics study in the wild-type epidermal growth factor receptor (EGFR) in cells [165].

Low populated states

Sensitivity enhancement of DNP is also useful in the effort to detect low populated states of biomolecules, for instance metastable species and thermodynamically or kinetically unfavored conformations. Studies on the neurotoxin II bound to nicotinic acetylcholine receptor (nAChR) [166], signal peptides bound to the SecYEG translocon [167], drugs bound to the influenza A proton transporter $M2_{18-60}$ [168], tetraphenylphosphonium (TPP+) bound to the multidrug efflux protein EmrE [169] and signals peptides inside the ribosome tunnel [110] were carried out. Apart from detection of weakly bound ligands, DNP also allowed investigation of low-populated structural players in big assemblies such as the expansin protein in plant cell walls [170] and the signal peptide SP1 in HIV-1 capsids [164]. Note that while most of the time such studies are conducted using specific labeling of the ligand or low-populated species, the use of targeted DNP could achieve same results in native, uniformly labeled cases (see Chapter V).

Proteins in native environments

DNP can be used as a way to detect proteins in their native environments. Here the "low populated" species is the protein compared to the background formed by all other components of the environment. For instance, study of the Mistic protein in native bacterial membranes [171], the outer membrane protein PagL in cell envelopes and whole cells [172], and the cytochrome b5 in whole cells [173] have been demonstrated. Conformational investigation of the fungal prion Sup35 in lysates [174] and dynamic studies on wild-type type 4 secretion system bacterial needle [163] and EGFR [165] in whole cells also have been successfully achieved. These approaches rely on introduction of labeled protein in unlabeled environments or overexpression of targets with change of medium for a labeled one after induction, but targeted DNP has been demonstrated to be a simple and robust approach as well and has been able to completely remove the background signal in Bcl-x_L protein spectra acquired in cell lysate ([141], also see Chapter V).

Bio-systems and investigated proteins

Biophysical methods can be developed and tuned in order to answer virtually any kind of scientific question. Nevertheless, sample preparation or applicability of those methods to the desired targets constitute limiting factors that need to be overcome. Knowledge of the underlying biochemistry and biology is therefore desirable in order to have an overview on the significance of experiments, the possibilities and limitations in sample preparation and the power and pitfalls of the methodologies in respect to the sample and question.

This section aims at briefly summarizing the bio-systems used in the work (expression systems and refolding of membrane proteins, i.e. membrane mimetics) as well as the models and targets of the different chapters in terms of biological background and state-of-the-art biophysical studies.

Expression systems

Ideally, target proteins should be expressed in cell culture of the right organism and right cell type according to each scientific question. Sometimes however, this is not achievable because of extremely low expression levels or impossibility of cultivating the cell type outside of its host organism. Therefore numerous ways to express any kind of protein in model systems have been developed. By far, the most common is *E. coli*, however also eukaryotic systems such as human cell culture transfectable with plasmid DNA (e.g. human embryonic kidney or HEK 293 cells) [175] or insect cells infectable by *baculoviridae* carrying DNA (e.g. *Spodoptera frugiperda* or *Sf*9 cells) [176] were developped. These systems have the advantage of carrying all the machinery of eukaryotic organisms including post-translational modifications (phosphorylation, glycosylation, lipidylation, etc.) often critical for folding and activity of proteins. They however have the disadvantage of yielding rather low amounts of proteins and of being very sensitive to growth media, making it difficult to express isotope-labelled targets. Thus, the focus here will be on two other expression systems, i.e. bacterial culture and cell-free expression.

Bacterial recombinant expression

The most widely used and in many cases most effective protein expression system relies on the use of the biochemical machinery in prokaryotic bacterial strains (e.g. from *E. coli*). Basically, DNA is transfected into the bacteria (bacterium transformation) and overexpression of the carried gene is chemically induced. Then bacteria are lysed and the target protein is purified. This requires several key steps: (i) preparation of plasmid DNA containing a *lac* promoter, an antibiotic resistance feature and the target gene, (ii) competent bacteria for transformation via e.g. heat shock or electroporation, (iii) a suitable bacterial strain for expression of the target and (iv) most of the time a construct containing affinity tags in order to be able to purify the target from background biomolecules [177]. The antibiotic resistance is used to select bacteria carrying the plasmid DNA from the ones that do not, *lac* operon is (usually) used because it can be activated easily by introduction of a lactose analogue, isopropylthiogalactopyranoside (IPTG) leading to overexpression of the plasmid gene.

The main issue in bacterial recombinant expression lies in the potential difficulty for prokaryotic organisms to express heterologous proteins that might be toxic for them. This is especially true when e.g. viral or membrane proteins are concerned. Even though, additionally to the original *E. coli* BL21 strain developed [178], a lot of derived strains exhibiting different properties e.g. enhanced membrane expression in the C41 and C43 strains [179] and protocols using different bacteria were designed, it still remains challenging to express some targets by this mean.

Cell-free expression

In the case of targets being toxic to the cells, *in vitro* expression setups containing the necessary biochemical machinery were developed. These so-called cell-free systems are based on the preparation of a cell-extract, mainly containing the host ribosomes in an active form. Additional enzymes, plasmid DNA and transfer RNA are added to form a reaction mixture. Another mixture containing energy sources and amino acids is also prepared. This feeding mixture can be separated from the reaction mixture, either by bilayer formation, or by a dialysis membrane in order to make the process last longer and improve yields [180]. Translation and transcription can be done in the same batch in some cases, e.g. *E. coli* cell-free or the latter is done independently beforehand using a simple polymerase reaction.

Cell-free expression extracts can be prepared from nearly all organisms but so far most systems have been developed using prokaryotic *E. coli* [181] which usually exhibits the best yields and using eukaryotic rabbit reticulocytes or wheat germ [182]. The last one provides fair yields (still significantly lower than *E. coli*) but has the ability to produce proteins that are toxic to prokaryotic ribosomes like some viral proteins and the advantage of having slower translation kinetics, which sometimes provides better folding of membrane proteins. *E. coli* based cell-free expression was the selected expression system in order to produce one of this work's target proteins, i.e. Barttin (see Chapter VII).

Membrane mimetics

For trivial reasons, membrane proteins are not well folded and thus not active when alone in water-based buffers, or even not soluble at all. Therefore, additional components, providing the required hydrophobic environment, become necessary. Membrane mimicking systems have been reviewed extensively both for biochemical and for NMR applications [183-186]. The paradigm relies on finding a system adequately mimicking natural membranes in terms of chemical content and physical properties but forming the smallest particles possible if solution NMR is to be used (for the reason explained in the dedicated section above). As such, over the time a number of systems have been developed. Here, a non-exhaustive list is presented.

Detergent micelles

By far the most simple and popular method in membrane protein solubilization for NMR is the use of surfactants (or detergents) [187]. Those small chemical compounds display a hydrophobicity gradient between a hydrophilic head and a hydrophobic tail and can be tuned to different surfactant powers. Nevertheless they stay rather small and thus soluble in high concentrations, up to a critical point where supramolecular assemblies form. Different assemblies are possible, the most common and useful being micelles, which form just above the critical micelle concentration (CMC). Micelles are nearly spherical arrangements of many detergent molecules with their polar heads outside of the sphere and their hydrophobic tails buried inside. Micelles are usually rather small (4-6 nm in diameter) and able to solubilize membrane proteins by shielding their exposed hydrophobic parts with detergent tails inside the sphere.

Notably, the static view of a sealed sphere is not close to the truth when micelles are concerned. In fact, detergent molecules are always exchanging between the micelle and a pool of soluble monomeric detergents at rather high rates. This is the reason why often detergents are detrimental to proper folding and activity of membrane proteins. They have a strong destabilizing [188] and sometimes denaturation effect [189]. Some very strong detergents like sodium dodecylsulfate (SDS) are thought to form extended assemblies with proteins, rather than well-packed micelles in the presence of proteins [190]. Some membrane proteins exhibit very low stability in micelles (see Chapter VII). Additionally, detergents are by composition and structure very far from natural lipids occurring in native membranes

and do not mimic in a good way neither chemical content (length, charge distribution, etc.) nor physical properties (curvature, high exchange rate, etc.).

Despite all these limitations, detergents micelles remain the easiest and best performing platform for solution NMR studies of membrane proteins. They can provide spectra of very good quality if detergent type and concentration is tuned correctly [191], help to improve the quality of data acquired from more advanced membrane mimetics [192] and are of use when the outcome can be compared with more native-like systems [193] or when activity assays can be performed. In the presented work two detergent micelle types have been used: (i) dodecylphosphocholine (DPC) in the study of OmpX as a "good quality" NMR data set positive control (see Chapter IV) and (ii) *N,N*-dimethyldodecylamine *N*-oxide (LDAO) after detergent screening in the study of Barttin (see Chapter VII). The main characteristics of these two detergents can be found below (see Table 7) [194, 195].

Detergent	Critical micelle concentration (mM)	Aggregation number	Micelle diameter (nm)
DPC	1.1	80	4.2
LDAO	2	76	3.7

Table 7. DPC and LDAO detergent micelle canonical characteristics

Bicelles and liposomes

To gain a more native environment, thus maximizing chances to get proper folding and activity of membrane proteins, naturally occurring phospholipids can be used in the form of liposomes. Lipids as compared to detergents have longer hydrophobic tails, are less soluble and exhibit very low CMC (in the range of nM for lipids with natural tail lengths). Besides, they are able to form bilayer arrangements of 25 to 2500 nm diameter, encapsulating aqueous medium inside.

The advantage of liposomes is to mimic native membranes in a good way since lipid composition, bilayer feature and low curvature are respected. They however are way above the size limitation of solution NMR but are the preferred membrane mimetic for solid-state NMR studies of membrane proteins.

A mixed approach is also possible in order to use the property of detergents to form small arrangements and the natural environment provided by lipids, i.e. bicelles. Bicelles are mixtures of a detergents (or short-chain lipid) and a long-chain lipid, they form ellipsoidal particles with more curved edges where the detergent assembles and a more or less (according to the long-to-short chain ratio) expanded near-to-planar bilayer [196] where lipids assemble. They can be a good alternative to conserve the benefits of liposomes in a smaller form, but still may exhibit high detergent destabilization effect.

Amphipols, lipodiscs and nanodiscs

As none of the aforementioned membrane mimetics are both accessible to solution NMR and exhibit close-to-native environment, more advanced and unconventional strategies have been developed. The first one is based on a history of membrane-penetrating polymer chemistry, and called amphipols. Amphipols are polyacrylates containing tuned amounts of hydrophobic octyl- and isopropyl-side chains [197]. They have the property to wrap around exposed hydrophobic surfaces of membrane proteins and conserve their structure. This methodology has been shown to be most effective for 7-transmembrane proteins, among which the important class of GPCR [198]. Nevertheless, amphipols also do not contain the lipids found in natural membranes. This can be an issue because specific

interaction of lipids with a lot of membrane proteins [199] and involvement in active processes [200] have been shown to be absolutely critical to structure [201, 202] and function [203].

Two attempts to find a small, lipid bilayer environment have been conducted. The first one, termed nanodiscs [204, 205] consists of a circular patch of lipids encircled by a membrane scaffold protein (MSP). The second one, named lipodiscs [206, 207] consists of a similar assembly but the scaffold is an amphiphilic styrene-maleic acid copolymer. While the first has the advantage of being very sable and extremely versatile in terms of sizes, lipid compositions, oligomeric states of membrane proteins (see Chapter III) and even shapes [208], the second has the power of solubilizing membrane proteins in a native form and native membrane patches without the need for any detergent step.

In the present work, the use of nanodiscs for solution and DNP-NMR is the main focus, thus a specific introduction and state-of-the-art review on the topic is presented in the Chapter III.

Target proteins

Bcl-x_L

B-cell lymphoma-extra large (Bcl-x_L) is a 26 kDa protein and an important anti-apoptotic player of the Bcl-2 family. The Bcl-2 family of proteins contains approximately 15 members, both anti- and pro-apoptotic, forming a large regulation interplay of the mitochondrial-dependent path of programed cell death. In short, anti-apoptotic members (e.g. Bcl-2, Bcl-x_L, Bcl-w) sequester pro-apoptotic members in the cytoplasm (e.g. Bax, Bak) which otherwise have the ability to form pores in the outer mitochondrial membrane, releasing cytochrome C and leading to apoptosis. In turn, Bcl-2-like members can be sequestered by so-called BH3-only factors (e.g. Bim) for additional regulation [209, 210].

Bcl-x_L has been reported to interact with many other proteins and have multiple modes of function. Among others, it has been shown that Bcl-x_L interacts with (i) Bax and Bak, as described before [211, 212] (ii) tumor suppressor p53 blocking the dependent apoptosis cascade [213], (iii) outer mitochondrial voltage-dependent anion channel VDAC [214] regulating production of reactive oxygen species and release of cytochrome C, (iv) cytochrome C itself inhibiting it [215] and (v) Apaf-1 preventing formation of Caspase 9 complex [216].

The structure of Bcl-x_L is known from X-ray crystallography as well as solution NMR experiments both alone [217] and in complex with e.g. Bak [218]. It exhibits seven α-helices including one at the C-terminus that has the propensity to anchor in membranes, and one long unstructured loop containing numerous phosphorylation sites. Three of these helices termed Bcl-2 homology 1 to 3 (BH1-3) are largely conserved throughout the family and forms a consensus binding pocket. Interestingly, it has been shown that this binding pocket in Bcl-x_L is either occupied by the hydrophobic tail making the protein conserved in the cytoplasm or by another member of the family. In the latter case the tail is free to anchor to the mitochondrial outer membrane. This structural mechanism is critical in the interplay of Bcl-x_L with its different ligands and functions [47, 219, 220].

Being at the center of such a large apoptosis interplay and approximately ten-fold more responsive to the chemotherapeutic agent Doxorubicin [221] than Bcl-2, Bcl-x_L is a significant target in oncologic drug development with a lot of efforts put in the design of ligands able to inhibit its pro-survival function in cancer cell lines [222-225].

Note that in this work (Chapter IV and Chapter V), Bcl-x_L is used merely as a well-behaved model for soluble proteins and thus a 20.8 kDa construct lacking the long unstructured loop and the hydrophobic tail was used.

OmpX

The outer membrane X (OmpX) is an 18.6 kDa protein identified first in *E. cloacae* [226] then in *E.coli* [227] and numerous other bacterial strains. Is it a member of the outer membrane proteins class (together with e.g. Ail and PagL), which are rigid β-barrels but do not exhibit any porin activity and are not OmpA-like. The function of OmpX still remains unclear but several proposals have been made among which: (i) regulation of porins expression level [228] e.g. through feedback on transcription active $E\sigma^E$ factor [227], (ii) antibiotic resistance [229], (iii) bacterial adhesion and neutralization of host defenses [230, 231], (iv) cation-selective channel activity in reconstituted membranes [232] and (v) role in protein export pathway [233]. Although still unclear, all propositions point to a central role in bacterial virulence [234].

The determination of its structure, both by X-ray crystallography [235] and solution NMR in detergent micelles [236] showed a canonical eight-stranded β-barrel, four long protrusions of strands into the extracellular milieu and two extracellular flexible loops. These loops and protrusions could be involved in interactions with host cells, in line with the virulence hypothesis.

OmpX exhibits a very rigid transmembrane part, high stability and yields very reproducible and high quality NMR spectra even using different membrane mimetics. For all these reasons, it quickly became a model protein for the development of NMR-based structural studies of membrane proteins. After initial experiments in dihexanoyl phosphatidylcholine (DHPC) micelles [237-239], detergent-to-protein correlations [240], urea unfolding processes [241] as well as water accessibility in amphipols [242] were investigated. Solid-state NMR using magnetic field oriented, glass-supported di-oleoyl-phosphatidylcholine (DOPC)/di-oleoylphosphatidylglycerol (DOPG) bilayers were applied as well [243, 244]. Finally, OmpX is the first (and so far only) membrane protein which structure was determined in nanodiscs [245], refined [246] and fully characterized [247].

OmpX both in DPC micelles and in nanodiscs was used in the present work as a model system in the development of new solution NMR methodology (see Chapter IV).

Apolipoprotein A-I

Apolipoprotein A-I (ApoA1) is a 30.8 kDa soluble protein with a very high propensity to interact with lipids [248] and form lipoparticles [249]. It is the major constituent of human plasma high density lipoproteins (HDL), which makes it a key player in cardiovascular transport of lipids and as such a very interesting target in numerous cardiovascular diseases. Its primary role is to reverse-transport cholesterol from the blood vessels to the liver for efflux, thus preventing atherosclerosis [250]. In short, ApoA1 initially forms HDL with phospholipids present inside the cell, and is then transported in the plasma. There, maturation of HDL through activation of lecithin:cholesterol acyltransferase (LCAT) and conversion of cholesterol to cholesteryl esters (which are included into the HDL) takes place [251]. The size as well as lipid type content in HDL changes up to a certain level at which it is metabolized by the liver.

Structural insights into ApoA1 and HDL formation and maturation has been a big topic in the past 50 years. ApoA1 is known to form amphipathic helices due to its specific distribution of hydrophobic, neutral and charged residues around an α-helical axis with a 11-reidue repeat manner [252]. The global maturation of HDL, from an initial close-to-discoidal shaped state containing phospholipids and two copies of ApoA1 to a final spherical state containing a high number of cholesteryl esters and between 4 and 6 copies of ApoA1 is also clear. This process of HDL assembly [253, 254] as well as maturation [255] has been extensively studied by molecular dynamic simulations but structural experimental evidences remain missing.

For this reason, and despite two crystal structures of lipid-free ApoA1 [256, 257], different structural models of lipid-bound ApoA1 have been proposed [258-260] among which: (i) the double-belt model [261] in which two copies of ApoA1 encircle a circular patch of bilayer in a belt-like fashion with the axis of the helices parallel to the membrane surface plane, (ii) the picket-fence model [262] in which numerous smaller helices with their axis perpendicular to the membrane plane cover the hydrophobic exposed edges and (iii) the double superhelix model [263] in which an ApoA1 dimer wraps around a ellipsoidal patch of lipids in the form of a bigger helix. Some sub-models have also been designed in order to accommodate restraints in the double-belt [264, 265]. Among these we can find the helical hairpin model [266], the twisted-belt model [267], the looped-belt [268], the belt-buckle model [269] or the solar-flares model [270]. Nonetheless, to date, the double-belt and related models have seen the most experimental evidences by a number of techniques including solid-state NMR [271, 272].

Interestingly, it is the ability of ApoA1 to form discoidal bilayers under the form of reconstituted HDL (rHDL) that was exploited in the design of nanodiscs as a membrane mimetic system [273]. The sequence of ApoA1 was engineered in order to optimize solubility, stability and yield of rHDL spontaneous assembly, leading to the discovery of the so-called membrane scaffold proteins (MSP) including the widely used MSP1D1 [274]. Then extended and truncated versions of it were designed as well [245, 275] (also see details in Chapter III), allowing structural studies by solution NMR and recent solving of MSP1D1ΔH5 structure in nanodiscs [276], also pointing to a double-belt arrangement of these proteins in rHDL.

In this work, the use of MSP in the assembly of nanodiscs and NMR studies is reviewed extensively (Chapter III) and two constructs of MSP, MSP1D1 and MSP1D1ΔH5 were used in the assembly of different types of nanodiscs with (Chapter IV and Chapter VII) or without (Chapter VI) membrane proteins inside.

α-Synuclein

α-Synuclein (αS) is a 14.5 kDa protein found in the human brain, predominantly at the presynaptic terminals of dopaminergic neurons. It is also the hallmark of so-called synucleinopathies, including multiple system atrophy, dementia with Lewy bodies and Parkinson's disease, all sharing the feature of being diagnose through the presence of plaques in the brain or Lewy bodies that are mainly constituted of αS [277-279]. The main process of these diseases is likely linked to abnormal aggregation of αS, leading to formation of amyloid fibrils and ultimately to plaques. The aggregation process and its determinants are still not fully understood despite big research efforts in the field in the past 15 years. A complex dependence on external conditions such as presence of surfaces [280], solution conditions [281], presence of lipids [282], among others, is thought to modulate the different stages of amyloid fibril formation *in vivo*.

αS is intrinsically disordered in solution, with its 140 amino acid long sequence exhibiting a gradient of hydrophobicity between its N-terminus and its highly negatively charged C-terminus. The middle region (amino-acids 60 to 100), i.e. the so-called non amyloid-β component (NAC) region, has been shown to be the one involved in β-sheet and fibril formation, whose structure was recently determined by solid-state NMR [283]. The N-terminus is known to interact with membranes [284, 285], forming a α-helical segment upon interaction. This interplay between α-helix, random-coil and β-sheet containing conformations is central in the modulation of αS function from its native one to the abnormal aggregation pathway.

The native function of αS also remains unclear to date, with different evidences pointing to its involvement in synaptic vesicle homeostasis [286, 287], assistance in SNARE-dependent vesicle fusion [288] upon binding to synaptobrevin [289] or even SNARE-like induction of vesicle fusion [290].

More details as well as a comprehensive study of αS binding to phospholipid bilayer nanodiscs by various techniques and its effect on aggregation can be found in Chapter VI.

Barttin

Barttin is a 35 kDa protein encoded by the *Bartter syndrome, infantile, with sensorineural deafness (BSND)* gene in which mutations lead to Bartter syndrome type IV. Bartter syndrome type IV is a rare disease causing severe salt-losing phenotype through the urinary kidney system as well as sensorineural deafness [291, 292]. Indeed, Barttin has been shown to be a necessary regulator for both chloride channels ClC-Ka and ClC-Kb [293] present in the stria vascularis of the inner ear and in the Henle's loop of kidneys, respectively. Other syndromes, also termed Bartter syndromes, were described. These, although due to mutations on different genes, also affect function of various ion channels. Bartter syndrome type III, for instance, is due to mutations in the ClC-Kb gene, leading to the same renal dysfunction but not to deafness. Only mutations in the common regulator protein gene results in a "double knock-out" phenotype with its canonical symptoms [294]. Specifically, impeding the function of ClC-Kb leads to deficient reabsorption of sodium chloride or renal failure, thus polyuria, metabolic alkalosis (too high serum pH), hypokalemia (too low potassium level) and sometimes low blood pressure. Impeding the function of ClC-Ka affects regulation of calcium efflux needed in the ear for information transmission machinery and can lead to cochlear sensorineural or nerve damage. While the firsts can be partially treated by an appropriate potassium diet, the latter irreversibly leads to hearing loss and deafness [295].

While the chloride channels have been extensively studied and characterized both in terms of function [296] and structure [297], the characteristics of the regulator protein Barttin still remain elusive. It is known that Barttin is able to increase the number of channels in the outer membrane [293] and change their distribution in the cell compartments [298] thus acting as an accessory protein. It is also able to change their glycosylation pattern [299] and to contribute to the full activation of the channels by voltage gating [300], even though the latter remains a point of debate [301]. In respect to this, the structure of Barttin was not solved so far and very little is known about the structure-function relationships. Barttin is predicted to have a two-transmembrane helix motif at its N-terminal region supposedly acting as a chaperone for the channels and a large C-terminal unstructured region which was shown not to interact with the channels [295]. Two features are predicted to be critical for this function, namely a speculative binding site to e.g. helices B and J of the ClC-Kb channel [302] and a palmitoylation site which could act as membrane anchoring mechanism [303].

In the presented work, a N-terminal construct of Barttin (I72X) reconstitution in LDAO micelles as well as nanodiscs and their NMR characterization is presented (see Chapter VII).

CHAPTER III – SPECIFIC INTRODUCTION – THE NANODISC SYSTEM FOR NMR-BASED STUDIES

This Chapter was published with the reference:
Viegas A., Viennet T. and Etzkorn M. The power, pitfalls and potential of the nanodisc system for NMR-based studies. *Biol. Chem.* 397 (12), 1335-1354 (**2016**)
DOI: 10.1515/hsz-2016-0224

The power, pitfalls and potential of the nanodisc system for NMR-based studies

Aldino Viegas[1§], Thibault Viennet[1,2§], Manuel Etzkorn[1,2*]

[1] Institute of Physical Biology, Heinrich-Heine-University Düsseldorf, Universitätsstr. 1, 40225 Düsseldorf, Germany

[2] Institute of Complex Systems, Forschungszentrum Jülich, Wilhelm-Johnen-Strasse, 52425, Jülich, Germany

[§] The authors contributed equally

[*] Corresponding author

The power, pitfalls and potential of the nanodisc system for NMR-based studies

Abstract

The choice of a suitable membrane mimicking environment is of fundamental importance for the characterization of structure and function of membrane proteins. In this respect, usage of the lipid bilayer nanodisc technology provides a unique potential for NMR-based studies. This review summarizes the recent advances in this field, focusing on (i) the strengths of the system, (ii) the bottlenecks that may be faced as well as (iii) promising capabilities that may be explored in future studies.

Introduction

The usage of the lipid bilayer nanodiscs (ND) system for Nuclear Magnetic Resonance (NMR)-based studies has led to both enthusiasm and frustration in many labs in the recent years. In this review we will give an overview of the power as well as the pitfalls of this intriguing system and will discuss its potential for future applications.

In general, structural studies can be strongly dependent on the target protein's environment. As such, the influence of the environment on the protein structure as well as on the used experimental technique has to be considered. This is particularly true for the NMR-based investigation of membrane proteins (MPs), which require a suitable membrane mimicking environment to promote a protein conformation that is, on the one hand, representative for its native behavior and, on the other, compatible with the requirements of NMR spectroscopy. While a variety of different membrane mimetics for solution and/or solid-state NMR have been established [186, 304-307], the lipid bilayer nanodisc system distinctively combines various potentially advantageous properties including a native-like lipid surrounding, the absence of detergents, sample homogeneity, isolation of defined oligomeric states, and good accessibility of extra membranous domains. Noteworthy, these properties also make the ND system attractive as a tool for structural studies for non-NMR techniques (see e.g. [205] for a recent review and [308] for a recent breakthrough in cryo-EM studies of membrane proteins in NDs).

History and background

The nanodisc technology was first described by Sligar and co-workers [309, 310] to support the study of the hepatic microsomal NADPH-cytochrome P450 reductase. The introduction of NDs as membrane mimetics provided a solution for studying membrane proteins in a native-like environment and allowed to overcome some of the problems encountered in other mimetics. In particular, the absence of detergent molecules is one of the great advantages of this technology [311-314].

Nanodiscs usually consist of an assembly of phospholipids held together by amphipathic apolipoproteins, normally called membrane scaffold proteins (MSPs), arranged in a discoidal bilayer (Figure 13) [312]. The MSPs are based on the sequence of the human serum apolipoprotein A-I (ApoA1), although other alternatives exist [315], and provide a hydrophobic surface facing the lipids, and a hydrophilic surface at the outside. This setup makes NDs highly soluble in aqueous solutions enabling the solubilization of embedded membrane proteins in the absence of detergents [309, 311]. Depending on the used variant of MSP, the size of the nanodisc particles normally span between 6 and

17 nm in diameter [316, 317]. For NMR-related studies the most commonly used versions are the MSP1D1 and MSP1D1ΔH5 [314, 318], which can result in soluble NDs with an overall particle mass below 200 kDa that are in general applicable for modern NMR techniques [319-321].

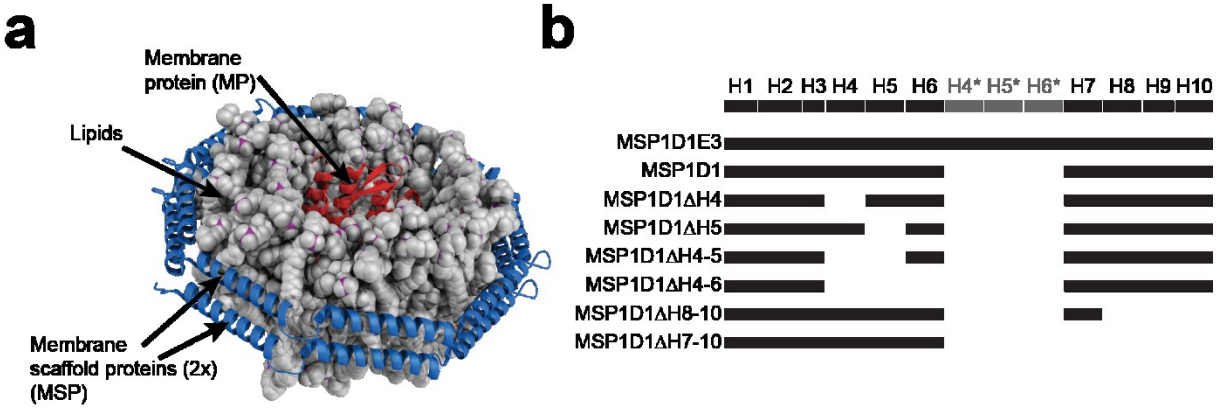

Figure 13. **The nanodisc system and the available membrane scaffold proteins. a)** Schematic representation of the nanodisc system. **b)** Representation of the different MSP constructs that have so far been used for NMR-based studies (bottom). The grey H4*, H5* and H6* helices are repeats in the MSP1D1E3 construct. The references for the different MSP construct can be found in section "Choosing the MSP construct" below.

Structure of nanodiscs

Nanodiscs are thought to closely resemble the natural early stage High Density Lipoproteins (HDL) involved in the reverse transport mechanism of cholesterol [322, 323]. These discoidal HDLs have been shown to contain two apolipoproteins and roughly 160 phospholipids. However, no high-resolution structure of nanodiscs has been reported so far. Nevertheless, several models exist [324-329] with the most accepted one being the so-called "double-belt" model [330]. This model is supported by the available crystal structure of lipid-free apolipoprotein A-I [331, 332] as well as geometrical considerations [330] and experimental data, such as, cross-linking and mass-spectrometry [269], small angle X-ray scattering [333] molecular dynamics (MD) simulations [334] and solid-state NMR data on the scaffold [335] as well as on the lipid-protein correlations [272] using PEG precipitated NDs. It seems plausible that the structure of the NDs is largely determined in the assembly process, which is driven mainly by hydrophobic interactions and protein-protein interactions, minimizing the hydrophobic exposure and maximizing the number of salt-bridges between the two MSPs [336, 337].

Working with nanodiscs

The usage of the nanodiscs system requires a number of steps that should be carefully considered to obtain optimal NMR insights into the desired target protein. While Figure 14 gives a schematic overview, selected steps will be discussed in more detail in the following.

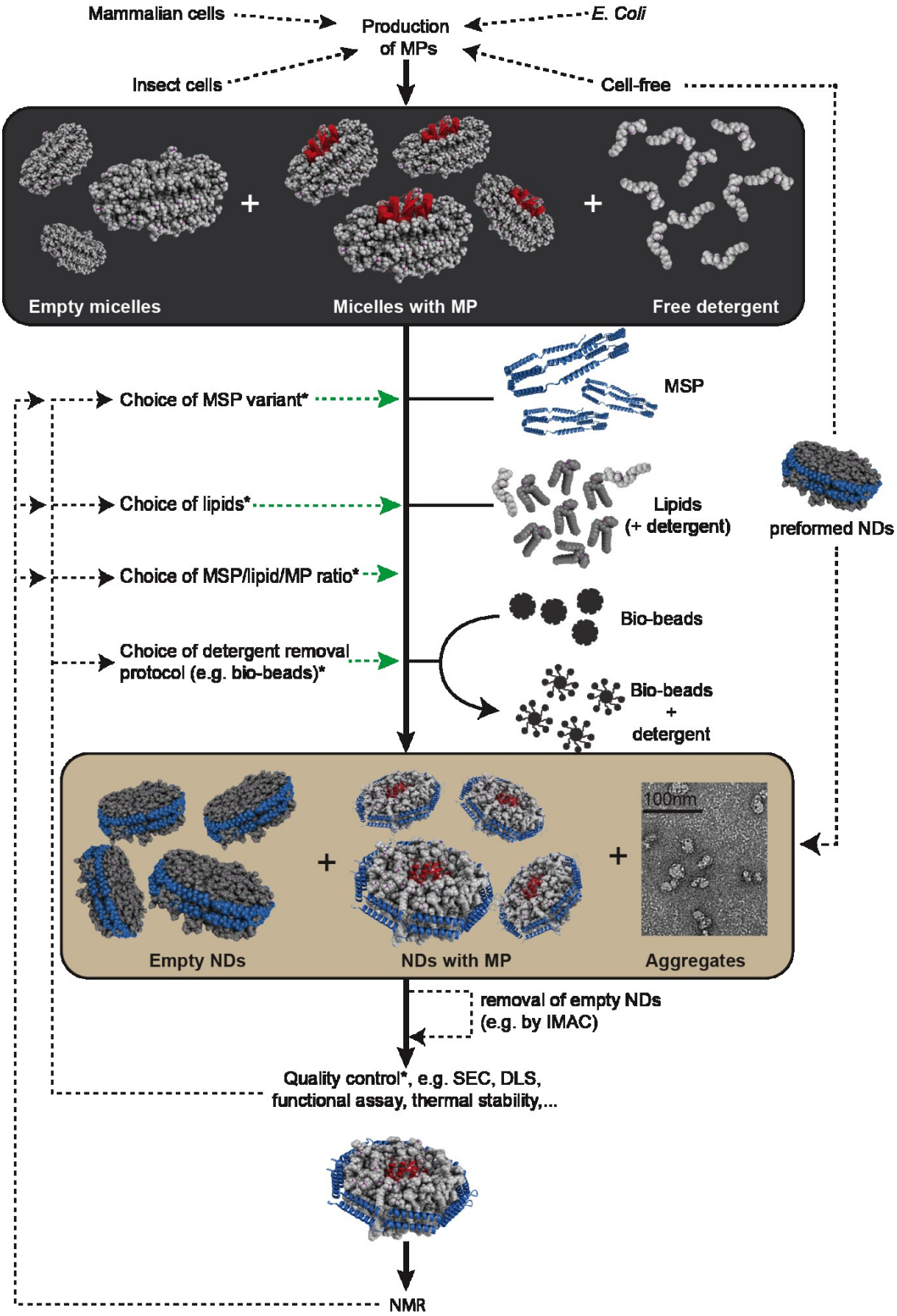

Figure 14. **Schematic overview of the process to obtain NMR samples of ND-embedded membrane proteins**. Black arrows indicate the normal process, dashed black arrows indicate optional/alternative options and green dashed arrows indicate optimization possibilities. *More details are given in the respective sections of the review.

Choosing the MSP construct

The geometry and size of NDs is defined by the scaffold protein MSP. Therefore, the choice of the MSP should be carefully and specifically evaluated for each application. Different MSP constructs have been engineered over the past 15 years, ranging from a length of 101 to 376 amino acid residues (Figure 13), and leading to diameters between 6 and 17 nm. Originally two constructs were produced [310], MSP1 and MSP2, both forming discs with diameters around 9.5 nm. The difference being that assembly requires either one MSP2 or two MSP1 for each nanodisc (MSP2 being a fusion of two MSP1 proteins, but leading to significantly lower yields). Noteworthy, albeit their lower yields and so far not explored properties for NMR structural studies, MSP2-based nanodisc carry an interesting potential due to their intrinsic architecture that features a closed circle of the scaffold protein potentially increasing stability and homogeneity. For MSP1 the first 12 amino acids were shown to not be involved in lipid binding and were thus removed, resulting in the so-called MSP1D1, which became the reference construct for production of NDs. Bigger constructs, called MSP1E1 to MSP1E3, were then introduced by extending the MSP1 by one to three helices, respectively (leading to diameters from 10.5 to 13 nm) [338]. Even bigger NDs were designed using MSP2N2 and MSP2N3 with diameters around 17 nm [317]. More recently, also smaller NDs were developed with deletions of (parts) of the amphipathic helices in the center of MSP, e.g. MSP1D1ΔH5 and MSP1D1ΔH4-6 [314], or deletions of C-terminal helices [316, 339]. Both were shown to form discs of 6-8 nm in diameter.

Most of the MSP constructs include an N-terminal polyhistidine tag for MSP purification and a TEV or Factor X cleavage site. Normally one would cleave the His-tag prior to assembly to allow separation of empty NDs from discs that have His-tagged membrane proteins embedded as well as to increase stability and NMR behavior [318]. Nevertheless, in some cases it may be useful to not cleave the His-tag from the MSP, e.g. when purifying from native microsomal membrane [340, 341] or for immobilization of NDs for use of surface plasmon resonance (SPR) or other techniques using Nickel-NTA or anti-His antibody coupling [342-344]. Other tags can be used as well for the same purpose, like C9 [345] or FLAG [343].

The size of the nanodiscs has to be chosen wisely according to the protein of interest. For instance, in the case of large integral membrane proteins, MSP1D1E3 is often preferred [346]. Interestingly, varying the size of the NDs can also determine/influence the oligomeric state of the studied protein. For instance, it was shown that a minimal diameter of 12 nm was necessary for incorporating bacteriorhodopsin trimers, whereas smaller NDs could either result in heterogeneous or monomeric populations [347].

While most biochemical and biophysical techniques will not be influenced by the available range of ND sizes, solution NMR applications will strongly favor smaller NDs in order to reduce the rotational correlation time and thus increase spectral resolution and sensitivity. In this respect, the MSP1D1ΔH5 construct has been shown to be very effective [314, 318]. On the contrary, for solid-state NMR applications, larger discs may be of interest [348-350] making use of their magnetic alignment properties.

Choosing the lipids

The choice of lipids used to study MPs is of particular importance to obtain/maintain the target protein in its native conformation. In general, lipid composition of biological membranes is very diverse. It will not only change between different cell types or membrane types of one cell, but may also change over time, e.g. during the life cycle of the cell. Therefore, it is often difficult to define the exact native lipid composition for a given membrane protein. Nevertheless, the nanodisc system is compatible with a broad range of lipids and, theoretically, allows to precisely control lipid composition and generate large amounts of homogenous particles that are stable over time. In this respect it is a powerful tool to

produce synthetic membranes tailored to adequately mimic a broad range of membrane properties including bilayer thickness, charge and fluidity. While standard phospholipids, including DMPC, DPPC or POPC are most commonly used for ND preparation, assembly has also been successful with phospholipid alkyl chains ranging from dilauroyl (DL, 12 carbons) to dielaidoyl (DE, 22 carbons), including unsaturated chains like dioleoyl (DO), and polar head groups varying from phosphocholine (PC, zwitterionic) to phospho-L-serine (PS, negatively charged) in different proportions up to 100% negative charges [333, 342, 344, 351-354]. Moreover, usage of other types of lipids were reported including cardiolipin up to 10% [351, 355, 356], ganglioside G_{M1} up to 15% [343, 357], sphingomyelin up to 30% [358] or cholesterol up to 30% [309, 359]. Although a broad range of lipids are in general compatible with the ND system, one should still keep in mind that when using lipid mixtures NDs are not necessarily formed with the statistical distribution of the lipids present during the assembly reaction. Instead, preferential interactions between lipids or between lipids and MSP might lead to a biased assembly. When using lipid mixtures, it is therefore advised to check the lipid content of the assembled ND. This can be done by e.g. using radio-labelled lipids [310, 342], ^{1}H NMR and HPLC-MS [360], analytical ultracentrifugation [361] or ion exchange chromatography [362].

Tuning the lipid content of nanodiscs was shown to improve MP activity [363, 364] as well as sample quality, stability and NMR behavior [318]. This may be related to the role of unsaturation, cholesterol or head groups' negative charges that may help to stabilize the functional conformation of the membrane protein. For instance, NDs with a 20/80% PG/PC content provided largely increased NMR spectral quality as 100% PC [314, 365] (Figure 15d,e, unpublished data). While lipid screens should be used to optimize sample properties for NMR, they can, of course, also be used to study the effects of the surrounding lipids on the conformation, activity [342, 360] or affinity [343, 366] of the inserted target protein.

As an alternative to synthetic lipid mixtures one can also directly use native membranes extracts. This can either be done by extracting lipids from the native cell membrane and using them as precursor for assembly with detergent purified MP [363, 366-368], or by directly solubilizing protein-containing membrane fractions with detergent and replacing the detergent with suitable MSP. This approach has been successfully carried out for cytochrome P450 monooxygenase [340] and the cytochrome P450 - P450 reductase complex from insect cell culture [341]. Note that native membrane extraction can also be carried out with amphipathic styrene-maleic acid (SMA) copolymer without the need for detergents (see section "Alternatives to MSP" below).

Choosing the MSP-to-lipid and MSP-to-MP ratios

The size, and thus the number of lipids a nanodisc contains, is largely determined by the chosen MSP [338]. Getting monodispersed NDs in high yield requires usage of a suitable ratio between the scaffold and the lipids during the assembly process. If too few lipids are present smaller, not-well characterized, particles can appear [347]. On the contrary if too many lipids are present, bigger aggregated particles are formed [310, 369]. Additionally, the absolute concentrations of MSP and lipids during assembly are critical, and a minimum lipid concentration of 4 mM is recommended [310, 370]. The number of lipids per ND can often be quite accurately predicted from simple geometrical calculation since is it mostly determined by the total surface area and the area each lipid will occupy. Dividing the inner surface of the disc (calculated from the length of the used MSP and assuming a circular arrangement) by the surface of the chosen lipid is sufficient as a first step [338, 346]. For instance, when forming empty NDs with MSP1D1, which has a single layer outer surface of 4400 Å^2, and DMPC, which has a head group surface of 57 Å^2, 77 lipids per single layer are needed [311].

When incorporating membrane proteins in NDs one has to compensate the bilayer area that will be occupied by the protein by reducing the respective number of lipids [342, 346]. For example, one needs to remove around 37 DMPC molecules to compensate for bacteriorhodopsin insertion [347], or

50 POPC molecules for bovine rhodopsin [371]. Exact lipid/MSP ratios may however also depend on other factors, such as the lipid binding behavior of the protein of interest and/or the phase of the resulting lipid bilayer. Thus, the best ratios for a specific MP-ND system should be empirically optimized around the expected values. For this, size exclusion chromatography (SEC) can be used as a readout to optimize towards homogenous particles of the expected size.

In addition to the MSP/lipid ratio, the MSP to target protein ratio (MSP/MP) can be critical to obtain nanodisc samples of good quality. The MSP/MP ratio can e.g. (partly) regulate the number of MPs per nanodisc. Increasing the MSP/MP ratio will normally increase the propensity to assemble NDs with no or only one inserted MP. Previous studies have used MSP/MP ratios ranging from 2:1 for the cytochrome P450 reductase to 150:1 for the β2-adrenergic receptor [342, 352, 363, 370-374]. For NMR structural studies a monomeric state of the target protein is often desired, which can be obtained with a high (> 6-fold) excess of MSP over the target membrane protein and/or the choice of a MSP construct that prevents insertion of multiple proteins due to limited surface area. When lower MSP/MP ratios are used one should keep in mind that the assembly of native oligomers is not always straightforward since membrane orientation of the inserted proteins may differ and/or lateral diffusion could be restricted, thus limiting reorientation in small discs. Therefore, it may be beneficial to assemble native oligomers before insertion (e.g. by detergent extraction of native membrane fragments). Previous studies have, however, succeeded in the preparation of NDs containing defined multimeric-states of membrane proteins. For instance, by varying the MSP/MP ratio, formation of dimers, trimers or even trimers of dimers has been observed [344, 363, 371, 375]. Insertion of bR trimers in a homogenous population of NDs was successfully obtained with a ratio of 2:3 [347, 364, 369, 376]. In addition to the study of oligomeric states of one membrane protein, also the characterization of the interaction between two different MPs inside a single ND was demonstrated with cytochrome P450 and its cytochrome P450 reductase starting from cell culture microsomes [341].

Noteworthy, instead of solely relying on the MSP/MP ratio to statistically drive the insertion of a desired multimeric state, which is often found to be randomly oriented in NDs [377], it has been shown that defined oligomeric states (dimers and trimers) in a defined orientation can be inserted into ND by making use of DNA origami [378] (see section "Perspectives/conclusion" below for more details).

Figure 15 shows some of our experimental data in respect to the role of the MSP/lipid/MP ratio. Using a non-optimal MSP/lipid ratio led to the formation of two populations of bR containing NDs that can be visualized and separated by SEC (Figure 15a). Negative stained Electron Microscopy (EM) (Figure 15b) shows that population A consisted of heterogeneously assembled ND (larger discs and clusters of discs) whereas population B shows a very homogenous particle distribution. Interestingly, as evident by the characteristic color of the samples, both populations contain correctly folded bR. Even though many biochemical and biophysical techniques will hence show a similar behavior of both populations, they have a dramatically different NMR behavior. While the smaller discs show a very well dispersed ^{1}H-^{15}N-TROSY-HSQC spectrum that nearly resolves all residues in bR, the larger discs (population A) only show few peaks at positions characteristic for unstructured proteins. In fact, for this population only the unstructured regions of bR (in particular the *termini*) are visible by conventional solution NMR spectroscopy [379]. Optimizing the MSP/lipid ratio resulted in generation of >90% of population B (data not shown).

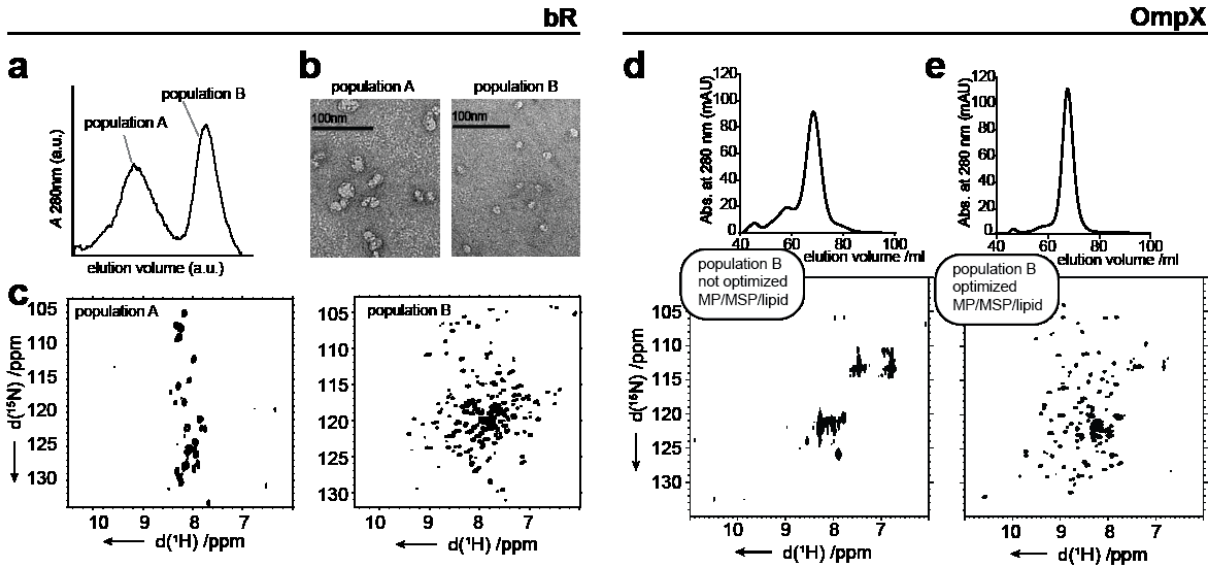

Figure 15. **Role of the MSP/lipid/MP ratios and lipid composition. a)** SEC profile for a non-optimal MSP/lipid ratio showing the formation of two separate populations (A and B) of bR containing NDs. **b)** Negative stained EM showing that population A consists of heterogeneously assembled ND (larger discs and clusters of discs) whereas population B shows a very homogenous particle distribution. **c)** Corresponding ^{1}H-^{15}N-TROSY-HSQC spectra showing that, while for population B the signals are very well dispersed, for population A only the peaks corresponding to the unstructured regions are visible. (Data in a-c reprinted form [379] with permission from Elsevier.) **d-e)** SEC profiles and corresponding ^{1}H-^{15}N-TROSY-HSQC spectra for the protein OmpX in NDs with different lipid composition and MSP:MP ratio, i.e. 100% DMPC and 4:1 (**d**) and 80/20% DMPC/DMPG and 6:1 (**e**).

Removing detergent

Although often neglected, an appropriate detergent removal protocol plays a key role in the ND's auto-assembly reaction. As such, detergent removal does not only initiate the ND assembly process out of a mixed solution of proteins, lipids and detergents but can also determine the speed of the assembly reaction. Before nanodisc assembly not only the MP of interest but also the chosen lipids are solubilized with detergent (Figure 14). Sodium cholate has been shown to be an efficient detergent for phospholipid solubilization [311] but sodium dodecylsulfate (SDS) or other detergents can be used as well [380]. In some cases the same detergent can be used for resuspending the lipids and solubilizing the membrane proteins [372, 381], e.g. when SDS-solubilized bacterioopsin is directly refolded into NDs [379], but often milder detergents are used to directly transfer a folded protein conformation into the NDs. Mixed detergent approaches with lipids resuspended in cholate and protein solubilized in maltosides [344, 370, 382], glycosides [352, 363, 371], polyethylene glycol (Brij) [375], digitonin [368], CHAPS [311], Triton X-100 [347, 375], Emulgen 913 [373], LDAO [378] and FOS-12 micelles [314, 353] have been successful.

To prevent interference of residual detergent molecules and release the full potential of the ND system as a detergent free membrane mimetic, an extensive detergent removal should be carried out. The two most common ways of detergent removal are dialysis and adsorption by porous polystyrene beads, known as bio-beads. While the removal efficiency will be detergent dependent (in particular dependent on the critical micelle concentration), as a rule of thumb a dialysis against three times 1000-fold volume of detergent free buffer or addition of 20 to 50% w/v beads are often used [310, 373]. Noteworthy, (particularly small) membrane proteins might themselves be adsorbed to the dialysis membrane or the bio-beads. In these cases, NDs can also be assembled by immobilizing the protein on agarose beads using, for instance, a His-tag [383]. Immobilization can also be used to wash the detergent out of the system, e.g. by using a conventional IMAC setting.

The rate of detergent removal determines the time scale of assembly and thus is of critical importance. While so far the exact mechanism is not fully understood, it may be pictured as a competition process between detergents and MSP as a stabilizing agent for the lipids. In this process, the absolute and relative concentrations of reactants, as well as the detergent removal rate, will be the factors that determine the overall yield and the sample homogeneity of the resulting NDs [338]. When MPs are to be inserted, the rate of detergent removal can also influence their oligomeric state. For instance, when monomers should be inserted into single NDs, the rate of detergent removal should be faster than the rate of oligomerization. In general the use of polystyrene beads with gentle agitation for a few hours produces well suitable detergent removal rates [347, 360]. However, also prolonged dialysis with two or three changes of buffer, or overnight use of adsorbent beads without agitation are common procedures. For some systems we have experienced that too fast detergent removal resulted in an increase of protein aggregates and we therefore commonly use a two steps protocol of 10-20% w/v bio-beads (first step overnight without shaking, second step 2-3 hours with shaking after bio-beads exchange). In some cases also the use of a detergent-removing gel is preferred over dialysis which is a slower process [377, 384].

Another important factor to consider is the temperature during ND assembly. The two main reasons for this are: (i) it will have an effect on the rate of detergent removal (see above) and (ii) it will determine the lipid bilayer phase. Usually it is recommended to carry out the reaction just below the phase transition temperature of the lipids which favors formation of the nanoscale bilayers. For example, temperatures of 38°C for DPPC (T_m=41°C), room temperature for DMPC (T_m=28°C) or ice water for POPC (T_m=-2°C) are commonly chosen [309, 370, 385]. When working with lipid mixtures in the ND assembly process, one should also consider that phase transition temperatures of the individual lipids may differ, which often results in a rather broad phase transition between the individual transition temperatures, indicative of lipid-lipid interactions, in the case of mixed liposomes. In this respect the assembly temperature may be used to either promote (all lipids are in same phase) or impede (different phases for different lipids) homogenous mixing and insertion of different lipids in NDs. Note that heating (gel-phase) assembled ND above the lipid phase transition can lead to reorganization of the lipids which may or may not be desired. Also note that it has been shown before that the phase transition properties of lipids are different in NDs as compared to liposomes [385, 386].

Quality control

NMR spectral quality will depend on the homogeneity and structural integrity of the inserted membrane protein as well as the homogeneity of the assembled NDs. Therefore, it is of central importance to check basic biophysical properties after the assembly process. Standard procedures can include SDS-Polyacrylamide Gel Electrophoresis (SDS-PAGE) to check the MSP/MP ratio (after removal of empty NDs), analytical SEC and/or DLS measurements to check particle sizes and distribution. Table 8 below summarizes common pitfalls that may result in low quality data.

Pitfall	Effect/Detection	Potential solution
non-functional MP	• functional assay • incorporation into ND (denatured MP normally do not insert into NDs)	• optimized refolding • detergent and lipid screen • co-translational ND incorporation in cell-free expression systems
wrong MP/lipid/MSP ratio	• not homogenous SEC profile • SDS-PAGE band ratios MP/MSP • bad HSQC spectra	• geometrical consideration • empirical optimization
not intact lipids	• bad reproducibility • ice crystals in frozen chloroform	• pre-warming cold chloroform stocks before opening • avoid contaminations with air, water, plastic tips, parafilm, etc. • purchase smaller aliquots
wrong MSP construct	• bad HSQC spectra • sample instability	• geometrical consideration • empirical optimization
wrong detergent removal	• SEC profile • SDS-PAGE	• step-wise addition of smaller quantities of bio-beads • usage of dilution/dialysis when (small) MPs are absorbed by bio-beads • MP immobilization using e.g. Ni-NTA beads

Table 8. Common pitfalls that may result in low quality data

In any case, a preparative SEC step, to pool only the homogenous (small) NDs, is always recommended before NMR measurements. In general, a decent SEC profile is a necessary condition to obtain good NMR data and can therefore be used as an initial readout for an iterative optimization of e.g. the MSP/lipid/MP ratio or the detergent removal protocol (Figure 14). Although necessary, a good SEC profile may not be sufficient to obtain good NMR spectra (Figure 15d). In this respect it may be useful to optimize e.g. the lipid content directly using a NMR readout. Noteworthy, while it is possible to use a 1D ^{1}H spectrum as readout (e.g. a 1D version of a ^{15}N-filtered TROSY-HSQC) one should not optimize towards maximum signal intensity of the strongest peaks (since these result most likely from extra membranous residues like loops and *termini*). Instead one should optimize towards the appearance of (often considerably weaker) peaks on regions outside the random coil region (Figure 16). If peaks of unfolded, solvent accessible protein regions are too intense and overshadow the membrane embedded protein regions, also higher pH values and temperatures can be used to increase water exchange in the water accessible regions, effectively reducing the respective NMR signals.

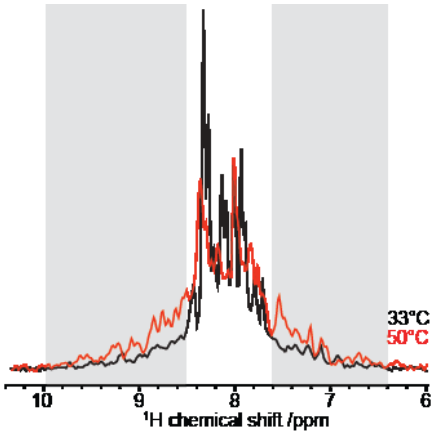

Figure 16. **Optimization of 1H-NMR spectral properties**. 1D versions of a ^{15}N-filtered TROSY-HSQC for bR in NDs formed with MSPD1 recorded at 33°C (black) and 50°C (red) are shown. When optimizing the conditions for NMR data acquisition, one should focus on the appearance of peaks on regions outside the random coil region (highlighted grey) instead of trying to maximize the intensity of the unfolded and solvent accessible regions. Note that while the maximum signal intensity is higher for the 33°C spectrum the overall NMR quality is significantly better at 50°C. (The resulting 2D spectra can be found in the supplementary figure S3g,h of [379].

In general, also optimization towards increased thermal stability (e.g. by thermal shift assays, differential scanning calorimetry, intrinsic tryptophan fluorescence, CD spectroscopy, etc.) can be useful, since spectral quality will also significantly increase with increased temperature during measurement (Figure 16). Note that the stability of empty NDs is in general very high with denaturation temperatures well above 80°C, so that transitions detected below e.g. 70°C should normally report on the inserted MPs.

If nanodiscs with a defined lipid mixture need to be assembled, it may also be useful to check the actual composition of the assembled discs. In cases where different charges should be inserted this can e.g. be done using ion exchange chromatography [362]. Of course also NMR measurements can and should be used to assess the actual lipid composition. For this quantitative 1D and/or 2D ^{1}H spectra can be recorded. Due to the specific relaxation properties of different lipid regions (e.g. solvent accessible head groups vs. membrane embedded hydrocarbon chains) the quantitative analysis of peak volumes however needs to be interpreted with care and may only be representative if peaks from different lipids with similar relaxation properties are compared.

Noteworthy, when assembling NDs from SDS solubilized bacterioopsin and SDS solubilized lipids, we observed that about 1-2 SDS molecules insert into the lipid bilayer [379]. While in this particular case no direct effect of SDS were visible, one should keep in mind that the assembled NDs system may also include small amounts of the used detergent in a membrane embedded (not in a soluble monomeric) form.

Alternative expression systems and initial MP solubilization

In general, when membrane proteins are recombinantly expressed in bacteria or in eukaryotic cell culture, solubilization and purification are regularly carried out using detergent micelles. The detergent step can however be detrimental to some MPs and can result in low yields of soluble, purified and functional MP.

As an alternative, cell-free expression (CFE) can be of great use for expression of various types of membrane proteins [387, 388]. CFE can be carried out with prokaryotic (*E. coli*) or eukaryotic (wheat germ, rabbit reticulocytes) extracts [389] and can enable co-translational folding into membrane mimetic. Due to the open nature of the CFE systems, the addition of different membrane mimicking systems (bicelles, liposomes, amphipols, etc.), including NDs is possible [359, 379, 390, 391]. In addition to membrane mimetics, also precursors and cofactors which can improve yield and folding as well as a wide range of isotopically labeled compounds can be added to an improved NMR insight [379, 392].

Co-translational incorporation of membrane proteins in NDs during CFE can be realized either by addition of preformed empty NDs to the reaction mixture [351, 354, 379, 387, 389], by addition of the individual components in a continuous exchange CFE chamber that can directly act as detergent removal dialysis chamber or by co-expression of the target protein and the MSP in a single reaction [393, 394]. For both the addition of preformed empty NDs to the reaction mixture and the co-expression of the target protein and the MSP in a single reaction, the comparison between the fraction of solubilized membrane protein with the total membrane protein revealed rather high yields (between 50 and 90%) of soluble and functional protein for several MPs [395-397]. However, for more challenging proteins, such as G protein-coupled receptors (GPCRs), co-translational incorporation of receptor into NDs resulted in lower yields (below 1%) for not stabilized receptor and yields in the range of 0.8 - 30 % of functional protein in NDs for thermostabilized receptors [354, 370]. A broad range of ND types, with various sizes and lipid contents, have been reported in this context [351, 354, 392]. The short time needed and the easiness of adding different reactants to small scaled CFE make this approach suitable for the screening of various types of effects including the study of membrane insertion itself [351].

However, despite the apparent benefits, the lack of a native membrane insertion and/or chaperon system that is either not inherent to the expression system (e.g. in the case of *E.coli* extract) or was separated from the (soluble) expression machinery (e.g. in the extract preparation) can still lead to inhomogeneous [393] or inactive [387] samples. Nevertheless, tuning of the membrane mimetic properties [351] or addition of a translocon system, chaperones, signal sequences and cofactors could overcome this issue in some cases [391].

Alternatives to MSP

The nanodisc technology invented by Sligar and co-workers is based on the human ApoA1 protein and its ability to assemble into high density lipoprotein particles and the above discussion focused on MSP constructs that are derivatives of this protein. However, the use of ApoA1 from other species, like zebra fish (zap1), has also been reported [377]. Additionally, alternatives to ApoA1 have also been used, including ApoE4 and the lipophorin ApoLpIII [315]. The truncated mutant ApoE422K provides e.g. good nanolipoprotein formation of around 15 nm in diameter and was used for incorporation of MPs during cell-free expression [389] and solubilization of an active hyperthermophile hydrogenase [398]. Moreover, formation of similar type of lipoproteoparticles (termed Salipro) has been reported using saposin A as a scaffold. This system was applied to the study of channels (T2), peptide transporters (PepT) and HIV spikes (gp) from viral-like particles [399].
The different apolipoproteins used as scaffold normally assemble into particles of 6 to 17 nm in diameter. However, for applications like self-alignment in the magnetic field (in order to extract dipolar couplings), also larger discs, formed using a 14-residue class A amphipathic α-helical peptide as scaffold and a diameter of roughly 30 nm (called macrodiscs), were used [349, 400]. It appears that usage of this scaffold peptide is possible for a broad range of particle sizes as it is not only defined by the length of the peptide but also by the scaffold to lipids ratio. Comparable effects were also seen using a similar 22-residue peptide [401].

An additional alternative method has been developed, entitled lipodisc, which is not based on a protein scaffold but on an amphipathic styrene-maleic acid (SMA) copolymer [402-405]. The SMA polymer assembles into 12 nm diameter sized discs and has been used for bR refolding and characterization [406] as well as for native membrane solubilization of mitochondrial respiratory proteins [407] and KcsA channel [408]. For the latter the lipodiscs were formed by directly extracting native membrane fragments from the cells over-expressing the MP of interest. Therefore, this method has not only the potential to circumvent a detergent solubilization step, but can also generate homogenous soluble particles of the native membrane [405]. Although the use of SMA lipodiscs for structure determination of MPs by NMR has not yet been demonstrated, they have been used for negative stain electron microscopy, yielding structures at a modest resolution (> 15 Å) in a short timeframe [409]. The slightly increased size in respect to MSP1D1-based NDs as well as potential heterogeneity of the native membrane fragments may on the one hand challenge NMR investigations but on the other hand may also provide exciting new possibilities to study MPs in their native environment. In general, solution as well as solid-state NMR techniques may be considered when structural studies of MPs in SMA lipodiscs are intended.

NMR-Applications

NMR spectroscopy has the intrinsic capability to determine the three-dimensional structure of membrane proteins and to describe their local and global motions in a lipid bilayer nanodiscs system. To date, several MPs were already successfully reconstituted into nanodiscs and studied by solution NMR, including Aam-I [410], the helical transmembrane domains of CD4 [411], KcsA [412, 413],VDAC-1 [414], KvAP [415], the Pf1 coat protein, the viral protein p7, and the G-protein-coupled receptor CXCR1 [349], VDAC-2 [416], bacteriorhodopsin [379], OmpX [314, 417], Integrin α_{IIb} [339],

YgaP [193], OmpA [418], Opa_{60} [419], μ-opioid receptor [420], BamA [421], STIM1-TM [316] and Cytb_5-CytP450 complex [401]. Also solid-state NMR has been applied to study MPs embedded into nanodiscs including the human CYP3A4 [348], proteorhodopsin [422] or the *Yersinia pestis* outer membrane protein Ail [350].

While the nanodisc systems offers unique potential for NMR-based structural studies [186, 205], it is also accompanied by several challenges. In addition to the above discussed complex samples preparation, even perfectly optimized NDs are approaching/crossing the size limit of conventional solution NMR techniques. A basic requirement is therefore the use of transverse relaxation optimized spectroscopy (TROSY)-based experiments [423, 424]. In addition, the usage of deuterium labeling is normally required to obtain detailed insights of MPs inside nanodiscs [379, 425]. However, even when using these techniques, it has been shown that more complex three or four dimensional NMR experiments are impeded by the fast relaxation mechanisms that result from the large rotational correlation times of the nanodiscs particles. It e.g. has been shown for bR and OmpX in MSP1D1 nanodiscs [314, 379] that while nearly all expected peaks are present in 2D ^{1}H-^{15}N-HSQC spectra and 3D HNCO spectra, no peaks of transmembrane protein regions could be detected in experiments that include a ^{13}C-^{13}C INEPT based magnetization transfer. In these cases, combinatorial isotope labeling can be used to allow (partial) resonance assignment [379]. Alternatively, NMR-optimized, smaller MSP constructs (see section "Choosing the MSP construct") can be used to sufficiently increase molecular tumbling and allow the usage of regular ^{13}C-^{13}C transfer sequences [314]. It has also been successfully shown that TOCSY-based ^{13}C-^{13}C transfer, combined with ^{13}C detection, can be used to study the transmembrane region of OmpX in MSDP1D1 NDs [426]. Remarkably, when using unified time-optimized interleaved acquisition (UTOPIA) setups this information can be obtained for free during the acquisition of e.g. a 3D NOESY-TROSY experiment [426].

In general, it has been shown for various systems that nanodiscs can largely increase thermal stability of the inserted membrane protein in comparison to detergent-based environments [354, 379]. This feature can and should be exploited by using increased temperatures and/or prolonged experimental times when recording solution NMR experiments. In this respect, the increased stability can party compensate for the increased molecular weight of NDs compared to micelles. In our experience, the spectral quality of MPs in nanodiscs considerably increase when measuring above 35 °C (note that in this case also the phase transition temperature of the lipids should be considered, also see section "Removing detergent" above).

Structure determination

One of the greatest potentials of using NMR spectroscopy to study MPs incorporated into nanodiscs is the possibility of determining their 3D structure in solution, in a close-to-native and active conformation. Although the molecular weight of the MP-ND complex is high, it should still be under 200 kDa and thus, suited to be studied by modern NMR techniques [319-321, 426]. The first MP structure determined by NMR and using the ND technology was of the 180-residues bacterial outer-membrane protein OmpX (PDB code: 2M06) [314]. In their work, the authors developed a short MSP (MSP1D1ΔH5) variant which resulted in smaller size NDs. The use of these NDs, allied with highly deuterated protein and lipids provided significant improvements for the structure determination process. Although the obtained structure revealed the same topology for the transmembrane part as previously shown by NMR [427] and X-ray crystallography [235], distinct differences were found for the extracellular extensions of the β-sheets. These differences were attributed to the immobilization of these segments due to the crystal packing and the cryogenic temperatures used for data collection. The constraining of the loops was not verified when using NDs and this result was in agreement with NMR and MD data. By determining the structure of OmpX in detergents but using otherwise identical buffer conditions as for the NDs, it was further shown that, when compared to the nanodisc structure, each strand was up to two residues shorter, giving a good example that the membrane mimetic can have a

significant impact on the determined structure. The difference was attributed to the slightly denaturing effect of the detergent at the water boundary and differences in hydrophobic coverage.

The structure of OmpX in NDs was later refined using residual dipolar couplings (RDCs) [417]. The authors obtained the RDCs with the OmpX protein embedded in nanodiscs (also using the MSP1D1ΔH5 variant) and using the Pf1 phage as alignment medium. The structure was calculated using the published experimental restraints [314] together with the measured RDCs and showed and improved accuracy including, in particular, better-defined orientations of the N-H bonds. This work proved that membrane protein bond orientation in nanodiscs can be obtained by measuring RDCs via Pf1 phages as alignment medium.

Further refinement of the 3D structure of OmpX in NDs was performed using a NOE-based approach to assign selectively (methyl) labeled protein [428]. In addition, RDCs were also obtained, using Pf1 phages as an alignment medium. By using the NOE information between the protonated head groups of the lipids and the side chain methyl groups and paramagnetic relaxation enhancement (PRE) experiments (obtained with Gd^{3+}-modified lipids), the authors were also able to determine the position of OmpX in the phospholipid bilayer.

A similar approach, coupled with chemical shift perturbation (CSP) analysis and backbone relaxation measurements, was used to study the structural and dynamic properties of the interactions between the membrane and the GTPase domain of tethered Rheb [429]. This study provided the first experimental evidence for membrane-dependent regulation of the structure and function of a GTPase at atomic resolution.

On another example, a mixed approach, using restraints determined with solution NMR spectroscopy in detergent micelles and NDs in conjunction with MD simulations in a lipid bilayer was used to determine the structure of opacity-associated protein Opa_{60} [419]. The final structural ensemble showed that the extracellular loops (which bind to the host receptors) interact with each other and are dynamic on the nanosecond time scale.

The conformation and ligand binding properties of the protein Bcl-x_L upon membrane integration was also studied by NMR, applying the nanodisc technology [430]. Bcl-x_L consists of a soluble domain and a membrane anchoring domain and all previous structures lacked the hydrophobic C-terminal membrane anchor, despite its potential importance for the protein function. In their work, the authors [430] tackled these issues by reconstituting the full-length Bcl-x_L into NDs, macrodiscs and liposomes which allowed a direct structural comparison of its various conformations. By comparing the ^{1}H-^{15}N-HSQC spectra acquired under different conditions, the authors showed that the soluble domain does not experience significant conformational changes upon membrane integration, contrary to some current models. Besides, it was shown that the membrane-integrated protein has higher affinity for a pro-apoptotic peptide than the truncated version, indicating that membrane integration alters the binding activity. In a later study [431], the authors used PRE data to show that, despite the C-terminal part of Bcl-x_L is inserted into the membrane, it still retains a high degree of conformational dynamics, which may facilitate its cleavage in aqueous solution.

Dynamics

In addition to the 3D structure, knowledge of the dynamic process underlying conformational changes or ligand recognition are key aspects to fully understand MPs' functional mechanisms in a native environment and therefore often the focus of NMR-based studies.

One example is given by the solution NMR investigation of the insertase BamA in three different membrane mimetics: LDAO micelles, DMPC:DiC_7-PC bicelles and MSP1D1:DMPC

nanodiscs [421]. Among their findings, the authors observed distinct time scales of dynamic behavior for the BamA β-barrel and its extracellular "lid loop" L6, which is essential for BamA function [432]. The results helped to understand why parts of this loop have poor electron densities in BamA crystal structures [432] and provided an important piece of information towards understanding the functional mechanism of the BamA insertase at the atomic level.

Another example is the investigation of the dynamics of the transmembrane and intracellular domains of p75NTR (a type I integral membrane protein) in NDs of various sizes and compositions [433]. The p75NTR has an extracellular domain (ECD), a helical transmembrane domain (TMD) and an intracellular domain, which, in turn, can be divided into three parts: the chopper domain and a linker region. Despite the availability of a proposed mechanism for the activity of the p75NTR receptor [434], the role of the chopper domain in the activation of the receptor or the connection between the conformations of the TMDs and ECDs and the state of the intracellular part remain poorly understood. By measuring longitudinal (T_1) and transverse (T_2) relaxation times, heteronuclear ^{1}H-^{15}N NOE, and cross-correlated relaxation rates of different constructs, the authors concluded that the motions of the death domain are uncoupled from the TM helix. Together with the structural data acquired, the results indicate that the previously proposed mechanism does fit *in vivo* data well but contradicts the structural information, therefore pointing the need to consider alternative mechanisms.

A similar approach was applied to the study of the protein synaptobrevin (composed by an ectodomain, containing a SNARE motif, and a transmembrane domain) inserted into NDs [435]. In this study the authors found that most of the residues belonging to the SNARE motif are unstructured and flexible in the presence of NDs, as opposed to what happens in the presence of DPC micelles. This leaves the SNARE motif accessible for SNARE complex formation and shows that NDs are a much better membrane mimetic than micelles.

Interaction studies

Nanodiscs can be an ideal tool to study the functional properties of integral membrane proteins in a lipid environment, under defined conditions [361]. They can e.g. allow the control of the oligomerization state of a given MP (also see section "Choosing the MSP-to-lipid and MSP-to-MP ratios" above) and offer high-precision control of lipid content [362], thus enabling the study of specific effects of different lipid environments. Unlike proteoliposomes, both the intra- and extracellular sides of the protein are directly accessible, ensuring homogenously accessible binding sites and allowing the investigation of signaling events that require binding events on both sides.

It is generally accepted that NDs offer good properties to examine lipid-protein interactions [436]. Still, when probing the interaction of protein/peptides with NDs, it should be tested whether the interaction partner unspecifically interacts with the MSP. Although, this could be the case with soluble MSP, it may no longer be true when nanodiscs have been formed. Upon formation of the NDs, the hydrophobic parts of MSP are not directly accessible anymore. Therefore, when testing whether an interaction partner unspecifically interacts with MSP, it is advised to not use soluble MSP but MSP in its nanodiscs conformation with neutral lipids. If NDs with only one kind of lipids (e.g. DMPC) do not show any interaction while NDs with different lipids do interact, unspecific MSP interaction can be largely excluded.

One illustration of the power of the combination between NMR and the nanodisc technology applied to the study of protein interactions is given by the study of the interaction between the Phosphoinositide (PI)-binding effector protein (FYVE domain of early endosome antigen 1 (EEA1) – EEA1 FYVE) and a PI incorporated into nanodiscs (PI(3)P) [437, 438]. Although models of EEA1 FYVE bound to a PI(3)P-embedded membrane existed (based on structural analyses using soluble PI(3)P and the NMR data in a micelle system), the relative orientations of EEA1 FYVE to the membrane

were not consistent in these two studies. Moreover, no experimental data had been reported to validate the binding mode of EEA1 FYVE with PI(3)P in the lipid bilayer system. In their study, the authors used CSP, transferred cross-saturation (TCS) and PRE experiments to map the residues of EEA1 FYVE involved in recognition of PI(3)P and to estimate a K_D value of about 105 μM. Besides, CSP experiments only in the presence of empty nanodiscs allowed to identify at least one residue involved in the interaction with the membrane. The TCS experiments determined the direct binding surface on EEA1 FYVE to PI(3)P incorporated membrane, and the orientation to the membrane was confirmed by the PRE experiments.

The interaction of the oncogenic protein K-Ras4B tethered to nanodiscs with effector protein RAS-binding domains was also studied by solution-state NMR spectroscopy [439]. Using selective ^{13}C-labelling in combination with molecular docking, the authors were able to gather important information on the orientation of the protein with respect to the lipid bilayer. Besides, the data also allowed to identify particular protein-lipid membrane interactions involved in molecular recognition and provided information about the dynamics of small-molecule-binding sites at the protein-lipid interface.

In another study, the interaction between the CC-chemokine receptor 5 (CCR5) reconstituted into nanodiscs and its ligand (MIP-1α) was investigated [440]. Due to the receptor's instability in detergents, structural studies have been difficult. Reconstitution of CCR5 in nanodiscs allowed to maintain its function for more than 24h, thus enabling structural analysis by solution NMR. Methyl-directed TCS experiments allowed to identify the residues of MIP-1α in close proximity of the receptor in the complex. The TCS data suggests that the protective influence on HIV-1 infection of a single nucleotide polymorphism of MIP-1α is due to its change in the interaction mode between MIP-1α and CCR5. The same group also studied the effect of different mimetic environments on the exchange rates for the conformational equilibrium of β_2-adrenergic receptor upon binding to various ligands. They found that the exchange rates were significantly different in detergents and nanodiscs. These fast timescales of GPCR signaling permit the rapid neurotransmission and sensory perception [425].

Another example is the study of the interaction of granuphilin-C2A domain with phosphatidylinositol 4,5-bisphosphate (PI(4,5)P2) head group and PI(4,5)P2-nanodisc [441]. NMR-based titration experiments proved the interaction and allowed to identify the binding site of granuphilin-C2A. These results were further confirmed by molecular docking, mutation and isothermal titration calorimetry (ITC) analysis and demonstrated that PI(4,5)P2 binds not only to the concave surface of granuphilin-C2A domain but also strand β5 is affected. The data provided a better understanding of the role of granuphilin-C2A domain in regulating exocytosis.

An important topic to address when studying MP-lipid interactions is the role the lipids themselves may have in the overall function of the protein (e.g. signal transduction). MP-lipid interactions may have an effect on the physical properties of the lipid bilayer and the behavior of its components. Besides interacting with the inserted proteins, lipid head groups may also interact with ions that influence the protein's function. In this sense, several NMR-based studies [412, 442-444] have been performed. For instance, solid-state NMR has been applied to study the influence of Ca^{2+} on the structure and dynamics of lipid bilayers [442]. Using the ^{1}H-^{1}H, ^{13}C-^{13}C, and ^{13}C-^{31}P dipolar interactions, distances up to ~6 Å could be measured between atoms and by combining this with MD simulations the authors showed a Ca^{2+}-induced conformational change and clustering of lipid head groups in POPC/POPS NDs. Because ^{31}P chemical shift anisotropy is sensitive to alterations in the orientation and motion of lipid head groups, it can be used as a probe for studying MP-lipid interactions. This approach was used to probe the change in the chemical environment of phospholipids in response to Ca^{2+} addition [443]. A similar spectrum was observed upon α-Synuclein binding, indicating that Ca^{2+} and α-Synuclein may interact with the same region in the lipid.

Limitations

Even if NDs are a very good model system for mimicking natural membranes, their nanoscale size and the presence of a scaffold protein still introduce a distinct environment. This can affect main physical parameters characterizing bilayers, including the temperature of main phase transition, the shape, the curvature, and the lateral pressure, which can be studied e.g. using SAXS, AFM, EM, NMR and/or fluorescence techniques. In general, the phase transitions are broadened and shifted to higher temperatures and it was found that the so-called boundary lipids do not melt at the main phase transition temperature but are further stabilized in the gel phase by their interaction with the scaffold [272, 385, 386]. This lack of cooperativity of a larger proportion of the lipids is, however, thought to mimic the natural membranes quite well, which often also comprises considerable protein crowding. Nevertheless, the fixed geometry due to the MSP can generally introduce a higher lateral pressure to the bilayer. Additionally, not all lipids may be suitable for ND formation and depending on the type of lipid used and their chain lengths, hydrophobic mismatch between the lipids and the scaffold may appear, leading to non-flat but curved surfaces and/or non-homogenous thickness [333, 385].

It may also not be clear for all proteins whether they insert in the center of the disc and are surrounded by lipids, or if unspecific interactions may favor nanodisc assembly with direct MP-MSP contacts. NMR studies have however shown that, at least for the OmpX protein, spectral quality will be compromised if not even one layer of lipids is around the inserted MP [314]. This observation suggests that, if given the option, OmpX preferentially resides in the center of the discs surrounded by lipids.

While in general NDs with different total amounts of charged lipids can be easily produced, a charge gradient between the two sides of the membrane (as found for several cellular membranes) cannot be generated using conventional self-assembly reactions However, in theory, it may be possible to incorporate MPs into differentially charged bilayers by, for instance, extracting native cellular membranes. In respect to the experimental characterization of the inserted MP, a substantial extinction as well as the high helical propensity of the MSP renders some techniques such as circular dichroism and the concentration determination using the absorbance at 280 nm wavelength difficult. The latter can interfere with the determination of the average number of inserted proteins per disc and may be partially overcome using quantitative SDS-PAGE, MS, or SEC under denaturing conditions.

Perspectives/conclusion

As outlined above, using NDs may be demanding in terms of sample preparation and NMR-data acquisition. Therefore, one should consider whether the study of the target MP, in particular also in respect to the scientific question that should be addressed, really benefits from the ND environment. It has e.g. been proposed to use the ND environment as a reference for the native MP state and, in cases where NMR-spectra in detergent micelles are similar (indicative of similar structures), to proceed with a more detailed structural characterization in the detergent system [193, 320, 418].

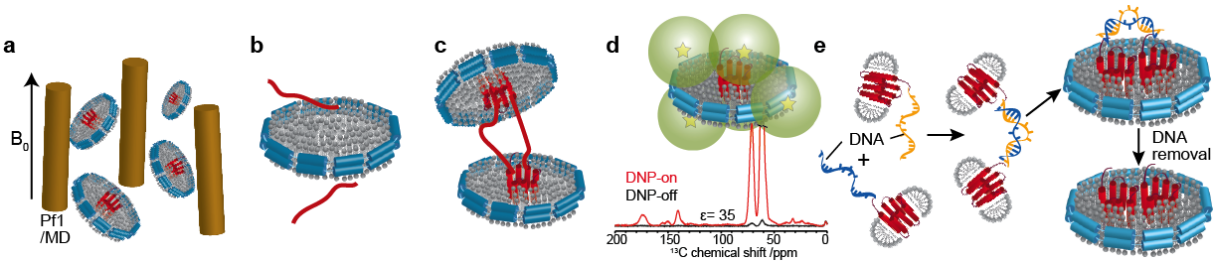

Figure 17. **Selected useful properties and future potential of NDs for NMR-based studies. a)** NDs can be used to measure RDCs using established alignment media [417, 428]. **b)** The good definition of and flexibility in the lipid content of NDs provides a suitable platform for studying lipid-protein interactions [443]. **c)** The ND system offers the potential to probe interactions between protein embedded into separate NDs. **d)** The good solvent accessibility of NDs can be used to generate a homogenous distribution of biradicals for dynamic nuclear polarization (DNP) experiments. Decent enhancement factors are e.g. found for bR in MSP1D1 nanodiscs, which enables characterization of low amounts (38 µg) of bR (unpublished data). **e)** ND systems offer the unique possibility to insert a defined (small) number of membrane proteins into one discs using, for instance, an DNA origami approach [378] allowing the study of MP-MP interactions within the same bilayer (adapted with permission from [378]. Copyright 2015 American Chemical Society).

Nevertheless, in addition to providing a near native local environment, there are unique properties of the nanodisc system with a great potential for NMR-based studies. These properties include in particular the clear definition and kinetic stability of the assembled NDs, meaning that molecular exchange processes are very slow and once formed the lipid composition, disc size and number of inserted MPs should not vary considerably over time. In addition to the absence of detergents, these features may not be given for other membrane mimetics systems such as e.g. bicelles. Figure 17 gives an overview of selected useful properties of the NDs for NMR-based studies. For instance, as discussed above, it has been shown that NDs, unlike micelles, can be used to RDCs using established alignment media [417, 428] (Figure 17a). This property may offer rather straight-forward means to e.g. check the topology of the target MP. In addition, it has been shown that large nanodiscs (i.e. macrodiscs) align themselves in magnetic field and can therefore be used as alignment media [349].

Due to the good definition of and flexibility in the lipid content of NDs, they offer an ideal platform to study peptide or protein-membrane interactions. It has e.g. already been shown for α-Synuclein that residue specific information regarding membrane association can be obtained with the combination of ND and NMR [443]. By varying the lipid content of the NDs, one could study the effects of different lipid properties on the peptide-membrane interaction (Figure 17b).

In principle, the ND system could also be used to not only study MP-MP interactions within the same membrane, but also MP-MP interactions of proteins embedded in two separate membranes as e.g. present in viral docking and/or membrane fusion (Figure 17c). In this respect the scaffold protein could prevent the actual fusion step, thus trapping the initial stages of the process.

The good solvent accessibility of the embedded MP can also be exploited in various scenarios. In addition to the (simultaneous) binding of interaction partners from both sides, this property could be useful to generate a rather homogenous distribution of biradicals for dynamic nuclear polarization (DNP) experiments of MPs, which are so far normally carried out in proteoliposomes that could introduce a radical gradient between the inside and outside of the liposome. Our initial DNP measurements confirm that the ND environment is well accessible to DNP techniques (Figure 17d, unpublished data).

Noteworthy, the ND systems provides unique possibility to insert a defined (small) number of membrane proteins into one disc. Using an DNA origami approach, it was shown that either two or three MPs can be inserted in a well-defined way into one single ND (Figure 17e) [378]. While DNA design and upscaling may be demanding, this approach combined with the 'exchange-stability' of the ND

system, can produce extraordinary oligomer homogeneity offering promising potential for studies of MP-MP interaction within the same bilayer.

Although the work with nanodiscs may be tedious, it should be pointed out that solution NMR studies of larger MPs in nanodiscs (up to a size of MSP1D1) are well suitable. Meaning that bad NMR spectra obtained on these systems are not a result of the total particles size but can either be attributed to not optimal sample preparation or intrinsic features of the MP. In this respect, if sample preparation is 'optimal' (e.g. according to the SEC profile and functional assays) the absence of decent NMR spectra may already be attributed to intrinsic properties of the MP, such as dynamic or heterogeneous conformations.

All in all, due to the intrinsic potential of the system paired with the recent advances in the field, it can be anticipated that nanodiscs will become a standard tool in the NMR-based studies of membrane proteins. In this respect it may offer a platform to obtain site-resolved insights into structure, function, dynamics and/or interactions of membrane associated processes in a near native environment.

Acknowledgements

The authors acknowledge access to the Jülich-Düsseldorf Biomolecular NMR Center, support by Dr. Fabien Aussenac (Bruker Biospin) and thank the DFG for support through the Emmy Noether grants ET103/2-1 to M.E. as well as the Marie Sklodowska-Curie Grant No. 660258 to A.V. T.V. acknowledges support from the International NRW Research School iGRASPseed.

CHAPTER IV – METHOD DEVELOPMENT – UTOPIA NMR

This Chapter was published with the reference:
Viegas A., Viennet T. Yu T.-Y., Schumann F., Bermel W., Wagner G.and Etzkorn M. UTOPIA NMR: activating unexploited magnetization using interleaved low-gamma detection. *J. Biomol. NMR.* 64 (1), 9-15 (**2016**)
DOI: 10.1007/s10858-015-0008-7

UTOPIA NMR: activating unexploited magnetization using interleaved low-gamma detection

Aldino Viegas[1§], Thibault Viennet[1,2§], Tsyr-Yan Yu[3], Frank Schumann[4], Wolfgang Bermel[4], Gerhard Wagner[3], Manuel Etzkorn[1,2*]

[1] Institute of Physical Biology, Heinrich-Heine-University Düsseldorf, Universitätsstr. 1, 40225 Düsseldorf, Germany

[2] Institute of Complex Systems, Forschungszentrum Jülich, Wilhelm-Johnen-Strasse, 52425, Jülich, Germany

[3] Department of Biological Chemistry and Molecular Pharmacology, Harvard Medical School, Boston, MA, USA

[4] Bruker Biospin GmbH, Rheinstetten/Fallanden, Germany/Switzerland

[*] Corresponding author

UTOPIA NMR: activating unexploited magnetization using interleaved low-gamma detection

Abstract

A growing number of nuclear magnetic resonance (NMR) spectroscopic studies are impaired by the limited information content provided by the standard set of experiments conventionally recorded. This is particularly true for studies of challenging biological systems including large, unstructured, membrane-embedded and/or paramagnetic proteins. Here we introduce the concept of unified time-optimized interleaved acquisition NMR (UTOPIA-NMR) for the unified acquisition of standard high-γ (e.g. ^{1}H) and low-γ (e.g. ^{13}C) detected experiments using a single receiver. Our aim is to activate the high level of polarization and information content distributed on low-γ nuclei without disturbing conventional magnetization transfer pathways. We show that using UTOPIA-NMR we are able to recover nearly all of the normally non-used magnetization without disturbing the standard experiments. In other words, additional spectra, that can significantly increase the NMR insights, are obtained for free. While we anticipate a broad range of possible applications we demonstrate for the soluble protein Bcl-x_L (ca. 21 kDa) and for OmpX in nanodiscs (ca. 160 kDa) that UTOPIA-NMR is particularly useful for challenging protein systems including perdeuterated (membrane) proteins.

Introduction

Nuclear magnetic resonance (NMR) spectroscopy has the intrinsic capability to obtain/maintain atomic resolution in challenging biological systems in a native environment [445]. However, as the complexity of the systems studied by NMR spectroscopy grows, the challenges to get the necessary information for accurate structural analysis also increase dramatically. Instrumental improvements, isotope labeling schemes [446] and developments in pulse sequences [447-459] can shorten the time for data acquisition and improve the spectral quality, thus partially compensating the growing sample complexity.

Several interesting concepts such as time-shared NMR [447-449, 455-457], BEST [450] and SOFAST [451-453] techniques, have been developed to use the available magnetization more effectively. In addition, the usage of a second receiver allows parallel signal acquisition of different nuclei [460-465]. While these techniques can offer significant benefits for a magnitude of sample conditions, they often face limitations in challenging systems where fast relaxation processes, labeling patterns and/or low protein concentrations impede their use. This is particularly true for perdeuterated proteins, which do not allow the selective excitations of amide and aliphatic protons.

In the following we present a complementary and generally applicable concept to convert normally not used magnetization into useful data. Our unified time-optimized interleaved acquisition (UTOPIA) setup optimizes polarization usage by the unified acquisition of high- and low-γ-detected experiments. Remarkably, UTOPIA-NMR is also very effective in challenging systems, i.e. the systems where the additionally accessible information is also needed the most.

Material and Methods

Bcl-x_L sample preparation

The uniformly [^{2}H,^{13}C,^{15}N] labeling truncated Bcl-x_L sample was prepared according to [214]. Bcl-x_L was first purified by Immobilized Metal Affinity Chromatography (IMAC) followed by size exclusion chromatography with a Superdex 75 column. NMR measurements were recorded with Bcl-x_L concentrations of 400 μM in 25 mM sodium phosphate, pH 7.0, 1 mM EDTA, and 2 mM TCEP.

OmpX in nanodiscs sample preparation

OmpX preparation

Preparation of OmpX in MSP1D1 nanodiscs was carried out according to [245]. *E. coli* BL21 (DE3) cells were transformed with the OmpX plasmid DNA in a pET21a vector. [U-^{2}H, ^{13}C, ^{15}N]-OmpX was expressed in inclusion bodies, the cells were grown in M9 medium [466] supplemented with 1 g/L [U-99% ^{15}N]-NH_4Cl and 2 g/L [U-99% ^{2}H-^{13}C]-glucose in 99% D_2O (Sigma Aldrich). Protein was resuspended with 6M Gu-HCl and purified by IMAC under the same denaturating conditions. The whole process was carried out at 4°C.

MSP preparation

E. coli BL21 (DE3) were transformed with the MSP1D1 plasmid DNA in a pET28a vector as reported in [467]. In short, cells were grown in LB medium. Protein was resuspended with 6M Gu-HCl and purified by IMAC (without denaturating agent). The elution fractions were pooled and dialyzed in order to remove imidazole. N-terminal His-tag was cleaved using TEV protease incubated overnight at 4°C. ΔHis MSP1D1 was separated from MSP1D1 by IMAC.

OmpX refolding

OmpX was refolded from 6 M Gu-HCl to n-dodecylphosphocholine (DPC, Avanti Polar Lipids) by dropwise dilution into 10-fold access of 50 mM Tris-HCl pH 8.5, 5 mM EDTA, 500 mM L-Arginine, 0.5% w/v DPC. Buffer was then exchanged against 20 mM Tris-HCl pH 8.5, 5 mM EDTA, 0.5% w/v DPC using 10 kDa cutoff Vivaspin concentrator. Secondary structure was checked by circular dichroism spectroscopy (Jasco J-715).

Nanodiscs assembly

Nanodiscs were assembled according to established protocols [274, 467]. 50 μM [U-^{2}H, ^{13}C, ^{15}N]-OmpX in DPC micelles, 300 μM ΔHis MSP1D1 and 21 mM lipids solubilized in 60 mM Na-cholate were mixed together in 20 mM Tris-HCl pH=7.5, 100 mM NaCl, 5 mM EDTA. The lipids used were a mixture between 1,2-dimyristoyl-*sn*-glycero-3-phosphocholine (DMPC, Avanti polar Lipids) and 1,2-dimyristoyl-*sn*-glycero-3-phospho-(1'-rac-glycerol) (DMPG, Avanti Polar Lipids) in the ratio 3:1. The molar ratio between OmpX and MSP1D1 was kept to 1:6 and between MSP1D1 and lipids to 1:70. 20% w/v of previously washed Biobeads SM-2 (Biorad) were added and the mixture incubated at room temperature overnight. The Bio-beads were removed by centrifugation and once again 20% w/v were added for an additional 4-5 hours. Nanodiscs containing OmpX were separated from empty ones by IMAC. Finally OmpX containing nanodiscs were purified by SEC on a HiLoad 16/600 Superdex 200 pg column (GE Healthcare) equilibrated with 20 mM sodium phosphate pH 6.8, 100 mM NaCl, 5 mM EDTA using a ÄKTA pure device running at 1 ml/min. The quality of nanodiscs preparation was inspected by the SEC chromatogram as well as by DLS (PSS Nicomp). The main peak from SEC was pooled and concentrated to 200 μM using a Vivaspin centrifugal device of 10 kDa MWCO, 10% w/w D2O and 0.01% w/w NaN_3 were finally added to the sample.

NMR Data acquisition

NMR experiments were performed on Bruker Avance III HD spectrometers operating either at 600 or 700 MHz, both equipped with a triple resonance TCI (^{1}H, ^{13}C, ^{15}N) cryoprobe or shielded z-gradients. For Bcl-x_L data was collected at 25ºC with sample concentration of 400 µM in 25 mM sodium phosphate pH 7.0, 100 mM NaCl, 1 mM EDTA, 1 mM TCEP, and 10% (v/v) D_2O. For OmpX in nanodiscs data was collected at 35ºC with sample concentration of 200 µM in 20 mM NaP_i pH 6.8, 100 mM NaCl, 5 mM EDTA, and 10% (v/v) D_2O. All NMR spectra were processed with TOPSPIN 3.2 (Bruker) and analyzed with CARA [468] and CCPN [469].

In order to properly compare the results obtained using the UTOPIA-NMR and conventional setups, reference and interleaved spectra were acquired using the same parameters. 3D ^{1}H,^{15}N-NOESY-TROSY was acquired (both interleaved and conventional) using a mixing time of 250 ms. Table S1 shows the NMR acquisition details for both reference and interleaved experiments. Backbone resonance assignments were extracted from Follis et al. [470]

For the determination of the H^N longitudinal relaxation time (T_1) a 180 degree hard pulse, followed by a delay, were placed at the beginning of a regular pulse sequence for solvent suppression using an excitation sculpting scheme with gradients [471]. Data for the determination of the H^N T_1 was obtained with 15 relaxation periods (0.01, 0.03, 0.04, 0.06, 0.08, 0.10, 0.15, 0.20, 0.30, 0.50, 0.70, 1.00, 1.50, 2.00, and 4.00 s). The spectral width was 14 ppm and the relaxation delay was 5 s. The central frequency was set on the solvent signal (water – 4.7 ppm) and data was analyzed with Topspin 3.2 (Bruker) (Figure 48a). The average of the determined values was taken as the T_1 value and multiplied by 1.3 to get the optimal relaxation delay [9]. Data for the determination of the ^{13}C longitudinal relaxation time (T_1) was obtained with 15 relaxation periods (0.05, 0.10, 0.20, 0.30, 0.50, 0.80, 1.00, 1.50, 2.00, 2.50, 3.00, 3.50, 4.00, 4.50 and 5.00 s). The spectral width was 200 ppm and the relaxation delay was 10 s. The central frequency for carbon was set at 100 ppm. Data was analyzed with Topspin 3.2 (Bruker) (Figure 48b-d). The optimal T_1 value was calculated as before. A summary of the parameters can be found in Table 9.

	Parameter		Number of points			Spectral width (ppm)			Central frequency (ppm)			Relax. delay (s) [a]	NS	Exp time (h)
			F3	F2	F1	F3	F2	F1	F3	F2	F1			
	Reference	**Bruker pp**												
	3D-^{1}H,^{15}N-NOESY-TROSY	*noesytretf3gp3d*	2048	40	120	14	36	14	4.7	119.5	4.7	1	16	**30**
	2D-^{13}C,^{13}C-FLOPSY	*c_ccflopsy16*	-	2048	120	-	200	80	-	42	42	2.75	320	**30**
	3D-^{1}H,^{15}N-HNCA	*trhncagp3d2*	2048	40	120	16	36	32	4.7	119.5	54	2	8	**23.5**
	2D-^{13}C,^{15}N-CON	*c_con_sq*	-	9216	120	-	300	45	-	54	119.5	2.01	320	**23.5**
	2D-COSY	*cosygpppqf*	-	2048	256	-	10	10	-	4.7	4.7	2.2	16	**2.8**
	2D-TOCSY	*dipsi2esgpph*	-	2048	256	-	10	10	-	4.7	4.7	2.2	16	**2.8**
	1D-13C	*zgig*	-	-	32768	-	-	240	-	-	100	2	4096	**2.8**
	UTOPIA													
Unified	3D-^{1}H,^{15}N-NOESY-TROSY	*Parent*	2048	40	120	14	36	14	4.7	119.5	4.7	0.87	16	**30**
Unified	2D-^{13}C,^{13}C-FLOPSY	*Child*	2048	*N/A*	120	200	*N/A*	80	42	*N/A*	42		320 [b]	
Unified	3D-^{1}H,^{15}N-HNCA	*Parent*	2048	40	120	16	36	32	4.7	119.5	54	1.66	8	**23.5**
Unified	2D-^{13}C,^{15}N-CON	*Child*	9216	*N/A*	120	300	*N/A*	45	54	*N/A*	119.5		320 [b]	
Unified	2D-COSY	*Parent*	-	2048	256	-	10	10	-	4.7	4.7	1.67	16	**2.8**
Unified	1D-^{13}C	*Child*	32768	*N/A*	*N/A*	240	*N/A*	*N/A*	-	100	4.7		4096	
Unified	2D-TOCSY	*Parent*	-	2048	256	-	10	10	-	4.7	4.7	1.63	16	**2.8**
Unified	1D-^{13}C	*Child*	32768	*N/A*	*N/A*	240	*N/A*	*N/A*	-	100	4.7		4096	

N/A – Not applicable.

[a] Note that values given for the relaxation delays in the UTOPIA setup represent the parameters defined in topspin, the setup however will in general have longer relaxation delays (comparable to the reference values) due to several processes that take some time but that do not interfere with the relaxation process.

[b] The child experiment was acquired only every second scan of the parent.

Table 9. NMR acquisition details for the reference and UTOPIA experiments applied to both Bcl-x_L and OmpX samples.

Results

In line with other techniques [448, 449, 461, 472, 473], our UTOPIA setup relies on the acquisition of several spectra using one single relaxation recycle period. Considering that in most NMR experiments the vast amount of time required to acquire a multidimensional spectrum is used up by this recycle period (i.e. waiting for the spins to relax back into a state that is close to the equilibrium), it is of fundamental importance that during each scan all of the available magnetization is used effectively (Figure 18). In this respect, it is surprising that the magnetization residing on the low-γ nuclei, which in perdeuterated proteins can account for about half of the total accessible magnetization, is discarded by nearly all standard ^{1}H-detected NMR experiments. While in general the possibility exists to transfer the low-γ magnetization to suitable protons for detection, low-γ direct detection has several advantages: (i) complementary information content (due to e.g. improved resolution in the direct dimension, direct detection of deuterated side chains and appearance of proline signals), (ii) favorable relaxation properties in particular in large protein systems additionally increasing resolution and paired with fewer transfer steps also increased sensitivity.

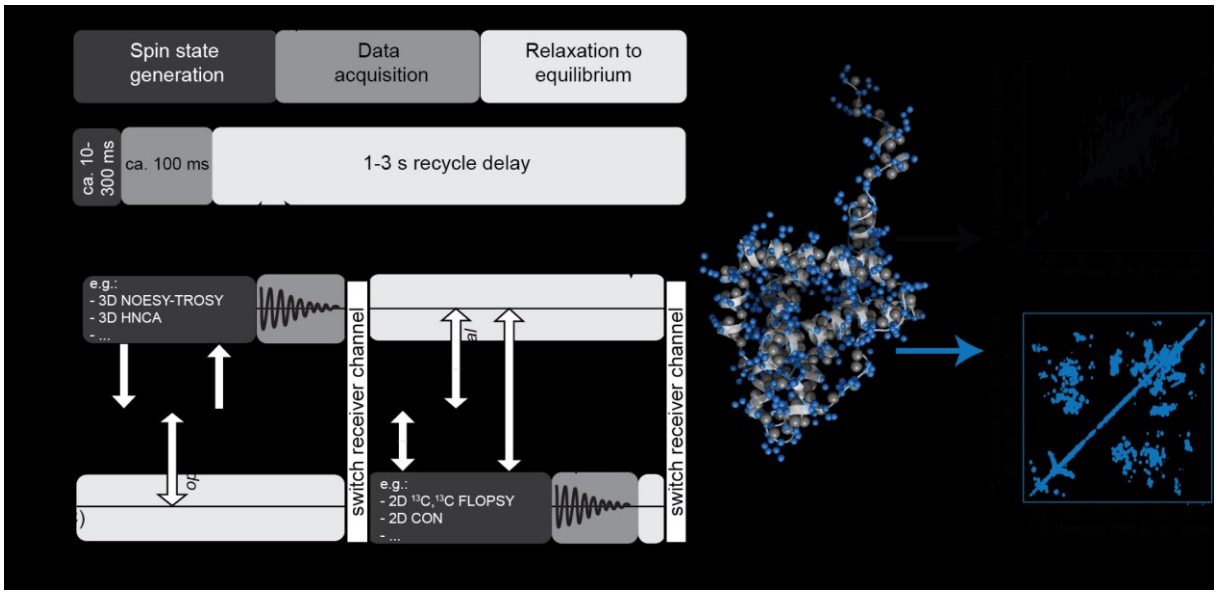

Figure 18. **Schematic representation of the UTOPIA-NMR setup. a)** Modules of a standard NMR experiment and their conventional time distribution. **b)** The UTOPIA-NMR concept relies on the acquisition of one (or more) low-γ nuclei detected experiment (child experiment) during the relaxation period of the conventional ^{1}H-detected experiment (parent). Switching the receiver channel twice during each scan allows for two direct acquisition periods on different channels (e.g. ^{1}H and ^{13}C) using only one recycle delay and a conventional single receiver system. The UTOPIA approach provides a large variety of possible combinations of magnetization pathways in parent and child that can be tailored for a broad range of applications. **c)** Visualization of the different sources of polarization used for UTOPIA-NMR, exemplified for the perdeuterated protein Bcl-x_L. Grey and blue spheres represent amide protons and ^{13}C atoms, respectively; sphere volumes are scaled by the ratio of the γ-values of the nuclei. UTOPIA-NMR allows excitation and detection of the normally not used low-γ polarization (here ^{13}C) during the acquisition of the conventional ^{1}H-detected (high-γ) experiments.

We therefore decided to activate non-used ^{13}C magnetization and read out the information using direct ^{13}C detection. State-of-the-art receivers allow the fast switching of the receiver channel, enabling the interleaved acquisition of e.g. a ^{1}H-detected and a ^{13}C-detected experiment using a single receiver system. Hence, using a joint recycle delay and the interleaved acquisition capability we can unify one ^{1}H-detected and one (or more) ^{13}C-detected experiment in a time-optimized way (Figure 18b,c). In the following, the high-γ-detected experiments will be referred to as parent experiment whereas the low-γ-detected experiment will be referred to as child. Note that this does not imply any hierarchy or polarization inheritance and is just used for simplicity and technical reasons (i.e. it is consistent with the terminology used by the Topspin software). This unified time-optimized interleaved acquisition offers a remarkable potential and flexibility for a multitude of applications.

In general UTOPIA-NMR can be applied to all areas of NMR spectroscopy that involve at least two different nuclei species, however it will be most applicable in systems were the additionally activated magnetization source is significant in comparison to the conventionally used one, and/or the additional spectra should be acquired anyways. We therefore anticipate that four areas of research will particularly benefit from the UTOPIA setup:

1. NMR analytics/screening of (small) compounds. Here the acquisition of 1D or 2D spectra of high-γ (e.g. ^{1}H, ^{19}F) and low-γ (e.g. ^{13}C, ^{15}N, ^{31}P) nuclei can be carried out simultaneously, significantly reducing the total measurement time and increasing throughput.
2. The investigation of small soluble proteins at higher concentrations. Here excess in sensitivity can be split into additional experiments (using shared evolution periods).
3. The characterization of intrinsically disordered and/or paramagnetic proteins, which often focuses on the acquisition of a set of low-γ-detected experiments. If low-γ-detected experiments are the priority, UTOPIA-NMR can offer ^{1}H-detected experiments for free.
4. The investigation of perdeuterated biological systems including membrane proteins or large complexes.

While aspects 1. and 2. are in line with experiments that have been designed using parallel acquisition on multiple receiver setups [460, 461, 474], the UTOPIA approach has the advantage that no additional receiver upgrade has to be made. Our data (*vide infra*, Figure 44, Figure 45, Figure 46 and Figure 47) shows that the application of UTOPIA-NMR for these systems is straightforward and can significantly reduce measurement time. The application of UTOPIA-NMR with a focus on the low-γ detection (3.) is in many aspects similar to (and often simpler as) the application on larger, perdeuterated proteins with focus on the ^{1}H detection (4.). Notably, due to reduced decoupling requirements, UTOPIA-NMR can most easily be combined with TROSY-based polarization transfer mechanism, directly enabling the usage of all available spin ½ polarization sources of the protein.

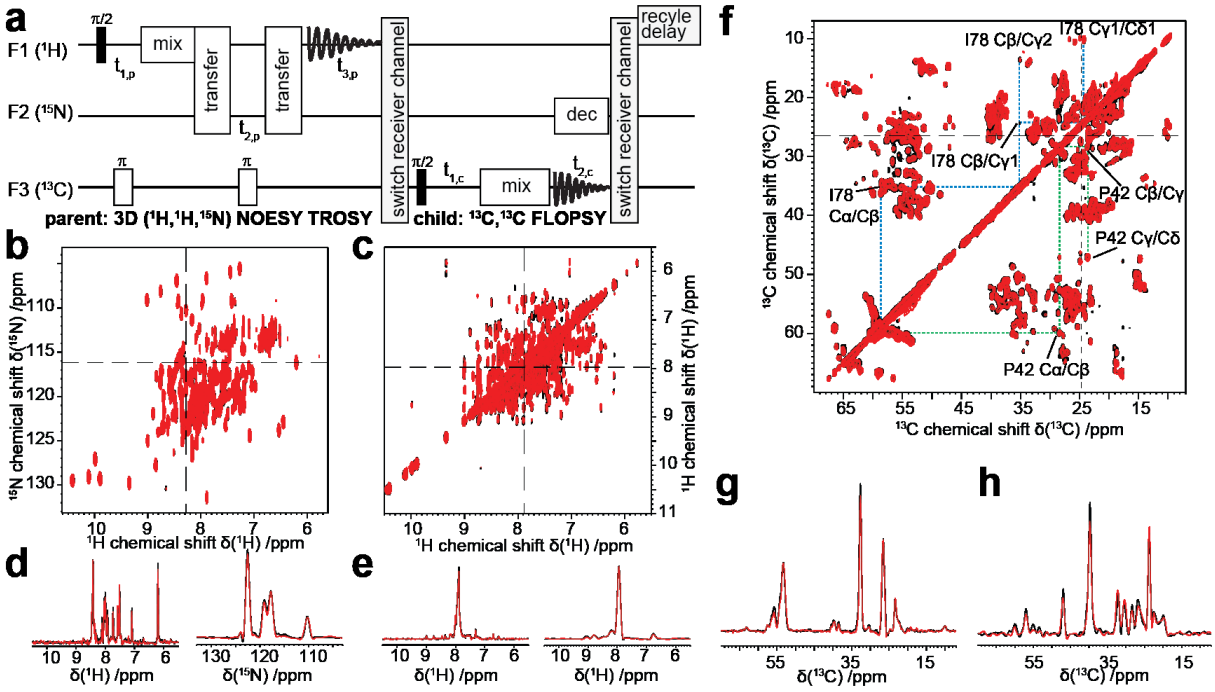

Figure 19. **Application of UTOPIA-NMR on soluble perdeuterated Bcl-x$_L$. a)** Simplified pulse scheme for the unified acquisition of a ^{1}H-detected NOESY-TROSY (parent) and a ^{13}C-detected CC-FLOPSY (child) (see Figure 20 for full pulse sequence). **b-h)** Superposition of spectra acquired conventionally (black) with data acquired in the UTOPIA setup (red). **b,c)** First HN and HH plane of the 3D NOESY-TROSY; **d,e)** 1D slices indicated in **(b,c)** respectively; **f)** 2D CC-FLOPSY and **g,h)** corresponding 1D slices. Note that the UTOPIA spectra (red) were recorded in exactly half of the time (i.e. 30 h) of the conventional ones (black, 2 x 30 h). Experimental conditions were 350 µM Bcl-x$_L$, 25°C, Bruker Avance III at 700 MHz (see supplementary methods for more details).

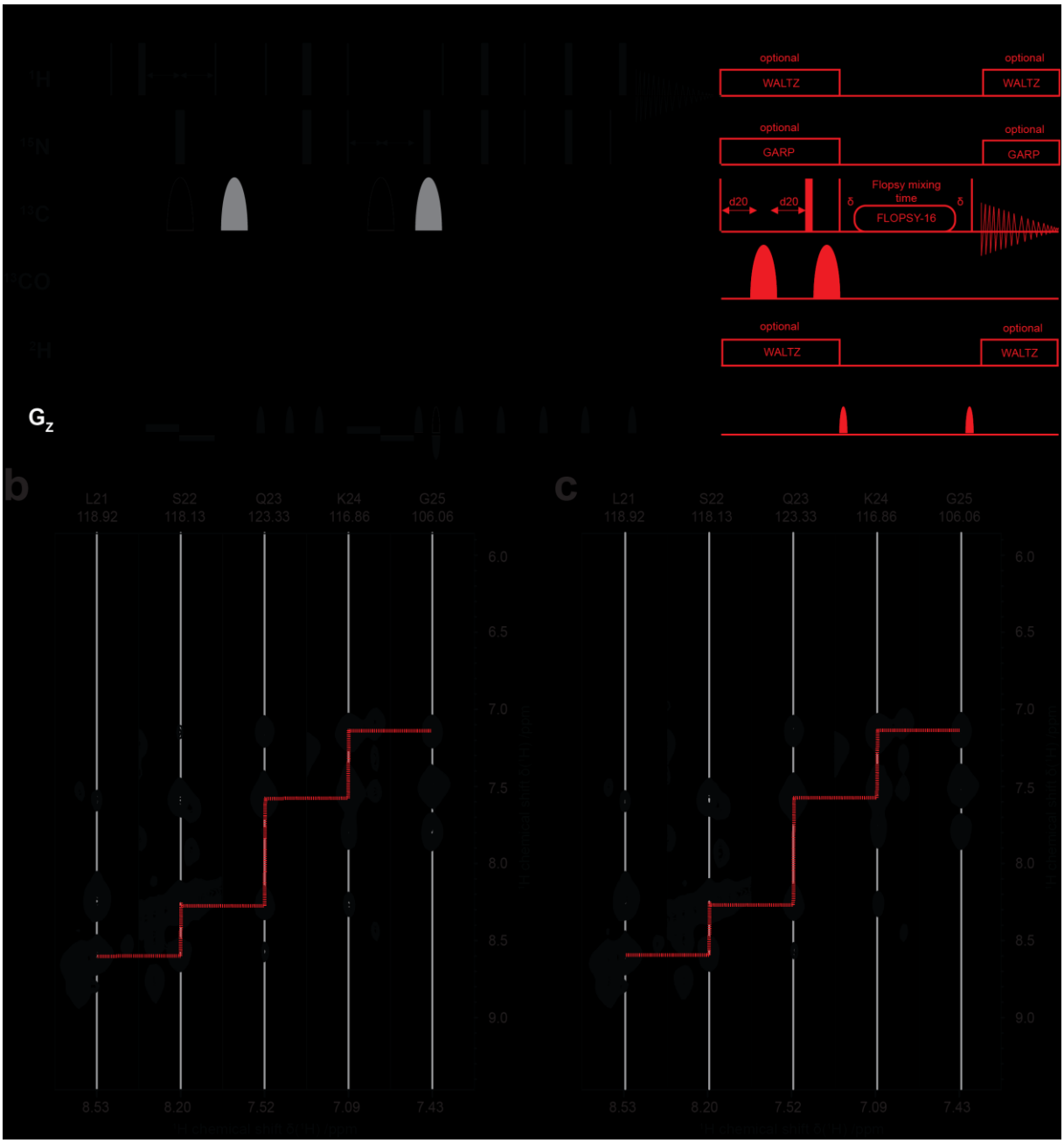

Figure 20. **Description of a unified NOESY-TROSY/CC-FLOPSY experiment. a)** Pulse sequence scheme for the unified acquisition of a $^{1}H,^{15}N$-NOESY-TROSY [475] (black) and a $^{13}C,^{13}C$-FLOPSY [476] (red). **b,c)** shows extracts of the corresponding parent experiment recorded in a conventional **(b)** and in an UTOPIA-NMR setup **(c)**. No significant differences are observed regarding the appearance and intensity of NOESY peaks in both spectra. Both parent and child pulse sequences were used with the standard parameters as found in the Bruker library. Note that in this study no scheme was introduced to eliminate $^{1}J_{CC}$ in the FLOPSY spectra, instead acquisition and processing parameters were selected that resulted in line widths above 50 Hz, i.e. not resolving $^{1}J_{CC}$. Nevertheless, if desired, techniques to reduce/eliminate $^{1}J_{CC}$ could be incorporated into the UTOPIA setup. Experimental conditions were 350 µM Bcl-x_L, 25°C, Bruker Avance III HD at 600 MHz.

In the following we will demonstrate the potential of the UTOPIA approach starting with the U-[$^{2}H,^{13}C,^{15}N$] labeled (fully ^{1}H back-exchanged) soluble Bcl-x_L protein (21 kDa). In general, the UTOPIA setup is most effective when spectra with similar total experimental time are combined. The unified acquisition of a $^{1}H,^{15}N$-NOESY-TROSY [475] with a $^{13}C,^{13}C$-FLOPSY [477] experiment not only fulfills this criterion but also combines two very useful experiments (Figure 19, also see Figure 20 and Table 9 for more details on pulse sequence and experimental parameters). The comparison of the UTOPIA parent (Figure 19b-e, red) with the same experiment recorded conventionally (Figure 19b-e, black) demonstrates that the unified acquisition of the child does not disturb the parent (see also Figure

20b,c for comparison of 3D slices). Interestingly, also for the UTOPIA child experiment (Figure 19f-g, red) only minor differences are visible in comparison with the reference data (Figure 19f-g, black). After analyzing the intensities in the corresponding 1D slices, we verify that we were able to recover about 95% of the reference (previously not used) carbon magnetization. In other words, the low-γ-detected spectrum (Figure 19f) can be recorded for free during the acquisition of a widely used standard experiment. The additional data can offer valuable information that can be used e.g. to easily cross validate Cα-Cβ assignments and/or to link Cα-Cβ to further carbons in the side chain and assign the full side chain in perdeuterated proteins. The latter is demonstrated for two selected residues of Bcl-x_L in Figure 19f (Pro42 and Ile78).

The UTOPIA setup may be modified for a given labeling scheme. When e.g. used for perdeuterated proteins, like shown here, ^{1}H decoupling during ^{13}C detection is often not required and hence the proton magnetization will be completely unperturbed by the presence of the child experiment. Therefore, the length of the recycle delay can be shortened by the time for spin-state generation and acquisition of the child experiment without losing magnetization for the parent. Notably, the T_1 relaxation time of the ^{13}C magnetization is often several times larger than the ^{1}H T_1 (see Figure 48 for ^{1}H and ^{13}C T_1 measurements in Bcl-x_L). The differences in T_1 relaxation times can be partly compensated by e.g. acquiring the child experiment only every second scan (as done for spectrum shown in Figure 19f). If ^{1}H composite pulse decoupling is required during the ^{13}C-detection period, which will often be the case in non-deuterated proteins, e.g. for the study of intrinsically disordered proteins, the total acquisition time will be prolonged by the time of the child experiment (spin-state generation and acquisition). In this case the child cannot be recorded completely for free. The cost for acquiring the child experiment in these conditions is however just the net time for pulsing and detection. For the UTOPIA setup shown in Figure 19a this only corresponds to ca. 5% of the total experimental time.

In general, the UTOPIA approach is very flexible, meaning that many different experiments can be designed, according to a particular sample or desired outcome. While the above shown setup combines two experiments with largely independent magnetization transfer pathways, the UTOPIA setup also has the potential to combine experiments with significant overlap in their transfer pathways. To demonstrate the flexibility of UTOPIA-NMR we developed a pulse sequence for the unified acquisition of a 3D ^{1}H,^{15}N-TROSY-HNCA experiment [478] with a 2D ^{13}C,^{15}N-CON experiment [479] (Figure 21b-f, Figure 22 and Table 9 for details on pulse sequence and acquisition parameters). Note that in this setup the disturbance of the ^{13}C magnetization of the child (CON) by the parent (TROSY-HNCA) can be minimized by introducing the joint recycle delay not at the end of the child (as it was the case for the UTOPIA setup shown in Figure 19) but between the parent and the child. As shown in Figure 21c-d, this setup, combined with suitable ^{1}H decoupling pulses in the child, also does not significantly disturb the ^{1}H excitation of the parent experiment (also see Figure 22a-b, for comparison of the parent NH plane and 1D slices, respectively). The comparison of the UTOPIA setup with the respective reference spectra again shows that while no difference in the information content of the parent spectra is observed, the additionally obtained CON spectrum provides valuable information such as a superior resolution in the CO dimension that can help to resolve ambiguities and correct peak positions in the conventional spectra (see Figure 22 for comparison). In addition, in the case of Bcl-x_L, it directly enables the assignment of all proline residues, filling the gaps often found in chemical shift assignments (again this information comes for free during the acquisition of a standard experiment).

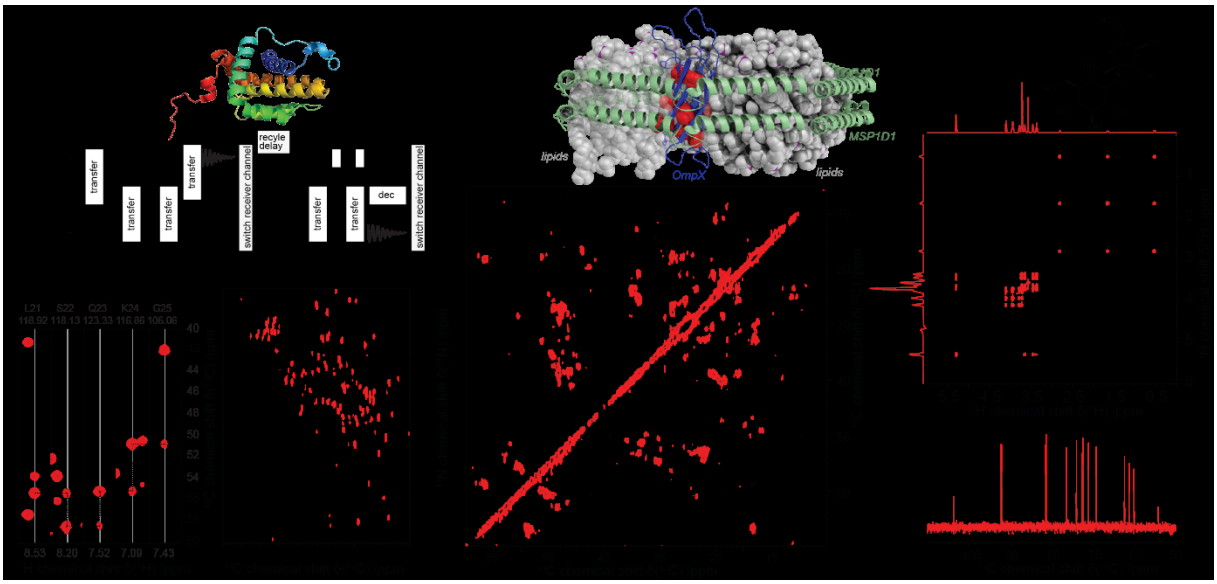

Figure 21. **Selected applications of UTOPIA-NMR. a)** Simplified pulse scheme for the unified acquisition of a ^{1}H-detected TROSY-HNCA (parent) and a ^{13}C-detected CON (child) experiment (see Fig. S5 for full pulse sequence). **b,c)** Superposition of spectra acquired conventionally (black) with data acquired in the UTOPIA setup (red). **b**) Extract of the 3D TROSY-HNCA, **c**) 2D CON. Total experimental time was 47 h for the conventional acquisition and 23,5 h for the UTOPIA data. Note that splittings in the CON spectrum due to CO-Cα J-couplings have been removed using maximum entropy deconvolution [480] using nmrPipe [481], resulting in well-resolved signals for nearly all residues in Bcl-x_L (including all prolines). **d)** Application of UTOPIA-NMR to large biological systems. ^{13}C-detected FLOPSY spectrum recorded on OmpX in nanodiscs (200 µM perdeuterated OmpX at 700 MHz, total acquisition time was 60 h). Only the child experiment is shown (red) and compared to a conventional spectrum (black). Labels show easily identifiable Cα-Cβ correlations in the transmembrane region of OmpX (red residues in model above). **e,f)** Typical NMR analytics spectra recorded on a sample of 2 mM unlabeled sucrose (2D ^{1}H,^{1}H TOCSY (e) and 1D ^{13}C (f)). In all cases the unified acquisition of parent and child allowed data acquisition in exactly half of the time as compared to the respective conventional setups.

To demonstrate the usage of UTOPIA for even more challenging biological systems, we tested the approach on the membrane protein OmpX in (not NMR-optimized) nanodiscs (formed with MSP1D1 [245, 274], 160 kDa - see supplementary methods for details on sample preparation). In previous studies of comparable samples we could e.g. not detect any Cα-Cβ connectivities in the membrane-embedded protein regions using conventional ^{1}H-detected experiments [245, 379]. Figure 21d demonstrates (i) that UTOPIA-NMR works well in these systems and (ii) that due to the favorable relaxation properties of direct ^{13}C detection (that does not require long transfer steps from and to the amide proton) combined with TOCSY-type of magnetization transfer, Cα-Cβ connectivities can be obtained in these challenging systems. Notably, in these systems the additional information is very much needed for detailed NMR characterization and once more the UTOPIA setup provides this information for free during the acquisition of e.g. a NOESY-TROSY spectrum (Figure 49).

Figure 21e-f shows an example for the application of the UTOPIA setup to analyze small molecules. Here the acquisition of a 2D ^{1}H-^{1}H TOCSY spectrum with a direct 1D ^{13}C-detected spectrum were combined and tested with a sample of 2 mM unlabeled sucrose. Our data shows that it is also possible for this completely different class of samples to obtain useful information on the low-γ nucleus without disturbing the conventional ^{1}H-detected experiment (see Figure 46 and Figure 47 for a more detailed discussion).

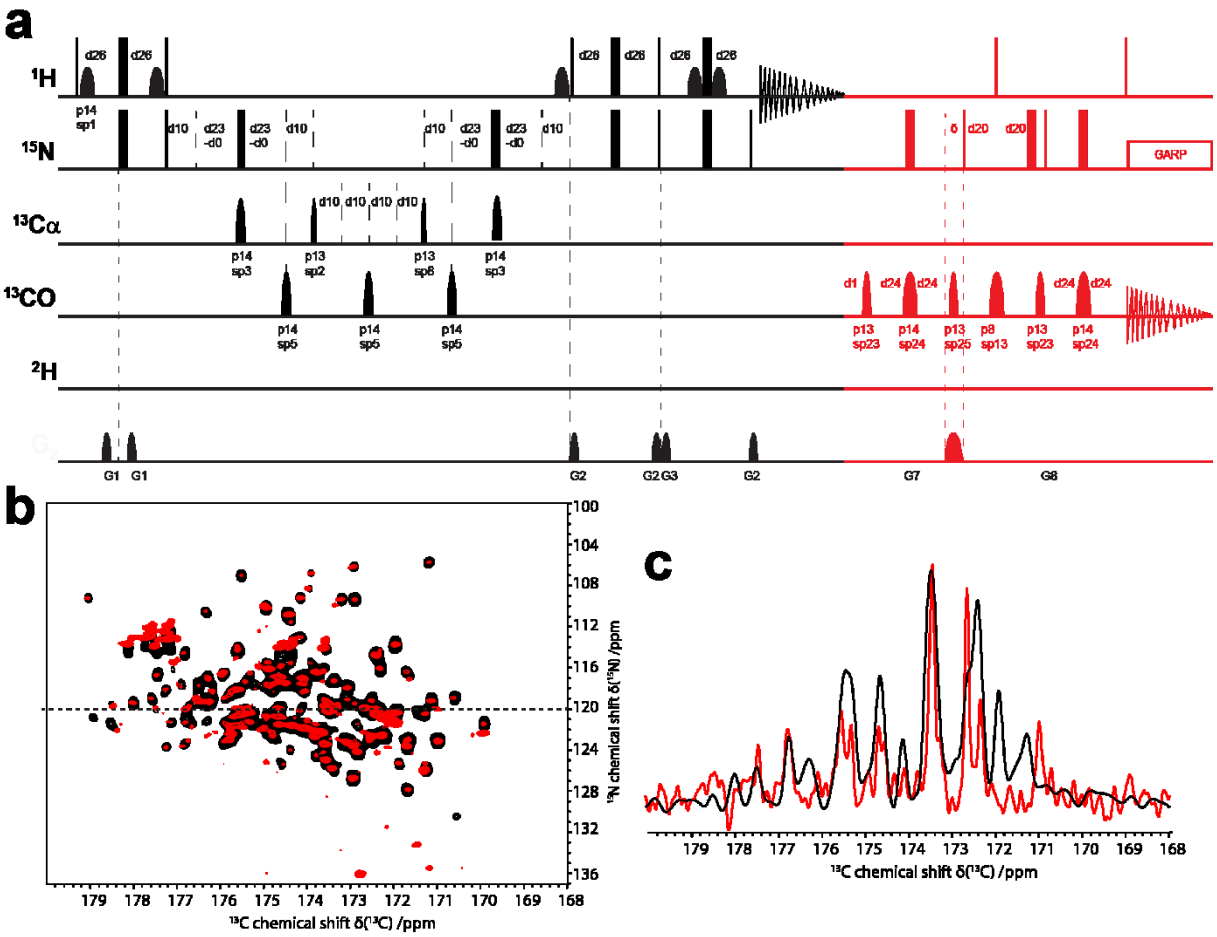

Figure 22. **Description of a unified TROSY-HNCA/CON experiment. a)** Pulse sequence scheme for the unified acquisition of a $^{1}H,^{15}N$-HNCA [478] (black) and a $^{13}C,^{15}N$-CON [479] (red). Both parent and child pulse sequences were used with the standard parameters as found in the Bruker library. Note that the relaxation delay (d1) is placed just before the child experiment which renders the usage of the standard (composite pulse) ^{1}H decoupling scheme in the child inefficient, as it would lead to significant loss of signal in the parent experiment. Instead, two ^{1}H π-pulses (one decoupling pulse in the middle of the ^{15}N evolution period and one recovery pulse directly after) were used and the time between the pulses was kept as short as possible to minimize ^{1}H magnetization losses. Using this sequence we do not observe reduced sensitivity for the parent or reduced resolution in the child (Figure 21). **b,c)** Comparison between the CON projection as extracted from a regular HNCO spectrum (black) and the direct ^{13}C detected CON spectrum (red) that can be recorded as child experiment in the UTOPIA setup shown in Fig. S7. A 1D slice through the indicated ^{15}N frequency (120 ppm) is shown on the right hand side. For acquisition of the conventional HNCO spectrum standard parameters were applied (i.e. 40/128 increments in the indirect $^{15}N/^{13}C$ dimension, respectively). Due to the direct ^{13}C detection the CON experiment naturally has a higher resolution in the ^{13}C dimension (2048 increments) and was acquired with 128 increments in the ^{15}N dimension. Analogous processing parameters were used for both spectra. In addition to the appearance of all proline residues the ^{13}C-detected spectrum may assist resolving the correct peak position of CO-N correlations in crowded regions

Perspectives/conclusion

In conclusion, the UTOPIA-NMR approach provides a convenient way to exploit non-used magnetization. Here we focused on a setup that allows the acquisition of a low-γ-detected experiment without disturbing the ^{1}H-detected experiment. In principle the acquisition of more than one parent and one child experiment as well as the usage of more than two different channels should be feasible and may provide exciting opportunities for future developments of the UTOPIA setup. In addition, also joint evolution periods are possible as previously reported using parallel acquisition (see Figure 46 and Figure 47 for a setup mimicking [461]). However, as compared to multi-receiver setups, small to considerable relaxation losses (depending on sample properties and experimental design) due to a delayed acquisition will be present in the interleaved setup. Moreover, one should consider that e.g. in protonated proteins,

in contrast to perdeuterated proteins, the additional ^{13}C magnetization source is substantially weaker as compared to the ^{1}H source. If, in these cases ^{13}C detection is still desired, it may be beneficial to start an UTOPIA child experiment from the ^{1}H magnetization (e.g. by using selective pulses). In general, the UTOPIA setup is complementary to many previously developed acquisition techniques and therefore can also be directly combined with fitting approaches including the use of paramagnetic relaxation reagents [482], non-uniform sampling [483] and, in suitable samples, also with selective proton excitation techniques.

Due to the flexibility of the approach, the wide range of possible applications, and the fact that acquiring the additional information is very useful and can be obtained completely for free, we anticipate that this approach should become standard for all measurements that benefit from the additional information. The unified acquisition of two or more spectra has the additional advantage that the different spectra are obtained under exactly identical conditions facilitating peak alignment and providing unique possibilities in time-resolved spectroscopy. Noteworthy, many NMR analytics facilities regularly record a direct ^{13}C-detected spectrum of their compounds in addition to 2D $^{1}H,^{1}H$ correlated spectra. Since ^{13}C detection is mostly done at natural abundance, this spectrum often requires about half of the measurement time spend for each sample. As demonstrated in Figure 21e-f, UTOPIA-NMR allows the detection of a ^{13}C spectrum during the acquisition of standard ^{1}H-detected experiments (also see Figure 44 and Figure 45). UTOPIA-NMR hence has the potential to nearly double the throughput of many NMR analytics facilities (the gain in efficiency may vary according to sample properties and the used setup, see Figure 44 for a more detailed discussion). Depending on the perspective, UTOPIA-NMR can either reduce the experimental time by a factor of about two or it can deliver additional information for free during the acquisition of a conventional set of experiments. In particular the combination of already developed low-γ-detected experiments (including the protonless NMR approach [21, 479]) with standard ^{1}H-detected experiments can directly provide valuable complementary information that may help to maintain reliable NMR-structural insights for increasingly complex samples.

Acknowledgements

The authors acknowledge access to the Jülich-Düsseldorf Biomolecular NMR Center. We thank Eriks Kupce for helpful discussions. This work was supported by grants from the German Academic Exchange Service (DAAD) and the German Research Foundation (DFG) (ET 103/2-1) to M.E. and from the European Union's Horizon 2020 research and innovation program under the Marie Sklodowska-Curie grant agreement Nº 660258 to A.V.. G.W. acknowledges support by the National Institute of Health (NIH) grants GM047467, GM075879. Acquisition and maintenance of instruments used for this research were supported by NIH grants EB002026 and S10 RR026417.

CHAPTER V – METHOD DEVELOPMENT – TARGETED DNP

This Chapter was published with the reference:
Viennet T., Viegas A., Kuepper A., Arens S., Gelev V., Petrov O., Grossmann T. N., Heise H. and Etzkorn M. Selective protein hyperpolarization in cell lysates using targeted dynamic nuclear polarization. *Angew. Chem. Int. Ed. Engl.* 55 (36), 10746-10750 (**2016**)
DOI: 10.1002/anie.201603205

Selective protein hyperpolarization in cell lysates using targeted dynamic nuclear polarization

Thibault Viennet[1,2], Aldino Viegas[1], Arne Kuepper[3], Sabine Arens[1], Vladimir Gelev[4], Ognyan Petrov[4], Tom N. Grossmann[3], Henrike Heise[1,2], Manuel Etzkorn[1,2*]

[1] Institute of Physical Biology, Heinrich-Heine-University Düsseldorf, Universitätsstr. 1, 40225 Düsseldorf, Germany

[2] Institute of Complex Systems, Forschungszentrum Jülich, Wilhelm-Johnen-Strasse, 52425, Jülich, Germany

[3] Chemical Genomics Center of the Max Planck Society, Otto-Hahn-Strasse, 44227, Dortmund, Germany

[4] Faculty of Chemistry and Pharmacy, Sofia University, 1 James Bourchier Blvd., 1164 Sofia, Bulgaria

[*] Corresponding author

Selective protein hyperpolarization in cell lysates using targeted dynamic nuclear polarization

Abstract

Nuclear magnetic resonance (NMR) spectroscopy has the intrinsic capabilities to investigate proteins in native environments. In general, however, NMR relies on non-natural protein purity and concentration to increase the desired signal over the background. We here report on the efficient and specific hyperpolarization of low amounts of a target protein in a large isotope labeled background by combining dynamic nuclear polarization (DNP) and the selectivity of protein interactions. Using a biradical-labeled ligand, we were able to direct the hyperpolarization to the protein of interest, maintaining comparable signal enhancement with about 400-fold less radicals than conventionally used. We could selectively filter out our target protein directly from crude cell lysate obtained from only 8 ml of fully isotope enriched cell culture. Our approach offers effective means to study proteins with atomic resolution in increasingly native concentrations and environments.

Introduction

Structural biology is gradually recognizing the indispensable link between the properties of the target protein and its native environment. Nuclear Magnetic Resonance (NMR) spectroscopy has contributed to this notion by e.g. enabling measurements in cells [484], cell envelopes [163] or cellular milieus [174]. The increasing complexity of such environments is however accompanied by two main challenges: (i) large contribution of unwanted background signals and (ii) low sensitivity of the target protein. Therefore, cellular NMR approaches so far rely on selective isotope labeling strategies that favor the target protein over the background, e.g. by changing the medium before protein overexpression [163] or (re)introducing the purified isotope labeled protein into an unlabeled environment [174, 484]. Dynamic Nuclear Polarization (DNP), i.e. the enhancement of NMR signal due to transfer of the high polarization of a free electron to the nuclei, has the potential to overcome sensitivity limitations associated with low protein concentrations [58, 59, 68, 146].

DNP relies, in general, on an empirically optimized statistical distribution of (bi)radicals in the sample [63, 95], and has been successfully applied to study challenging biological systems [155, 158, 163, 171, 172, 174]. Additionally, the concept of placing the radical in a more defined position has recently emerged, e.g. attached to a nanocrystalline peptide [138], endogenously paramagnetic interaction partners or proteins [134, 154], lipid-anchored radicals [133, 135] and radicals directly attached to membrane proteins [137, 139, 140]. In line with these localized DNP techniques, we here report on a broadly applicable approach to selectively excite a target protein over a large background. Basis of this targeted DNP approach is the covalent attachment of the biradical TOTAPOL [95] to an interaction partner of the target protein. The selectivity of the protein interaction is then exploited to specifically direct the hyperpolarization to the protein of interest. Using the 20 kDa protein Bcl-x_L (target) and its binding partner, the Bak peptide (ligand), we show that comparable protein signal enhancements can be achieved with several hundred fold less radicals than conventionally used, largely confining the hyperpolarization to the targeted protein instead of the whole sample.

We demonstrate the potential of the setup by selectively hyperpolarizing our target protein directly in its crude, fully isotope-enriched cell lysate. Notably, except for the standard protein overexpression, our DNP data were obtained without increasing the protein levels (concentration or purity) as compared to the living cells.

Material and Methods

Synthesis and characterization of a maleimide modified TOTAPOL radical (mTP)

A cysteine reactive maleimide moiety was attached readily to the commercially available 1-(TEMPO-4-oxy)-3-(TEMPO-4-amino)propan-2-ol (TOTAPOL) by acylating the secondary amino group on the linker connecting the two (2,2,6,6-Tetramethylpiperidin-1-yl)oxyl (TEMPO) radical units (Figure 23a). 3-maleimidopropionic acid (Figure 50a) was pre-activated with chloroethyl formate and triethylamine in Tetrahydrofuran (THF). Coupling attempts with Fluoro-N,N,N',N'-tetramethylformamidinium hexafluorophosphate (TFFH) or dicyclohexyl carbodiimide (DCC) were less successful. A solution of 85 mg 3-maleimidopropionic acid (0.50 mmol, Fluorochem) and 90 µl triethylamine (0.65 mmol) in 2.5 mL dry THF was chilled on ice under inert atmosphere. Ethyl chloroformate (60 µl, 0.50 mmol, Merck) was added, and the mixture was stirred for 20 minutes on ice. 200 mg TOTAPOL (0.50 mmol, Dynupol) was dissolved in 5 ml dry THF, chilled on ice under inert atmosphere and added in one portion to the activated maleimidopropionic acid solution by using a syringe. The reaction mixture was stirred for 12 hours at room temperature. Thin Layer Chromatography (TLC) using 1:1 hexane:ethyl acetate as eluant revealed two major products, the desired product (estimated ~80% by TLC-UV light) and a minor higher running by-product (estimated ~20% by TLC-UV light). The reaction solvent was evaporated under reduced pressure, the residue was taken up in 20 ml ethyl acetate, extracted twice with 0.5 M hydrochloric acid (HCl) and twice with aqueous potassium carbonate (1 g/L), and the combined organic fractions were dried with sodium sulfate and evaporated under reduced pressure. The resulting crude TOTAPOL-maleimide conjugate was dissolved in 0.8 ml of ethyl acetate:hexane (1:1) and purified by silica gel flash chromatography using a hexane - ethyl acetate gradient. The minor reaction by-product eluted at 50% ethyl acetate and had mass consistent with the ethyl carbamate of TOTAPOL (M+H 473.35, 472.33 calculated for C24H47N3O6). The desired product eluted at 60-70% ethyl acetate. Solvent removal yielded 215 mg of TOTAPOL-maleimidopropionamide mTP (78%). ESI-MS [M+H] 552.35 (551.34 calculated for C28H47N4O7) is shown on Figure 50b.

Synthesis and characterization of Bak derived peptides

Bak derived peptides synthesis was carried out manually on H-Rink Amide ChemMatrix® resin (Sigma-Aldrich) according to standard fluorenylmethyloxycarbonyl chloride (Fmoc)-based solid-phase peptide synthesis (SPPS) [485]. Amino acids were coupled using four equivalents of Fmoc-protected amino acids relative to the initial amine-loading of the resin. The Fmoc-protected amino acids were mixed with four equivalents of benzotriazole-1-yl-oxy-tris-pyrrolidino-phosphonium hexafluorophosphate (PyBOP) and eight equivalents of N,N-diisopropylethylamine (DIPEA) in N-methyl-2-pyrrolidinone (NMP) and twice incubated with the resin for 1 h. Fmoc-deprotection was carried out with 25% piperidine in NMP for 15 minutes. After each double-coupling step, unreacted amines were blocked with NMP/DIPEA/acetic anhydride (10:1:1; capping solution) for 10 min.

A [2-[2-(Fmoc-amino)ethoxy]ethoxy]acetic acid (Fmoc-PEG2-OH) building block as linker at the N-terminus was inserted prior to coupling the cysteine or not. For the final N-terminal modification the Bak derived peptides were deprotected as aforementioned and twice reacted for 10 minutes with capping solution for acetylation. The Bak derived peptides were finally cleaved from the resin applying trifluoroacetic acid/water/1,2-ethanedithiol/triisopropylsilane (94:2.5:2.5:1) for 4 h and precipitated with diethyl ether at -20 °C. After this final cleavage, the crude products were dissolved in water/acetonitrile (7:3) and purified by reverse-phase high-performance liquid chromatography (HPLC) using a Nucleodur C18 reverse-phase column (10 mm x 125 mm, 110 Å, particle size 5 µm, Macherey-Nagel; solvent A: water + 0.1 % trifluoroacetic acid (TFA), solvent B: acetonitrile + 0.1% TFA; flow rate: 6 mL·min-1). Obtained pure product fractions were combined, frozen in liquid nitrogen and lyophilized with a Heto PowerDry® LL1500 freeze drying system (Thermo Scientific). Product identification and purity was assessed by a HPLC/ESI-MS (high-performance liquid chromatography/electrospray ionization-mass spectrometry) 1200 system equipped with a Zorbax Eclipse XDB-C18 reverse-phase column (4.6 mm x 150 mm, particle size 5 µm, Agilent Technologies; solvent A: water + 0.1 % TFA, solvent B: acetonitrile + 0.1 % TFA; flow rate: 1 mL·min-1) connected to a liquid chromatography quadrupole Advantage Max (Finnigan™) mass

spectrometer (Figure 51). Analytical data are shown in Table S1. The Bak derived peptides were gravimetrically quantified.

Ligation and characterization of a N-terminally cysteinylated Bak derived peptide with maleimide modified TOTAPOL

The ligation of a N-terminally cysteinylated Bak derived peptide with maleimide modified TOTAPOL was carried out in a 20 mM sodium phosphate reaction buffer at pH 7.4. The peptide was dissolved in double-distilled water (ddH2O) and TOTAPOL in acetonitrile providing initial stock solutions of 10 mM and 440 mM, respectively. To minimize oxidation and therefore formation of disulfide bridges 10 mM peptide was incubated with 8.5 mM tris(2-carboxyethyl)-phosphine (TCEP) in reaction buffer for 30 min on ice (stock A). Furthermore, a 10-fold excess of TOTAPOL (100 mM) in reaction buffer for the later proceeding reaction was prepared (stock B). To start the ligation 110 µL stock A and 110 µL stock B were combined and incubated for 1 h on ice resulting in final concentrations of 5 mM and 50 mM, respectively. Product (Bak-mTP) identification was assessed by a HPLC/ESI-MS (high-performance liquid chromatography/electrospray ionization-mass spectrometry) 1200 system equipped with a Zorbax Eclipse XDB-C18 reverse-phase column (4.6 mm x 150 mm, particle size 5 µm, Agilent Technologies; solvent A: water + 0.1% trifluoroacetic acid (TFA), solvent B: acetonitrile + 0.1% TFA; flow rate: 1 mL·min-1) connected to a liquid chromatography quadrupole Advantage Max (Finnigan™) mass spectrometer. Purification of Bak-mTP was accomplished by reverse-phase high-performance liquid chromatography (HPLC) using a Nucleodur C18 reverse-phase column (10 mm x 125 mm, 110 Å, particle size 5 µm, Macherey-Nagel; solvent A: water + 0.1% TFA, solvent B: acetonitrile + 0.1% TFA; flow rate: 6 mL·min-1). Obtained pure ligation product fractions were combined, frozen in liquid nitrogen and lyophilized with a Heto PowerDry® LL1500 freeze drying system (Thermo Scientific). Product identity and purity was verified by HPLC/ESI-MS as aforementioned (Figure 52). Analytical data are shown in Table S1.

Bcl-x_L protein expression and purification

The uniformly [^{13}C,^{15}N] labeled truncated Bcl-x_L sample was expressed and prepared according to [214] . Bcl-x_L was first purified by Immobilized Metal Affinity Chromatography (IMAC) followed by Size Exclusion Chromatography (SEC) with a Superdex 75 preparative grade column (GE Healthcare). A stock solution of 40 µM in 25 mM sodium phosphate, pH 7.0, 100 mM sodium chloride, 1 mM Ethylenedinitrilo-tetraacetic acid (EDTA) and 2 mM Tris(2-carboxyethyl)phosphine (TCEP) was used for storage. Buffer was exchanged via dialysis in order to reduce the concentration of EDTA and TCEP to a minimum before use for sample preparation.

Solution Nuclear Magnetic Resonance (NMR) sample preparation

The stock solution of labeled Bcl-x_L after dialysis was used directly. When needed, lyophilized Bak peptide or Bak-mTP was resuspended directly with the stock solution in order to obtain a 1:1 molar ratio of protein-peptide complex at 40 µM. Stability of the complex in close to DNP conditions, i.e. in the presence of Dimethyl Sulfoxyde (DMSO) and glycerol, was tested by adding 10% v/v of DMSO and then an additional 10% v/v of glycerol and comparing the ^{1}H-^{15}N TROSY-HSQC spectra (data not shown). For the Paramagnetic Relaxation Enhancement (PRE) experiments, after acquiring a spectrum of Bcl-x_L:Bak-mTP (oxidized radical), the radical was reduced by addition of a 5-fold free electron molar equivalent ascorbic acid (400 µM), incubated in the spectrometer at 25 °C for one hour and another spectrum was recorded (reduced, reference). Note that the final sample contained 5% v/v of DMSO-d_6 and 5% v/v D_2O (Figure S4).

Dynamic Nuclear Polarization (DNP) samples preparation

The stock solution of labeled Bcl-x_L was dialyzed and concentrated to the appropriate molarity using a 10 kDa cutoff centrifugation device (Amicon® Ultra) with simultaneous exchange of the buffer against its deuterated

equivalent. All samples were prepared in the same way by mixing 40% volume of Bcl-x_L stock solution in D2O based buffer with 10% volume of Bak or Bak-mTP stock solution in DMSO-d_6. For the low TOTAPOL reference spectra, a 1 mM stock solution in deuterated buffer was used. Else, the mixture was used to dissolve the appropriate amount of TOTAPOL as powder (in order to obtain 20 mM final concentration) and/or to resuspend [^{13}C-^{15}N]-glycine lyophilizate attaining a 1:100 molar excess. Finally, 50% glycerol-d_8 was added and the mixture packed in a 3.2 mm sapphire rotor and quickly frozen in liquid nitrogen before injection in the DNP low-temperature probehead.

All the spectra for the initial results (Figure 24, Figure 25 and Figure 54) were recorded with a final amount of Bcl-x_L of 23 µg, corresponding to 45 µM. For the two-dimensional and the glycine background experiments (Figure 26 and Figure 55), spectra were recorded with 52 µg Bcl-x_L, corresponding to 100 µM and 10 mM glycine.

Crude lysate DNP sample preparation

Approximately 8 ml of culture pellet (either of uniformly [^{13}C,^{15}N] labeled truncated Bcl-x_L or of uniformly [^{13}C,^{15}N] labeled 6xHis-GB1-ACTH (Adrenocorticotropic hormone) as negative control were resuspended in 20 mM sodium phosphate, pH 7.0, 150 mM sodium chloride D2O based buffer. Cells were lysed using a sonication bath for 30 min in the presence of lysozyme. Cell debris were removed by centrifugation (30 min, 15000·g) and the supernatant was dialyzed twice (7 kDa cutoff) against 100-fold buffer. Finally the lysate was concentrated to its original concentration (vide infra) using a 10 kDa cutoff centrifugation device (Amicon® Ultra). Bradford assay and Sodium Dodecyl Sulfate-Polyacrylamide Gel Electrophoresis (SDS-PAGE) showed a total protein concentration of approximately 35 mg/ml and a content of 10% Bcl-x_L (based on relative intensity of SDS-PAGE bands). This corresponds to 88 µg Bcl-x_L or 168 µM in the final sample. Based on these results 200 µM of Bak-mTP were added for the targeted setup and DNP measurements were carried out in fully deuterated buffer in the proportions 40:10:50 D2O:DMSO-d_6:glycerol-d_8 (Figure 27 and Figure 57).

Two ways to estimate the effective cell volumes were used:

- Based on cell mass: The pellet of the cell culture has a (wet) weight between 2.5-3 g per liter of cell culture leading to a total weight of 20-24 mg in 8 ml, which would translate to a maximal volume of 20-24 µl. (It can be estimated that around 20% of the total mass is 'dry mass' and that only around 25% of the dry cell mass (lipids, etc..) is not in the lysate [486], leading to an estimated volume of 19-23 µl.
- Based on cell density: An optical density (OD_{600}) of one is found for a cell density of 109 cells/ml [487]. The OD_{600} before harvesting was 1.61. Assuming a volume of 1.1 µm^3 for one *E.coli* cell [488] results in a total volume of 14 µl.

The sapphire MAS-rotor is filled with a sample volume of 23-25 µl, therefore both estimates strongly suggest that the total protein concentration (including that of the target protein) of 8 ml cell culture inside the rotor is not higher than in the living cell before lysis.

Solution NMR data acquisition

Solution NMR experiments were performed on a Bruker Avance III spectrometer operating at 600 MHz, equipped with a triple resonance TCI (^{1}H, ^{13}C, ^{15}N) cryoprobe and shielded z-gradients. Data was collected at 25 ºC with a sample concentration of 40 µM in 25 mM NaP_i pH 7.0, 100 mM NaCl, and 10% (v/v) D2O. [^{1}H-^{15}N]-Transverse relaxation-optimized Heteronuclear Single Quantum Correlation (TROSY-HSQC) [32] were all recorded with 160 increments and 208 transients, with a recycle delay of 1.5 s (total experimental time 15 hours). All NMR spectra were processed with TOPSPIN 3.2 (Bruker) and analyzed with CCPN [469].

Magic Angle Spinning-DNP (MAS-DNP) data acquisition

Magic-angle spinning solid-state DNP experiments were performed on a Bruker Avance III spectrometer operating at 600 MHz, equipped with a 395.18 GHz second-harmonic gyrotron and a 3.2 mm $^{1}H,^{13}C,^{15}N$ triple resonance low-temperature MAS probe. Data were collected at 108 K, 8 kHz MAS speed and 9 W continuous-wave microwave power for on-experiments. Sample characteristics are detailed above. All experiments were recorded using a ^{1}H-^{13}C Cross Polarization (CP) contact time of 250 µs and a recycle delay of 5 s. 2D ^{13}C-^{13}C Proton Driven Spin Diffusion (PDSD, 20 ms mixing time) [55] were acquired with 64 t1 increments and 512 or 1024 transients for DNP-on and DNP-off experiments respectively (total experimental time 2 days and 4 days respectively). All NMR spectra were processed with TOPSPIN 3.2 (Bruker). Glycerol scaling was carried out by manually aligning the glycerol specific peak at 75 ppm. Projections of the Cα-CO were extracted from 47 to 73 ppm in the indirect dimension.

Results

To generate the radical-labeled ligand, we introduce a simple one-step synthesis of maleimide modified TOTAPOL (mTP) which allows the covalent attachment to cysteine side chains (Figure 23a). Purified mTP was then ligated to a version of the Bak peptide containing an N-terminal cysteine connected by a PEG linker to a 16-residue Bak fragment which is known to interact with Bcl-x_L [218] (Figure 23b, Figure 50, Figure 51 and Figure 52). Binding of the modified Bak peptide can be detected by chemical shift perturbations in solution NMR spectra. Analysis of the peak volumes of bound and free Bcl-x_L shows that around 90% of Bcl-x_L is bound to modified Bak (Fig. 1d, molar ratio 1:1). This fits well the expected ratio of 91.2%, based on a KD of 340 nM found for the unmodified Bak peptide [218]. We also performed Paramagnetic Relaxation Enhancement (PRE) measurements that identified only one well-defined region of Bcl-x_L affected by the presence of the biradical (Figure 23e and Figure 53). Overall the solution NMR data could confirm binding of the modified ligand, report on at least a partial integrity of the unpaired electron spin and allow for an initial estimation of the location of the radicals in our system.

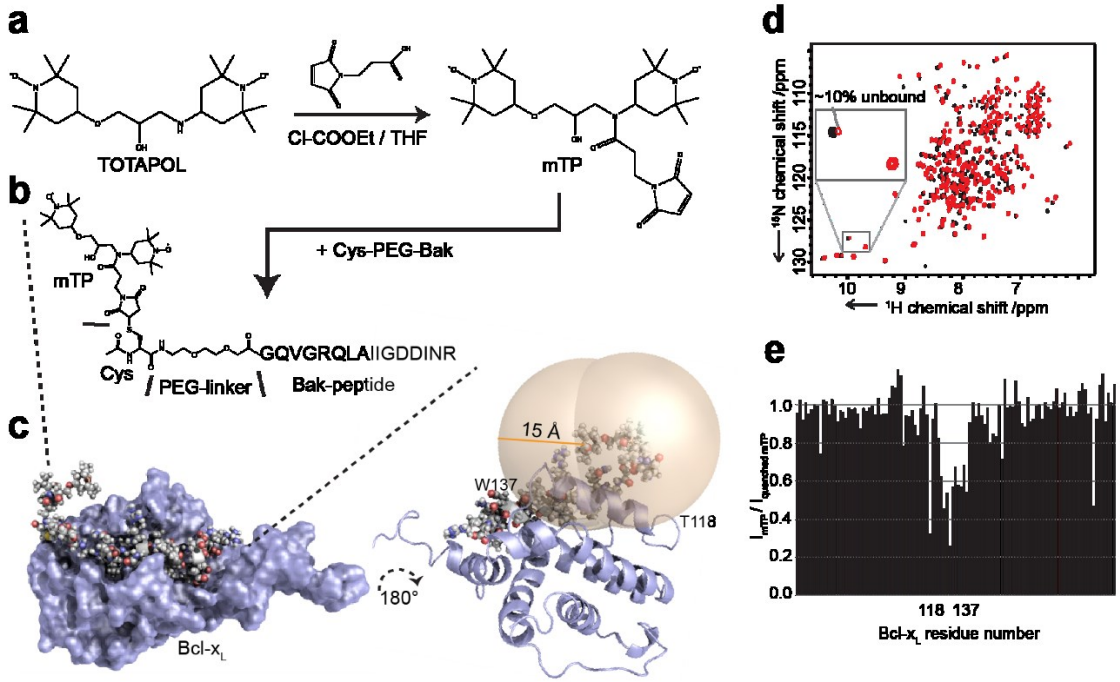

Figure 23. **Preparation of radical-labeled ligand (Bak-mTP) and characterization of its interaction with the target protein (Bcl-x_L). a)** One step reaction for mTP synthesis. **b)** Ligand design (see SI for more details). **c)** Structural model of the complex between Bak-mTP and Bcl-x_L [218]. **d)** Comparison of [^{15}N-^{1}H]-HSQC spectra of free Bcl-x_L (black) vs. complex (red, 1:1 molar). **e)** PRE plot as the ratio of peak volumes in oxidized vs. reduced radical states for all resolved Bcl-x_L residues. A well-defined protein region is affected by the biradical (in line with the radical localization shown in **c**).

We subsequently tested our setup under DNP conditions (Figure 24). All DNP spectra were recorded at 600 MHz proton resonance frequency at 108 K. Initially we recorded reference spectra under conventional DNP conditions using 20 mM soluble TOTAPOL and 23 µg of uniformly ^{13}C,^{15}N labeled Bcl-x_L in standard buffer conditions [489] (50% glycerol-d_8, 10% DMSO-d_6, 30% D_2O and 10% H_2O). Note that this buffer only slightly differs from the optimal 'DNP-juice' by replacing 10% of the glycerol with DMSO to ensure solubility of the ligand. Using these conditions, an enhancement factor ε (ratio of signal-to-noise in the presence and absence of microwaves) of 20 was obtained (Figure 24a).

Placing the radical in a well-defined (close) distance should allow the usage of only one biradical per target protein. Using a protein concentration of about 50 µM will then reduce the free radical concentration 400-fold as compared to the conventional setup. To test the DNP properties of these low radical concentrations we recorded reference spectra of 50 µM Bcl-x_L in the presence of 50 µM free TOTAPOL. As expected, this low radical concentration does not sufficiently hyperpolarize the sample (ε around 1). Surprisingly, we experienced also weak enhancement factors (ε = 2) when using the targeted setup under standard buffer protonation level (10%). We attribute this to spin diffusion effects that may pull the polarization away from the protein and into the buffer [117]. Indeed, when changing to a fully deuterated buffer the enhancement factor of the targeted setup is drastically increased leading to a value of ε = 18. Note that this should translate to a value between 27 and 40 at 400 MHz [93] for which most previous values are reported.

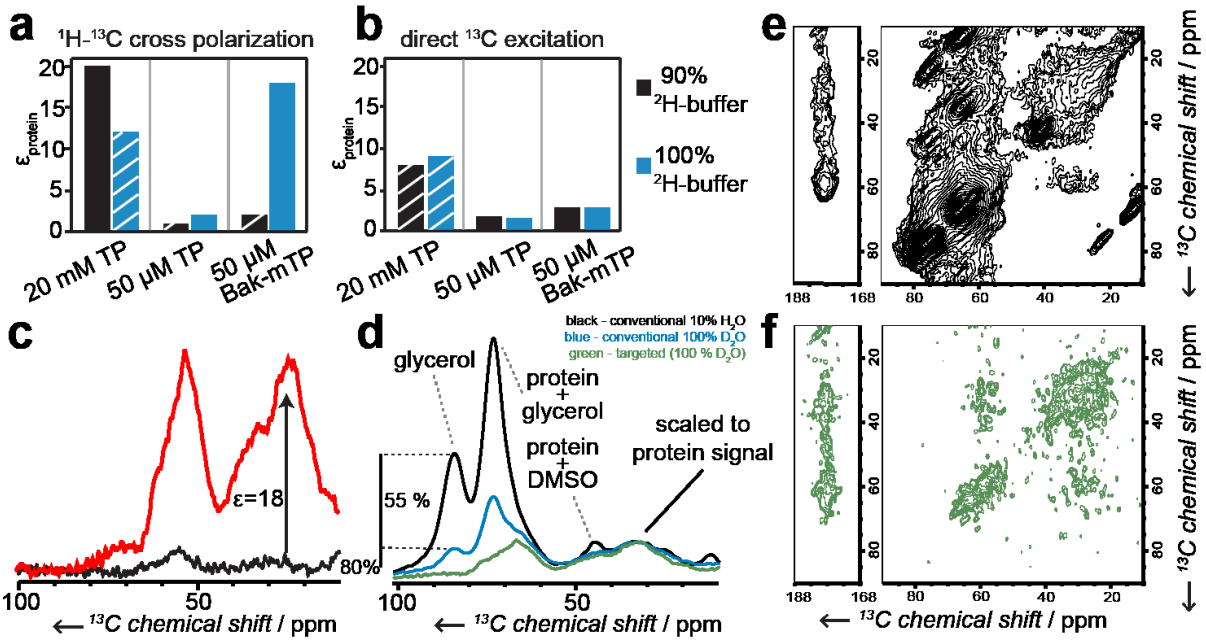

Figure 24. **Targeted DNP provides effective and selective hyperpolarization. a)** DNP enhancements of ^1H-^{13}C cross polarization for Bcl-x_L in the presence of indicated amounts of soluble TOTAPOL (TP) or in the Bak-mTP targeted setup. All experiments were recorded using 23 µg of purified Bcl-x_L and either conventional 10% protonation (black) or fully deuterated buffers (blue). Stripe pattern indicate values that were determined with less accuracy (see Figure 54 for all experimental data). **b)** Same samples as in **a)** but using direct ^{13}C excitation. **c)** ^1H-^{13}C cross polarization spectra of the optimized targeted DNP setup in the presence (red) and absence (black) of microwave irradiation. **d)** ^1H-^{13}C cross polarization spectra of purified Bcl-x_L using targeted DNP (green, 100 µM Bak-mTP, 100% D_2O), conventional DNP in fully deuterated buffer (blue, 20 mM TOTAPOL, 100%D_2O) and conventional DNP with 10% buffer protonation (black, 20 mM TOTAPOL, 10% H_2O). Spectra are scaled to the protein signal to demonstrate the reduction of the unwanted background signal. Full deuteration of the buffer leads to a 55%, reduction of the glycerol signal. Targeted hyperpolarization leads to an additional 80% reduction of the glycerol signal. Note that the protein enhancement factor was roughly 2-fold lower in the deuterated buffer for the conventional approach (blue) as compared to the other two setups (black, green). **e)** [^{13}C-^{13}C]-PDSD spectrum of purified Bcl-x_L using a conventional DNP approach (20 mM TOTAPOL, 10% H_2O). **f)** PDSD spectrum of purified Bcl-x_L using the targeted DNP approach (100 µM Bak-mTP, 100% D_2O). A strong reduction of background (glycerol) signal and related artifacts (side-bands) is visible.

The hypothesis of ^1H-polarization leakage into the protonated buffer is supported by the enhancement factors of direct carbon excitation, which are not affected by buffer protonation levels (Figure 24b). Noteworthy, the rather low enhancement of the ^{13}C nuclei in the targeted setup may indicate that the distance between the

biradical and the ^{13}C enriched protein is too long for an effective hyper-polarization and hence may contribute to the fundamental understanding of the effective enhancement radius of the biradical. On the proton side, we detected an increase in the DNP-buildup time τ_{DNP} for the covalently bound biradical (Figure 25a-d) and see a strong effect of the buffer protonation level but we do not experience a far-reaching quenching and/or depolarization effect (Figure 25e). The herein observed significantly higher enhancement factor, as compared to most previous localized DNP studies, is likely directly related to the latter findings and may be attributed to the low total amount of radicals used in our setup.

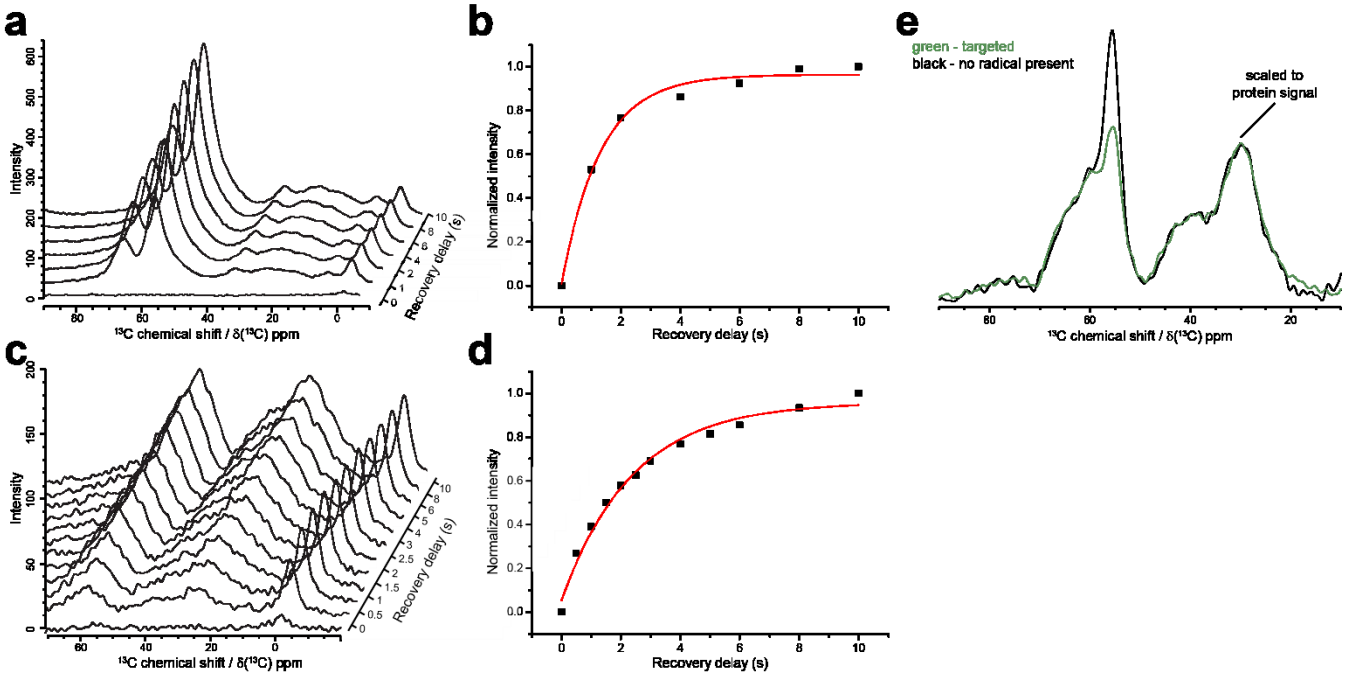

Figure 25. **Characterization of the DNP behavior of Bak-mTP. a)** Magnetization buildup data (^{1}H-^{13}C CP) of Bcl-x_L (and glycerol) in the conventional case (20 mM TOTAPOL, 10% protonated buffer). **b)** Fit (red line) of the measured normalized intensities (black) squares) leads to a buildup constant τ_{DNP} of 1.31 ± 0.14 s. The data for the targeted DNP setup **c)** and **d)** shows a τ_{DNP} of 2.39 ± 0.24 s. e) Quenching/depolarization effect of Bak-mTP. ^{1}H-^{13}C cross polarization spectra with microwaves off in the presence (green) or in the absence (black) of radical-labeled ligand. Both samples have the identical protein-to-glycerol content, and no difference is seen in the protein-to-glycerol signal ratio. Since a clear protein selective hyperpolarization is seen in the microwaves-on spectra (see e.g. Figure 24), the unchanged protein-to-glycerol signal ratio in the DNP-off spectra strongly suggests that no selective quenching/depolarization effects are detected for the target protein. Note that the peak at 52 ppm is dominated by the spinning side band of a background signal of the sample container which had different intensities in both samples.

A comparison of the conventional and targeted 1D DNP spectra demonstrates the selectivity of the targeted setup (Figure 24d). While the protein-specific signal (peak at 25 ppm) has a similar magnitude, the background-specific peak (at 75 ppm) is largely reduced in the targeted setup. All in all, the initial DNP characterization of our targeted setup reveals that (i) one biradical provides hyperpolarization in the target protein with an enhancement factor similar to that of a proton network polarized with 400-fold more radicals, (ii) the quenching/depolarization effects of the mTP are rather moderate and (iii) the directed hyperpolarization drastically improves the protein-over-background signal. Due to the large effects of buffer protonation, all further targeted experiments were carried out in fully deuterated buffer. Note that while the herein used buffer condition was chosen to allow a fair comparison between conventional and targeted DNP, it in general deviates from the native cellular environment. It has been shown before that localized DNP setups, however, can extend the range of suitable DNP buffer conditions and, depending on the biological system and scientific question, an alternative buffer may be selected to reduce potential artifacts from non-native buffer conditions [139].

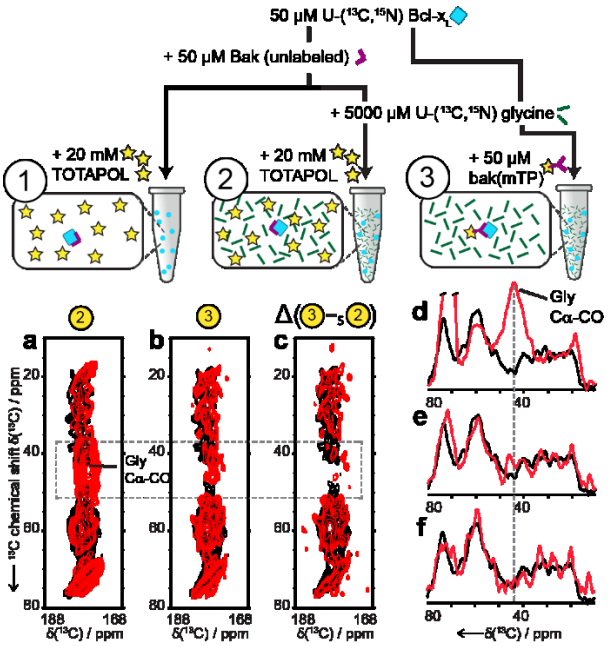

Figure 26. **Targeted DNP can selectively enhance a protein over a large isotope labeled background.** A schematic of the used samples (top) and overlay of the CO-Cx region of [^{13}C-^{13}C]-PDSD spectra of pure Bcl-x$_L$ (black, sample 1) with data obtained in the presence of 100-fold molar excess of labeled glycine using conventional DNP (**a**, red, sample 2), targeted DNP (**b**, red, sample 3) and **c)** difference between the targeted and conventional DNP spectra (scaled to the same glycerol intensity). 1D projections of the 2D spectra in **a-c** onto the indirect dimension are shown in **d-f**, respectively and visualize the decrease of the glycine background.

To test our targeted approach in an isotope-labeled background, we used samples of Bcl-x$_L$ with 100-fold molar excess of isotope-labeled glycine. Due to the good separation of glycine Cα signals from other aliphatic carbons, the Cα-CO cross peaks in the 2D PDSD spectrum provide an estimate of the labeled background over Bcl-x$_L$ signal. While in the conventional setup the glycine signal largely exceeds the protein specific signals (Fig 3a,d, red), it is significantly reduced (by around 80%) in the targeted setup (Figure 26b-e, red, also see Figure 55).

Theoretically, this selective enhancement should allow to obtain a pure spectrum of the target protein by subtracting a non-selective spectrum scaled to the same background level. Note that the quality of the difference spectrum will predominantly depend on the selective enhancement factor (see Figure 56). The non-selective spectrum could be a DNP-off spectrum or a DNP-on spectrum in a conventional setup. While the first could be obtained using only one sample, it may be limited by insufficient signal intensity. Here we subtracted the signal of the conventional DNP-on sample scaled to match the same glycerol intensity (Figure 26c-f, red). For this approach the protein to glycerol ratio needs to be identical in both samples, which can easily be achieved by splitting the same stock solutions. Indeed, the resulting difference spectrum does not show any apparent signals indicative of the glycine background anymore. This alludes that the targeted setup has the potential to selectively hyperpolarize one in a hundred molecules, enabling the investigation of small amounts of target protein in large, fully isotope-labeled backgrounds.

We subsequently applied our approach to study Bcl-x$_L$ directly in its cell lysate using only one buffer exchange step and no protein purification. To challenge our approach, cell growth and protein expression were carried out in the same medium, leading to the same degree of labeling of background and target protein. Each DNP sample was prepared using only 8 ml of cell culture for which we estimate that the respective cell volume reflects the volume of the sample rotor (see SI for calculation) resulting in samples with protein levels similar to the living cell. Four different samples were prepared including lysates in a targeted (sample I) and a conventional setup (sample II), as well as a positive (sample III) and a negative control (sample IV) (Figure 27a). 1D spectra of the targeted and conventional samples are shown in Figure 27b. Due to the homogenous hyperpolarization in the conventional setup the contribution of Bcl-x$_L$ to the total signal should be given by its abundance, which we estimate based on our biochemical data to be about 10% of the total protein content. Scaling the obtained spectra to the same background signal (glycerol) reveals a protein specific enhancement in the targeted setup (Figure 27c).

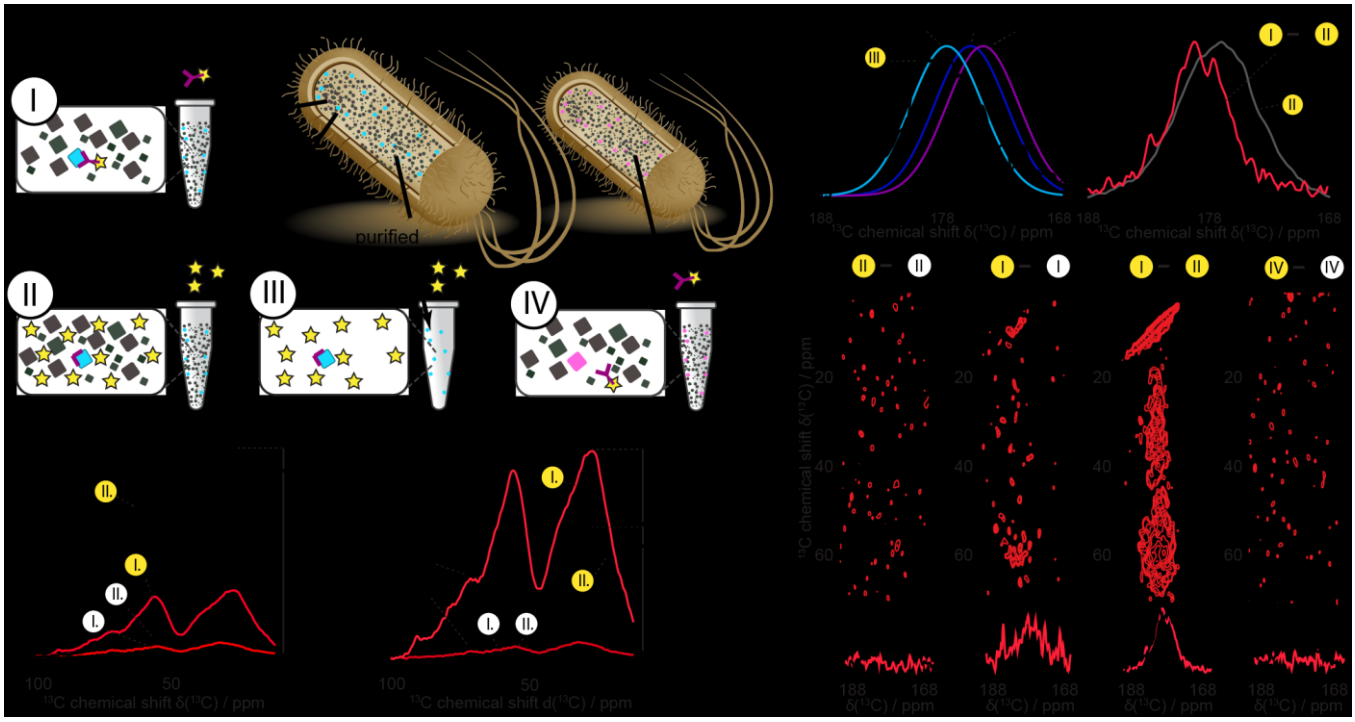

Figure 27. **Targeted DNP is applicable to proteins at low abundance in crude cell lysates. a)** Schematic of used samples. **b)** 1D spectra in the presence (yellow label) and absence (white label) of microwaves for the conventional (black) and targeted (red) setup. Expected signal contributions are indicated. **c)** Same spectra as in (b), but scaled to the glycerol background. **d)** Predicted CO signals for indicated secondary structure elements overlaid with a Cα-CO projection of a 2D PDSD spectrum of purified Bcl-x_L (sample III). **e)** Comparison of the projections obtained from conventional DNP (sample II) and its difference to the targeted approach (sample I). A clear shift towards α-helical structure is visible. **f-i)** Comparison of indicated difference spectra (red) to the purified Bcl-x_L reference (sample III, grey) and corresponding Cα-CO projections. Note that in all cases (**f-i**) a non-selective spectrum of the lysate was subtracted suggesting that residual signal, which is only found in the targeted DNP approach and only in the presence of Bcl-x_L (**g, h**), originated from a selective protein polarization.

Interestingly, the Bcl-x_L protein differs from the average protein in the lysate due to an exceptionally high content in α-helical secondary structure. Since ^{13}C chemical shifts are indicative of secondary structure [490] we used a projection of the Cα-CO cross peaks to assess the secondary structure content of the spectra [174]. While a comparison of the experimental data of purified Bcl-x_L to the predicted pure secondary structure elements [490] reflects the high α-helical content of the protein (Figure 27d), the conventional DNP spectrum of the cell lysate (Figure 27e, black) shows a considerable contribution of all secondary structure elements as expected for a heterogeneous cell lysate. Noteworthy, the signal difference between the targeted and the conventional DNP spectrum (after scaling to the same glycerol level) has a clear increase in α-helical content (Figure 27e, red), consistent with selectively filtering out the Bcl-x_L signal from the background.

To further validate the selectivity of the setup, a series of 2D PDSD difference spectra were measured (Figure 27f-i, red) and compared to the spectrum of purified Bcl-x_L (Figure 27f-i, black)). As expected the difference of a conventional DNP-on and DNP-off spectrum (Figure 27f, red), results in an empty spectrum. The respective difference in the targeted setup (Figure 27g, red) contains a weak signal in the Cα-CO region (also see projection). Here the relative low signal-to-noise ratio is related to the weak signal of the DNP-off spectrum. Instead of recording a very long DNP-off spectrum, we subtracted a conventional DNP-on 2D PDSD spectrum of the same lysate preparation (scaled to the same glycerol signal). The resulting difference spectrum has a higher signal-to-noise ratio and nicely overlaps with the reference Bcl-x_L spectrum (Figure 27h). To further corroborate this observation, we designed a negative control with cell lysate grown under the same conditions but expressing a GB1-protein construct instead of Bcl-x_L. The difference spectrum of the lysate containing GB1 using the same amount of Bak-mTP as before does not show any signal, confirming that this cell lysate does not specifically interact with the radical labeled Bak peptide (Figure 27i).

Perspectives/conclusion

In summary the lysate data indicate that (i) the targeted DNP setup specifically enhances protein signal over glycerol signal (Figure 27c), (ii) the additionally enhanced protein signal is predominantly α-helical (Figure 27e), (iii) the signal also largely overlaps with the signal of purified Bcl-x_L (Figure 27h) and (iv) subtracting an unspecific spectrum of the lysate results in a non-empty spectrum only for the targeted DNP enhanced spectrum and only in the presence of the target protein (Figure 27f-i, also see Figure 57 and Figure 58). These data strongly suggest that the signal seen in Figure 27g,h originated from a specific interaction of Bak and Bcl-x_L.

Due to the power of DNP we could obtain spectra from only 8 ml of non-purified cell culture. In addition to a large reduction of workload and sample losses, the low amount of required isotopes will also facilitate usage of expensive labeling strategies. While the herein used target protein primarily serves as a suitable test system and will in general also be accessible to in-cell solution NMR approaches, we anticipate that future applications of the targeted DNP setup may also involve systems that are not soluble, cannot be easily purified, reintroduced into a cellular context and/or require expensive isotope labeled media, such as e.g. membrane proteins and/or eukaryotic expression systems. When combined with established selective and protein-over-background isotope labeling techniques, the targeted DNP setup may help to specifically visualize the target protein in front of a massive background and e.g. probe the effects of molecular crowding, the native membrane environment and interactions with other cellular components on a residue specific level.

Acknowledgements

We acknowledge access to the Jülich-Düsseldorf Biomolecular NMR Center and funding through a Major Equipment Initiative (HE3243/4-1), two Emmy Noether grants of the DFG, ET103/2-1 to M.E. and GR3592/2-1 to T.N.G., a Marie Sklodowska-Curie Grant (No. 660258) to A.V. and support from the International NRW Research School iGRASPseed to T.V.. We thank Dr. Dora Angelicheva from FB Reagents for assistance with flash chromatography. T.N.G. and A.K. were supported by AstraZeneca, Bayer CropScience, Bayer Health-Care, Boehringer Ingelheim, Merck KGaA and the Max Planck Society.

CHAPTER VI – APPLICATION TO A MEMBRANE ASSOCIATED PROTEIN – α-SYNUCLEIN

Modulation of structural and kinetic determinants of α-Synuclein aggregation by stable, planar, lipid bilayer nanodiscs

Thibault Viennet[1,2], Michael M. Woerdehoff[1], Hamed Shaykhalishahi[1], Boran Uluca[2], Henrike Heise[1,2], Alexander K. Buell[1], Wolfgang Hoyer[1] and Manuel Etzkorn[1,2*]

[1] Institute of Physical Biology, Heinrich-Heine-University Düsseldorf, Universitätsstr. 1, 40225 Düsseldorf, Germany

[2] Institute of Complex Systems, Forschungszentrum Jülich, Wilhelm-Johnen-Strasse, 52425, Jülich, Germany

[*] Corresponding author

Modulation of structural and kinetic determinants of α-Synuclein aggregation by stable, planar, lipid bilayer nanodiscs

Abstract

The protein α-Synuclein (αS) is naturally found in presynaptic neurons and linked to Parkinson's disease through its intracellular abnormal aggregation. This mechanism is thought to consist of a complex interplay between free cytosolic and membrane-bound forms of αS. Therefore, a better understanding of the molecular determinants of αS membrane association as well as its implications for protein aggregation may offer important insights into the origins of Parkinson's disease.

Following previous studies using micelles and vesicles, we here report on the comprehensive in vitro study of the interaction of αS with phospholipid bilayer nanodiscs. Usage of this well-defined membrane mimetic allowed us to characterize the influence of the lipid charge density and the membrane fluidity with respect to interactions with αS at a residue specific level by solution Nuclear Magnetic Resonance (NMR). Insights into the bound conformation could be obtained using dynamic nuclear polarization (DNP) solid-state NMR. In addition, distinct effects of the lipid composition on αS aggregation were detected. The N-terminally acetylated form of αS, i.e. its natural state, is used and compared with the non-acetylated form revealing specific differences both in terms of membrane affinity and aggregation behavior.

Introduction

The protein α-Synuclein (αS) is a major player and eponym in various synucleinopathies, including Parkinson's disease, through its abnormal aggregation, fibril formation and formation of Lewy bodies [277-279, 283]. Although the natural function of αS is still a matter of debate, it is found in natural synaptic vesicles and supposed to be involved in membrane interactions, e.g. in synaptic vesicles homeostasis [286, 287] and SNARE-like vesicle-to-vesicle or vesicle-to-membrane fusion [289, 290]. Moreover, membrane association of αS has been shown to modulate its aggregation propensity [491, 492] and αS oligomeric species have been proposed to be the toxic species in Parkinson's disease, especially through membrane pore formation mechanisms [493, 494]. Interestingly, αS has been shown to be naturally N-terminally acetylated, which is a major mode of regulation for protein-membrane association [484, 495, 496].

Previous data recorded using micelle and vesicle preparations already provided valuable information of the αS-lipid interactions, including binding and lipid specificity [285, 497, 498], effect of mutations on membrane association [290, 499] micelle-bound structure [500], vesicle-bound structural insights [501-503] and conformational dynamics [503-505]. Taken together, two structural models of lipid-bound αS were proposed: the "extended helix" consisting of one roughly 100-residue long α-helix [506] and the "horse-shoe" consisting of two helices of different lipid affinities separated by a kink at residues 42-44 [507]. Furthermore, various effects of lipids for αS aggregation were also reported including both inhibition of aggregation [508] and triggering of fibrillation [282, 509]. Binding and effect on aggregation have been shown to be strongly dependent on chemical properties of the lipids including head groups' charge content [507] and hydrocarbon chain types [510].

The intrinsic features of the phospholipid bilayer nanodisc system [204] offer the potential to provide additional insights that are complimentary to the information obtained on micelle and vesicle preparations. Notably, NDs have been used before to study the effect of calcium ions on the membrane interaction of αS [511]. In general, NDs are very homogenous, stable in a wide buffer range [512] and allow the preparation of well-defined lipid mixtures with an accurate estimate of the bilayer size [513], charge [514], and lipid molarity [515]. The increased stability offers e.g. the possibility to accurately determine the interaction with a stable planar bilayer surface. In

contrast, it is known for small unilamellar vesicles (SUVs) that the interaction with αS will considerably and rapidly change the lipid environment (e.g. from homogenous SUVs to very heterogeneous particles [290, 516, 517]). Additionally, the smaller size of the NDs should, in theory, allow the detection of the lipid bound state using suitable solution NMR techniques [245, 379, 518]. Furthermore, the well-defined size and lipid composition of NDs, paired with their homogeneity and stability also permits quantitative insights into membrane association as well as its role in aggregation.

Here we report on a comprehensive investigation of the effects of lipid charge, lipid phase and bilayer fluidity, residue-specific affinities competing for accessible membrane surface areas, as well as αS acetylation on membrane association. For our study, we used more than 40 NMR samples and complimentary biophysical data to characterize globular affinity, and αS aggregation kinetics. Our study provides (i) insights into the different lipid binding modes of αS, (ii) insights into the effect of the binding modes on αS aggregation, (iii) an estimate of the number of lipid-associated αS proteins that are required to form a seed for aggregation, and (iv) allows to propose a first thermodynamic and kinetic model of αS binding to (limited) membrane surfaces and its effect on the aggregation pathway.

Material and Methods

αS and N-terminally acetylated αS expression and purification

Codon-optimised αS in the pT7-7 vector was expressed in *E. coli* BL21 DE3. For acetyl-αS, the N-terminal acetylation enzyme NatB from *Schizosaccharomyces pombe* was coexpressed in a second vector, pNatB [519]. PNatB (pACYCduet-naa20-naa25) was a gift from Dan Mulvihill (Addgene plasmid # 53613). Expression was conducted in 50 mM phosphate-buffered 2YT-medium (pH=7.2) with 0.4% glycerol and 2 mM $MgCl_2$, protein production was induced at OD 1-1.2 with 1 mM IPTG and run for 4 h at 37 °C. For ^{15}N-labelled protein, αS or acetylated αS was expressed in M9 medium with 0.2% $^{15}NH_4Cl$.

Sparse labelled αS for DNP experiments was non-acetylated, expression was done in a similar way, in M9 medium using 0.4% [2-^{13}C]-glucose and 0.2% $^{15}NH_4Cl$. The expression of Phe, Gln, Glu, Pro, Asn, Asp, Met, Thr, Lys, and Ile was suppressed by supplementing sufficient quantities (150 µg/ml of each) of these amino acids, unlabeled, in the expression media as reported previously [520].

Purification of αS or acetyl-αS was carried out as previously described [521], some changes to the original protocol have been made. Except for sparse labelled αS for which previous lysis in 20 mM Tris-HCl pH=8.0, 1 mM EDTA was done, cell lysis and release of αS or acetyl-αS was performed by directly boiling the frozen cell pellet at 95 °C in a 3-fold volume of 20 mM sodium phosphate buffer, pH=7.4, for 30 min. Thermostable αS or acetylated αS remained in the supernatant after 30 min of centrifugation at 15000·g and 4 °C and was subsequently subjected to an ammonium sulfate precipitation by slowly adding saturated ammonium sulfate solution to 50% saturation at 4 °C. Precipitated protein was pelleted at 15000·g and 4 °C, dissolved in 50 mL of 50 mM Tris-HCl pH=8, sterile-filtered and loaded onto an ion exchange chromatography column (HiTrap Q FF, GE Healthcare), where αS or acetyl-αS eluted at around 300 mM NaCl in 50 mM Tris-HCl pH=8. Elution fractions containing αS or acetyl-αS were subjected to another ammonium sulfate precipitation and finally purified by an SEC run (Superdex 75 10/300, GE Healthcare) in 20 mM sodium phosphate pH=7.4, 50 mM NaCl.

N-terminal acetylation of acetyl-αS was checked by HPLC and mass spectrometry and proved to be ~95% when co-expressed with NatB.

Nanodisc assembly

E. coli BL21 (DE3) bacteria were transformed with the MSP1D1 or MSP1D1ΔH5 [245] plasmid DNA in a pET28a vector as reported before [522]. In short, cells were grown in LB medium. Protein was solubilized with 6M Gu-HCl and purified by IMAC (without denaturating agent). The elution fractions were pooled and dialyzed in order to remove imidazole. N-terminal His-tag was cleaved using TEV protease incubated overnight at 4°C. ΔHis MSP1D1 or MSP1D1ΔH5 was separated from MSP1D1 or MSP1D1Δ5 by IMAC.

Nanodiscs were assembled according to established protocols [513]. In short, lipids' chloroform stocks were dried under nitrogen flow to obtain a lipid film and stored under vacuum overnight. ΔHis MSP1D1 or MSP1D1ΔH5 and the appropriate amount of lipids solubilized in 60 mM Na-cholate were mixed together in 20 mM Tris-HCl pH=7.5, 100 mM NaCl, 5 mM EDTA. The scaffold-to-lipid molar ratio was calculated from geometrical considerations. If not stated otherwise, the lipids used were a mixture between 1,2-dimyristoyl-*sn*-glycero-3-phosphocholine (DMPC) and 1-palmitoyl-2-oleyl-*sn*-glycero-3-phospho-(1'-*rac*-glycerol) (POPG) in different ratios (see Results). 20% w/v of previously washed Biobeads SM-2 (Biorad) were added and the mixture incubated at room temperature overnight. The Biobeads were removed by centrifugation and once again 20% w/v were added for an additional 4-5 hours. Finally they were purified by SEC on a HiLoad 16/600 Superdex 200 pg column (GE Healthcare) equilibrated with 20 mM sodium phosphate pH=7.4, 50 mM NaCl using a Äkta pure device run at 1 ml/min. The quality of NDs preparation was appreciated by the SEC chromatogram as well as by DLS (PSS Nicomp). NDs were concentrated to the desired molarity using a Vivaspin centrifugal device of 10 kDa MWCO.

Bio-layer interferometry (BLI)

NDs were immobilized on the sensor surface of amine reactive biosensors (AG2R) (fortéBIO, PALL Life Science) after EDC/NHS activation to a final level between 1.2 and 1.8 nm depending on the NDs type using an Octet RED96 instrument (fortéBIO, PALL Life Science). All biosensors were quenched with 1 M ethanolamine for 3 min. All experiments were carried out in multi cycle kinetics at 25 ºC. Association of αS in running buffer (20 mM sodium phosphate pH=7.4, 50 mM NaCl) on NDs and reference biosensors was recorded for 120 s, followed by a dissociation phase of 360 s. Sensorgrams were double referenced using the reference biosensors and a buffer cycle. Steady-state analysis was realized by fitting the αS concentration dependency of the highest response with a simple 1:1 binding model. After normalization, all on and off curves were fitted against simple exponential build-up or decay and led to similar on- and off-rates.

Solution NMR spectroscopy

If not stated otherwise, all NMR experiments were performed on a Bruker Avance III spectrometer operating at 600 MHz ^{1}H Larmor frequency, equipped with a triple resonance TCI (^{1}H, ^{13}C, ^{15}N) cryoprobe and shielded z-gradients. For all experiments data were recorded at 10 ºC with αS concentration of 50 µM in 20 mM sodium phosphate pH=7.4, 50 mM NaCl, 10% (v/v) $^{2}H_2O$. If not stated otherwise, the NDs concentration was set to 25 µM (1 αS per membrane leaflet). All [^{1}H-^{15}N]-TROSY-HSQC NMR spectra were acquired with 32 scans and 256 increments, processed with TOPSPIN 3.2 (Bruker) and analysed with CCPN [469]. Peaks were automatically integrated and the ratio of volumes in the presence and absence of NDs plotted against the primary sequence. Clear outliers were removed (non-transferable assignments in the acetylated case, peaks sharing their volumes, etc.).

ThT fluorescence aggregation assays

For the aggregation assays, 50 µM of αS or acetylated αS was mixed with either 25 µM (2:1), 3.125 µM (16:1) or 0.781 µM (64:1) nanodiscs with different ratios of POPG to DMPC. Assays were conducted in 20 mM

sodium phosphate buffer pH=7.4 or 20 mM acetate buffer pH=5 with 50 mM NaCl, 0.02% NaN_3 and 10 µM Thioflavin T. Per sample, triplicates of 120 µl were pipetted into 96-well half area well plates with non-binding surface (Corning No. 3881, black, clear bottom, Corning) containing a glass ball for mixing and incubated at 37 °C for up to 7 days. Orbital shaking at 217 rpm was used for 15 s every 20 min. Thioflavin T fluorescence was excited at 445 nm and measured at 485 nm, after each shaking event, in a plate reader (Tecan Spark 10M, Tecan infinite M1000PRO, Tecan Group Ltd.).

For the seeded experiments, fibril seeds of αS/acetyl-αS were prepared as follows: 300 µl of 100 µM αS or acetylated αS was fibrillated at 37 °C and 800 rpm for 3 days in a 2 mL tube containing glass balls in a Thermomixer (Eppendorf). The fibril solution was diluted to 50 µM and sonicated with a tip sonicator (Bandelin Sonopuls HD3200, BANDELIN electronic) at 10% power (20 W) for 60 s, with 1 s pulses on and 4 s off in between. Seed solution was diluted 20-fold for the aggregation assays (2.5 µM, 5%).

Kinetic curves were corrected by subtracting the curve of buffer (containing NDs) in the presence of ThT and normalized to highest fluorescence intensity according to quantification of fibril mass using SDS-PAGE. Only in the case of seeded assays no normalization was applied.

Sodium dodecylsulfate – Polyacrylamide gel electrophoresis (SDS-PAGE)

In order to compare the amounts of soluble and fibrillated αS or acetyl-αS in the aggregation samples, 100 µl of each triplicate sample were taken out of the well plate, combined in 1.5 mL tubes and spun down at 20000·g and 20 °C for 30 min. Supernatants (~290 µl) were taken off and the pellets were resuspended in 280 µl buffer. Reducing SDS-sample buffer (4-fold) was added and the samples, which were then boiled for 15 min at 98 °C. 10 µl of these samples were loaded onto a 15% SDS-gel together with standards of αS or acetyl-αS and nanodiscs.

Dynamic Nuclear Polarization (DNP) NMR spectroscopy

Magic-angle spinning solid-state DNP experiments were performed on a Bruker Avance III spectrometer operating at 600 MHz ^{1}H Larmor frequency, equipped with a 395.18 GHz second-harmonic gyrotron and a 3.2 mm [^{1}H,^{13}C,^{15}N] triple resonance low-temperature MAS probe. Data were collected at 100 K, 9 kHz MAS speed and 9 W continuous-wave microwave power. The samples were prepared from C_2-glucose isotopically labelled non-acetylated αS (250 µg) in the presence or in the absence of 2:1 molar ratio of 100% POPG nanodiscs and filled into 3.2 mm sapphire rotors. Final sample conditions were 15 mM sodium phosphate pH=7.4, 25 mM sodium chloride, 30% $^{2}H_2O$, 60% glycerol-d_6 and 2.5 mM AMUPOL [100]. Two-dimensional [^{13}C-^{13}C]-Proton-Driven Spin Diffusion (PDSD) with 1 s mixing time experiments were used. ^{1}H decoupling using SPINAL64 with a decoupling field of 104 kHz was employed during evolution and detection periods. Both experiments were conducted using 300 t_1 increments with 16 and 48 scans for αS in the absence and in the presence of nanodiscs, respectively. A recycle delay of 5 s was used in both experiments. Spectra were processed using Topspin 3.2 (Bruker).

Results

Effect of phospholipid head-group charge on αS membrane binding mode

To obtain residue specific insights into the interaction interface of αS with lipid bilayer nanodiscs (NDs) of various compositions, we recorded a series of solution NMR 2D TROSY-HSQC spectra (see Table 13 for full list of measured samples). The NMR spectrum of αS in the presence of NDs containing only DMPC lipids perfectly overlays with the spectrum of αS in the absence of NDs (Figure 28a-b). This finding provides additional evidence that αS does not interact with non-charged lipid bilayers [497], a point that is still controversial in the literature

[284]. Additionally, it also shows that αS does not interact with the membrane scaffold protein (MSP), confirming that the effects described in the following are not biased by (unspecific) αS-MSP interactions.

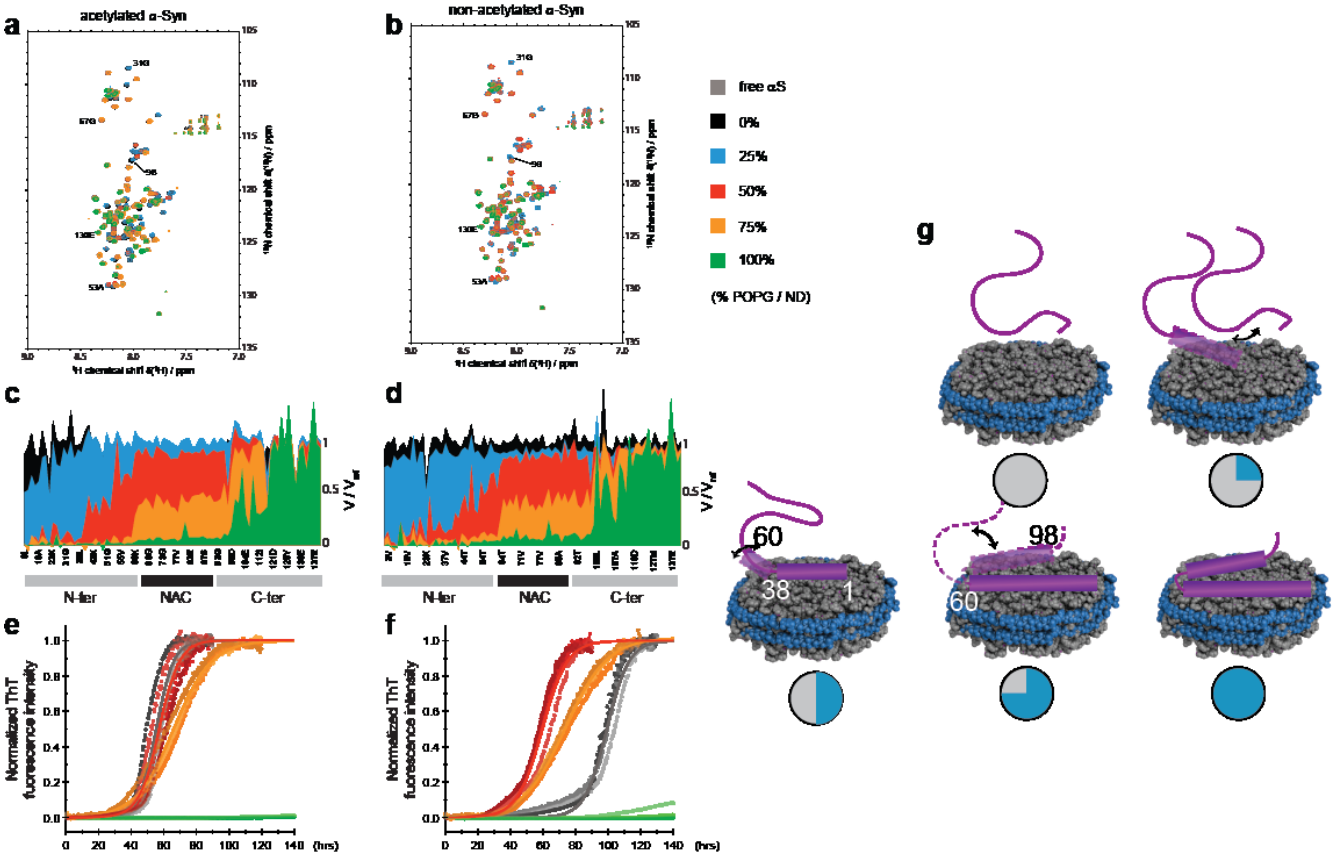

Figure 28. **αS binding modes to NDs and aggregation propensity depend on phospholipid head group negative charge content.** NMR spectra of [^{15}N]-αS (50 µM) in the absence or in the presence of 25 µM NDs (1 αS per leaflet) of different POPG (negative charges) contents. [^{15}N-^{1}H]-TROSY-HSQC spectra of acetylated (**a**) and non-acetylated (**b**) αS. Spectra in the absence (grey) or in the presence of NDs containing 0% POPG (black), 25% POPG (blue), 50% POPG (red), 75% POPG (orange) and 100% POPG (green) are displayed. Chosen assignments corresponding to parts of the sequence differently affected by the binding modes are shown. The corresponding attenuation profiles, i.e. the ratio of peak volume in the presence over the absence of NDs are plotted against αS primary sequence in (**c**) and (**d**) respectively. Normalized ThT fluorescence kinetic curves for some of the conditions are respectively plotted in (**e**) and (**f**) using the same color code. Molecular model visualizing the gradual binding of αS to NDs as successive α-helices is shown in (**g**) and explains previous results according to the negative charge content inside NDs (represented as filled circles, negative charges in blue).

In a similar way as reported previously using liposomes [507, 523], we further tested the influence of increasing amounts of negatively charged lipid head groups on αS membrane association, keeping a stoichiometry of one αS molecule per membrane leaflet (Figure 28a-d)[1]. Note that lipid ratios and proper mixing of the different lipid types inside the nanodiscs was also observed by NMR (see Figure 59). Our NMR data clearly show a gradually increasing bilayer interaction region of αS with increasing charge content. Four distinct regions with different binding behaviors can be identified. The first region spans the N-terminal residues 1-38, which are already weakly interacting at 25% content of negatively charged lipid head groups and strongly interacting at 50% (or higher) charge content. The region of residues 38-60 interacts more gradually at 50% charge content. Amino-acids 60-100 (corresponding approximately to the non-Amyloid-β or NAC region) displays some interaction with membranes containing 75% charges and strongly interacts at 100% charge content. The 98-120 region shows mild interaction with 100% charge content only. Finally, the C-terminal 20 residues never show membrane interaction. This data is largely in line with an expected predominantly electrostatic model (the first 60 residues displaying a positive net

[1] Note that a similar approach was also used to study the interaction of ACTH, a melanocortin neuropeptide, with membranes and its modulation by calcium ions (see list of related publications)

charge, contrary to the last 40 residues, and the NAC region being mostly hydrophobic), as well as the three regions dynamic model reported before using SUVs [503].

Using Thioflavin T (ThT) fluorescence as a reporter for fibril formation, we also measured aggregation kinetics of αS in the absence and presence of the different NDs that were used for NMR (Figure 28e-f). These experiments were performed in polystyrene multi-well plates under conditions where αS amyloid fibrils form spontaneously through nucleation on the polymer surface [280], as well as the air-water interface [524]. These experimental conditions are therefore specifically designed to detect a potential interference of the nanodiscs with the lipid-independent aggregation pathway of αS. Strikingly, despite the fact that the NMR data shows an interaction, the presence of NDs up to a negative charge content of 50% does not appear to affect aggregation kinetics (note that the free non-acetylated αS reference (Figure 28e, grey) shows a different behavior. This point will be discussed in the section dedicated to the effect of acetylation below). When increasing negative charge content to 75% the aggregation half-time is slightly higher, and no aggregation could be detected within 120 hours in the presence of NDs with 100% charge content.

While the NMR data visualize the modes of binding of αS to membranes of different charge contents, the ThT kinetic data allow to directly link these molecular determinants to their role in the different stages of αS aggregation. The interaction being gradually augmented from the N-terminus to the C-terminus of αS upon increasing charge content, a 38-residue long helix [502, 503] would first appear on the surface of the membrane showing transient binding at 25% and tight binding from 50% charged head groups. A break is visible at amino-acid 38 leading to a second binding mode that features transient interactions at 50% and tight interactions at 75%. This mode is most likely an elongation of the first helix. Lastly, a third binding mode comprises residues forming the NAC region of αS (60-98), with transient interaction at 75% and tight binding at 100% (Figure 28g). Interestingly, at these high lipid:protein ratios the third binding mode. i.e. the membrane association of the NAC region, seems to be the only interaction that has an effect on αS aggregation behavior. The data shows that lipid interaction of the NAC region can protect the protein from aggregation.

Nanodisc bound state of αS is predominantly α-helical

It is worth noting that the NMR results described above mainly refer to the decrease in peak intensity as a reporter for interactions, which is in line with the effects seen before using SUVs [498]. While it is clear that SUVs have particle sizes (associated with slow tumbling rates) well above the detection limit of conventional solution NMR techniques, the smaller size of the ND system should, in principle, allow detection of NMR signals, as has been reported before for several ND-bound or ND-integrated proteins [518]. We thus measured Transverse Relaxation Optimized Spectroscopy (TROSY) [32] for longer time (12 h, i.e. 10-fold longer as for spectra shown in Figure 28a-b, data not shown) but no new set of NMR signals was visible. In order to increase the chances of detecting the bound-conformation of αS we additionally performed the experiment at higher temperature (35°C) and using a smaller construct of the membrane scaffold protein (MSP1ΔH5) [245] forming NDs of smaller size and higher tumbling rates (also see Figure 60a-b for comparison of binding modes to the MSP1D1 construct in the same conditions as above). The resulting spectrum however (Figure 29a) still does not show appearance of a new set of peaks indicative for the bound sate (and the presence of slow exchange processes) nor does it show a collective shift of peaks (indicative of fast on-off exchange processes). In theory, three effects may explain this observation and obstruct detection of the ND bound residues of αS: (i) the bound-to-free exchange rate is of the order of the NMR time scale (so-called intermediate exchange), (ii) the presence of a non-negligible part of αS protruding out of the ND (namely residues 98-140 in any case), slowing down molecular tumbling and increasing homogeneous line broadening beyond the detection limit, and/or (iii) membrane-bound αS shows a significant amount of plasticity leading to inhomogeneous broadening of the NMR lines. While intermediate exchange can be largely ruled out due to the observed binding kinetics (*vide infra*, Figure 31a-b, T_{on} and T_{off} of 4 μs·M and 75 s, respectively, and in Figure 59d the co-elution during SEC) it is at this point difficult to further distinguish between slower tumbling and molecular plasticity (or combinations thereof) that interfere with solution NMR detection of the bound conformation.

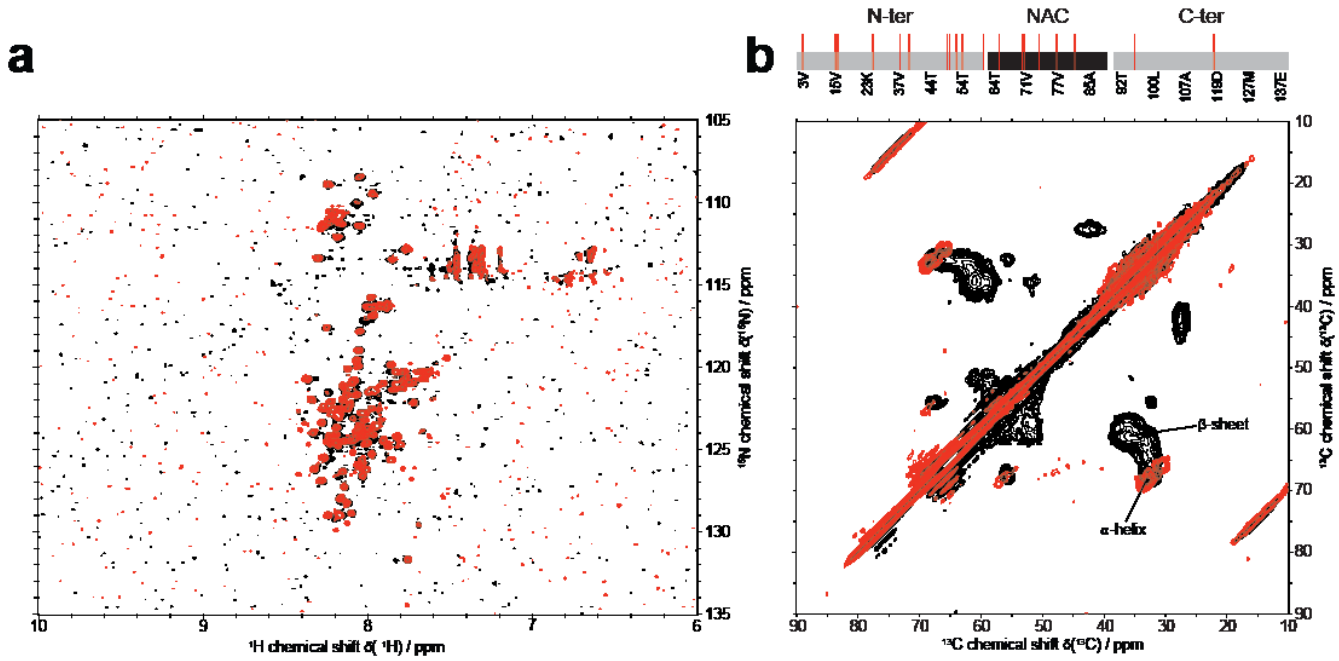

Figure 29. **Nanodisc binding induces α-helical structure in αS binding site.** [^{15}N-^{1}H]-TROSY-HSQC spectra of 50 µM αS in the presence (red) or absence (black) of 25 µM 75% POPG NDs assembled using MSP1D1ΔH5 (diameter of 7 nm), acquired at 35 °C over 12 h, is plotted in (**a**). No sub-conformation of αS (additional set of peaks) corresponding to its membrane-bound state is visible. [^{13}C-^{13}C]-Proton Driven Spin Diffusion MAS-DNP spectra of frozen αS free in solution (black) and when bound to 100% POPG NDs (red) is shown in (**b**). Selective isotope labelling was used to specifically monitor Valine Cα-Cβ chemical shift distribution. Peaks position indicative of the β-sheet and α-helical secondary structure are labelled. Occurrence of Valine residues in the αS sequence are shown on top (18 out of 19 valines are present in the expected binding site of the used ND).

It should be noted that the strong helical character of the MSP protein interferes with the usage of circular dichroism (CD) spectroscopy. In order to overcome this issue and to gain insight into the conformation of αS bound to NDs, we made use of magic angle spinning (MAS) solid-state NMR which is not subject to size effects. Moreover, we make use of the very low temperatures (100 K) used in Dynamic Nuclear Polarization (DNP) to additionally eliminate exchange processes, as well as to increase the sensitivity of the experiment. To avoid problems of signal overlap arising from severe inhomogeneous line broadening often seen in this range of temperatures [130], we used a scarce isotope labelling scheme, leading to the simplification of [^{13}C-^{13}C] spectra to valine Cα-Cβ cross-correlations. Notably according to the αS primary sequence (Figure 29b, top) and our solution NMR observations (Figure 28a-b), 95% of the valine residues (i.e. 18 out of the 19) should be in the membrane bound conformation at the used charge content and αS-to-ND ratio. While in the absence of NDs the DNP [^{13}C-^{13}C] spectrum (Figure 29b, bottom, black) shows a continuous distribution of the Val Cα-Cβ cross peaks reflecting the carbon chemical shifts of the allowed Ramachandran space (expected for an intrinsically disordered protein such as αS), a very strong peak shift to a defined α-helical structure is visible after addition of NDs[2] (Figure 29b, bottom, red). The DNP data shows that αS binds the ND lipid surface in α-helical conformation and thus independently corroborates previous studies using CD and vesicles, solution NMR and detergents micelles, and solid-state NMR and SUVs [282, 500, 503].

Lipid properties modulate αS binding to stable planar membranes

While Figure 28 shows the effect of gradually increasing the level of POPG in DMPC lipids it should be noted that both lipids do not only differ in their head group charge but also in their hydrocarbon chain length and number of unsaturated bonds (according to nomenclature for POPG and DMPC – 16:0-18:1 PG and 14:0 PC – number of carbons in the tails:number of unsaturations). Both of these features will affect the phase transition

[2] Note that the ensemble conformations of αS in different stages (free, membrane-bound, in fibrillar form, in the presence of interaction partners) was more extensively studied using DNP (see list of related publications).

temperature of the lipid bilayer. Native membranes are not only composed of various lipids of different types but also many different proteins. It is known that the phase properties of lipids can be strongly influenced by protein-lipid interactions. In that respect the MSP-lipid interactions may not only be seen as an artificial border of the bilayer but it was also suggested that it may, in general, partly mimic protein-lipid interaction occurring in native membranes [512]. While the usage of additional transmembrane proteins is rather restricted due to the limited bilayer area of the NDs, the usage of different heterogeneous lipid mixtures might mimic other properties of native membranes that may be important for αS membrane interaction.

To further investigate the effect of lipid properties (other than charge) we recorded additional NMR spectra of αS in the presence of NDs containing different lipids and lipid mixtures. Data recorded with 100% POPC does again not show interaction (Figure 30a black) demonstrating that in the absence of negative charges on the head groups, properties such as an increased chain length and unsaturation level as compared to DMPC, does not induce a significantly stronger interaction. We also used lipid mixtures where charged and uncharged lipids have the same hydrophobic tails (i.e. POPG/POPC and DMPG/DMPC) or mixtures where the position of negative charge and hydrocarbon chain is swapped (i.e. DMPG/POPC vs. POPG/DMPC). In these mixtures, we kept the overall charge content constant at 50%. Our data shows that the heterogeneous mixtures DMPG/POPC and POPG/DMPC behave very similarly (Figure 30a, blue and red, respectively) suggesting that the position of the charge in respect to the chain length and unsaturation level is not critical in the tested conditions. Also, when using a more homogenous mix of POPG/POPC a similar pattern is evident (Figure 30a, orange), suggesting that 'surface roughness' of the membrane, as potentially introduced by the heterogeneous lipid chain length, does not significantly change the αS-membrane interaction.

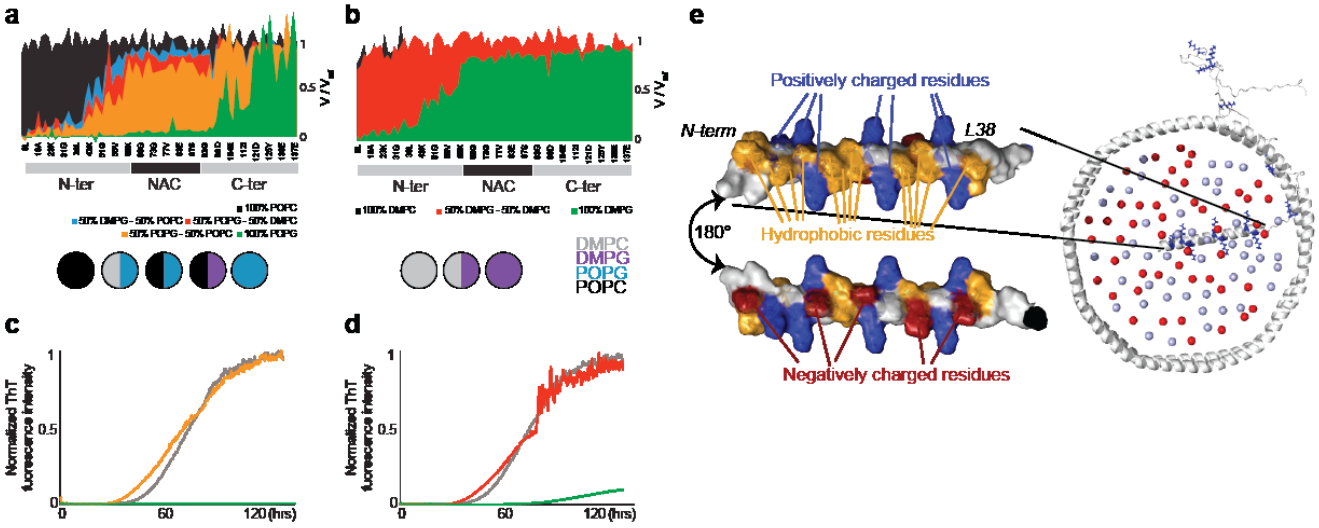

Figure 30. **αS binding modes to NDs depend on the fluidity of lipid bilayers.** Attenuation profiles, i.e. the ratio of peak volume in the presence of 2:1 molar ratio (αS-to-NDs) over the absence of NDs with indicated lipid composition (color code) are plotted against αS primary sequence in (**a**) and (**b**) respectively according to the estimated lipid phase at 10°C (temperature at which NMR is performed). Corresponding ThT aggregation assays at the same ratio of 2:1 for some of the conditions are plotted in (**c**) and (**d**) respectively. (**e**) αS structural model of key lipid binding mode (see text for more details). Periodically and symmetrically appearing lysine residues (blue) form a positively charged 'grid'. Nanodiscs (generated with the Charmm nanodisc builder [525, 526]) formed with 50% DMPC (light blue) and 50% POPG (red). Only the position of the head group (i.e. phosphor atom) of one lipid layer is shown. Position of αS 'charge grid', without rearrangement of lysine side chain and lipid charges, is shown in the correct scale.

Interestingly, when using a homogeneous mix with fully saturated lipids (DMPG/DMPC), albeit having the same charge content of 50%, a very different pattern showing no significant interaction with αS is visible (Figure 30b, red). Notably, at 10°C where the NMR measurements take place, the bilayer formed by DM lipids is in the gel phase (T_m around 23-24°C). This data is line with previous data on SUVs that identified an important role of the lipid phase for αS-lipid interaction [510]. When increasing the charge content to 100%, but remaining in the gel phase, (100% DMPG, Figure 30b green) the first 60 residues of αS show a clear interaction with the membrane resembling a binding mode that is found for 50% charge content in the fluid phase (e.g. Figure 30a,

orange). While increasing the temperature during the NMR measurements above T_m leads to a loss of NMR signals due to amide-water exchange processes for most residues relevant for the interaction (Figure 60), lowering the pH from 7.4 to 5.3 can counter this effect and allows to confirm that when measuring the interactions to DMPG lipids in the fluid phase a much larger binding interface is found, comparable to the binding mode found for 100% POPG (Figure 28b). Consequently, when the lipid charge density is high enough also the lipid phase state and related bilayer fluidity, in a stable planar bilayer, plays an important role in αS association.

Taken together, these data on αS-lipid association can be summarized as follows: (i) unsaturations in the hydrocarbon chains, leading to increased membrane fluidity, are not sufficient to induce binding, (ii) the presence of heterogeneity in lipid hydrophobic tails and the combination of charge and unsaturation on the same lipid molecule are not critical and (iii) in addition to charge, the physical properties of the membrane, i.e. the phase state (also related to bilayer fluidity), are important for binding in case sufficiently charged lipids are present.

We also performed ThT aggregation assays with NDs containing selected lipid mixtures investigated by NMR, again under conditions in which spontaneous aggregation of αS is observed in the absence of lipids. All mixtures that contain 50% negatively charged lipids, independently of phase, tail heterogeneity, etc. show consistently unaffected aggregation behavior (Figure 30c-d). While the αS NMR attenuation profile measured in the presence of 100% DMPG NDs largely resembles a POPG-DMPC 50% mix at 10°C, the attenuation profile of the 100% DMPG is in line with 100% POPG when data are recorded above the phase transition of DMPG (Figure 60). Since aggregation assays were measured at 37°C (i.e. above the DMPG phase transition), our NMR data suggest that the αS is in a lipid binding mode that inhibits aggregation. Indeed, our data clearly shows that aggregation of αS in the presence of 100% DMPG NDs at 37°C is dramatically impeded (Figure 30d, green).

From the evaluation of the different membrane interaction modes of αS with NDs observed in this study, it is clear that, in particular, the initial 38 residues comprise a central lipid binding motif. Based on previously reported solid-state NMR data [503] and CD data [282, 285] of vesicle preparations as well as the DNP solid-state NMR data of αS in the presence of NDs that we report here, it is clear that the lipid interacting residues of αS form a helical secondary structure. Analysis of the primary sequence and secondary structure of this interacting region highlights key features of its architecture which is highly suitable for interactions with charged lipid bilayers (Figure 30e). These features include the very exposed and symmetric distribution of positively charged lysine side chains (Figure 30e, blue), the occurrence of hydrophobic residues on one side of the helix (Figure 30e, yellow) and the distribution of negative charges on the opposite side (Figure 30e, red). Based on this architecture it is tempting to speculate that the positively charged residues will interact with negative charged lipid head groups, the hydrophobic residues will be oriented towards the hydrophobic lipid chains and the negative charged residues will be oriented towards the solvent (and compensate the net charge of the protein). In this picture, it would be likely that the lipids as well as the lysine side chains (partly) rearrange, from their 'unbound' conformation, to ideally accommodate electrostatic interactions in the bound conformation (Figure 30e). This rearrangement may be favored by a more fluid lipid phase, which would explain the lower interaction found for ND with DMPG lipids below the phase transition.

NDs can simultaneously interact with multiple αS proteins facilitating formation of fibril seeds

While our NMR data clearly reveal binding modes with different contributions of the αS primary sequence, we were also interested in the overall affinity of the protein towards the NDs. We therefore measured interaction kinetics using bio-layer interferometry (BLI) with immobilized NDs of different charge content. In line with the NMR data, no αS binding was detected when NDs containing 100% DMPC were immobilized (data not shown). Furthermore, no clear signature of binding could be obtained from experiments using NDs with 50% charge content. In these cases, the response upon addition of αS was of the same order as the non-specific binding to the empty sensor tips, suggesting a weak affinity, with a K_D of 50 μM or higher (data not shown). In the case where NDs with 100% negative charge content were immobilized, a clear response upon addition of different concentrations was observed (Figure 31a-b) and a dissociation constant K_D in the order of 80 nM (one αS to one

ND) could be calculated. In addition, kinetic information could be extracted which show a tight binding with a fast association phase and a slow off-rate of approximately 10^{-2} s^{-1}, also in line with the co-elution of αS with 100% POPG NDs in SEC (Figure 59d).

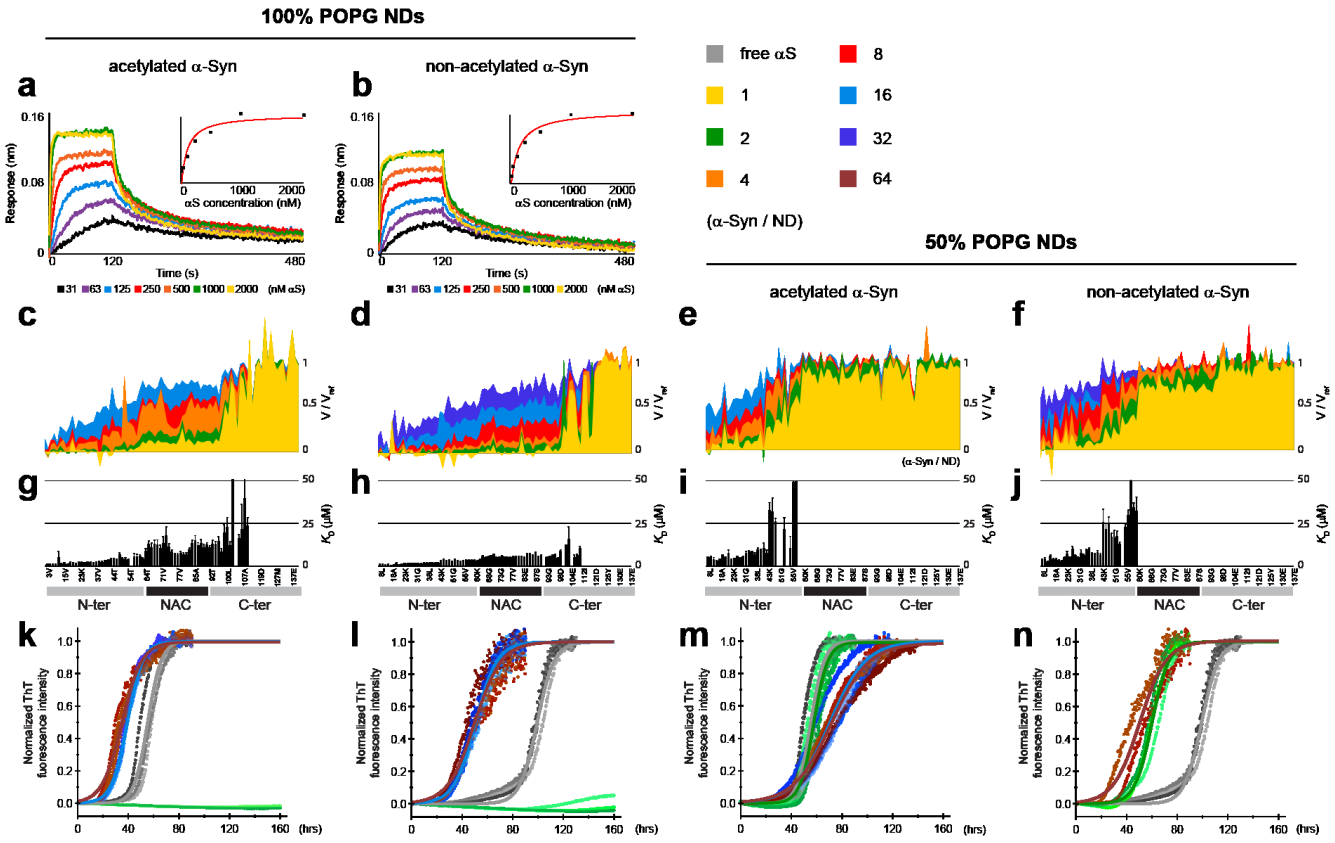

Figure 31. **Global and specific affinities of αS to NDs lead to reverse effects on its aggregation propensity.** BLI sensorgrams of acetylated αS (**a**) and non-acetylated αS (**b**) in different concentrations ranging from 31 (black) to 2000 nM (yellow) when 100% POPG NDs are immobilized on the sensortips. Corresponding steady-state response plots and 1:1 binding model fits are shown on top-right corners. The extracted K_D are about 60 and 100 nM respectively. Attenuation profiles corresponding to [^{15}N-^{1}H]-TROSY-HSQC spectra peak intensities throughout NMR titration of 50 μM acetylated (**c,e**) or non-acetylated (**d,f**) by 100% POPG (**c-d**) or 50% POPG (**e-f**) NDs in αS-to-NDs molar ratios ranging from 32:1 to 1:1 (see color code). Corresponding residue-specific affinities (K_D) extracted from exponential decrease fit of the previous are plotted in (**g-j**). Normalized ThT fluorescence kinetic curves for some of the conditions, as well including molar ratio of 64:1, are shown in (**k-n**) using the same color code.

In order to obtain residue-specific insights into the membrane affinity of αS, we additionally conducted NMR titration experiments using NDs with 50% as well as 100% charge content (Figure 31c-f). In general, dissociation constants can be extracted from NMR titrations attenuation profiles by fitting the concentration dependency of the attenuation with a single exponential decay for each resolved peak (corresponding to one assigned residue) (Figure 31g-j). Our data reveals differential membrane affinities for different regions of the αS primary sequence. The regions with differential affinities largely overlap with the regions of the different binding modes identified before. Four distinct regions of decreasing affinity range are found in the case of 100% POPG (1-38, 39-60, 61-98, 99-140) and three in the case of 50% POPG (1-38, 39-60, 61-140).

Importantly, it appears that one ND with 100 % negative charged lipids can simultaneously interact with up to 16 αS (8 per leaflet) in the course of the NMR time scale, as seen from the almost complete disappearance of the signals of the very N-terminal residues (Figure 31e-f, light blue). Moreover, while these first residues are interacting with the membrane independently of the number of αS molecules bound to one ND, the binding of the NAC region is strongly modulated by the number of bound αS molecules, suggesting that, due to the higher lipid affinity of this region as compared to the NAC region, the free energy of the system is minimized by favoring N-terminal interactions in cases where the accessible membrane surface is limited.

To characterize the effect of the accessible membrane surface area (as given by the αS:ND ratio) on αS aggregation behavior, we measured ThT aggregation kinetics on samples with different αS:ND ratios ranging from 2:1 to 64:1 (Figure 31k-n). While the different conditions tested for NDs with 50% negatively charged lipids at low αS:ND ratios are consistently showing no effect on aggregation half-times, the data at higher ratios are less reproducible and show a slight tendency to prolonged half-times (Figure 31m-n). While at this point it is not clear whether this feature has mechanistic relevance or is just an artifact caused by the limited reproducibility we found for these conditions, the effect of NDs with higher charge density (i.e. 100% POPG) seem to be more reproducible and clearer in its consequences. Here a higher ratio of αS:ND leads to a prominent decrease in aggregation lag-times (Figure 31k-l). This data shows, in line with previously reported behavior on SUVs [282, 509], that under specific conditions lipid bilayers can accelerate the fibrillation process. Here these conditions represent a limited membrane surface area with a high charge density. According to our NMR data this will introduce a lipid binding mode that brings several αS molecules with exposed NAC regions in close proximity.

The molecular, (thermo)dynamic and kinetic determinants of membrane-modulated αS aggregation

It has recently been shown in a systematic study that under appropriate conditions, lipid bilayers (in the form of small unilamellar vesicles) can accelerate the nucleation of αS amyloid fibrils by more than three orders of magnitude as compared to the situation when the nucleation proceeds at the air-water interface or in bulk solution [282]. This quantitative insight was enabled through a combination of experimental conditions that minimize the intrinsic nucleation rate (quiescent conditions and protein repellent plate surfaces) and theoretical analysis of the kinetic data. The magnitude of the accelerating effect is determined by the protein-to-lipid ratio, in the absence of lipids, as well as in the presence of an excess of lipids no aggregation is observed under these experimental conditions.

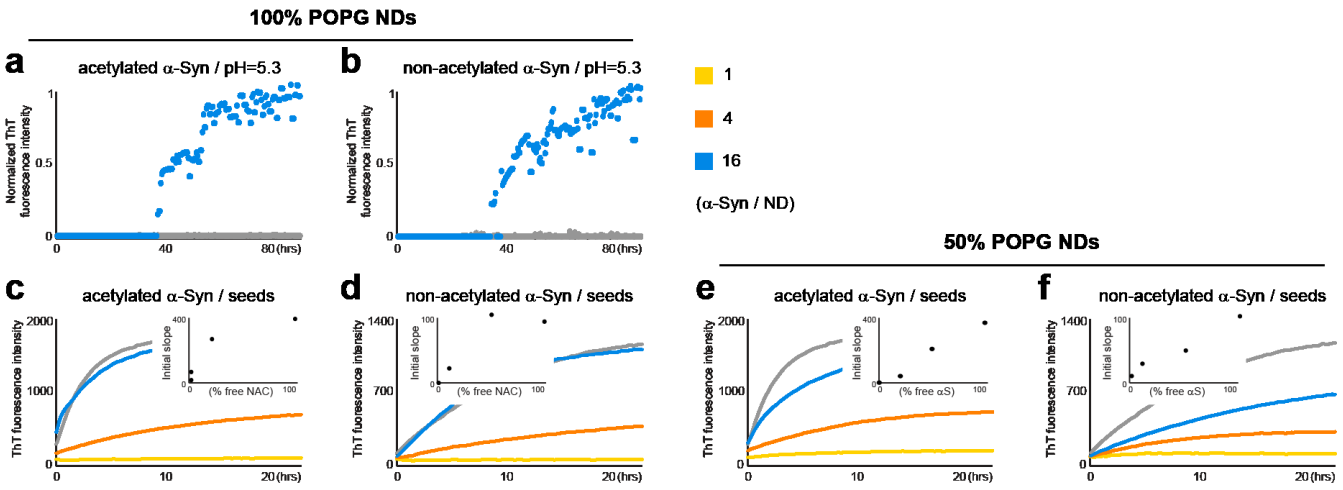

Figure 32. **Nanodiscs affect elongation rates and nucleation processes of αS.** Raw data of quiescent ThT fluorescence aggregation assays in the presence of 2.5% preformed seeds for acetylated (**a,c**) or non-acetylated (**b,d**) αS in the presence of different molar ratios (see color code) of 100% (**a,b**) or 50% (**c,d**) POPG NDs are displayed. Dependency of the initial slope on the amount of unbound NAC region (**a-b**) or αS (**c-d**) is plotted as well. Normalized kinetic data in quiescent conditions, absence of preformed seeds and at a pH of 5.3 is shown in (**e**) and (**f**) for the acetylated or non-acetylated αS respectively in the absence (grey) or presence (blue) of 16:1 molar ratio of 100% POPG NDs.

In order to determine whether NDs can have a similarly accelerating effect, we performed ThT aggregation experiments under conditions where monomeric αS is in excess (Figure 32a-b). These experiments were performed at mildly acidic pH (5.3), as it was recently shown that under these conditions, αS amyloid fibrils can amplify autocatalytically through surface-catalyzed secondary nucleation [281]. These conditions were chosen because they enable, in principle, even very low primary nucleation rates to be detected through autocatalytic amplification. Additionally, the binding behavior of αS was checked by NMR in this new condition for 100% POPG NDs (see supplementary Figure 60e-f). The same region comprising residues 1-96 interacts in an identical way as at neutral pH (Figure 28b). While 50% POPG NDs were found to be unable to induce nucleation (data not shown), the

samples with 100% POPG NDs do display aggregation, indicating that this type of membrane is indeed enhancing primary nucleation to a sufficient degree for the subsequent secondary nucleation to lead to detectable quantities of amyloid fibrils (Figure 32a-b).

Interestingly, since our data also allow an estimation of the total number of αS monomers that are brought in close proximity due to their interaction with the same ND, this result may also provide a first approximation of the number of αS monomers needed for the formation of a nucleus, which we estimate to be between 4 and 8.

In order to be able to disentangle the effect of the NDs on the various individual steps in the αS aggregation pathway, we next designed strongly seeded aggregation assays under quiescent conditions at neutral pH, where fibril elongation is the only process that occurs at significant rate (Figure 32c-f) [281]. The reduction in initial elongation rate shows a linear dependency on the concentration of NDs with 50% negative charge, consistent with monomers being sequestered by the NDs. This is surprising since the unseeded αS aggregation process does not seem to be affected by the presence of the same kind of NDs (Figure 28c). This data is currently difficult to explain given that elongation is, in all cases of amyloid formation, responsible for the generation of the bulk of fibril mass. Hence, its inhibition should slow down the overall aggregation kinetic, also under non-seeded conditions. One potential explanation could be that the primary nucleation step is not affected by the NDs. Given that nucleation is much lower than elongation, the overall kinetics in the non-seeded case are limited by the kinetics of nucleation. In other words, the limiting step is the generation of a new fibril, not its subsequent growth. The growth is still possible, even in the presence of nanodiscs, as the binding of αS to NDs is highly dynamic (absence of detectable BLI signal and of co-elution in SEC, see Figure *59*b) and bound and free monomers exchange on a timescale much faster than the overall unseeded aggregation kinetics [527].

Seeding experiments carried out in the presence of 100% charged (POPG) NDs also show a clear reduction in elongation rate with increasing ND concentration (Figure 32c-d). While at high molar excess of αS (16:1, αS:ND), according to our NMR data, nearly all αS monomers should interact through their most N-terminal regions with the NDs, no significant effect on the elongation rate was observed (Figure 32, blue). At molar ratios of 4:1 (Figure 32, orange) a decrease in elongation is observed, however at this ratio our NMR data clearly indicates that all αS monomers are interacting with the NDs. Nevertheless, in both cases (molar ratios of 16:1 and 4:1) larger fractions of the monomer population still have accessible NAC regions, suggesting that for the seeding experiments with the 100% charged lipids not the free αS monomer concentration but the concentration of accessible NAC regions is correlated with the elongation rate of the fibrils (Figure 32c-d, insert). Our data indicate that it is possible that free as well as membrane-bound monomers can participate in fibril elongation as long as their NAC region remain accessible. It cannot be excluded, however, that the dynamic nature of membrane association leads to a certain population of free monomeric αS at any given time, which would be responsible for the observed elongation. This is schematically summarized in Figure 33.

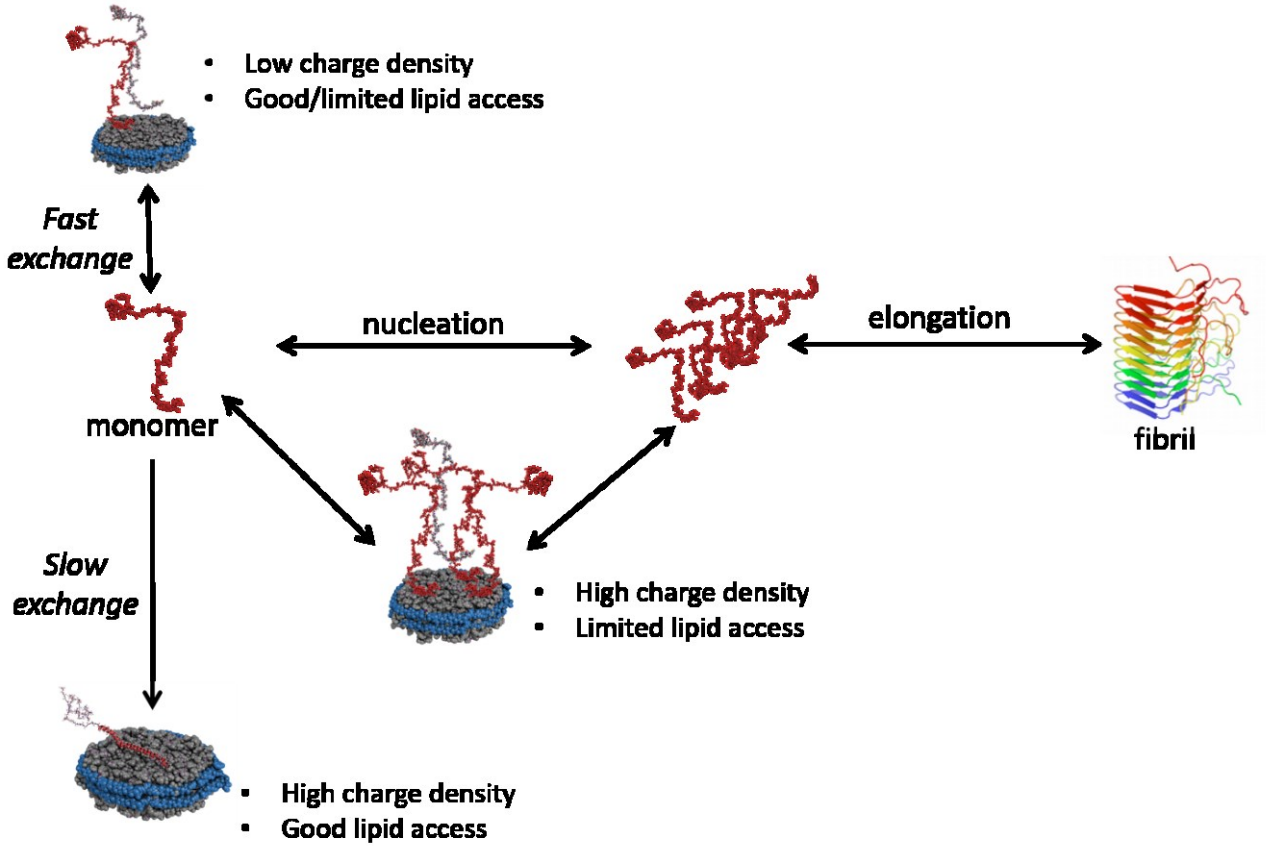

Figure 33. **Nanodiscs influence aggregation pathways of αS in various ways.** Model summarizing thermodynamic as well as kinetic data and presenting a molecular interpretation. Depending on the charge content and the amount of NDs, different pathways are possible or not, leading to either unchanged, impeded or favoured nucleation and elongation.

N-terminal acetylation does not dramatically affect modes of binding but changes significantly aggregation behavior

As visible in Figure 28, Figure 31 and Figure 32, in addition to using the N-terminal acetylated form of αS, which represents the native post-translational modification of αS and is known to be relevant for its membrane association propensity [484, 495], we also recorded most experiments with the non-acetylated form of αS, which is obtained using 'standard' expression conditions in *E.coli* (see Material and Methods for more details). In line with what was reported before, N-terminal acetylation leads to clear chemical shift perturbations for the first 10 αS residues (Figure 28a-b) [528].

Overall, most of the above discussed features of αS membrane interaction are rather similar in acetylated and non-acetylated αS, however there are a number of distinct differences. For instance, the peaks which are already shifted in free αS due to the acetylation are also the ones that are affected the most by the presence of nanodiscs with low amount of charges (close to physiological concentration) [284]. Our data (Figure 28a-d) show a rather small but significant increase in the membrane association of the first 15 due to the N-terminal acetylation, which is in line with previous observation using SUVs [496, 529]. αS acetylation is known to increase N-terminal helix propensity [528, 530], which may facilitate formation of the initial binding mode and be of significance for naturally occurring processes.

A similar effect is also seen for the global binding as determined by BLI, which shows a (slightly) higher membrane affinity of the acetylated (Figure 31a, K_D of 68 nM) form, as compared to the non-acetylated αS construct (Figure 31b, K_D of 100 nM). When looking deeper into the NMR titration data, it appears that another effect takes place, namely a slightly increased membrane affinity of the NAC region for the non-acetylated αS NAC region

(Figure 31c-g *vs.* d-h). At the current stage, it is not easy to explain why a modification at the N-terminus will affect the lipid interaction of a protein region that is sequentially separated by roughly 60 residues. Such a behavior could however either be related to intermolecular interactions and/or long range intramolecular interactions (in a 'horseshoe' conformation) that may or may not be artificially introduced by the limited surface area of the NDs.

Strikingly, the reference kinetic curve of non-acetylated αS always shows, very reproducibly, a strongly delayed aggregation. In the used setup, primary nucleation processes are likely to happen at the air-water or plate-water interface [280, 524], thus a lower hydrophobic propensity of non-acetylated αS (in line with BLI and NMR data) could explain this effect. While this may be the dominant process in the absence of lipids, it may not be the case anymore in the presence of NDs [282], either because NDs shield these interfaces or because nucleation happens primarily at the membrane surface. The much lower differences due to acetylation state in the presence of NDs fit this explanation, as well as additional tests we ran using different type of plates (data not shown). Higher order processes, namely different fragmentation behaviors, can however not be excluded.

In general, the acetylation state does not lead to high discrepancies of the aggregation behavior of αS when NDs are present. Nevertheless when having a closer look some minor differences can be detect including a less pronounced reduction of lag- and half-times in the presence of low number of 100% charged NDs in the non-acetylated αS case (Figure 29k *vs.* l). This is in line with the higher affinity of its NAC region for the membrane seen by NMR (thus non-accessible to nucleation processes) and the lower stoichiometry measured by the absolute value of BLI response at saturation (Figure 31a-b). Furthermore, seeded aggregation assays (Figure 32c-f) show slightly reduced elongation rates when αS is not N-terminally acetylated.

It appears that overall the biggest effect of acetylation is related to assay parameters that are normally not the matter of interest, which nevertheless may be important for future studies [523]. Still the results from systematic measurement of the effects of N-terminal acetylation via different methods point to subtle changes in membrane interaction in respect to NAC region specific affinities at high lipid charge densities as well as to N-terminal binding at a lipid charge density comparable with the overall composition found for membranes in e.g. synaptic vesicles [290]. Hence both effects may be of particular importance under physiological conditions.

Perspectives/conclusion

Overall our data demonstrate that the nanodisc system allows to study the interaction of αS with stable, planar, membranes in a quantitative and site-resolved way. It also provides initial insights into the correlation between the identified membrane binding modes and binding kinetics and their consequences for αS fibril formation.

Taken together, our data point out several effects: (i) affinities of the N-terminal region of αS for membranes are rather similar for NDs containing either 50% or 100% negatively charged lipids, (ii) for 100% negatively charged lipids αS can adopt a significantly elongated binding mode as compared to 50% negatively charged lipids, potentially leading to a higher global affinity, (iii) the exchange rate between free αS in solution and membrane-bound αS is rather slow in the 100% negatively charged case and likely to be rapid in the 50% case, (iv) region-specific affinities and kinetics (especially the NAC region) are correlated with aggregation kinetics, (v) at sufficient excess of lipids and sufficient charge density, NDs can inhibit aggregation of αS, (vi) competition of αS monomers for highly charged lipids induces a membrane-bound αS conformation that can induce primary nucleation, and (vii) the number of αS monomers that are brought together on one ND and which can promote nucleation is in the order of 4-8 monomers. Figure *33* summarizes the molecular, (thermo)dynamic and kinetic determinants of membrane-modulated αS aggregation.

While our *in vitro* data shows strongest effects at lipid charge density well above average lipid compositions of native membranes, the membrane composition may vary locally in physiological membranes. Due

to the normally found high lipid diffusion rates, clusters of higher negative charges may form spontaneously and/or be induced by the initially transient αS interactions. For the latter, the N-terminal acetylation may play an important role, since it increases membrane interaction at close-to-native lipid charge densities. Our data suggest that cluster of around 60-80 negatively charged lipids suffice to form a strong interaction (this may however not be the lower limit). Sporadically formed lipid charged cluster could also induce a competition of several αS monomers for the accessible surface area. Our data shows that due to the different residue-specific membrane affinities this will generate a binding mode that, once the rather low critical oligomerization number is reached, can act as initial seed for subsequent protein aggregation. For these reasons, modulation of αS aggregation through membrane association is likely to be relevant, *in vivo*, in the development of Parkinson's disease. This hypothesis is in line with recent results on animal models, showing that providing membrane association of αS, using a drug that competes with αS for the membrane, is able to prolong the healthy life-time of *C. elegans* [531].

Acknowledgements

The authors acknowledge access to the Jülich-Düsseldorf Biomolecular NMR Center. We thank Dr. Céline Galvagnion for fruitful discussions. This work was supported by grants the German Research Foundation (DFG) (ET 103/2-1) to M.E. and from the European Union's Horizon 2020 research and innovation program under the Marie Sklodowska-Curie grant agreement Nº 660258 to A.V.. T.V. and M.W.W. acknowledge support from the International North-Rhine-Westphalia Research School iGRASPseed.

CHAPTER VII – APPLICATION TO AN INTEGRAL MEMBRANE PROTEIN – BARTTIN

Reconstitution and NMR characterization of an ion-channel regulator membrane protein in detergents and bilayer nanodiscs

Thibault Viennet[1,2], Stefanie Bungert-Plümke[2], Shantha Elter[1], Aldino Viegas[1], Christoph Fahlke[2] and Manuel Etzkorn[1,2*]

[1] Institute of Physical Biology, Heinrich-Heine-University Düsseldorf, Universitätsstr. 1, 40225 Düsseldorf, Germany

[2] Institute of Complex Systems, Forschungszentrum Jülich, Wilhelm-Johnen-Strasse, 52425, Jülich, Germany

[*] Corresponding author

Reconstitution and NMR characterization of an ion-channel regulator membrane protein in detergents and bilayer nanodiscs

Abstract

Barttin is necessary for the basal function of chloride channels, for this reason it is relevant in some related diseases. It is predicted to be a two-transmembrane helices integral membrane protein. Even though a topology model was proposed, little is known about its structural features. The need for better structural models in the understanding of Barttin's function and physiology as well as the mechanisms of related diseases is thus apparent. Here we report on results towards structural characterization of Barttin in native-like *in vitro* systems. This includes expression and purification protocols as well as refolding in detergent micelles and phospholipid bilayer nanodiscs. Stability, folding and NMR data quality are reported as well as a suitable assignment strategy, paving the way to its structural characterization.

Introduction

Barttin is a protein encoded by the *Bartter syndrome, infantile, with sensorineural deafness (BSND)* gene in which some mutations lead to Bartter syndrome type IV. Bartter syndrome type IV is a rare disease causing severe salt-losing phenotype through the urinary kidney system as well as sensorineural deafness [291, 292]. Indeed, Barttin has been shown to be necessary for the function of both chloride channels ClC-Ka and ClC-Kb [293] present respectively in inner ears and in kidneys. It is known that Barttin is able to increase the number of channels in the plasma membrane [293], to change their distribution in the cell compartments [298], acting as an accessory protein, but also to change their glycosylation pattern [299] and is required for proper activation of the channels by voltage gating [300], even though the latter remains a point of debate [301]. Barttin is predicted to have a two-transmembrane helices motif in its N-terminal region, supposedly acting as a chaperone for the channels and a large C-terminal unstructured region which was shown not to interact with them [295]. Two features are predicted to be critical for this function, namely a speculative binding site to e.g. helices B and J of the ClC-Kb channel [302] and a palmitoylation site which could act as membrane anchoring mechanism [303]. Despite this model and features, the structural characteristics of Barttin remain elusive, pointing to the need for proper investigation of the protein, aiming to better understand the pathophysiology, the effect of *BSND* mutations [294, 532] and hoping to discover targets for drug development [533].

While detergent micelles are most commonly used for structural studies of membrane proteins, both by X-ray crystallography and NMR, they exhibit severe destabilization [188] and denaturation effects [189]. Phospholipid bilayer nanodiscs (NDs), however, have proven to be a useful alternative membrane mimetic. They have the advantage of allowing the use of numerous types of lipids, and have the power of mimicking the natural properties of membranes [512] thus providing more native environments to membrane proteins. The nanodisc system has been successfully applied in the dynamic and structural studies of β-barrel proteins such as Opa_{60} [534] and OmpX [245], which structure was determined *de novo* in nanodiscs but also of the tumor necrosis factor receptor p75NTR [535] which contains a single transmembrane domain or to the seven-transmembrane helices protein bacteriorhodopsin [379]. Although a powerful technique on the way to structural investigation in native-like environments, NDs still exhibit an overall large size which can render the study complicated in some cases, despite the availability of smaller constructs [245]. As such, pursuing a mixed study using both detergent micelles and nanodiscs in order to make the best out of both NMR data quality and physiologically relevant information can be a valid approach. This was done in the case of Opa60, where restraints derived from NMR in both dodecylphosphocholine (DPC) and 1,2-dimyristoyl-*sn*-glycero-3-phosphocholine (DMPC) bilayer NDs were used as well as molecular dynamic simulations [534].

Here we report on the optimization of Barttin refolding procedures both in detergent micelles and in phospholipid bilayer nanodiscs. The influence of lipid types as well as detergent removal procedure on the quality of nanodisc preparations and NMR data is carefully investigated. Comparison of the two membrane mimicking systems in terms of Barttin stability, folding and NMR data quality is also reported. Ultimately, a residue-specific assignment strategy of Barttin in detergent micelles is presented, opening the way to its structural study.

Material and Methods

Barttin expression and purification

A N-terminal construct of Barttin containing a His-tag (His-I72X) was cloned into a pET21a vector and plasmid DNA was produced. Barttin was expressed in an *E. coli*-based cell-free expression system following established protocols [181, 187]. Either triple labeled Algal mix supplemented with missing four amino-acids or custom-made mix with different isotope labeling schemes (combinatorial, see Table 11) was used. Dialysis mode reactions were carried out at 28 °C with or without presence of nanodiscs. After 12–16 h, the reaction mix was centrifuged for 10 min at 12000·*g*. The pellet was washed once with 5 to 10 volumes of buffer containing 50 mM NaH_2PO_4 pH=8.0, 300 mM NaCl (buffer A, all reagents from Sigma Aldrich if not stated otherwise) and Complete protease inhibitors (Roche). The resulting pellet was stored at −20 °C until further use.

For detergent solubization tests, pellets were directly solubilized in 50 mM NaH_2PO_4 pH=8.0, 150 mM NaCl supplemented with either 20 mM sodium dodecylsulfate (SDS), 100 mM decylphosphocholine (FOS-10, Cube Biotech) 100 mM dodecylphosphocholine (FOS-12 or DPC, Cube Biotech), 100 mM *N,N*-dimethyldodecylamine *N*-oxide (LDAO, Cube Biotech), 42 mM lyso-myristoylphosphatidylglycerol (LMPG, Avanti polar lipids), 250 mM n-decyl-β-*D*-maltoside (DM, Anatrace) or 196 mM n-dodecyl-β-*D*-maltoside (DDM, Cube Biotech) at 37°C, 800 rpm for 2 h, without further purification.

For small scale test NMR samples and combinatorial labeled samples, pellets were directly solubilized with NMR buffer (20 mM sodium phosphate pH=7.0, 100 mM NaCl, 2 mM TCEP, 0.2% (v/v) NaN_3 and 10% (v/v) D_2O) supplemented with either 100 mM DPC, 42 mM LMPG or 100 mM LDAO at 37°C, 800 rpm for 2 h, without further purification.

For large scale, triple labeled (^2H,^{13}C,^{15}N) samples, pellet was solubilized at room temperature, end-over-end for 30 min with 10 volumes of buffer A supplemented with 2 mM DTT, 50 mM LDAO and Complete protease inhibitors, then centrifuged at room temperature, 16000·g for 30 min. The supernatant was incubated with previously washed Ni-NTA agarose chemical beads (Macherey-Nagel) at room temperature, end-over-end for 1 h. The slurry was transferred to a column, washed with 10 column volumes of buffer A supplemented with 2 mM DTT and 10 mM LDAO. Barttin was eluted using buffer A supplemented with 2 mM DTT, 10 mM LDAO and 300 mM imidazole, fractions containing Barttin were pooled and applied to a desalting column equilibrated with NMR buffer supplemented with 10 mM LDAO. Finally the eluate was concentrated in a Vivaspin concentrator of 10 kDa MWCO.

Barttin reconstitution in nanodiscs

MSP preparation

E. coli BL21 (DE3) were transformed with the MSP1D1 or MSP1D1ΔH5 plasmid DNA in a pET28a vector as reported in [245, 467]. In short, cells were grown in LB medium. Protein was resuspended with 6M Gu-HCl and purified by IMAC (without denaturating agent). The elution fractions were pooled and dialyzed in order to remove imidazole. N-terminal His-tag was cleaved using TEV protease incubated overnight at 4°C. ΔHis MSP1D1 or MSP1D1ΔH5 was separated from MSP1D1 or MSP1D1ΔH5 by IMAC.

Barttin purification in SDS

Barttin was purified from washed CFE pellets to SDS following similar procedure as in LDAO. In short, pellets were solubilized in buffer containing 20 mM SDS, supernatant was diluted to 10 mM SDS previous to binding to Ni-NTA agarose beads. Either the slurry or the pooled elution fractions was used for nanodiscs assembly.

Nanodiscs assembly

In all other cases, Barttin in SDS, 6-fold ΔHis MSP1D1 or MSP1D1ΔH5 and 450-fold or 270-fold lipids solubilized in 60 mM Na-cholate, respectively, were mixed together in 20 mM Tris-HCl pH=7.5, 100 mM NaCl, 2 mM DTT, 10 mM SDS. Different lipids (all from Avanti polar Lipids) were used including 1,2-dimyristoyl-*sn*-glycero-3-phosphocholine (DMPC), a mixture of 1-palmitoyl-2-oleoyl-*sn*-glycero-3-phospho-(1'-*rac*-glycerol (POPG) and 1-palmitoyl-2-oleoyl-*sn*-glycero-3-phosphocholine (POPC) in the ratio 1:4 and a mixture of 1,2-distearoyl-*sn*-glycero-3-phospho-L-serine (DSPS), 1,2-dipalmitoyl-*sn*-glycero-3-phosphocholine (DPPC), 1,2-distearoyl-*sn*-glycero-3-phosphocholine (DSPC) and 1,2-diarachidoyl-*sn*-glycero-3-phosphocholine (DAPC) in ratio 1:3:3:3 [536, 537].

Detergent removal procedure was empirically optimized. Different approaches including usage of Biobeads SM-2 (Biorad) on-column or in the purified product, dialysis through a 10 kDa MWCO membrane (Thermo Scientific), on-column fast and stepwise wash of the detergent were tested. For more information see Results section.

For all off-column procedures an additional IMAC purification was done in order to separate nanodiscs containing Barttin from those which did not. Finally, Barttin-containing NDs were purified by SEC on a HiLoad 16/600 Superdex 200 pg (for big scale) or Superdex 13/300 gl (for small scale) column (GE Healthcare) equilibrated with 20 mM sodium phosphate pH=7.0, 100 mM NaCl, 2 mM DTT using a ÄKTA pure device running at 1 ml/min. The quality of nanodiscs preparation was inspected by the SEC chromatogram. The main peak from SEC was pooled and concentrated using a Vivaspin centrifugal device of 10 kDa MWCO, 2 mM TCEP, 10% w/w D2O and 0.01% w/w NaN_3 were finally added to the samples.

For co-translational incorporation of Barttin into NDs, empty nanodiscs assembled with DMPC according to established protocols [274, 467] were used in the cell-free system's reaction mix at a concentration of 58 µM.

SDS-PAGE

Proteins were analyzed using denaturing, non-continuous tricine-sodium dodecyl sulfate-polyacrylamide gel electrophoresis according to published methods [538]. The gel consists of three parts, a 17% acrylamide separation gel, a 10% intermediate gel and a 5% stacking gel. The gel is suited to separate proteins of low molecular masses or peptides. To separate the proteins in an electric field, the following anode buffer (200 mM Tris-HCl pH=8.9) and cathode buffer (200 mM Tris-HCl, 100 mM Tricine and 0.1% SDS) were used. The PageRuler Plus prestained protein ladder (ThermoFisher) was used as protein standard. Proteins were visualized after Coomassie blue staining.

Circular Dichroism

A sample of 10 µM Barttin in LDAO micelles was investigated using circular dichroism (Jasco J-715) in 20 mM NaPi pH=6.8, 100 mM NaCl, 2 mM TCEP and at room temperature. Measurement from 260 to 200 nm was done at a constant bandwidth of 1 nm, with a data pitch of 0.2 nm and repeated 10 times for averaging. Data was converted to mean-residue molar ellipticity and deconvoluted using the K2d protocol.

NMR Data acquisition

NMR experiments were performed on Bruker Avance III HD spectrometers operating either at 600 or 700 MHz, both equipped with a triple resonance TCI (^{1}H,^{13}C,^{15}N) cryoprobe and shielded z-gradients. Data was collected at 35ºC in 20 mM NaPi pH=6.8, 100 mM NaCl, 2 mM TCEP, 0.2% (v/v) NaN_3 and 10% (v/v) D_2O. For

experiments using LDAO micelles, the detergent concentration was estimated, after concentration, to roughly 100 mM. All experiments used contained transverse relaxation optimized spectroscopy (TROSY) components [32, 34]. The 2D ^{13}CO- and ^{13}Cα-filtered TROSY-HSQC pulse sequences were designed from their respective 3D experiments. All NMR spectra were processed with TOPSPIN 3.2 (Bruker) and analyzed with CARA [468] and CCPN [469].

Results

Barttin can be incorporated into nanodiscs

Ideally, structural biologists would like to obtain data *in vivo*, or at least in a native environment of their target in order to ensure relevant folding and necessary cofactors for function, without introducing bias due to *in vitro* handling, purification, refolding, etc. While some techniques theoretically have the power to do so, such as in-cell NMR [539] or dynamic nuclear polarization NMR [141], they are limited in their applications respectively by sensitivity and resolution. Thus, "native-like" in vitro procedures can still be useful in a lot of cases. For membrane proteins, the presence of a phospholipid bilayer with similar chemical composition and physical properties as the native membrane, as provided by NDs [204], is desired. Nanodiscs, as compared to other membrane mimetics such as detergent micelles, bicelles or amphipols exhibit several key advantages: (i) they do have a proper lipid bilayer, (ii) both sides of the bilayer are accessible in solution, (iii) they have high stability and low exchange rates, (iv) the presence of scaffold protein creates a crowded environment like in natural membranes and (v) a large range of lipids (charge, length, unsaturations, non-phospholipids, etc.) can be incorporated allowing mimicking of properties of various types and states of membranes [512].

For this reason we investigated the possibility of refolding Barttin from precipitated proteins (during cell-free expression) into nanodiscs. While canonical protocols do exist, they need to be empirically optimized for each target protein on some key points such as the target protein:scaffold protein and scaffold protein:lipid ratios, the detergent type and the removal procedure, etc. [512]. Initially, the most standard procedure, i.e. the usage of Barttin in SDS, MSP1D1 as a scaffold, DMPC lipids solubilized in sodium cholate and adsorbent polystyrene beads as a way to remove detergents was tested. Although empty NDs assembly was detected, Barttin was not incorporated (data not shown, see Table 10). Changing the detergent in which lipids are solubilized to SDS, and the lipid mixture to DPMG:DMPC 1:4 (20% negatively charged head groups), previously shown to drastically improve quality of data [245] did not lead to any improvement. The most probable explanation is that Barttin, a rather hydrophobic and low molecular weight (10.1 kDa) protein, would adsorb to the polystyrene beads, thus another detergent removal procedure was tested, i.e. dialysis. The same conditions concerning lipids and detergents were tested and successful incorporation of Barttin in nanodiscs was detected (Figure 34a, Table 10). Although the yield (defined as the recovery of Barttin from the input to the purified NDs) remained very low, estimated to less than 1% (see Table 10). Additionally another detergent for Barttin solubilization was tested as well, DPC which is known to provide good results in other cases [245, 534], but no incorporation was detected. Notably in all previous experiments, the quality of nanodisc preparation, i.e. its homogeneity as seen from a size exclusion chromatogram, were poor (see Figure 34a) which in part explains the low yields (see Table 10).

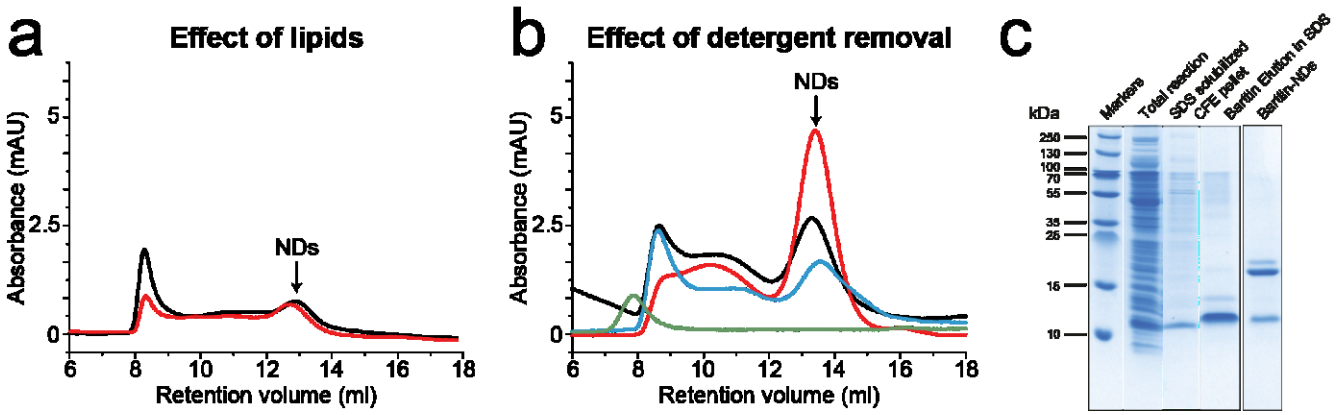

Figure 34. **Optimization of Barttin refolding into D1 NDs. a)** SEC profiles of Barttin-NDs (MSP1D1) assembled with DMPC (black) and DMPG:DMPC 1:4 (red) upon sodium cholate dialysis. **b)** SEC chromatograms of Barttin-NDs (MSP1D1) assembled with DMPC upon detergent dialysis (black), on-column biobeads adsorption (red), on-column fast dilution (blue) and on-column step dilutions (green). **c)** Coomassie blue-stained SDS-PAGE of CFE expressed Barttin (total reaction), solubilized CFE pellet, SDS-purified Barttin and purified (IMAC, before SEC) Barttin-NDs (MSP1D1) assembled with DMPC upon on-column biobeads adsorption (the difference in height is due to running behavior of the samples, see full gel in Figure 61).

Having found initial conditions allowing for Barttin incorporation into nanodiscs, further conditions were screened in order to improve yields and homogeneity of preparations. As the detergent removal step seemed critical, three different approaches were tested using on-column procedures successfully reported before [540]. In short, Barttin in SDS was immobilized through its histidine tag to Ni-NTA agarose column, incubated with MSP and lipids and the detergents were removed either by introduction of adsorbent beads, fast dilution or stepwise dilutions of the slurry. The latter did not allow any NDs assembly, which we attribute to a too low detergent removal rate, kinetically favoring lipid aggregation over nanodisc formation as seen from the SEC profile (see Figure 34b). The other protocols were successful in producing sizeable amounts of Barttin-containing NDs, with an overall higher homogeneity and yield for the on-column polystyrene beads adsorption of detergents (see Figure 34b and Table 10). Another important factor in ND refolding is the oligomeric state of the membrane protein, which is difficult to handle and to measure accurately [512, 541]. Nevertheless, it can be estimated from the relative intensities of bands arising from MSP and Barttin in a SDS-PAGE gel, after IMAC purification the relative intensities are in line with a monomeric state of Barttin in NDs formed with MSP1D1 (1 Barttin for 2 scaffold proteins) (see Figure 34c).

Smaller nanodiscs are known to provide better NMR results as well as better control of the oligomeric state of membrane proteins, due to their higher tumbling rate and smaller membrane surface, respectively. We thus decided to test the assembly protocol for MSP1D1ΔH5-based NDs. Additionally, we tested the possibility of refolding Barttin in a more "native-like" phospholipid mixture based on aliphatic chain lengths distribution and negative charge content found in the kidney cells' plasma membrane [536, 537]. Note that we didn't take into account the potential presence of unsaturations at this step. The mixture chosen was DPPC:DSPC:DAPC:DSPS 3:3:3:1. For both standard DMPC and the new lipid mix, we tested the refolding using either dialysis or on-column adsorbent beads removal. All conditions worked out and provided fair homogeneity of preparations (see Figure 35a). Notably, the usage of the "native" lipid mix, however, provided lower yields (see Figure 35a and Table 10). The oligomeric state of Barttin in MSP1ΔH5-based NDs was also estimated to 1 Barttin per ND (see Figure 35b).

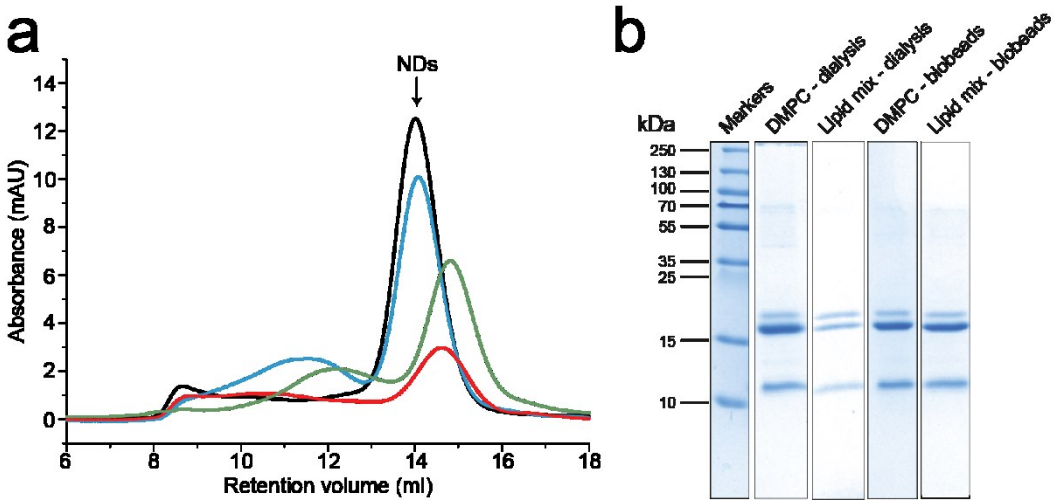

Figure 35. **Optimization of Barttin refolding into Δ5 NDs. a)** SEC profiles of Barttin-NDs (MSP1ΔH5) assembled with DMPC (black) and "native" lipid mix (red) upon detergent dialysis, respective profiles for on-column biobeads adsorption for DMPC (blue) and lipid mix (green). **b)** Coomassie blue-stained SDS-PAGE gel of the corresponding Barttin-NDs samples, purified via IMAC, before SEC.

All previous experiments were done using a low amount of Barttin (from small scale 100 µl cell-free expression system) and relative overall small scale. NMR studies, however, require higher amounts of material, in the mg range, and thus up-scaling of the protocols is required. We performed the two best conditions from small scale experiments, i.e. "native" lipid mix together with on-column detergent adsorption and DMPC together with detergent dialysis, from bigger cell-free pellets (from 3 ml CFE reactions). Some points of the protocol have to be adapted (washing pellets several times with smaller buffer amounts, using bigger dialysis cassettes and columns, etc.) and as expected the yields dropped, by 30% and 60%, respectively (see Figure 36a and b, respectively, and Table 10). Nevertheless this allowed to produce sufficient amounts of ^{15}N-Barttin in MSP1ΔH5-based NDs for initial NMR characterization (*vide infra*).

Figure 36. **NMR sample preparation of Barttin in Δ5 NDs. a)** SEC profile of up-scaled Barttin-NDs (MSP1ΔH5) assembled with "native" lipid mix upon on-column biobeads adsorption. **b)** SEC profile of up-scaled Barttin-NDs (MSP1ΔH5) assembled with DMPC upon dialysis. The fraction collected in the corresponding NMR samples are shown in grey background.

Another approach in nanodisc-incorporated membrane protein production is to perform cell-free expression in the presence of preformed NDs, in the hope that the target will be co-translationally incorporated. This has been successfully done before [512, 542]. We tested this approach in a small scale CFE reaction using preformed MSP1ΔH5-based nanodiscs assembled with DMPC lipids, which yielded fair quality and amount of Barttin-containing NDs (see Figure 37 and Table 10).

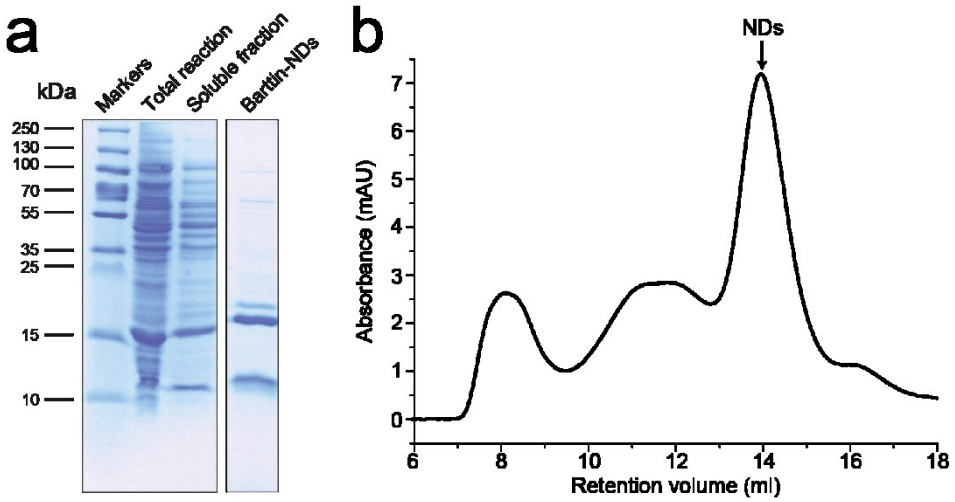

Figure 37. **Co-translational refolding of Barttin into Δ5 NDs. a)** Coomassie blue stained gel of total CFE reaction in the presence of preformed NDs (MSP1ΔH5, DMPC), soluble fraction and IMAC purified Barttin-NDs. (Different heights are due to the running behavior, see full gel in Figure 61) **b)** SEC chromatogram corresponding to the latter sample.

Scaffold	Detergent for Barttin	Detergent for lipids	Lipids	Detergent removal	Yield (%)
D1	SDS	Na-cholate	DMPC	Biobeads	(0)
D1	SDS	SDS	DMPC	Biobeads	(0)
D1	SDS	Na-cholate	DMPG:DMPC	Biobeads	(0)
D1	SDS	SDS	DMPG:DMPC	Biobeads	(0)
D1	DPC	Na-cholate	DMPC	Dialysis	(0)
D1	DPC	Na-cholate	DMPG:DMPC	Dialysis	(0)
D1	SDS	Na-cholate	DMPC	Dialysis	N.D.
D1	SDS	Na-cholate	DMPG:DMPC	Dialysis	N.D.
D1	SDS	Na-cholate	DMPC	On-column step dilution	(0)
D1	SDS	Na-cholate	DMPC	On-column fast dilution	4.7
D1	SDS	Na-cholate	DMPC	On-column biobeads	8.2
D1	SDS	Na-cholate	DMPC	Dialysis	5.8
Δ5	SDS	Na-cholate	DMPC	On-column biobeads	14
Δ5	SDS	Na-cholate	"Native" mix	On-column biobeads	9
Δ5	SDS	Na-cholate	DMPC	Dialysis	19.3
Δ5	SDS	Na-cholate	"Native" mix	Dialysis	3.7
Δ5	SDS	Na-cholate	DMPC	Dialysis / Up-scale	8.2
Δ5	SDS	Na-cholate	"Native" mix	On-column biobeads / Up-scale	6.2
Δ5	Cell-free	-	DMPC	-	12.8

Table 10. **Summary of tested conditions for Barttin refolding in NDs.** Scaffold protein type, detergents and lipids used, detergent removal procedure are indicated together with the respective yields (N.D. = no detectable level (<1%) of Barttin but successful incorporation ; (0) = not incorporated into NDs).

Taken together, screening of these numerous conditions allows to conclude some key points: (i) Barttin is likely to adsorb into polystyrene beads, (ii) various types of phospholipid mixtures lead to successful incorporation, (iii) the rate of detergent removal is critical and (iv) Barttin co-translationally inserts into preformed NDs during cell-free expression.

Barttin exhibits secondary structure in LDAO micelles

Although having the advantage of theoretically allowing structural study of membrane proteins in lipid bilayers with properties very close to the natural membrane, nanodiscs still remain tedious in most NMR-based studies due to their large size as compared to detergent micelles (roughly 30 kDa for Barttin in LDAO micelles *versus* 110 kDa for Barttin in MSP1ΔH5-based NDs). For this reason, making use of the two membrane mimetic systems in parallel would allow to obtain from one side better NMR spectra and from the other side complementary, presumably more physiologically relevant, information.

To obtain Barttin in detergent micelles, we initially performed detergent screening by directly solubilizing Barttin from cell-free pellets, following previous approaches [187]. A range of detergents were tested for which numerous NMR studies have been reported before: FOS-10, DPC, LDAO, LMPG, DM and DDM (see Figure 38a). All of them but DM and DDM lead to similar solubilization levels as seen from the intensities of the corresponding bands in SDS-PAGE. Three of them were selected for initial NMR screening for their capacity to form very small micelles (LDAO, LMPG) or their reported good NMR properties (LDAO, DPC) [245, 543]. 1D ^{1}H-spectra of Barttin solubilized in the respective micelles without further purification were acquired and compared (see Figure 38b). While the shape of the amide region signal is overall similar for all three, more intense and resolved peaks on the edges, which is a sign for better signal of the transmembrane regions [512], as well as appearance of a signal for tryptophan side chain amide suggest that Barttin is better folded or at least more resolved in LDAO micelles. All successive stages were therefore performed using this detergent.

In order to further check the characteristics of Barttin in LDAO micelles, circular dichroism (see Figure 38c) as well as 2D NMR (see Figure 38d) were performed. The CD spectrum shows a double minimum around 225 and 215 nm, indicative of α-helices, which is expected for folded Barttin. Indeed, according to the proposed topology models [295], the I72X construct should be 45% helical. Deconvolution of the CD spectrum (K2d method) leads to an amount of α-helices of 37%, in line with the latter. The [^{15}N-^{1}H]-HSQC spectrum of isotopically labeled Barttin in LDAO micelles shows dispersed and mostly resolved peaks, a rough peak-picking allows to count 65 out of the 77 expected (cysteine, glutamine, asparagine and tryptophan are not ^{15}N-labeled in the cell-free set-up used). Taken together these results point towards Barttin having a proper secondary structure folding and yielding good NMR data in LDAO micelles.

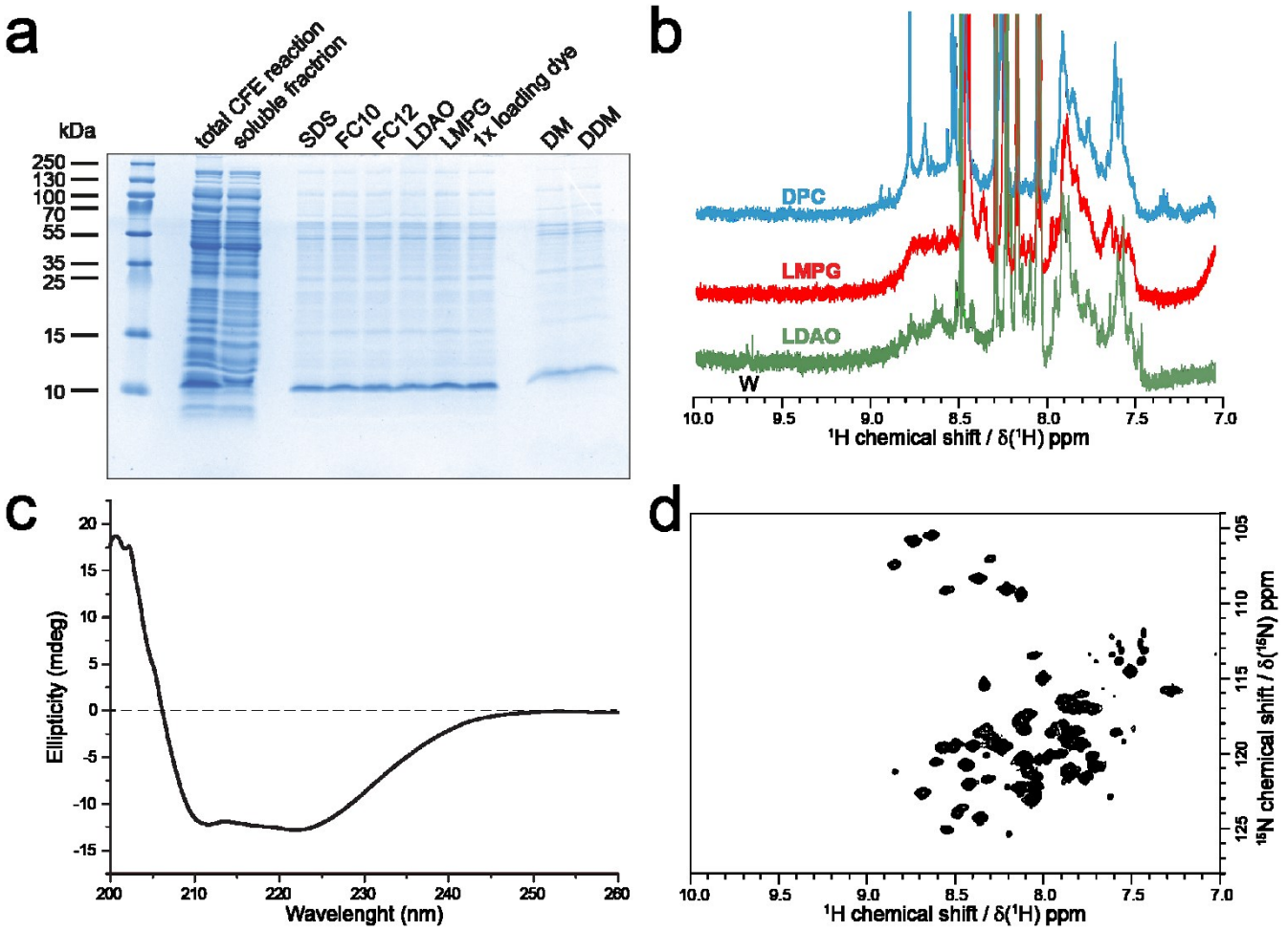

Figure 38. **LDAO micelles provide suitable environment for NMR studies of Barttin. a)** Coomassie stained SDS-PAGE gel of Barttin CFE and solubilization by a range of detergents, no remaining pellets were visible after centrifugation at 20000·g. **b)** ^{1}H 1D NMR spectra of Barttin solubilized in DPC (blue), LMPG (red) and LDAO (green). **c)** Circular dichroism spectrum of Barttin in LDAO micelles. **c)** [^{15}N-^{1}H]-HSQC spectrum of [U-^{2}H-^{13}C-^{15}N]-labeled Barttin in LDAO micelles (Cys, Asn and Trp are unlabeled).

LDAO micelles yield better NMR data but lower stability than nanodiscs

One disadvantage of the nanodisc system as compared to e.g. detergent micelles, amphipols or polymer-based lipodiscs is that the presence of a scaffold protein impedes light absorption-based experiments such as concentration determination at 280 nm or circular dichroism spectroscopy [512]. Thus, the same characterization of Barttin secondary structure in NDs was not feasible, however NMR will only report on Barttin since it is the only isotope labeled compound. The [^{15}N-^{1}H]-HSQC spectra acquired for Barttin in nanodiscs (see Figure 39a) show much less signal, in line with homogenous line broadening of bigger particles. Only 15 of the expected 77 peaks are visible. The most probable explanation for this is that only signals from residues situated in *termini* or in the extra-membrane loop appear because they should have much more favorable dynamic properties, leading to better resolution and higher intensities. Without proper residue-specific assignments, however, only assumptions can be made. Looking more in details, it is clear that the position of the visible peaks is largely different from LDAO to NDs, some residues are significantly shifted or appear in spectral regions where no signal of Barttin in LDAO stands. This indicates that the conformation of the protein is significantly different in the two membrane mimetics. Even if only the extra-membrane residues can be compared this can be relevant because the conformation and dynamics of those regions usually play important physiological roles and are likely to be affected e.g. by the denaturation effect of detergents at the micelle-water interface as it was postulated in the case of OmpX [247]. Finally, a large overlap between the pure DMPC and the “native” lipid mix are visible pointing to a similar fold. Small changes do arise but they are much less prominent than from LDAO micelles, and can be attributed to the

different properties of the bilayers, thickness and charge, leading to slightly different properties of the trans-membrane helices edges.

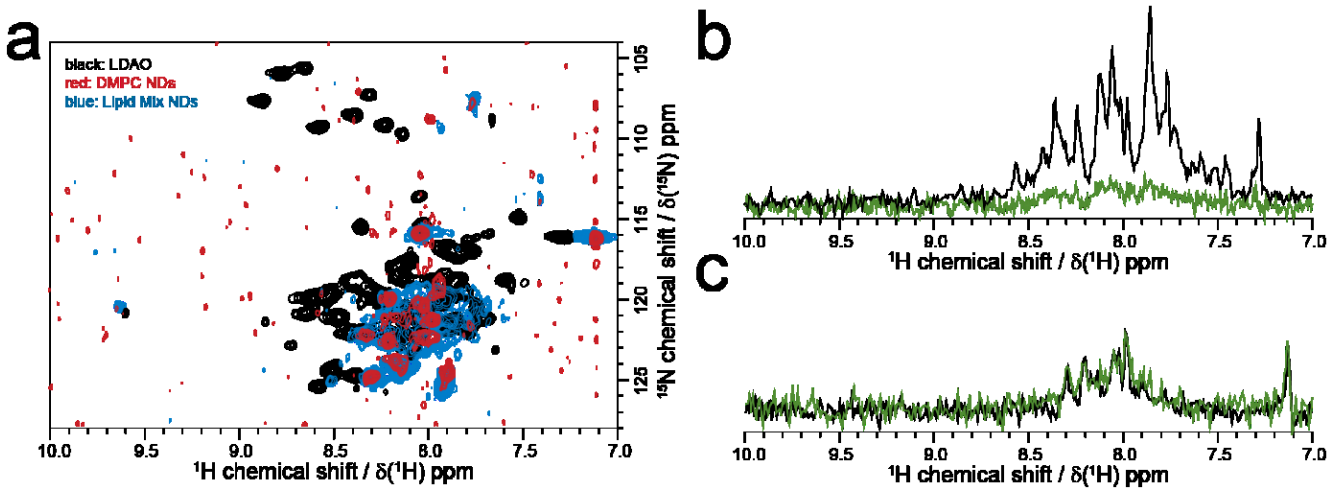

Figure 39. **Barttin has different properties in LDAO and NDs. a)** [^{15}N-^{1}H]-HSQC spectra of ^{15}N-labeled Barttin in LDAO micelles (black), DMPC NDs (red) and "native" lipid mix NDs (blue). **b)** ^{15}N-filtered ^{1}H 1D spectra corresponding to the first FID of the HSQC experiments of ^{2}H-^{13}C-^{15}N-labeled Barttin in LDAO micelles at time point 0 (black) and after 14 days (green). **c)** ^{15}N-filtered ^{1}H 1D spectra corresponding to the first FID of the HSQC experiments of ^{15}N-labeled Barttin in DMPC NDs at time point 0 (black) and after 18 days (green).

While NMR data acquired for Barttin in LDAO micelles are clearly of much better quality, the stability of the sample is also much lower than in NDs. Indeed, we could observe gradual degradation of the HSQC signal over time when performing long-time measurements. This usually arises when protein degradation or aggregation happens on the time course of the NMR measurement. A nearly complete disappearance of the signals happened over 14 days (see Figure 39b) making the acquisition of spectra of sufficient quality for NMR backbone sequential assignment very difficult (*vide infra*). Note that in an attempt of characterizing Barttin in SDS, we could see that complete degradation of the signal happens in only 2 days (data not shown), for Barttin in nanodiscs however no degradation was detected over 18 days (see Figure 39c).

A combinatorial labeling strategy for Barttin assignment in LDAO micelles

Sequential backbone assignment, i.e. the attribution of each HSQC peak to its corresponding amide system and as such specific residue in the sequence of the protein, is the first and necessary step of every NMR structural study of proteins. This is usually done using 3D experiments able to correlate amide signals with various types of carbon signals including carbonyl, Cα and Cβ of the same residue and the previous residue in the sequence, thus allowing sequential links to be made and ultimately assignment of the spin systems. Nevertheless, for the reason explained above, i.e. the degradation or aggregation of Barttin during the acquisition of such 3D experiments, the quality of data obtained is poor and does not allow much of the process. While some links and 10 assignments can be unambiguously made, exemplified with the S44-H45-D46 sequence (see Figure 40), most of the spectra have very low signal-to-noise ratio, especially when [^{13}C-^{13}C]-INEPT transfers are involved. This is a well-known phenomenon is large systems due the unfavorable relaxation properties and can be overcome by using other types of magnetization transfers [518] but renders the assignment process very difficult.

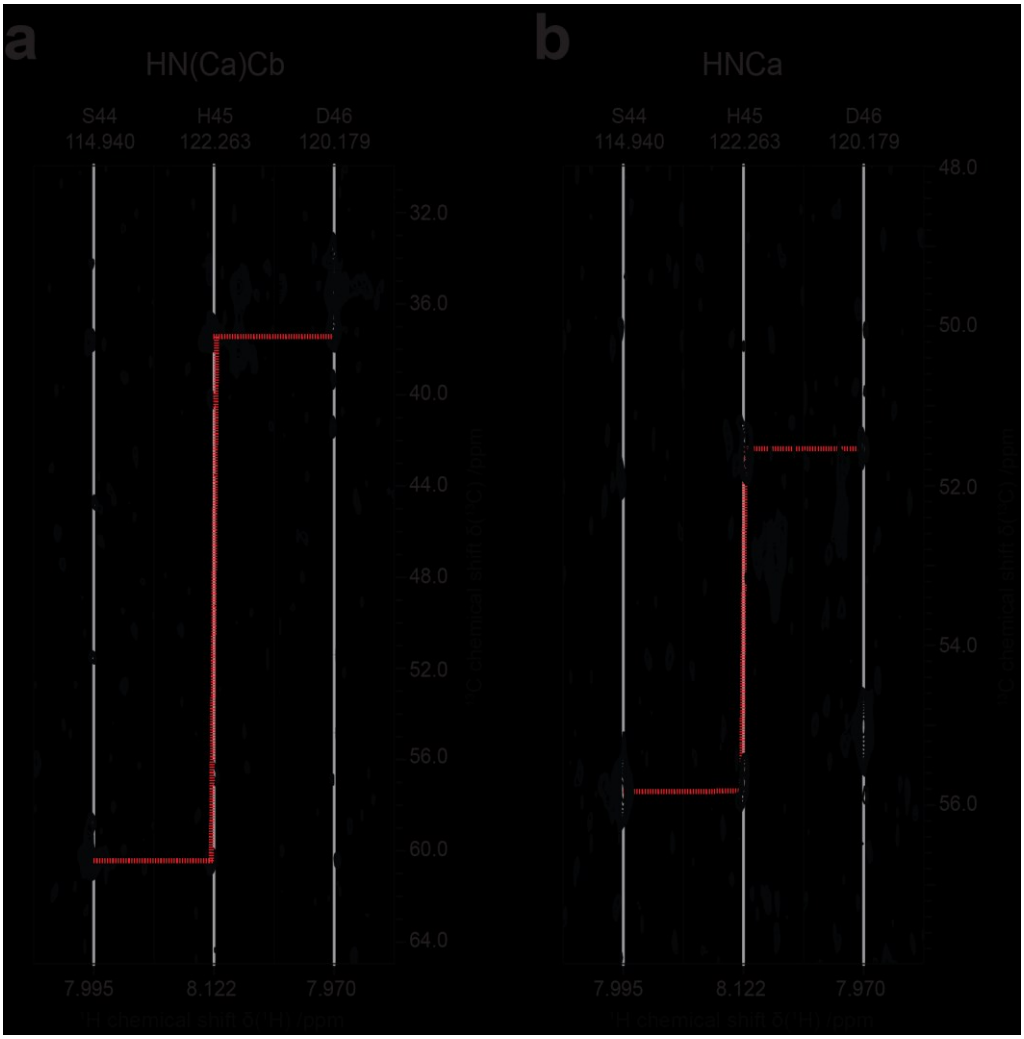

Figure 40. **Barttin standard assignment procedure is impeded by the quality of NMR data in LDAO. a)** Strips of the HNCa spectrum of ^{2}H-^{13}C-^{15}N-labeled Barttin in LDAO micelles corresponding to the S44-H45-D46 fragment, sequential links through Cα signals are exemplified by arrows. **b)** Strips of the HN(Ca)Cb spectrum of ^{2}H-^{13}C-^{15}N-labeled Barttin in LDAO micelles corresponding to the S44-H45-D46 fragment, sequential links through Cβ signals are exemplified by arrows. Note that the signal-to-noise ratio is very limited in these spectra.

To address this issue, we decided to pursue a different assignment strategy which does not rely on using 3D experiments, i.e. combinatorial labeling [544]. The principle is to produce several samples with different types of amino acids that are isotopically labeled with either only ^{15}N, only ^{13}CO or ^{13}C-^{15}N, i.e. different labeling schemes each time. Comparison of 2D spectra from [^{15}N-^{1}H]-HSQC, ^{13}CO-filtered HSQC and $^{13}C\alpha$-filtered HSQC between each other lead to amino acid type assignment and ultimately to residue-specific assignments. This is made easy by the use of cell-free expression, which allows to introduce single amino acids with the desired labeling types that are directly transferred into the protein sequence, at the exception of the interconversions between glycine and serine and between asparagine, aspartate, glutamine and glutamate in prokaryotic ribosomes [545, 546]. In order to optimize the number of possible assignments out of a fixed number of experiments (and of samples), the design of the labeling schemes has to be made such as to maximize the number of unique signals coming from unique sequential pairs of amino acids, with a ^{13}CO or $^{13}C\alpha$-labeled residue followed by a ^{15}N-labeled residue in the sequence. We chose a 4-sample approach (see Table 11) and initial results from the first combinatorial sample (see Figure 41) already allow the additional unambiguous assignment of 3 residues and one ambiguous pair. We predict the complete process to provide 23 *de novo* unambiguous assignments. Note that the correlation of those new assignments with sequential links visible in the 3D spectra might increase this number.

Amino acid type	sample 1	sample 2	sample 3	sample 4
Alanin (A)	^{15}N	^{13}CO	^{15}N	^{15}N
Arginin (R)		^{15}N	^{13}CO	
Asparagin (N)			^{13}CO	
Aspartate (D)		^{13}CO		
Cystein -C-	^{15}N			
Glutamate (E)			^{13}CO	
Glutamin (Q)				
Glycin (G)				
Histidin (H)				
Isoleucin (I)			^{15}N	U-^{13}C-^{15}N
Leucin (L)	^{15}N	U-^{13}C-^{15}N	^{15}N	^{13}CO
Lysin (K)		^{13}CO	^{15}N	
Methionin (M)	^{13}CO	^{15}N	^{15}N	
Phenylalanin (F)				^{15}N
Prolin (P)				
Serin (S)	1^{15}N			
Threonin (T)		^{15}N		^{15}N
Tryptophan (W)				
Tyrosin (Y)		^{15}N	^{13}CO	^{15}N
Valin (V)	U-^{13}C-^{15}N		U-^{13}C-^{15}N	

Table 11. **Combinatorial labeling schemes for Barttin NMR assignment.** The type of isotope labeling for each amino-acid type, i.e. either only ^{15}N, only carbonyl ^{13}C or uniform ^{13}C-^{15}N, is indicated for the 4 samples.

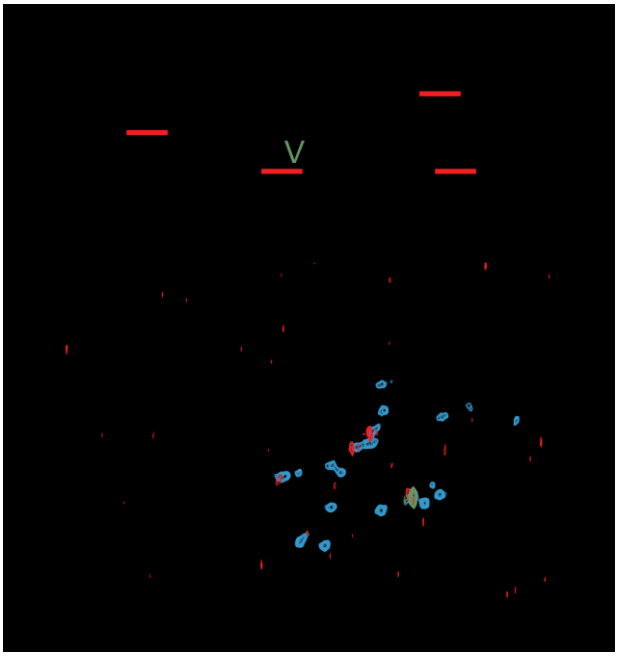

Figure 41. **Initial results of the combinatorial assignment strategy for Barttin in LDAO. a)** Sequence of Barttin with the relevant unique sequential pairs for the 2D HN(CO) experiment underlined in red and residue V62, the only one having its own carbons and the previous carbonyl labeled, in green. **b)** Overlay of [^{15}N-^{1}H]-HSQC acquired on [^{2}H-^{13}C-^{15}N]-labeled Barttin in LDAO micelles (black), HSQC acquired on combinatorial sample 1 (see Table 11, blue), [^{15}N-^{1}H] plane of the respective HNCO (red) and [^{15}N-^{1}H] plane of the respective HNCa (green). The assigned residues V62 (present in all spectra due the reasons mentioned before) and C71 (present in blue and red only due to sample 1's labeling scheme and to the fact that the reference spectrum had CNW non-labeled, see Figure 38) obtained by the approach are indicated, remaining arrows to the ambiguous pair A19-L31.

Perspectives/conclusion

We here report on the optimization of NMR sample preparation for the supposedly two-transmembrane helices protein Barttin in two membrane mimetic systems, detergent micelles and phospholipid bilayer nanodiscs. Conditions were found for which cell-free expressed Barttin is successfully incorporated into nanodiscs. LDAO micelles yield NMR spectra of better quality, and Barttin seems to adopt a similar secondary structure as predicted, it is however impossible to conclude that it adopts its native structure at this stage. Furthermore, comparison with the samples in nanodiscs, potentially providing more native conditions (presence of a lipid bilayer), reveals significant differences arising most probably from the extra-membrane residues. Due to the very low spectral quality of the nanodisc samples, NMR experiments, however, focused on LDAO micelles. Nevertheless, the obtained results should be interpreted wisely and compared to the piece of information obtained in nanodiscs, as well as complementary cell assays and mutagenesis studies, in order to make the most relevant conclusions for the physiology of Barttin.

We also report on design and application of a combinatorial isotope labelling strategy for NMR assignment of Barttin in LDAO micelles, since conventional NMR assignment strategies fail in that case. Completion of the process will pave the way to structural characterization of Barttin with, primarily, investigation of the secondary structure (from chemical shifts [547]) and of the topology (e.g. from solvent and hydrophobic paramagnetic relaxation enhancements [247]) at a residue-specific level, and ultimately, perhaps, to the determination of its structure. This would be a key point in understanding the structure-function relationships of Barttin, the effect of disease-relevant mutations in its sequence (R25L, R25W, G27S, V50L, and G64R, according to histidine tagged I72X construct) and the modes of interactions with the chloride channels. Indeed we could show that those mutants, identified from Bartter syndrome type IV patients, diminish the activity of chloride channels *in vivo* by patch clamp measurements (S. Bungert, data not shown) but the rationale of this effect is not clear so far. Their cell-free expression and *in vitro* characterization is now ongoing in our laboratory with the aim to identify structural effects that can explain the *in vivo* data.

Acknowledgements

The authors acknowledge access to the Jülich-Düsseldorf Biomolecular NMR Center. This work was supported by grants the German Research Foundation (DFG) (ET 103/2-1) to M.E. and from the European Union's Horizon 2020 research and innovation program under the Marie Sklodowska-Curie grant agreement Nº 660258 to A.V.. T.V. acknowledges support from the International North-Rhine-Westphalia Research School iGRASPseed.

CHAPTER VIII – PERSPECTIVES AND CONCLUSION

Future potential of the nanodisc technology

We aimed at contributing to the field of structural biology, more precisely to the structural study of membrane and membrane-associated proteins by nuclear magnetic resonance. In this respect we studied and applied an unconventional membrane mimicking systems, lipid bilayer nanodiscs (Chapter III), to several targets. We optimized sample preparation in a target-dependent way (Chapter IV, Chapter VI and Chapter VII) and developed a new way of acquiring NMR experiments, that is especially suited to this type of samples (Chapter IV). Moreover we developed an alternative methodology for the study of proteins in close-to-native environments, without the need for purification or, potentially, membrane protein refolding (Chapter V). In respect of sample preparation and NMR methodology, we hope to have provided new approaches, that are complementary to previous ones, and may or may not be better suited to given scientific questions.

Review on the usage of lipid bilayer nanodiscs (Chapter III), with a focus on their NMR applications, shed the light on a more and more established technology. Further developments are however still ongoing [208] and lead to significant improvements and applicability to new types of experiments. Moreover, it also pointed out the missing knowledge about a range of key features of nanodiscs, e.g. the structure of the scaffold protein in NDs, its plasticity, its interactions with the lipids, the potential effects of different lipids or of the presence of membrane proteins on their structure, the way nanodiscs assemble, were indeed not known. Recently a first breakthrough was achieved with the structure determination of a scaffold protein in the ND assembly [276]. This already provides precious information and will be the ground stone of further characterization. However more experimentation will be needed in order to address the aforementioned questions. We started to work in this respect and got some initial results.

The effect of having different lipid mixtures inside nanodiscs is an important factor since they are supposed to mimic natural membranes and define the physical properties of the bilayer. For instance, many different lipid mixtures can be found in the different cells or cell compartments as well as during their life stages and may be used in NDs. Their actual behavior however remains unclear, for instance phase transitions are usually broader and up-shifted as compared to pure bilayers [548]. These differences may be explained by the presence of interactions of some lipids with the scaffold protein, leading e.g. to a lack of cooperativity and/or a tighter packing. For this reasons we decided to study the scaffold protein via solution NMR, and especially how it behaves upon changes in the lipid content of the NDs. [^{15}N]-isotopically labeled MSP1ΔH5 has been produced and used to assemble nanodiscs, with lipids containing either no or 20% negatively charged lipids (DMPG:DMPC). The results (see Figure 42a) show significant chemical shift perturbations, many of which clustering in the *termini* of MSP (Figure 42b). In general it is clear that residues that are more exposed to the solvent (more prone to plasticity) are also more affected by changing the lipid content in NDs. According to the structure of MSP1ΔH5 [276], there could be a correlation between the electrostatic potential and the chemical shift perturbation, but this is difficult to established at this stage (Figure 42c). Closer investigation of this as well as other effects on the scaffold (plasticity, lipid length, presence of unsaturations, presence of cholesterol, presence of a membrane protein, etc.) is now ongoing.

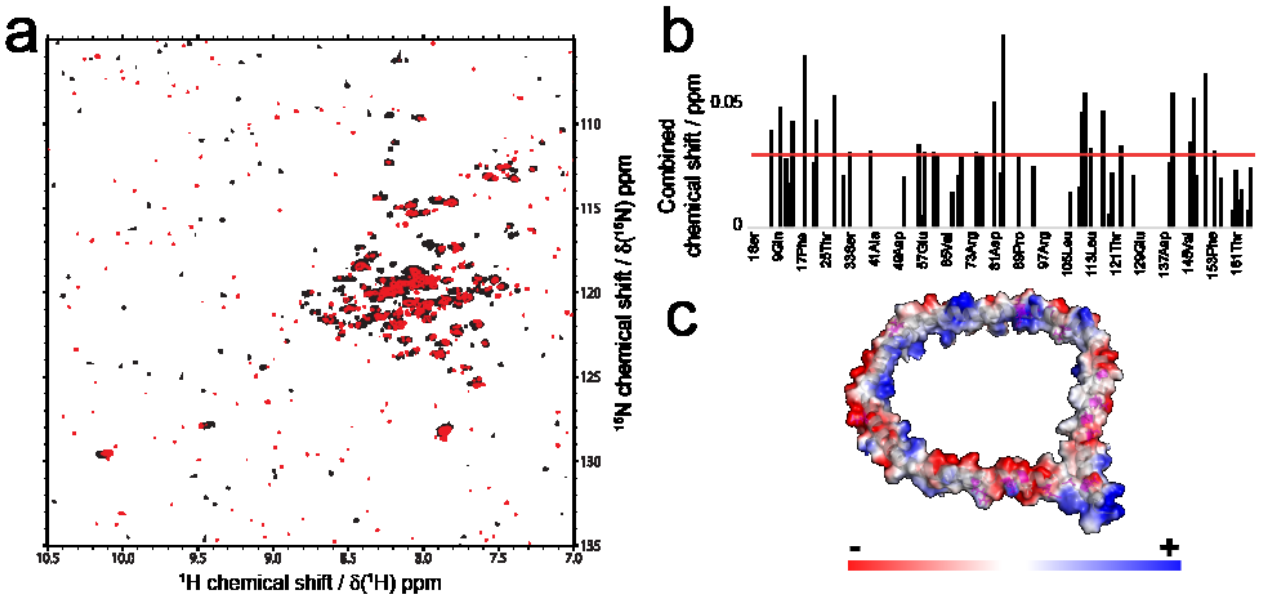

Figure 42. **Changes in the scaffold of MSP1ΔH5 nanodiscs in the presence of negatively charged lipids. a)** [^{15}N-^{1}H]-TROSY-HSQC spectra of NDs assembled with ^{15}N-labeled MSP1ΔH5 and DMPG-DMPC 1:4 (black) or 100% DMPC (red). **b)** Combined chemical shift perturbations [547] plotted against the primary sequence of MSP1ΔH5. Non-assigned residues were attributed a value of 0. Standard deviation threshold is shown in red. **c)** Structure of MSP1ΔH5 [276] with its electrostatic surface potential. Residues exhibiting significant chemical shift perturbations are displayed in red sticks (higher than the threshold).

Interestingly, combination of the ND technology with the targeted DNP approach introduced in this work [141] is possible via radical conjugation to the scaffold proteins. This could lead to a powerful and universal platform for DNP investigation of membrane proteins, and could also enable the study of low populated states of membrane associated proteins (e.g. membrane-bound α-Synuclein in the presence of a large excess of free monomer, which is supposedly the most relevant state for *in vivo* primary nucleation). In the latter, targeted DNP would take place *in vitro* but allow to characterize specifically low-populated states, which normally requires single molecule techniques. We initiated work in that respect, produced mutants of the scaffold proteins and conjugated them to TOTAPOL. As a first step we characterize the targeted DNP behavior of empty NDs. Nanodiscs were assembled with a mixture of ^{15}N-labeled MSP1ΔH5 and unlabeled MSP1ΔH5 with a mutations of Gly27 to a cysteine, which can be used to attach a maleimide modified TOTAPOL (mTP). For this reason, statistically half of the NDs will contain one isotopically labeled copy of the scaffold and one biradical.

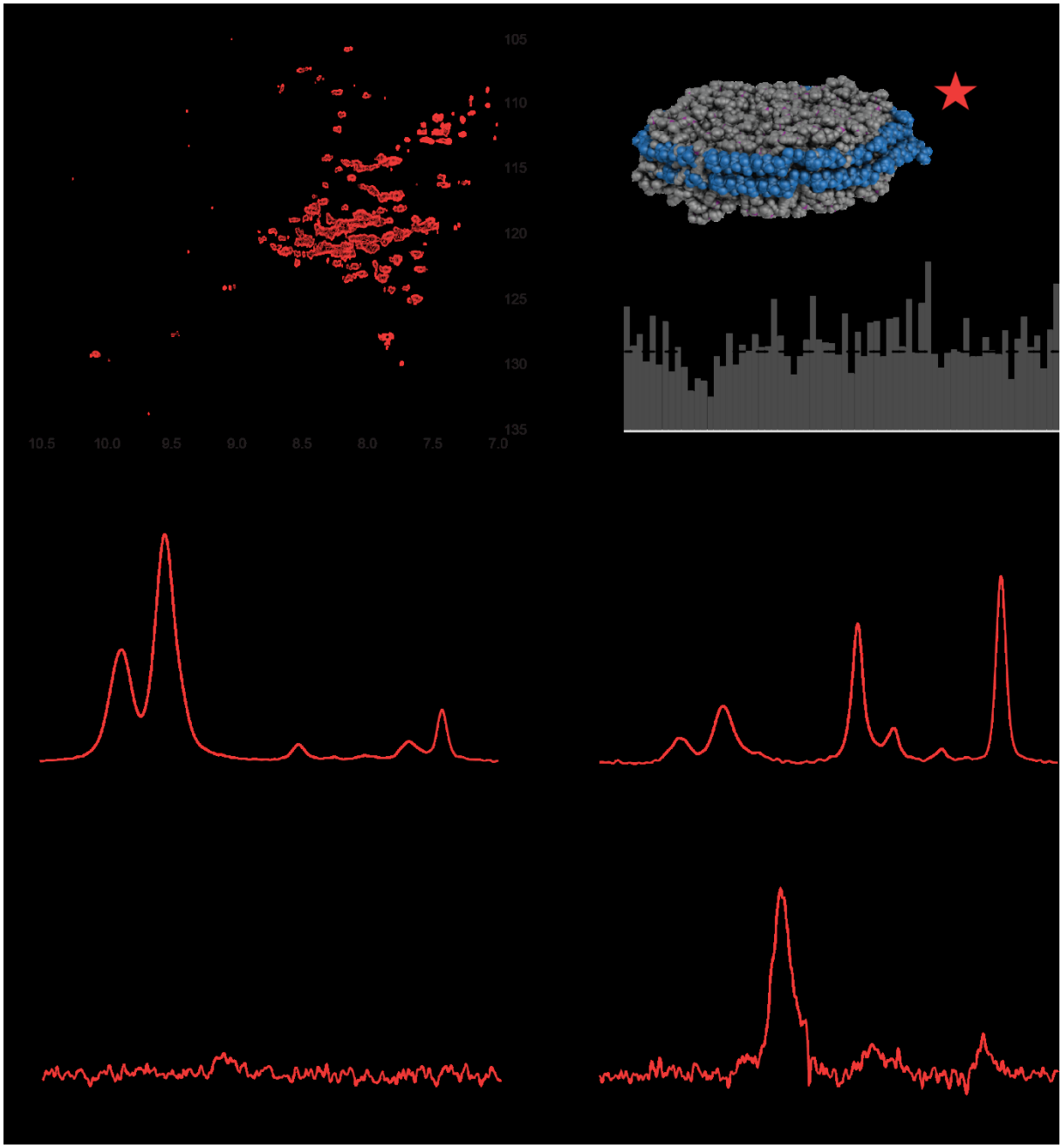

Figure 43. **Targeted DNP is able to specifically enhance the signal of the scaffold in nanodiscs.** A scheme of the sample is shown in the top right corner. The biradical linked to one of the MSPs is displayed as a red star. **a)** [^{15}N-^{1}H]-TROSY-HSQC spectra of NDs assembled with ^{15}N-labeled MSP1ΔH5:unlabeled MSP1ΔH5G27C 1:1 and DMPG-DMPC 1:4 before (black) and after (red) conjugation with maleimide-TOTAPOL (mTP). **b)** Ratios of peak volumes plotted against the primary sequence of MSP1ΔH5. The volume of corresponding signal of the mTP-conjugated ND has been divided by the respective mTP free ND signal, after calibration using Phe149 (supposedly unaffected). The residues undergoing PRE effects are located in helix 2 (25-35). **c)** [^{1}H-^{13}C]-CP spectra of mTP free NDs in the presence of 20 mM TOTAPOL, in DNP conditions (105 K) with 10% H_2O, with microwaves turned off (black) or on (red). **d)** Respective [^{1}H-^{15}N]-CP spectra. **e)** [^{1}H-^{13}C]-CP of mTP-conjugated NDs, in DNP conditions (105 K) with 100% $^{2}H_2O$, with microwaves turned off (black) or on (red). **f)** Respective [^{1}H-^{15}N]-CP spectra. Measured DNP enhancement factors (ε) on glycerol (background), lipids and protein are indicated.

We characterized the sample by solution NMR using PRE experiments (see Figure 43a). Comparison of the HSQC spectra before and after mTP conjugation reveals specific signal reduction of residues situated in the second helix of MSP1ΔH5 (residues 25 to 35, Figure 43b). The latter result proves that (i) mTP conjugation was successful, (ii) the radical is active, (iii) both species of scaffolds are mixed inside single NDs and (iv) the radical is located on a defined position in the structure. The same samples were used for DNP experiments, a series of cross polarization (CP) experiments was acquired in order to measure DNP enhancements obtained and to compare

the behavior of the sample under conventional or targeted DNP conditions (20 mM free TOTAPOL, 10% H_2O *vs* conjugated mTP, 100% ^2H_2O, see Chapter V for more details). While conventional DNP significantly hyperpolarizes the background (probed by the buffer's glycerol signal) but fails in efficient lipid or protein-enhancement, targeted DNP is able to enhance the signal of all three to the same level. Note that the enhancement factors obtained on the protein and lipids (ε=8) in the targeted case are significantly lower than in previous experiments (ε=18, see Chapter V). Many reasons could contribute to this, for instance too high ^1H spin density inside NDs due to the lipids and residual methyl rotation dynamics, which can act as polarization sinks [128]. While it is difficult at this point to explain this, the data may provide a first reference for the size of the spin network that can be hyperpolarized using a single biradical. In this respect, the obtained enhancement factors are actually larger than initially anticipated (on average one biradical would be able to fully hyperpolarize 5000-7000 ^1H), proving that the approach has a large potential for future applications.

Conclusion and key achievements

We applied the nanodisc technology to the investigation of α-Synuclein binding modes to lipid bilayers and their effect on aggregation (Chapter VI). Combination of complementary methods allowed us to obtain insights at the molecular level on (i) the secondary structure of αS bound to NDs, (ii) the effect of lipid's negative charge content on αS association, (iii) the effect of the lipid's hydrophobic chain's type on the binding of αS, (iv) the effect of the stoichiometry i.e. the αS to ND ratio and (v) the correlation of these modes of binding to the aggregation propensity of αS in the presence of membranes. Moreover, we characterized the ion channel regulator protein Barttin in different membrane mimetics (Chapter VII). The comparison of NMR data quality and stability of Barttin in detergent micelles and nanodiscs is paving the way to the first structural study of this protein.

We contributed to the time efficiency of solution NMR experiments by the implementation of UTOPIA NMR (Chapter IV), which allows to get additional information without the need for extra time or sample. Additionally, we chose to investigate the possibility of using Dynamic Nuclear Polarization (DNP) solid-state NMR in the investigation of proteins in close-to-native environments. Development of the "targeted DNP" methodology on a soluble construct of the protein Bcl-x_L allowed us to achieve specific hyperpolarization in the protein's cell lysate background, with the need of only one dialysis step and the use of only 8 ml of bacterial culture (Chapter V). In other words, the method allows structural investigation of proteins at the molecular level with reduced sample amount and with minimal *in vitro* perturbation, getting closer to native conditions.

Furthermore, targeted DNP using interaction partners of the target proteins (see Chapter V) has a very broad range of applications, since radical-conjugated peptides, small molecules or small proteins binding to many targets are known or can be designed. Additionally, is has the power of doing so in fully native environments, because those binders can by electroporated in cells (if not acting in the extracellular milieu). As an interesting application of this, we are now developing targeted DNP methodology for the study of G-protein coupled receptors in whole cells, using radicals bound to their cognate hormones.

Finally, we investigated several approaches in the development of more efficient and more relevant methods for the sample preparation and NMR study of proteins. Proofs-of-concept and initial applications have been shown in the different chapters of this work. We hope to have demonstrated the complementarity of the methods and to have initiated further developments by showing their applicability and potential.

The key findings and achievements presented in this work can be summarized as follows:

- A new, time efficient, way of acquiring selected NMR experiments was developed and implemented, termed UTOPIA NMR.
- UTOPIA NMR was shown to be especially informative for perdeuterated proteins and proteins refolded in nanodiscs.
- Specific hyperpolarization of proteins was demonstrated using targeted DNP.
- Targeted DNP allows to study reduced amounts of (unpurified) proteins in their cell lysate.
- Molecular insights into α-Synuclein binding to lipid bilayers were investigated, which may enlighten the possible relevance of membrane association for early stage fibril formation in Parkinson's disease.
- Initial characterization of Barttin in micelles and nanodiscs is paving the way for further NMR studies.

SUPPLEMENTARY DATA

Supplementary data

UTOPIA NMR

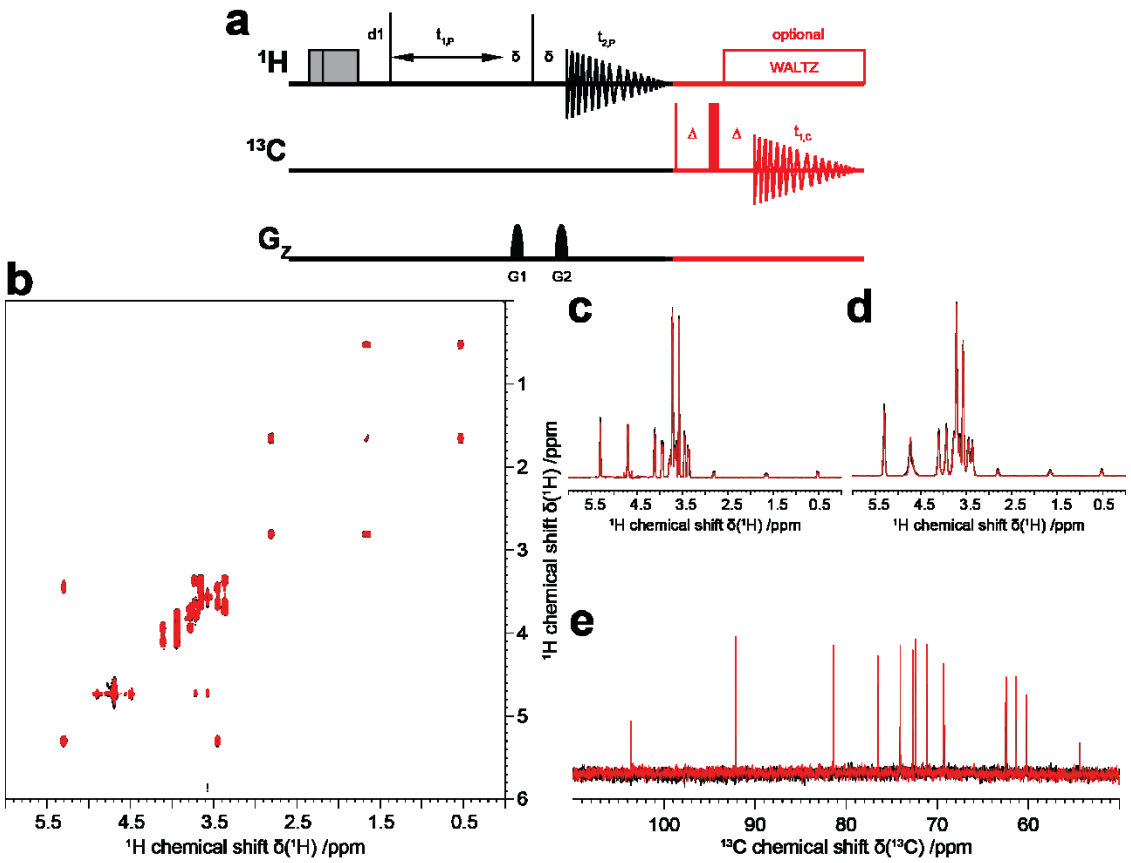

Figure 44. **Description of a unified COSY/^{13}C 1D experiment. a)** Pulse sequence scheme for the unified acquisition of a ^{1}H,^{1}H-COSY spectrum (black) and a 90°-^{13}C spectrum (red). Both parent and child pulse sequences were used with the standard parameters (i.e. pulses, phases, delays, etc., see Table S1 for name of used Bruker pulse sequences) as found in the Bruker library. Note that the refocusing step (with a delay Δ = 20 µs) in the ^{13}C-detected experiment was introduced due to RF ringdown effects, which only appeared in one of three spectrometers on which we tested the sequence. In general, it may hence be favorable to omit refocusing. Note that, in the shown setup the UTOPIA child has slightly higher signal intensity as compared to the conventional spectrum due to the effects of the parent experiment. Despite both the UTOPIA child and the respective reference spectrum were acquired without NOE enhancement (i.e. in the absence of power gated decoupling), the presence of the UTOPIA parent will lead (as expected) to increased intensity of the ^{13}C-detected experiment. This enhancement will, however, be lower (for protonated carbons) than the one obtained with a standard NOE-enhanced experiment. Nevertheless, in this setup the UTOPIA parent is not disturbed by the child, meaning that the child (although slightly lower in intensity as a conventional NOE enhance experiment) is obtained for free. Alternatively, a power gated decoupling period could be included in the UTOPIA sequence (directly after 1H detection). The duration of this period will however prolong the experimental time and therefore effectively lead to a reduction in the parent sensitivity (signal per time). In this respect it also provides a possibility to adjust the relative sensitivity of parent and child to some extend. **b)** Superposition of the conventional (black) and interleaved (red) 2D ^{1}H,^{1}H-COSY spectra. **c, d)** Superposition of the corresponding projections in the direct and indirect dimension, respectively. **e)** Superposition of the conventional (black) and interleaved (red) 1D ^{13}C spectra. Note that the ^{1}H decoupling during ^{13}C detection will interrupt ^{1}H relaxation and hence, if short recycle periods are used, may lead to a decrease in the ^{1}H detected signal intensity in comparison with a conventional experiment. This will be in particular true in cases were ^{13}C-T_2 values are in the order of ^{1}H-T_1 values and relaxation delays are specifically optimized for the ^{1}H-T_1 properties of the sample. However, in routine screening of small molecules inter-scan relaxation delays are often not specifically optimized for each sample, instead fixed values of e.g. 1-4 s are used. This was also done for the data shown here, where a relaxation delay of 2 s was set for the ^{13}C detected experiment. Our data show that in this view and for the sucrose sample used, the ^{1}H detected experiment can be recorded for free during the acquisition of the ^{13}C detected experiment, resulting in identical information content in exactly half of the measurement time as compared to the conventional data. Note that in the context of small molecule analysis also the previously published PANSY experiments [460] can be very beneficial and that PANSY experiments can be converted into an UTOPIA setup without the need for an additional receiver in cases where the polarization of one species (high- or low-γ) can be satisfactorily stored during the acquisition period of the other nucleus (also see Figure 46 and Figure 47).

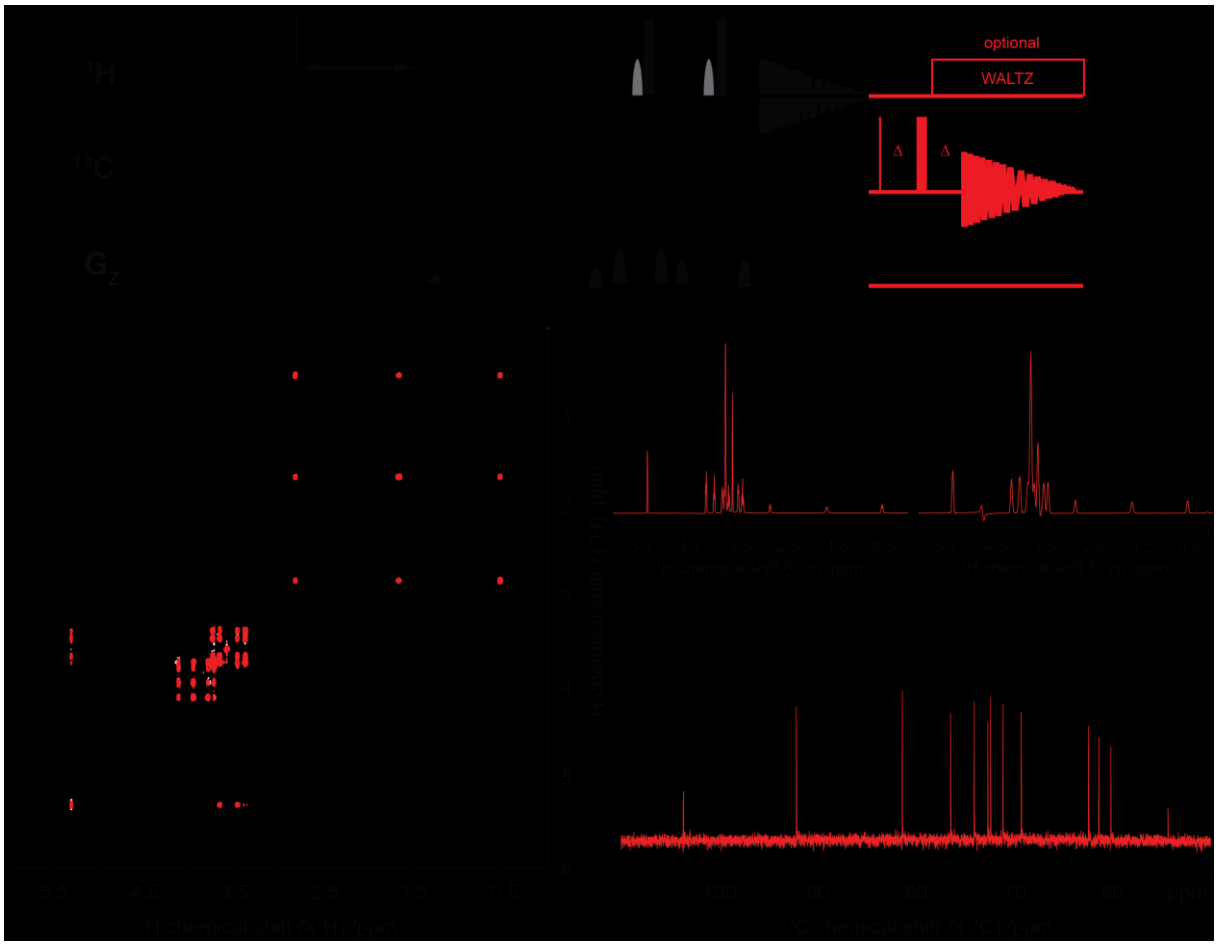

Figure 45. **Description of a unified TOCSY/^{13}C 1D experiment. a)** Pulse sequence scheme for the unified acquisition of a ^{1}H,^{1}H-TOCSY (black) and a 90°-^{13}C (red). Both parent and child pulse sequences were used with the standard parameters as found in the Bruker library. As in the example above (Fig. S1), a refocusing setup was added in the ^{13}C-detected experiment to tackle RF ringdown effects. **b)** Superposition of the conventional (black) and interleaved (red) 2D ^{1}H,^{1}H-TOCSY spectra. **c, d)** Superposition of the corresponding direct and indirect projections, respectively. **(e)** Superposition of the conventional (black) and interleaved (red) 1D ^{13}C spectra. Data were recorded on 2 mM unlabeled sucrose. (Also see comment regarding refocusing and T_1 relaxation in Figure 44).

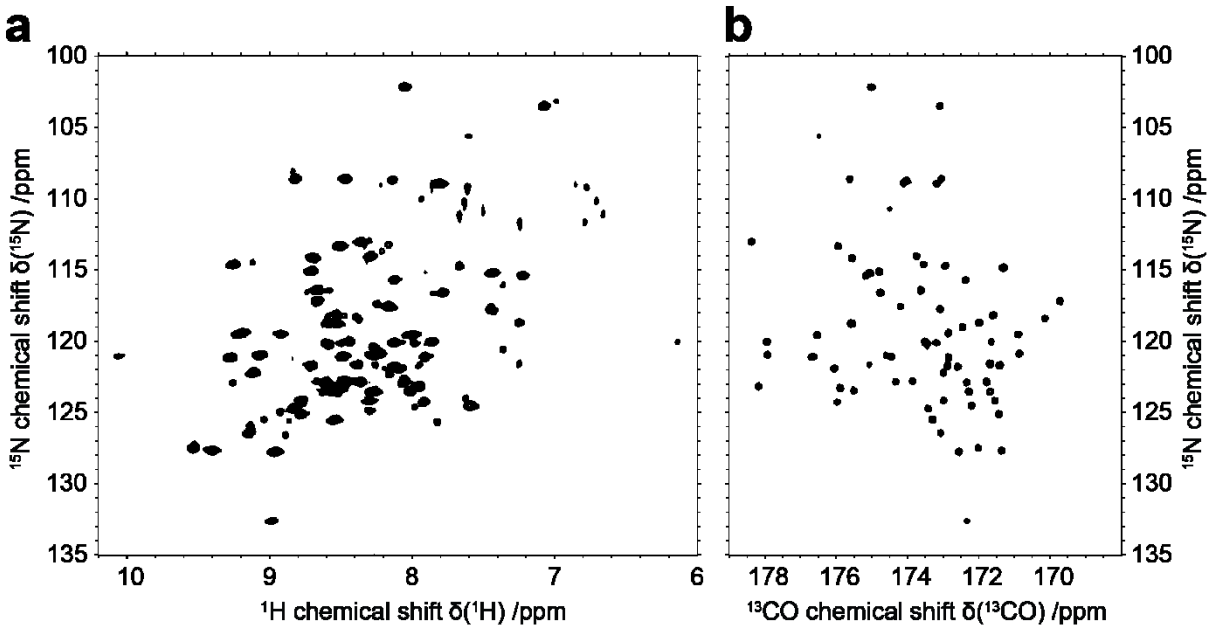

Figure 46. **Description of a unified HSQC/CON experiment.** Interleaved acquisition of a ^{1}H,^{15}N-HSQC (parent) and a ^{13}C,^{15}N-CON (child) following the parallel acquisition setup described in [460, 461, 464] but using a single receiver. **a)** ^{1}H,^{15}N-HSQC; **b)** ^{13}C,^{15}N-CON. Note that in this setup the initial magnetization is split into parent and child leading to reduced measurement times but also lower sensitivity for both spectra (as compared to conventional setup). Data were recorded on a 2 mM U-[^{1}H,^{13}C,^{15}N] Ubiquitin sample at 30°C and 600 MHz. Total acquisition time for the unified acquisition was 32 min.

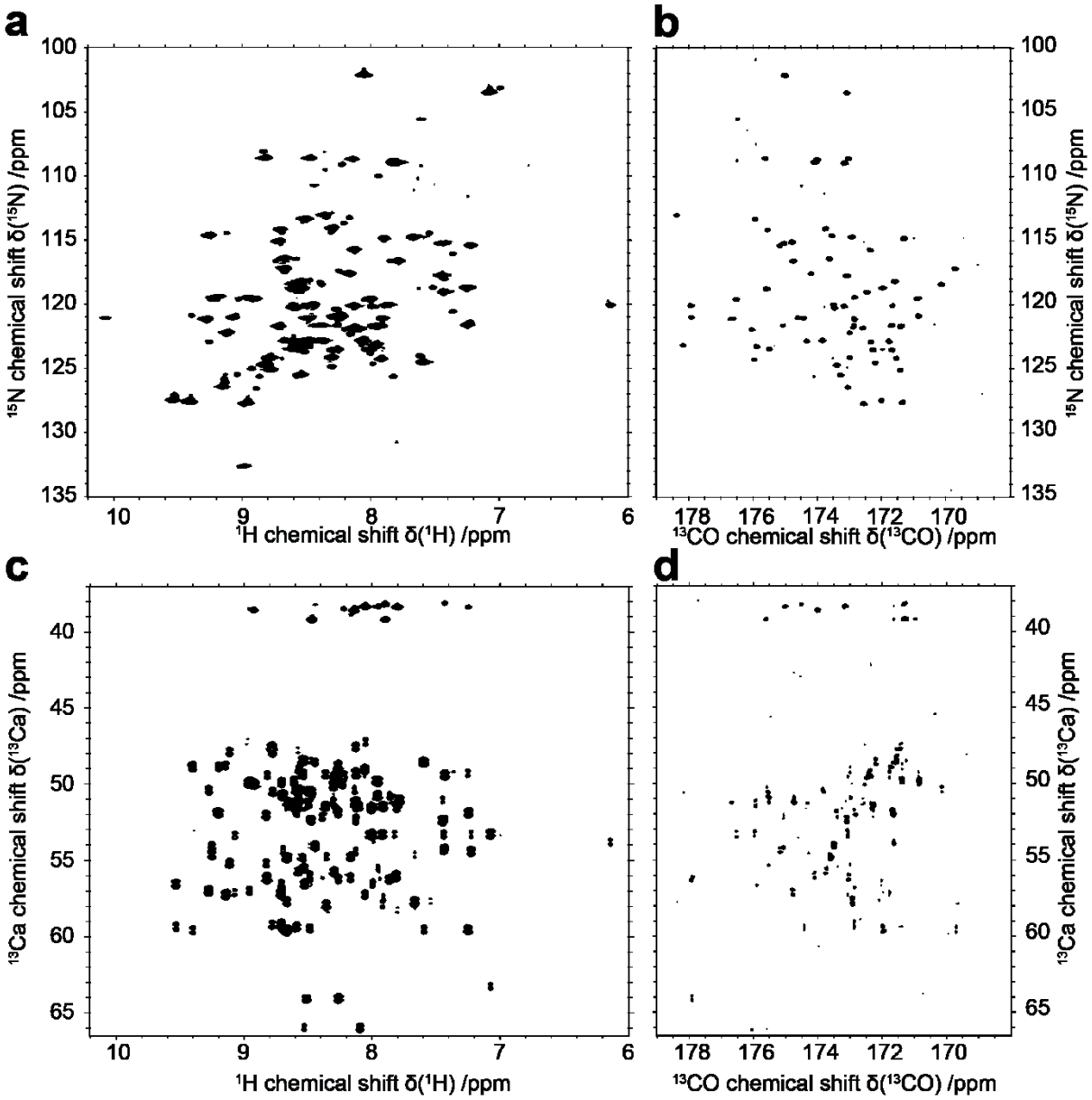

Figure 47. **Description of a HNCA/HNCANCO experiment.** Interleaved acquisition of a 3D ^{1}H,^{15}N-HNCA [549] (parent) and a ^{13}C,^{15}N-HNCANCO [550] (child) following the parallel acquisition setup but using a single receiver. **a)** first ^{1}H,^{15}N-plane (parent); **b)** first ^{13}C,^{15}N-CON (child); **c)** first ^{1}H,^{13}CA plane (parent); **d)** first ^{13}CO,^{13}CA plane (child). Data were recorded on a 2 mM U-[^{1}H,^{13}C,^{15}N] Ubiquitin sample at 30°C and 600 MHz. Total acquisition time for the unified acquisition of both 3Ds was 2h 12 min. Note that in comparison with parallel acquisition setups, in the UTOPIA setup the magnetization of one nuclear species needs to be stored during the acquisition of the other. Depending on sample properties and experimental design this may be feasible with minor or major signal losses. Therefore, if a multi-receiver system is available parallel acquisition should be used, whereas UTOPIA may be useful to translate previously published multi-receiver experiments to single receiver setups without any hardware upgrade. Data were recorded on a 2 mM U-[^{1}H,^{13}C,^{15}N] Ubiquitin sample at 30°C and 600 MHz.

Figure 48. **Bcl-x_L relaxation properties.** Bcl-x_L $^{1}H^{N}$ **(a)** and ^{13}C relaxation data, data for aromatic carbons **(b)**, carbonyls **(c)** and aliphatic carbons **(d)** are shown respectively. See supplemental methods for more details on data acquisition.

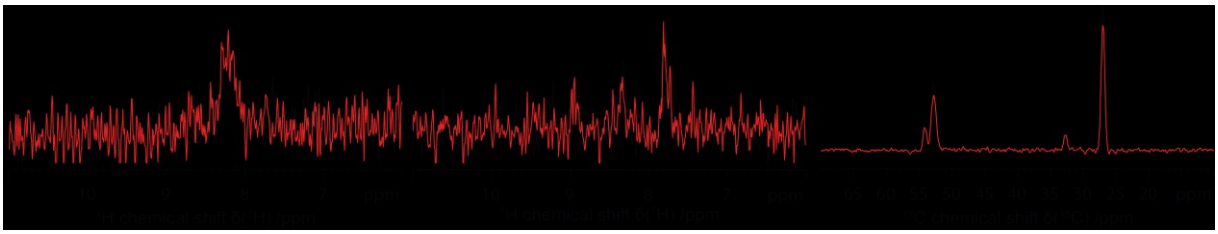

Figure 49. **Sensitivity comparison of conventional and UTOPIA setup.** OmpX in nanodiscs was measured using $^{1}H,^{15}N$-NOESY-TROSY [475] as parent and a $^{13}C,^{13}C$-FLOPSY [476] as child. 1D slices through the HH (NOESY) plane **(a)** and the HN-plane **(b)** of the parent as well as of the CC plane of the child **(c)**. Identical peaks were chosen for conventional (black) and UTOPIA data (red).

Targeted DNP

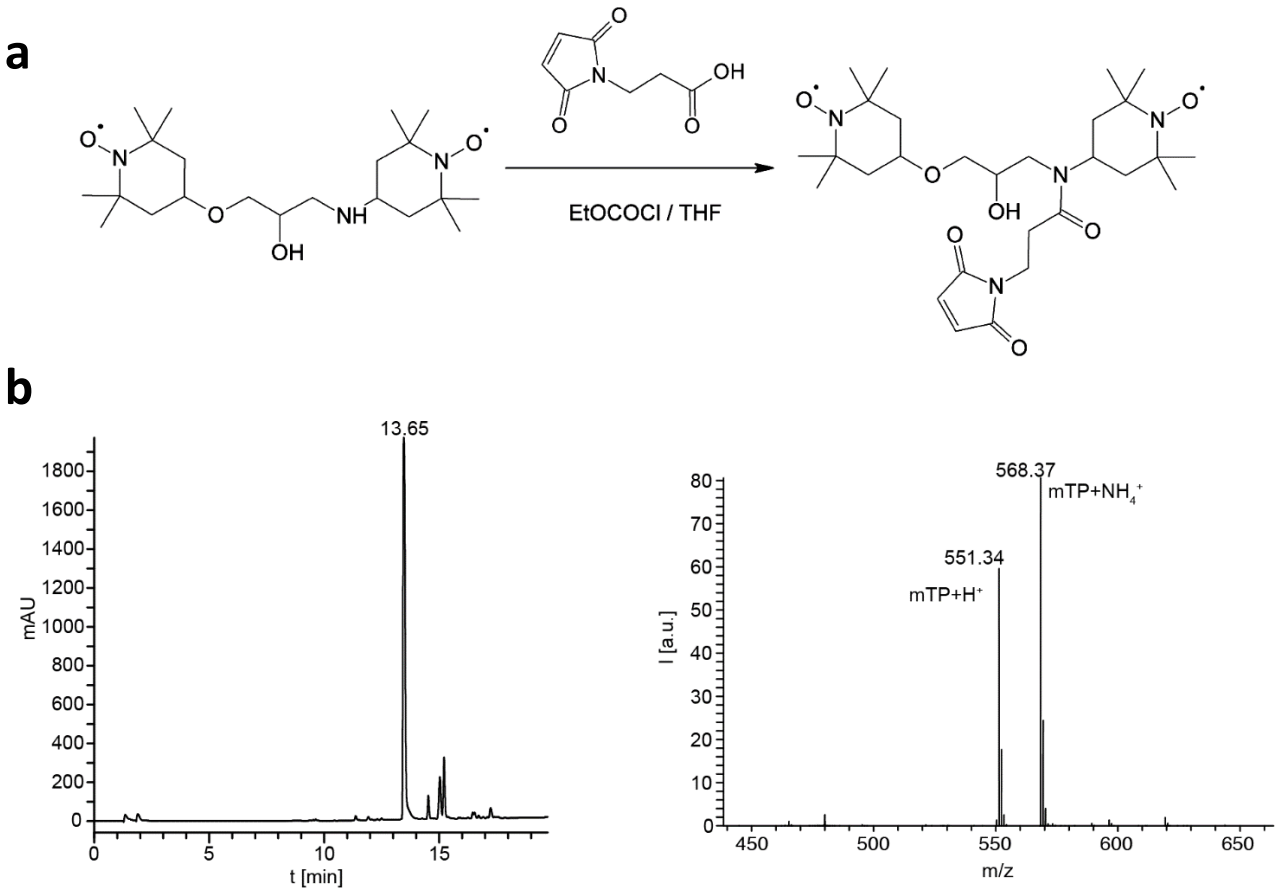

Figure 50. **Synthesis and characterization of mTP. a)** mTP synthesis simplified reaction scheme. **b)** Purity and identity were validated by HPLC/ESI-MS showing the eluting peak in HPLC chromatogram in the left and the corresponding mass spectrum in the right panel. Retention times in minutes [min] and determined masses for charged ions are denoted.

Peptide	Sequence	Molecular formula	MW [g·mol^{-1}]	Calculated [m/z]	Measured [m/z]
Bak	Ac-PEG_2-GQVGRQLAIIGDDINR	$C_{80}H_{139}N_{27}O_{27}$	1911,15	956.6/638.1	956.2/638.1
Bak-C	Ac-C-PEG_2-GQVGRQLAIIGDDINR	$C_{83}H_{144}N_{28}O_{28}S$	2014,29	1008.2/672.4	1007.7/672.3
Bak-mTP	Ac-C(mTP)-PEG_2-GQVGRQLAIIGDDINR	$C_{111}H_{190}N_{32}O_{35}S^{2\bullet}$	2564,99	1283.5/856.0	1283.3/855.7

Table 12. **List of Bak derived peptide constructs** (including mTP ligated cysteinylated) from N- to C-terminus with C-terminal amide including the corresponding sequence, molecular formula, molecular weight (MW; [g·mol^{-1}]), calculated molecular masses [m/z] for charged ions ($[M+2H]^{2+}$/$[M+3H]^{3+}$), and measured masses [m/z] determined by ESI-MS. Amino acids are given in the one-letter code, Ac = acetylation, PEG_2 = 8-amino-3,6-dioxaoctanoyl, mTP = maleimide modified TOTAPOL.

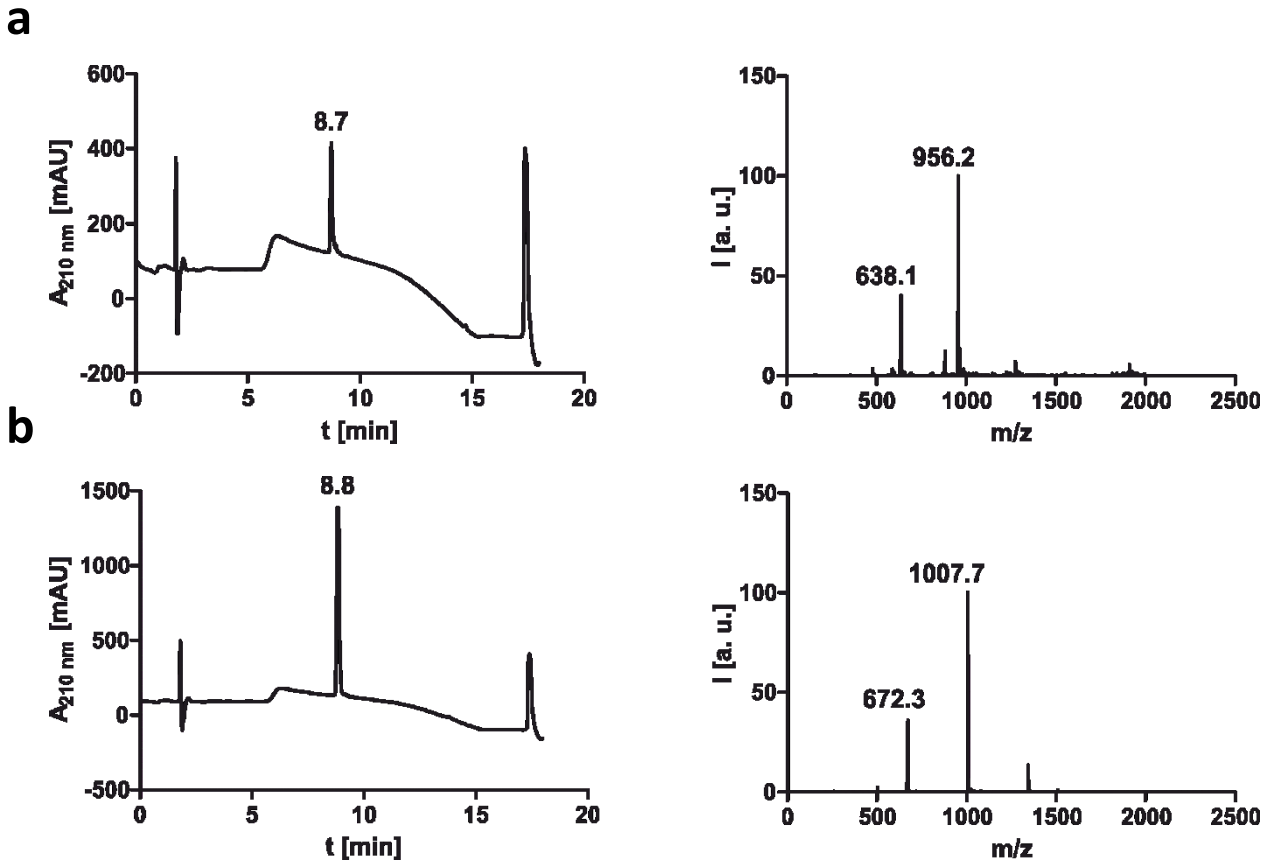

Figure 51. **Analytical data of Bak derived peptides. a)** Bak and **b)** Bak-C. Purity and identity were validated by HPLC/ESI-MS showing the eluting peak in HPLC chromatogram in the left and the corresponding mass spectrum in the right panel. Retention times in minutes [min] and determined masses for charged ions ($[M+2H]^{2+}$ and $[M+3H]^{3+}$) are denoted.

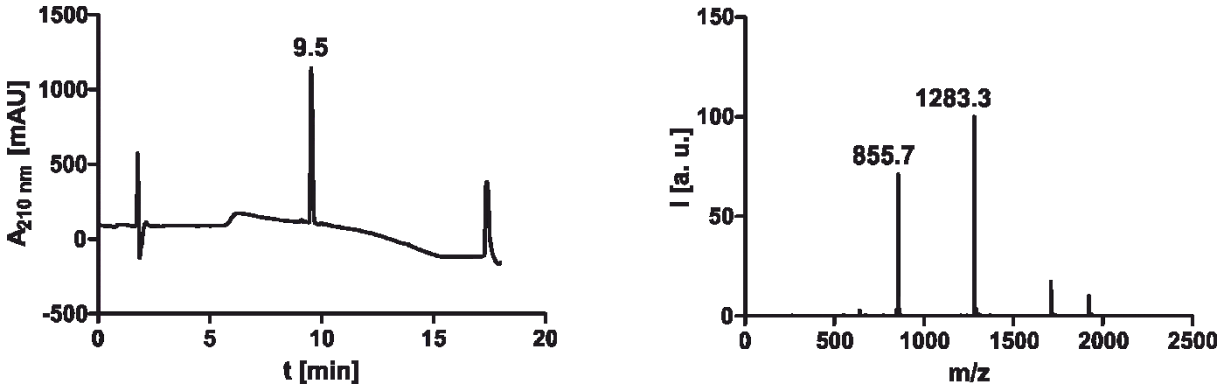

Figure 52. **Analytical data of a N-terminally cystenylated Bak derived peptide with maleimide modified TOTAPOL (Bak-mTP).** Purity and identity were validated by HPLC/ESI-MS showing the eluting peak in HPLC chromatogram in the left and the corresponding mass spectrum in the right panel. Retention times in minutes [min] and determined masses for charged ions ($[M+2H]^{2+}$ and $[M+3H]^{3+}$) are denoted.

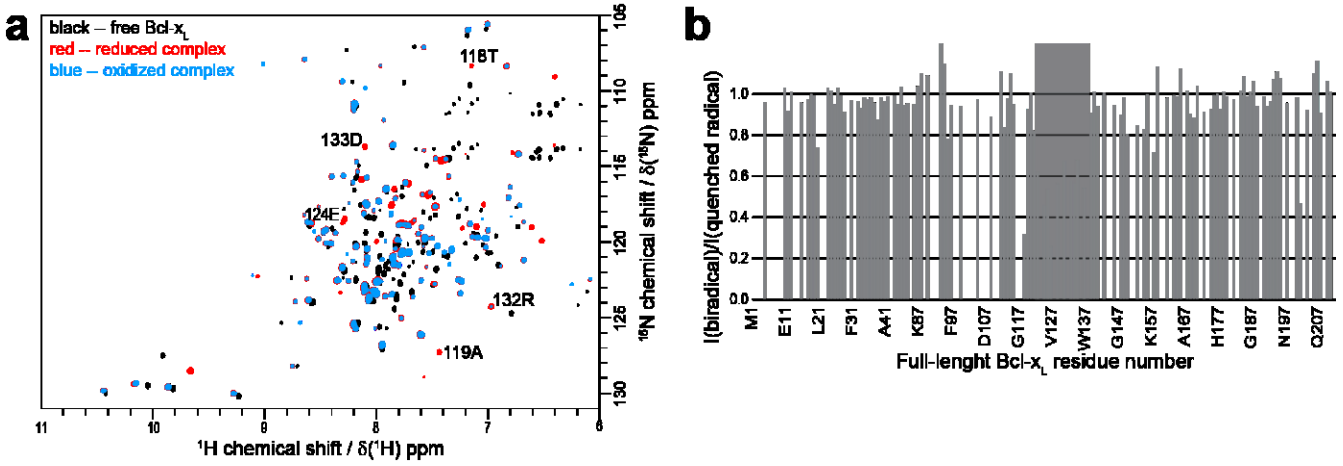

Figure 53. **Solution NMR characterization of the Bcl-xL:Bak-mTP complex. a)** [^{1}H-^{15}N] Transverse Relaxation Optimized – Heteronuclear Single Quantum Correlation (TROSY-HSQC). Free Bcl-xL is shown as reference (black), showing clear chemical shift perturbations upon addition of the Bak-mTP ligand. Spectra of the complex before and after reduction of the radical by ascorbic acid are shown in blue and red respectively. Examples of assigned peaks affected by PREs are shown. **b)** Plot of the ratios of intensities (intact radical / quenched radical) of all resolved peaks. The full sequence of Bcl-xL is shown, not resolved residues appear with a ratio of zero. The region clearly affected by the presence of the radical is highlighted.

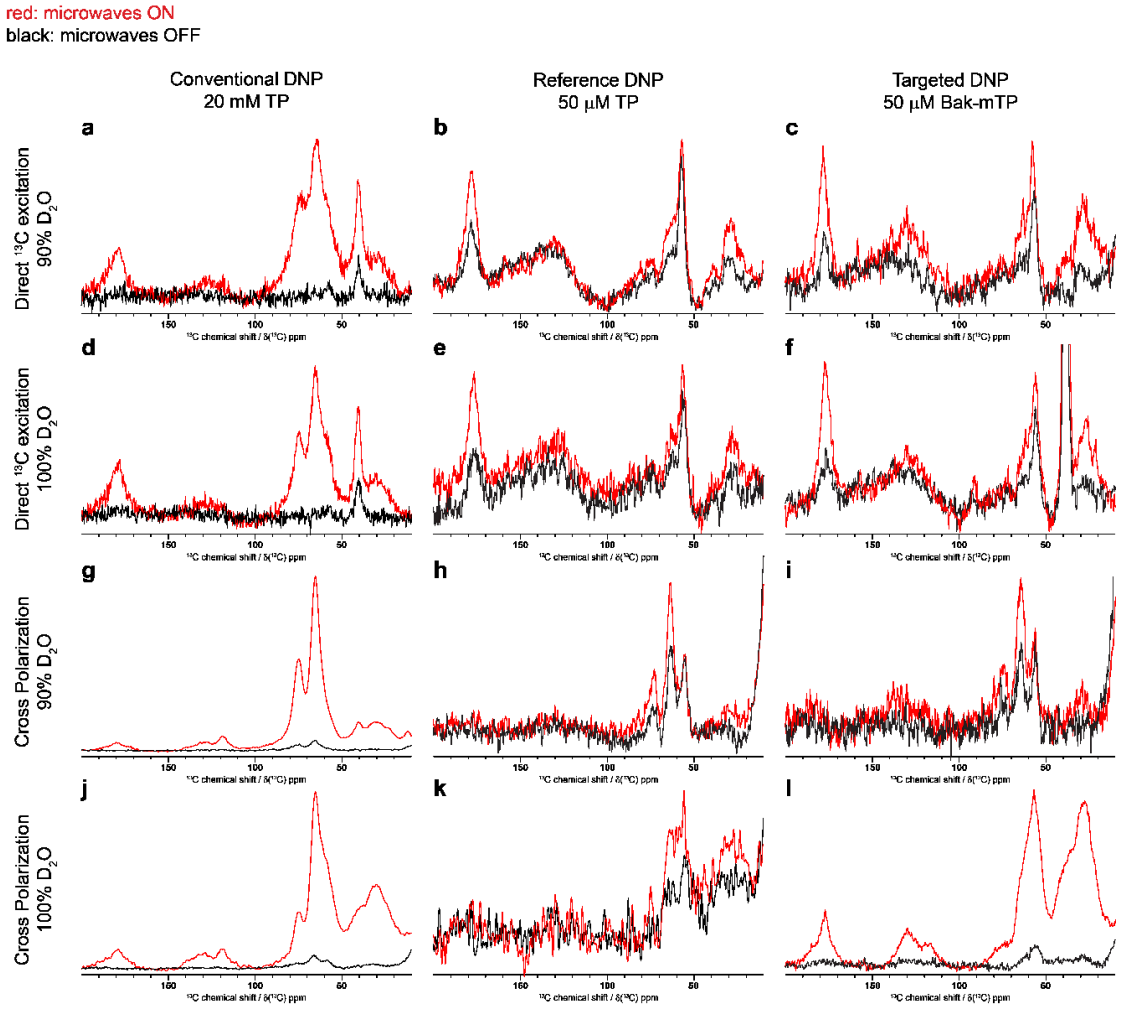

Figure 54. **Optimization of buffer conditions for targeted DNP. a) b) c)** Direct ^{13}C excitation, 90% D_2O, 20 mM TOTAPOL, 50 µM TOTAPOL and 50 µM Bak-mTP respectively. **d) e) f)** Direct ^{13}C excitation, 100% D_2O, 20 mM TOTAPOL, 50 µM TOTAPOL and 50 µM Bak-mTP respectively. **g) h) i)** ^{1}H-^{13}C Cross Polarization, 90% D_2O, 20 mM TOTAPOL, 50 µM TOTAPOL and 50 µM Bak-mTP respectively. **j) k) l)** ^{1}H-^{13}C Cross Polarization, 100% D_2O, 20 mM TOTAPOL, 50 µM TOTAPOL and 50 µM Bak-mTP respectively. The amount of Bcl-xL protein used was 23 µg corresponding to 45 µM and a 1:1 molar ratio of either Bak-mTP or TOTAPOL.

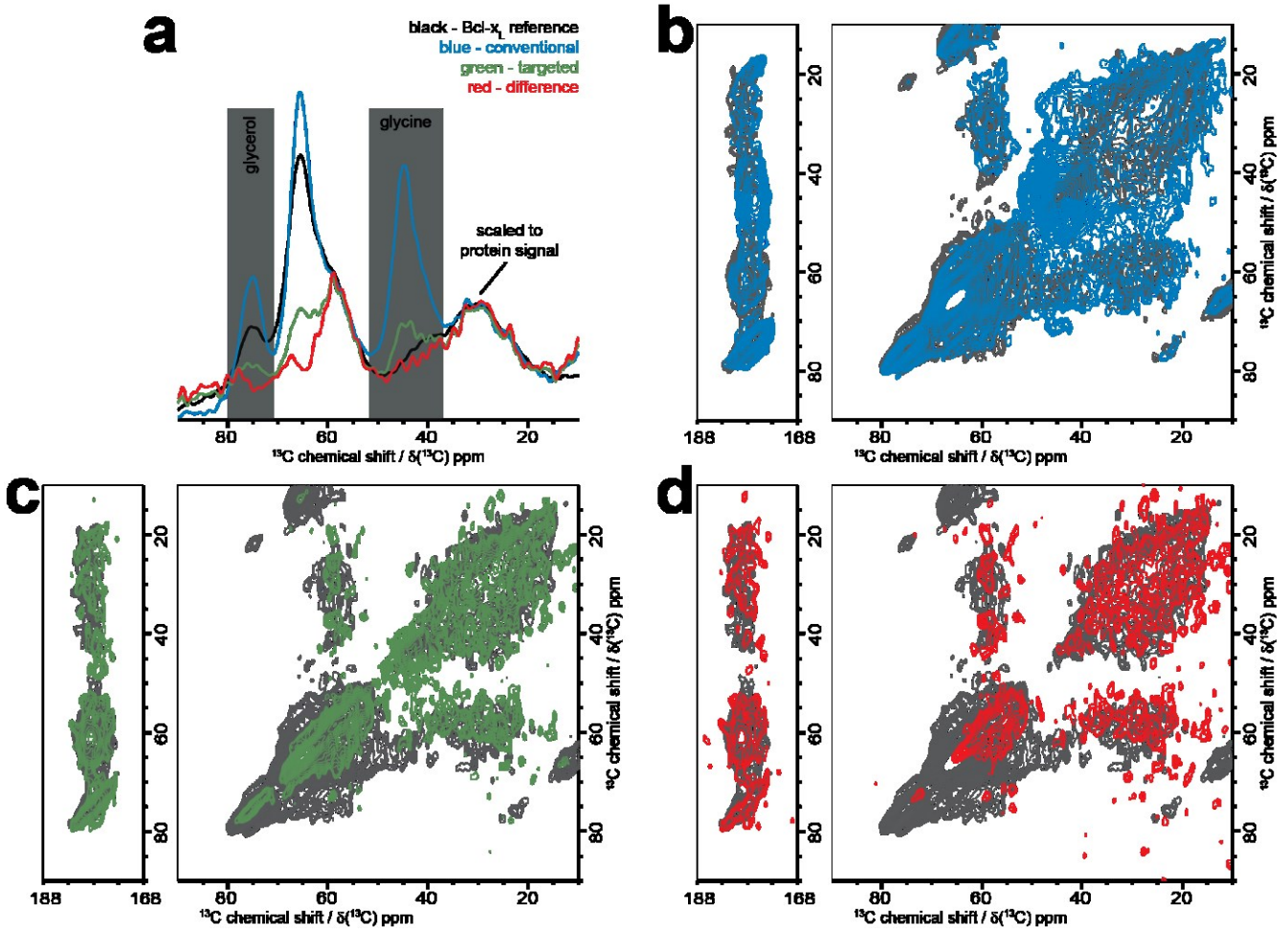

Figure 55. **Targeted DNP is able to selectively enhance a protein over a large background of labeled glycine. a)** ^{1}H-^{13}C cross polarization spectra of reference Bcl-x$_L$ (black), in the presence of a 100-fold excess of glycine using conventional DNP (blue) or targeted DNP (green). The difference spectrum (targeted – conventional; scaled to same glycerol signal) is shown in red. Spectra are scaled to the protein specific carbon signal (around 25 ppm) thus showing the gradual reduction of unwanted signals, i.e. glycine and glycerol. **b)** [^{13}C-^{13}C]-PDSD spectrum using a conventional DNP approach (blue). **c)** PDSD spectrum using the targeted DNP approach (green). **d)** PDSD difference spectrum (targeted – conventional, red)). The reference purified Bcl-x$_L$ spectrum is always overlaid (black).

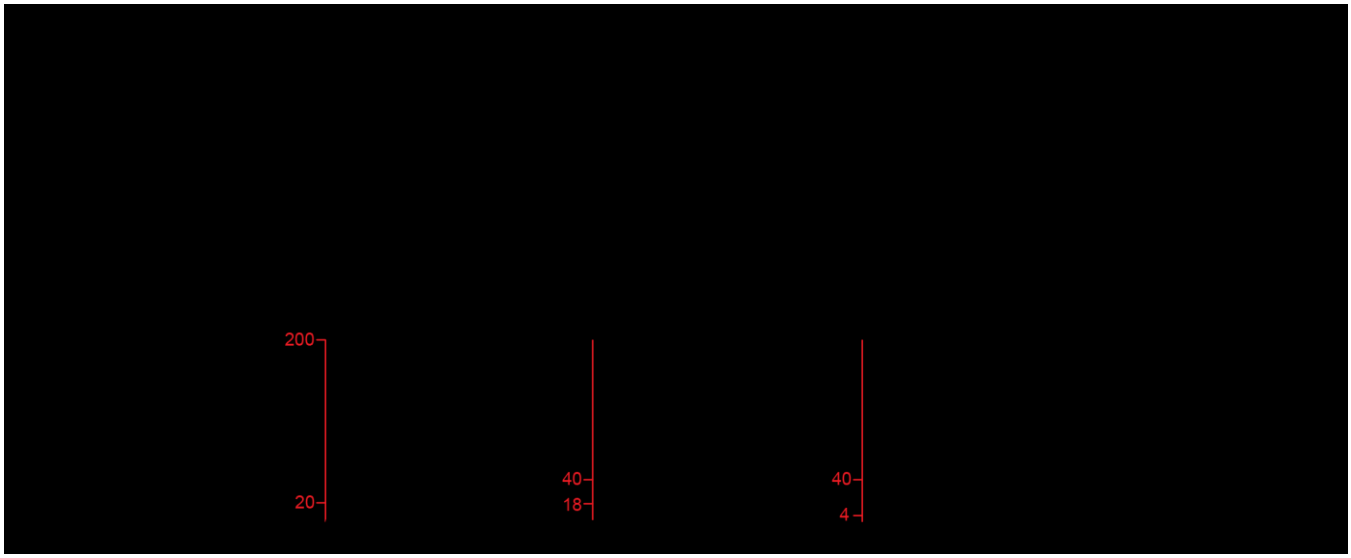

Figure 56. **Schematic visualization of the selectivity that can be obtained with targeted DNP.** Top row gives an example for same signal intensities of background and target. Bottom row gives an example for a target with 10% of the background signal (similar to Bcl-x_L in its lysate). **a)** DNP-off model spectra showing the regular signal levels of either 1:1 (top) or 10:1 (bottom) background-to-target. **b)** Conventional DNP-on model spectra, assuming an enhancement factor of 20. Signal of both background and target are 20-fold higher. **c)** Targeted DNP-on model spectra, assuming a targeted enhancement factor of 18 and an "unselective" enhancement factor of 4 for the background. Comparison of **b)** and **c)** shows an about 5-fold reduction of the background signal in the targeted setup as compared to conventional DNP. **d)** Conventional DNP-on model spectra (same as in **b**) but scaled to the same level of the background signal as present in the targeted DNP-on spectra. Alternatively a DNP-off spectrum (same as in a) but scaled to match the background level) can be used instead of the conventional DNP-on spectrum. In this case a difference spectrum can be obtained with only one sample, however the noise of the non-enhanced spectrum may be a limiting factor. **e)** Resulting difference spectra (targeted DNP-on – scaled spectrum). Using the model spectra the background is completely removed in the difference spectra. Note that the enhancement factors used in the model spectra largely resemble the values found experimentally. Also note that in the difference spectra the residual signal of the target does not depend on the background-to-target ratio. Therefore a general "selective" enhancement factor can be defined as the difference of the total minus the unspecific enhancement factors in the targeted setup. Here this selective enhancement factor has a value of 14. The quality of the difference spectra will largely depend on this value (for real spectra the noise level may also be considered, *vide infra*). It should be pointed out that the difference spectrum relies on a scaling to the same background levels. Due to the good separation of the glycerol signal, it can be used for this purpose, assuming that the glycerol-to-target ratio is identical in the conventional and targeted setup.

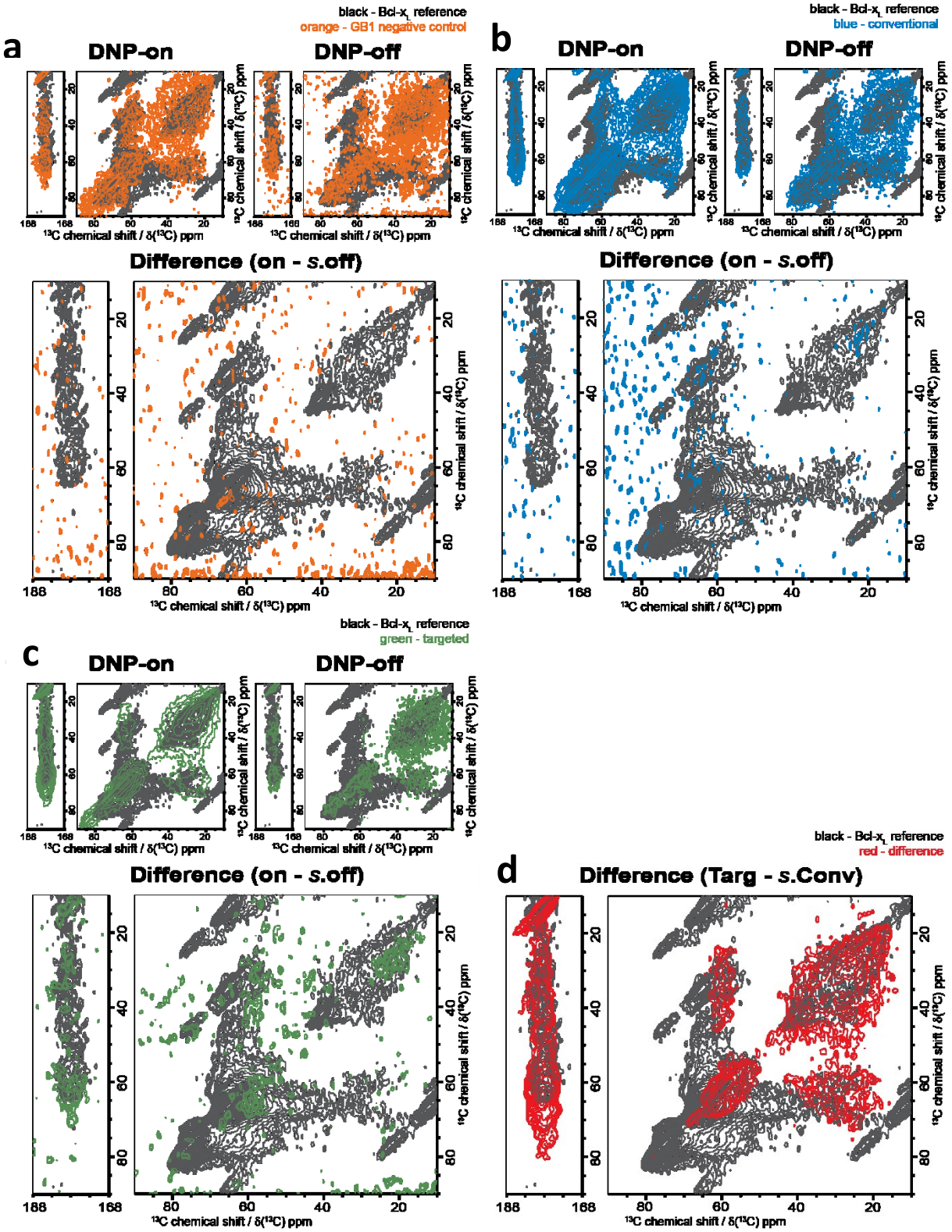

Figure 57. **Aliphatic and carboxyl regions of PDSD spectra obtained on Bcl-xL for characterization of lysate measurements. a)** DNP-on/off and difference [^{13}C-^{13}C]-PDSD spectra of GB1 lysate as a negative control using the targeted DNP approach. **b)** DNP-on/off and difference PDSD spectra of Bcl-x$_L$ lysate using a conventional DNP approach. **c)** DNP-on/off and difference PDSD spectra of Bcl-x$_L$ lysate using the targeted DNP approach. **d)** Difference of targeted DNP – conventional DNP (scaled to same glycerol signal). All spectra are overlaid with the same PDSD spectrum of purified Bcl-x$_L$ (black) as a reference.

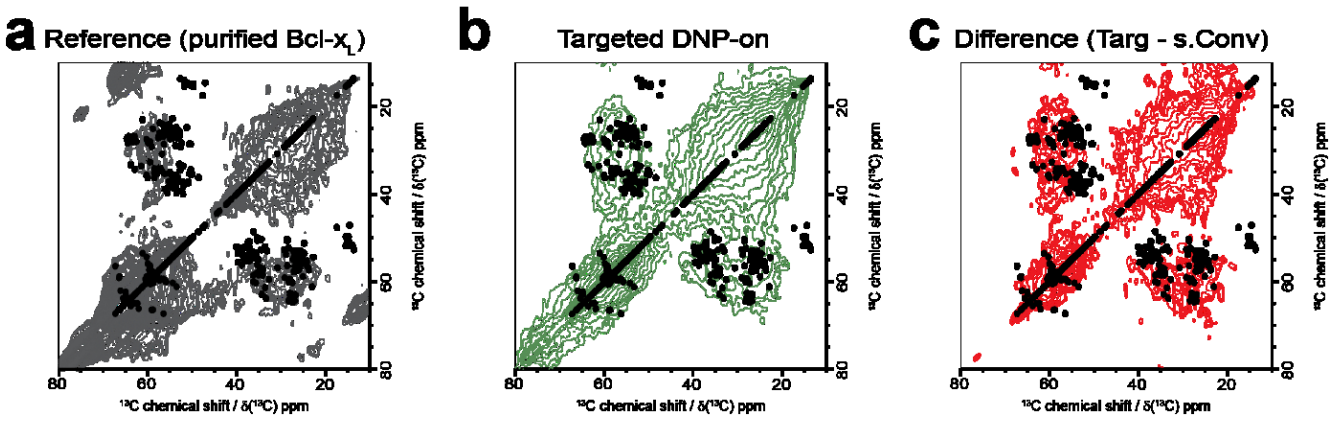

Figure 58. **Comparison of aliphatic region of selected 2D PDSD spectra with predicted peak position. a)** Conventional DNP-on spectrum of purified Bcl-x_L (note that this spectrum slightly differs from the reference spectra in Fig. S14 and the spectra in **b)** and **c)**, due to a different spectral width in the indirect dimension). **b)** Targeted DNP-on spectrum of Bcl-x_L in its lysate (same as in Fig. S14c). **c)** Difference spectrum (targeted – scaled conventional) of Bcl-x_L in its lysate (same as in Fig. S14d). All spectra are overlaid with a prediction based on Bcl-x_L Cα and Cβ solution NMR assignments (black circles).

Modulation of αS aggregation by nanodiscs

αS type	pH	MSP type	Lipids in ND	αS-to-ND ratio
acetylated	5.3	-	-	-
	7.4	D1	100% DMPC	2:1
			25% POPG – 75% DMPC	
			50% POPG – 50% DMPC	1:1
				2:1
				4:1
				8:1
				16:1
			75% POPG – 25% DMPC	2:1
		Δ5		
		D1	100% POPG	1:2
				1:1
				2:1
	5.3			2:1
				4:1
				8:1
				16:1
			100% POPC	2:1
			50% POPG – 50% POPC	
			50% DMPG – 50% POPC	
			50% DMPG – 50% DMPC	
			100% DMPG	
	5.3			
non-acetylated	7.4	-	-	-
		D1	100% DMPC	2:1
			25% POPG – 75% DMPC	
			50% POPG – 50% DMPC	1:1
				2:1
				4:1
				8:1
				16:1
				32:1
			75% POPG – 25% DMPC	2:1
			100% POPG	1:1
				2:1
				4:1
				8:1
				16:1
				32:1

Table 13. **Summary of the NMR samples used in the study.** [^{15}N-^{1}H]-TROSY-HSQC spectra of 50 µM αS with different acetylation states and buffer conditions (pH) and in the presence of various amounts of nanodiscs of different lipid contents (negative charge and hydrocarbon chain, their melting phase transition is given) and sizes (different membrane scaffold protein constructs) were measured. In total 41 different samples were produced during the study.

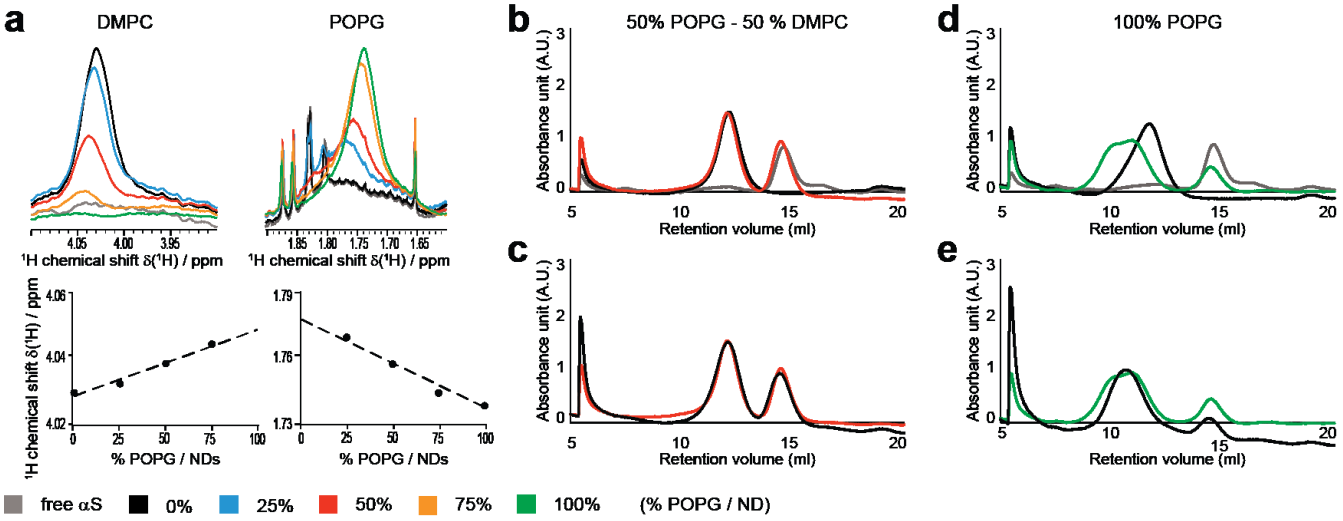

Figure 59. **NDs accurately report on lipid mixtures and are stable upon αS association.** NMR ^{1}H 1Ds of αS in the presence of NDs containing different POPG-to-DMPC ratios are shown in (**a**) corresponding to the same samples as in Figure 28a-b. Chemical shifts ranges reporting on either DMPC (left. choline methyl groups) or POPG (right, ^{1}H 9 and 10 next to the unsaturation) are displayed. The volumes of the peaks are in a range of 10% around the aimed composition of lipids. Significant chemical shifts perturbations of both lipids are visible and follow a rather linear dependence on the composition, pointing to the presence and mixing of both lipid types in single nanodiscs. SEC profiles of αS (grey), 50% POPG NDs (black) and the complex (red) are shown in (**b**). No co-elution of αS with nanodiscs points out to a fast kinetic exchange between free and bound αS. SEC profiles before (red) and after (black) being incubated 24 h at room temperature are shown in (**c**). The integrity of NDs after αS association is conserved, proving their stability. The complex between αS and 100% POPG NDs (**d**, green) however co-elutes thus proving tight interaction. In that case also the integrity of nanodiscs is conserved after 24 h at room temperature (**e**, green vs. black).

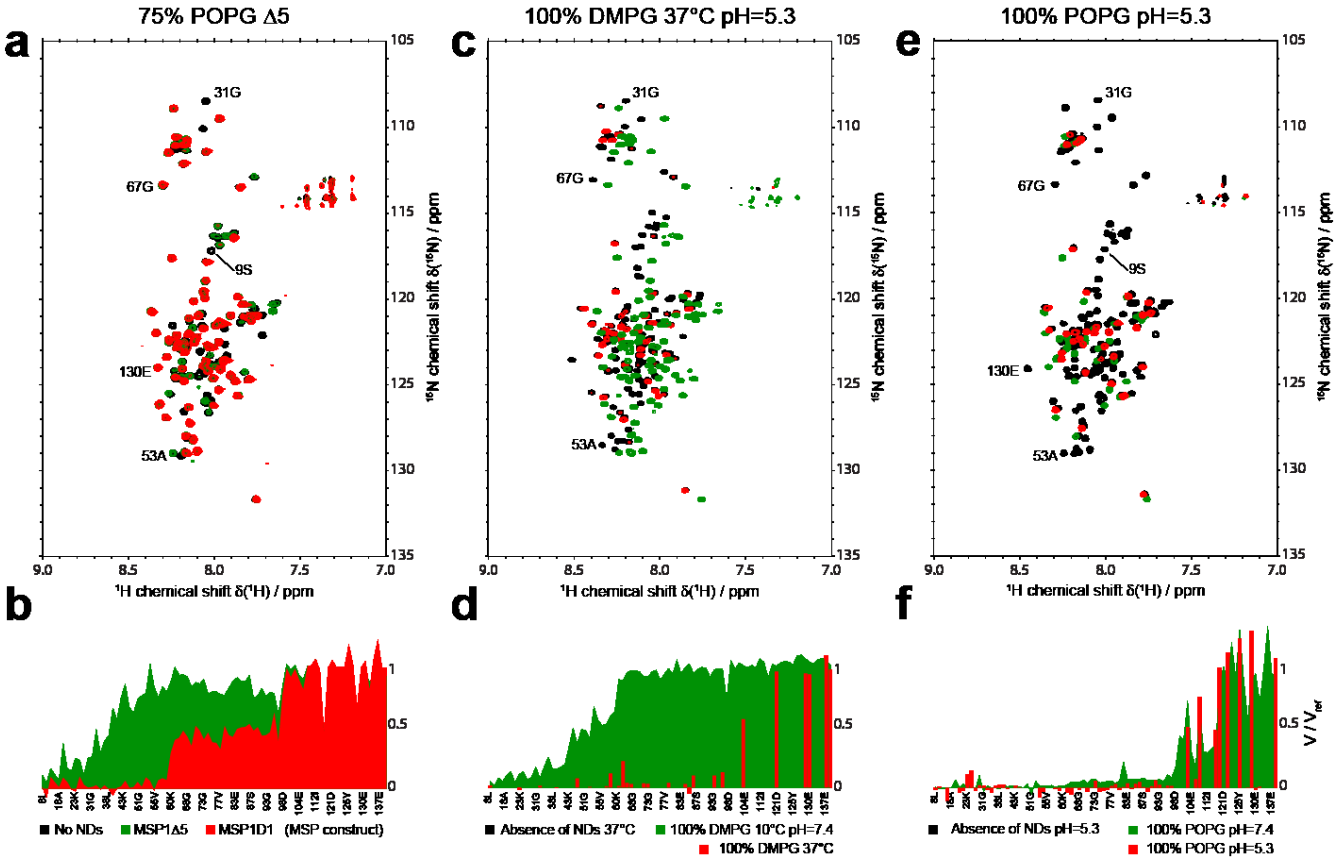

Figure 60. **αS binds to high negative charge content NDs in different conditions.** NMR spectra of [^{15}N]-acetylated-αS (50 µM) in the absence or in the presence of 25 µM NDs with 75% POPG content, assembled using the regular MSP1D1 construct (green) or with the smaller MSP1ΔH5 (red) are shown in (a) and the respective attenuation profiles in (b). Spectra (c) and attenuation profiles (d) corresponding to the binding of αS to NDs containing 100% DMPG lipids in their gel state (10°C, green) or their fluid state (37°C, red). Higher temperature leading to dramatic chemical exchange broadening, the 37°C experiment was done at pH=5.3 where binding is known to occur (see (e) and (f)). Unambiguously transferable assignments show that the full binding region (residues 1-96) is recovered as expected from 100% negatively charged NDs for DMPG in the fluid phase. Spectra (e) and attenuation profiles (f) corresponding to the binding of αS to NDs containing 100% POPG lipids at pH=7.4 (green) and pH=5.3 (red). Unambiguously transferable assignments show that no significant difference in binding mode is visible upon pH variation. Chosen assignments corresponding to parts of the sequence differently affected by the binding modes are shown. Reference spectra of the free αS are shown in black.

NMR characterization of Barttin in detergents and nanodiscs

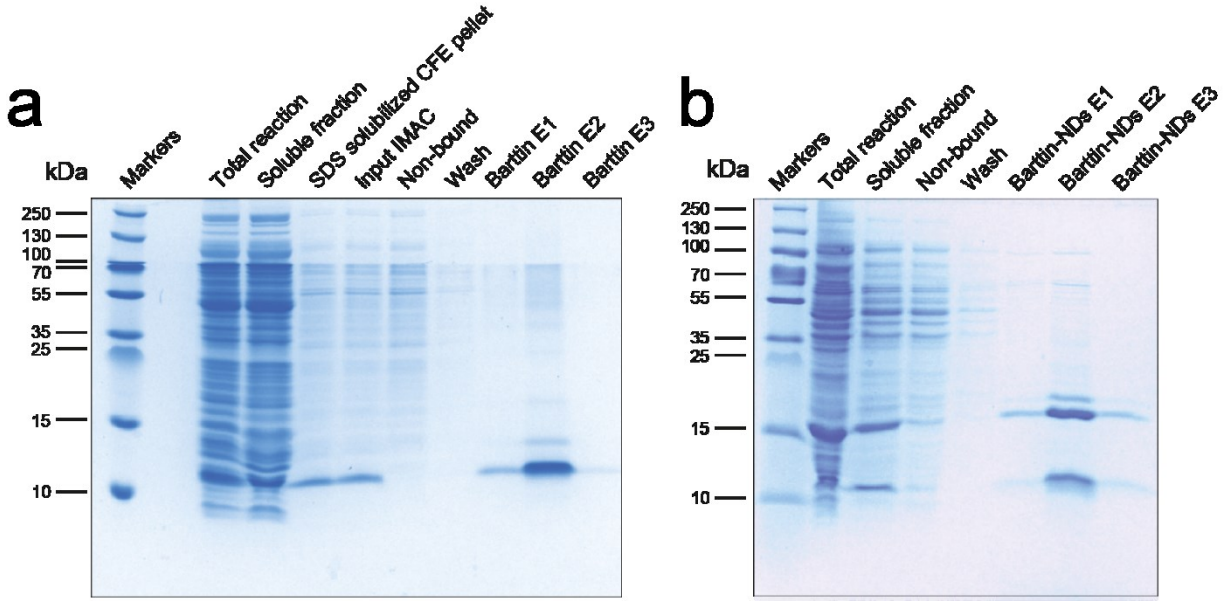

Figure 61. **Refolding vs. co-translational incorporation of Barttin into NDs**. **a)** Coomassie blue-stained SDS-PAGE of CFE expressed Barttin (total reaction), soluble fraction of the reaction, solubilized CFE pellet, input for IMAC purification in SDS, non-bound fraction, washing fraction and three elution fractions of SDS-purified Barttin (full gel of Fig. X). **b)** Coomassie blue-stained SDS-PAGE of CFE expressed Barttin in the presence of DMPC Δ5 NDs (total reaction), soluble fraction of the reaction,, input for IMAC purification, non-bound fraction, washing fraction and three elution fractions of Barttin-NDs (full gel of Fig. X).

BIBLIOGRAPHY

Bilbiography

1. Shi, Y., *A glimpse of structural biology through X-ray crystallography.* Cell, 2014. **159**(5): p. 995-1014.
2. Fernandez-Leiro, R. and S.H. Scheres, *Unravelling biological macromolecules with cryo-electron microscopy.* Nature, 2016. **537**(7620): p. 339-46.
3. Bai, X.C., et al., *An atomic structure of human gamma-secretase.* Nature, 2015. **525**(7568): p. 212-7.
4. Anfinsen, C.B., *Principles that Govern the Folding of Protein Chains.* Science, 1973. **181**(4096): p. 223-230.
5. Foster, M.P., C.A. McElroy, and C.D. Amero, *Solution NMR of large molecules and assemblies.* Biochemistry, 2007. **46**(2): p. 331-40.
6. Mainz, A., et al., *NMR spectroscopy of soluble protein complexes at one mega-dalton and beyond.* Angew Chem Int Ed Engl, 2013. **52**(33): p. 8746-51.
7. Wallin, E. and G. von Heijne, *Genome-wide analysis of integral membrane proteins from eubacterial, archaean, and eukaryotic organisms.* Protein Sci, 1998. **7**(4): p. 1029-38.
8. Kang, C. and Q. Li, *Solution NMR study of integral membrane proteins.* Curr Opin Chem Biol, 2011. **15**(4): p. 560-9.
9. Rovnyak, D., et al., *Resolution and sensitivity of high field nuclear magnetic resonance spectroscopy.* J Biomol NMR, 2004. **30**(1): p. 1-10.
10. Karplus, M., *Vicinal Proton Coupling in Nuclear Magnetic Resonance.* Journal of the American Chemical Society, 1963. **85**(18): p. 2870-2871.
11. Morris, G.A. and R. Freeman, *Enhancement of Nuclear Magnetic-Resonance Signals by Polarization Transfer.* Journal of the American Chemical Society, 1979. **101**(3): p. 760-762.
12. Overhauser, A.W., *Polarization of Nuclei in Metals.* Physical Review, 1953. **92**(2): p. 411-415.
13. Overhauser, A.W., *Paramagnetic Relaxation in Metals.* Physical Review, 1953. **89**(4): p. 689-700.
14. Solomon, I., *Relaxation Processes in a System of Two Spins.* Physical Review, 1955. **99**(2): p. 559-565.
15. Aue, W.P., E. Bartholdi, and R.R. Ernst, *Two-dimensional spectroscopy. Application to nuclear magnetic resonance.* The Journal of Chemical Physics, 1976. **64**(5): p. 2229.
16. Braunschweiler, L. and R.R. Ernst, *Coherence transfer by isotropic mixing: Application to proton correlation spectroscopy.* Journal of Magnetic Resonance (1969), 1983. **53**(3): p. 521-528.
17. Wuthrich, K., *NMR studies of structure and function of biological macromolecules (Nobel lecture).* Angew Chem Int Ed Engl, 2003. **42**(29): p. 3340-63.
18. Eletsky, A., *A novel strategy for the assignment of side-chain resonances in completely deuterated large proteins using 13C spectroscopy.* Journal of Biomolecular NMR, 2003. **26**(2): p. 167-179.
19. Bodenhausen, G. and D.J. Ruben, *Natural abundance nitrogen-15 NMR by enhanced heteronuclear spectroscopy.* Chemical Physics Letters, 1980. **69**(1): p. 185-189.
20. Takeuchi, K., et al., *Nitrogen-detected TROSY yields comparable sensitivity to proton-detected TROSY for non-deuterated, large proteins under physiological salt conditions.* J Biomol NMR, 2016. **64**(2): p. 143-51.
21. Bermel, W., et al., *Complete assignment of heteronuclear protein resonances by protonless NMR spectroscopy.* Angew Chem Int Ed Engl, 2005. **44**(20): p. 3089-92.
22. Kay, L.E., et al., *Three-dimensional triple-resonance NMR spectroscopy of isotopically enriched proteins.* Journal of Magnetic Resonance (1969), 1990. **89**(3): p. 496-514.
23. Clubb, R.T., V. Thanabal, and G. Wagner, *A constant-time three-dimensional triple-resonance pulse scheme to correlate intraresidue 1HN, 15N, and 13C' chemical shifts in 15N□13C-labelled proteins.* Journal of Magnetic Resonance (1969), 1992. **97**(1): p. 213-217.
24. Bax, A. and M. Ikura, *An efficient 3D NMR technique for correlating the proton and15N backbone amide resonances with the α-carbon of the preceding residue in uniformly15N/13C enriched proteins.* Journal of Biomolecular NMR, 1991. **1**(1): p. 99-104.
25. Grzesiek, S. and A. Bax, *An efficient experiment for sequential backbone assignment of medium-sized isotopically enriched proteins.* Journal of Magnetic Resonance (1969), 1992. **99**(1): p. 201-207.
26. Hiller, S., et al., *Sequence-specific resonance assignment of soluble nonglobular proteins by 7D APSY-NMR spectroscopy.* J Am Chem Soc, 2007. **129**(35): p. 10823-8.
27. Wuthrich, K., *The second decade--into the third millenium.* Nat Struct Biol, 1998. **5 Suppl**: p. 492-5.
28. Murray, V., et al., *A novel bacterial expression method with optimized parameters for very high yield production of triple-labeled proteins.* Methods Mol Biol, 2012. **831**: p. 1-18.
29. Lipsitz, R.S. and N. Tjandra, *Residual dipolar couplings in NMR structure analysis.* Annu Rev Biophys Biomol Struct, 2004. **33**: p. 387-413.
30. Tugarinov, V., V. Kanelis, and L.E. Kay, *Isotope labeling strategies for the study of high-molecular-weight proteins by solution NMR spectroscopy.* Nat Protoc, 2006. **1**(2): p. 749-54.
31. Tugarinov, V., et al., *Cross-correlated relaxation enhanced 1H[bond]13C NMR spectroscopy of methyl groups in very high molecular weight proteins and protein complexes.* J Am Chem Soc, 2003. **125**(34): p. 10420-8.
32. Pervushin, K., et al., *Attenuated T2 relaxation by mutual cancellation of dipole-dipole coupling and chemical shift anisotropy indicates an avenue to NMR structures of very large biological macromolecules in solution.* Proceedings of the National Academy of Sciences, 1997. **94**(23): p. 12366-12371.
33. Takeuchi, K., H. Arthanari, and G. Wagner, *Perspective: revisiting the field dependence of TROSY sensitivity.* J Biomol NMR, 2016.
34. Salzmann, M., et al., *TROSY-type Triple-Resonance Experiments for Sequential NMR Assignments of Large Proteins.* Journal of the American Chemical Society, 1999. **121**(4): p. 844-848.
35. Griffith, O.H. and H.M. McConnell, *A nitroxide-maleimide spin label.* Proc Natl Acad Sci U S A, 1966. **55**(1): p. 8-11.

36. Kosen, P.A., *Spin labeling of proteins.* Methods Enzymol, 1989. **177**: p. 86-121.
37. Bloembergen, N., E.M. Purcell, and R.V. Pound, *Nuclear Magnetic Relaxation.* Nature, 1947. **160**(4066): p. 475-476.
38. Clore, G.M. and J. Iwahara, *Theory, Practice, and Applications of Paramagnetic Relaxation Enhancement for the Characterization of Transient Low-Population States of Biological Macromolecules and Their Complexes.* Chemical Reviews, 2009. **109**(9): p. 4108-4139.
39. Gillespie, J.R. and D. Shortle, *Characterization of long-range structure in the denatured state of staphylococcal nuclease. I. Paramagnetic relaxation enhancement by nitroxide spin labels.* J Mol Biol, 1997. **268**(1): p. 158-69.
40. Gillespie, J.R. and D. Shortle, *Characterization of long-range structure in the denatured state of staphylococcal nuclease. II. Distance restraints from paramagnetic relaxation and calculation of an ensemble of structures.* J Mol Biol, 1997. **268**(1): p. 170-84.
41. Battiste, J.L. and G. Wagner, *Utilization of site-directed spin labeling and high-resolution heteronuclear nuclear magnetic resonance for global fold determination of large proteins with limited nuclear overhauser effect data.* Biochemistry, 2000. **39**(18): p. 5355-65.
42. Jeschke, G., *Conformational dynamics and distribution of nitroxide spin labels.* Prog Nucl Magn Reson Spectrosc, 2013. **72**: p. 42-60.
43. Fawzi, N.L., et al., *A rigid disulfide-linked nitroxide side chain simplifies the quantitative analysis of PRE data.* J Biomol NMR, 2011. **51**(1-2): p. 105-14.
44. Buffy, J.J., et al., *Solid-state NMR investigation of the depth of insertion of protegrin-1 in lipid bilayers using paramagnetic Mn2+.* Biophysical Journal, 2003. **85**(4): p. 2363-2373.
45. Niccolai, N., et al., *Hot spot mapping of protein surfaces with TEMPOL: Bovine pancreatic RNase A as a model system.* Biochim Biophys Acta, 2016. **1865**(2): p. 201-207.
46. Kemmerer, S., J.C. Voss, and R. Faller, *Molecular dynamics simulation of dipalmitoylphosphatidylcholine modified with a MTSL nitroxide spin label in a lipid membrane.* Biochim Biophys Acta, 2013. **1828**(11): p. 2770-7.
47. Yao, Y., et al., *Characterization of the membrane-inserted C-terminus of cytoprotective BCL-XL.* Protein Expr Purif, 2016. **122**: p. 56-63.
48. Rovo, P., et al., *Proton Transverse Relaxation as a Sensitive Probe for Structure Determination in Solid Proteins.* Chemphyschem, 2015. **16**(18): p. 3791-6.
49. Linser, R., et al., *Sensitivity enhancement using paramagnetic relaxation in MAS solid-state NMR of perdeuterated proteins.* J Magn Reson, 2007. **189**(2): p. 209-16.
50. Wickramasinghe, N.P., et al., *Nanomole-scale protein solid-state NMR by breaking intrinsic 1HT1 boundaries.* Nat Methods, 2009. **6**(3): p. 215-8.
51. Pintacuda, G., et al., *NMR structure determination of protein-ligand complexes by lanthanide labeling.* Acc Chem Res, 2007. **40**(3): p. 206-12.
52. Andrew, E.R., A. Bradbury, and R.G. Eades, *Removal of Dipolar Broadening of Nuclear Magnetic Resonance Spectra of Solids by Specimen Rotation.* Nature, 1959. **183**(4678): p. 1802-1803.
53. Lowe, I.J., *Free Induction Decays of Rotating Solids.* Physical Review Letters, 1959. **2**(7): p. 285-287.
54. Bockmann, A., M. Ernst, and B.H. Meier, *Spinning proteins, the faster, the better?* J Magn Reson, 2015. **253**: p. 71-9.
55. Szeverenyi, N.M., M.J. Sullivan, and G.E. Maciel, *Observation of spin exchange by two-dimensional fourier transform 13C cross polarization-magic-angle spinning.* Journal of Magnetic Resonance (1969), 1982. **47**(3): p. 462-475.
56. Hartmann, S.R. and E.L. Hahn, *Nuclear Double Resonance in the Rotating Frame.* Physical Review, 1962. **128**(5): p. 2042-2053.
57. Bloembergen, N., *On the Interaction of Nuclear Spins in a Crystalline Lattice.* Physica, 1949. **15**(3-4): p. 386-426.
58. Ardenkjaer-Larsen, J.H., et al., *Facing and Overcoming Sensitivity Challenges in Biomolecular NMR Spectroscopy.* Angew Chem Int Ed Engl, 2015. **54**(32): p. 9162-85.
59. Ni, Q.Z., et al., *High Frequency Dynamic Nuclear Polarization.* Accounts of Chemical Research, 2013. **46**(9): p. 1933-1941.
60. Carver, T.R. and C.P. Slichter, *Polarization of Nuclear Spins in Metals.* Physical Review, 1953. **92**(1): p. 212-213.
61. Carver, T.R. and C.P. Slichter, *Experimental Verification of the Overhauser Nuclear Polarization Effect.* Physical Review, 1956. **102**(4): p. 975-980.
62. Gerfen, G.J., et al., *High frequency (140 GHz) dynamic nuclear polarization: Polarization transfer to a solute in frozen aqueous solution.* The Journal of Chemical Physics, 1995. **102**(24): p. 9494.
63. Hall, D.A., *Polarization-Enhanced NMR Spectroscopy of Biomolecules in Frozen Solution.* Science, 1997. **276**(5314): p. 930-932.
64. Rosay, M., et al., *Sensitivity-enhanced NMR of biological solids: dynamic nuclear polarization of Y21M fd bacteriophage and purple membrane.* J Am Chem Soc, 2001. **123**(5): p. 1010-1.
65. Rosay, M., et al., *Two-dimensional (13)C-(13)C correlation spectroscopy with magic angle spinning and dynamic nuclear polarization.* J Am Chem Soc, 2002. **124**(13): p. 3214-5.
66. Rosay, M., et al., *High-frequency dynamic nuclear polarization in MAS spectra of membrane and soluble proteins.* J Am Chem Soc, 2003. **125**(45): p. 13626-7.
67. Hu, K.N., et al., *High-frequency dynamic nuclear polarization using biradicals: a multifrequency EPR lineshape analysis.* J Chem Phys, 2008. **128**(5): p. 052302.
68. Akbey, U., et al., *Dynamic nuclear polarization enhanced NMR in the solid-state.* Top Curr Chem, 2013. **338**: p. 181-228.
69. Rosay, M., M. Blank, and F. Engelke, *Instrumentation for solid-state dynamic nuclear polarization with magic angle spinning NMR.* J Magn Reson, 2016. **264**: p. 88-98.
70. Thurber, K.R., et al., *Solid state nuclear magnetic resonance with magic-angle spinning and dynamic nuclear polarization below 25K.* Journal of Magnetic Resonance, 2013. **226**: p. 100-106.
71. Barnes, A.B., et al., *A 250 GHz gyrotron with a 3 GHz tuning bandwidth for dynamic nuclear polarization.* J Magn Reson, 2012. **221**: p. 147-53.

72. Barnes, A.B., et al., *Dynamic nuclear polarization at 700MHz/460GHz.* Journal of Magnetic Resonance, 2012. **224**: p. 1-7.
73. Maly, T., et al., *Dynamic nuclear polarization at high magnetic fields.* The Journal of Chemical Physics, 2008. **128**(5): p. 052211.
74. Ravera, E., C. Luchinat, and G. Parigi, *Basic facts and perspectives of Overhauser DNP NMR.* J Magn Reson, 2016. **264**: p. 78-87.
75. Can, T.V., et al., *Overhauser effects in insulating solids.* J Chem Phys, 2014. **141**(6): p. 064202.
76. Haze, O., et al., *Water-soluble narrow-line radicals for dynamic nuclear polarization.* J Am Chem Soc, 2012. **134**(35): p. 14287-90.
77. Jeffries, C.D., *Polarization of Nuclei by Resonance Saturation in Paramagnetic Crystals.* Physical Review, 1957. **106**(1): p. 164-165.
78. Smith, A.A., et al., *Solid effect dynamic nuclear polarization and polarization pathways.* J Chem Phys, 2012. **136**(1): p. 015101.
79. Hovav, Y., A. Feintuch, and S. Vega, *Theoretical aspects of dynamic nuclear polarization in the solid state - the solid effect.* J Magn Reson, 2010. **207**(2): p. 176-89.
80. Hwang, C.F. and D.A. Hill, *Phenomenological Model for the New Effect in Dynamic Polarization.* Physical Review Letters, 1967. **19**(18): p. 1011-1014.
81. Hwang, C.F. and D.A. Hill, *New Effect in Dynamic Polarization.* Physical Review Letters, 1967. **18**(4): p. 110-112.
82. Wollan, D.S., *Dynamic nuclear polarization with an inhomogeneously broadened ESR line. I. Theory.* Physical Review B, 1976. **13**(9): p. 3671-3685.
83. Wollan, D.S., *Dynamic nuclear polarization with an inhomogeneously broadened ESR line. II. Experiment.* Physical Review B, 1976. **13**(9): p. 3686-3696.
84. Hovav, Y., A. Feintuch, and S. Vega, *Theoretical aspects of dynamic nuclear polarization in the solid state – The cross effect.* Journal of Magnetic Resonance, 2012. **214**: p. 29-41.
85. Hu, K.N., et al., *Dynamic nuclear polarization with biradicals.* J Am Chem Soc, 2004. **126**(35): p. 10844-5.
86. Borghini, M., *Spin-Temperature Model of Nuclear Dynamic Polarization Using Free Radicals.* Physical Review Letters, 1968. **20**(9): p. 419-421.
87. Farrar, C.T., et al., *Mechanism of dynamic nuclear polarization in high magnetic fields.* The Journal of Chemical Physics, 2001. **114**(11): p. 4922.
88. Hovav, Y., A. Feintuch, and S. Vega, *Theoretical aspects of dynamic nuclear polarization in the solid state--spin temperature and thermal mixing.* Phys Chem Chem Phys, 2013. **15**(1): p. 188-203.
89. Mentink-Vigier, F., et al., *Fast passage dynamic nuclear polarization on rotating solids.* Journal of Magnetic Resonance, 2012. **224**: p. 13-21.
90. Thurber, K.R. and R. Tycko, *Theory for cross effect dynamic nuclear polarization under magic-angle spinning in solid state nuclear magnetic resonance: the importance of level crossings.* J Chem Phys, 2012. **137**(8): p. 084508.
91. Mentink-Vigier, F., et al., *Theoretical aspects of Magic Angle Spinning - Dynamic Nuclear Polarization.* Journal of Magnetic Resonance, 2015. **258**: p. 102-120.
92. Corzilius, B., *Theory of solid effect and cross effect dynamic nuclear polarization with half-integer high-spin metal polarizing agents in rotating solids.* Phys Chem Chem Phys, 2016. **18**(39): p. 27190-27204.
93. Mance, D., et al., *The magnetic field dependence of cross-effect dynamic nuclear polarization under magic angle spinning.* The Journal of Chemical Physics, 2015. **142**(23): p. 234201.
94. Rosay, M., et al., *Solid-state dynamic nuclear polarization at 263 GHz: spectrometer design and experimental results.* Physical Chemistry Chemical Physics, 2010. **12**(22): p. 5850-5860.
95. Song, C., et al., *TOTAPOL: a biradical polarizing agent for dynamic nuclear polarization experiments in aqueous media.* J Am Chem Soc, 2006. **128**(35): p. 11385-90.
96. Matsuki, Y., et al., *Dynamic nuclear polarization with a rigid biradical.* Angew Chem Int Ed Engl, 2009. **48**(27): p. 4996-5000.
97. Perras, F.A., et al., *Effects of biradical deuteration on the performance of DNP: towards better performing polarizing agents.* Phys Chem Chem Phys, 2016. **18**(1): p. 65-9.
98. Akbey, U., et al., *Dynamic nuclear polarization of deuterated proteins.* Angew Chem Int Ed Engl, 2010. **49**(42): p. 7803-6.
99. Kiesewetter, M.K., et al., *Dynamic nuclear polarization with a water-soluble rigid biradical.* J Am Chem Soc, 2012. **134**(10): p. 4537-40.
100. Sauvee, C., et al., *Highly efficient, water-soluble polarizing agents for dynamic nuclear polarization at high frequency.* Angew Chem Int Ed Engl, 2013. **52**(41): p. 10858-61.
101. Kubicki, D.J., et al., *Rational design of dinitroxide biradicals for efficient cross-effect dynamic nuclear polarization.* Chem. Sci., 2016. **7**(1): p. 550-558.
102. Michaelis, V.K., et al., *High-field 13C dynamic nuclear polarization with a radical mixture.* J Am Chem Soc, 2013. **135**(8): p. 2935-8.
103. Shimon, D., et al., *Static (1)H dynamic nuclear polarization with the biradical TOTAPOL: a transition between the solid effect and the cross effect.* Phys Chem Chem Phys, 2014. **16**(14): p. 6687-99.
104. Corzilius, B., et al., *High-field dynamic nuclear polarization with high-spin transition metal ions.* J Am Chem Soc, 2011. **133**(15): p. 5648-51.
105. Linden, A.H., et al., *Cryogenic temperature effects and resolution upon slow cooling of protein preparations in solid state NMR.* J Biomol NMR, 2011. **51**(3): p. 283-92.
106. Corzilius, B., et al., *Paramagnet induced signal quenching in MAS-DNP experiments in frozen homogeneous solutions.* J Magn Reson, 2014. **240**: p. 113-23.
107. van der Wel, P.C., et al., *Dynamic nuclear polarization of amyloidogenic peptide nanocrystals: GNNQQNY, a core segment of the yeast prion protein Sup35p.* J Am Chem Soc, 2006. **128**(33): p. 10840-6.

108. Barnes, A.B., et al., *Resolution and polarization distribution in cryogenic DNP/MAS experiments.* Phys Chem Chem Phys, 2010. **12**(22): p. 5861-7.
109. Fricke, P., et al., *High resolution observed in 800 MHz DNP spectra of extremely rigid type III secretion needles.* J Biomol NMR, 2016. **65**(3-4): p. 121-6.
110. Lange, S., et al., *Structural analysis of a signal peptide inside the ribosome tunnel by DNP MAS NMR.* Sci Adv, 2016. **2**(8): p. e1600379.
111. Nagaraj, M., et al., *Surface Binding of TOTAPOL Assists Structural Investigations of Amyloid Fibrils by Dynamic Nuclear Polarization NMR Spectroscopy.* Chembiochem, 2016. **17**(14): p. 1308-11.
112. Ravera, E., et al., *Dynamic nuclear polarization of sedimented solutes.* J Am Chem Soc, 2013. **135**(5): p. 1641-4.
113. Liao, S.Y., et al., *Efficient DNP NMR of membrane proteins: sample preparation protocols, sensitivity, and radical location.* J Biomol NMR, 2016. **64**(3): p. 223-37.
114. Kiesewetter, M.K., et al., *High field dynamic nuclear polarization NMR with surfactant sheltered biradicals.* J Phys Chem B, 2014. **118**(7): p. 1825-30.
115. Takahashi, H., S. Hediger, and G. De Paepe, *Matrix-free dynamic nuclear polarization enables solid-state NMR 13C-13C correlation spectroscopy of proteins at natural isotopic abundance.* Chem Commun (Camb), 2013. **49**(82): p. 9479-81.
116. Takahashi, H., et al., *Rapid natural-abundance 2D 13C-13C correlation spectroscopy using dynamic nuclear polarization enhanced solid-state NMR and matrix-free sample preparation.* Angew Chem Int Ed Engl, 2012. **51**(47): p. 11766-9.
117. Hovav, Y., A. Feintuch, and S. Vega, *Dynamic nuclear polarization assisted spin diffusion for the solid effect case.* The Journal of Chemical Physics, 2011. **134**(7): p. 074509.
118. Kagawa, A., et al., *Optimization of 1H spin density for dynamic nuclear polarization using photo-excited triplet electron spins.* J Magn Reson, 2009. **197**(1): p. 9-13.
119. Zagdoun, A., et al., *Improved dynamic nuclear polarization surface-enhanced NMR spectroscopy through controlled incorporation of deuterated functional groups.* Angew Chem Int Ed Engl, 2013. **52**(4): p. 1222-5.
120. Kubicki, D.J., et al., *Amplifying dynamic nuclear polarization of frozen solutions by incorporating dielectric particles.* J Am Chem Soc, 2014. **136**(44): p. 15711-8.
121. Takahashi, H., et al., *Optimization of an absolute sensitivity in a glassy matrix during DNP-enhanced multidimensional solid-state NMR experiments.* J Magn Reson, 2014. **239**: p. 91-9.
122. Perez Linde, A.J., et al., *Rotation-induced recovery and bleaching in magnetic resonance.* Phys Chem Chem Phys, 2015. **17**(9): p. 6415-22.
123. Thurber, K.R. and R. Tycko, *Perturbation of nuclear spin polarizations in solid state NMR of nitroxide-doped samples by magic-angle spinning without microwaves.* J Chem Phys, 2014. **140**(18): p. 184201.
124. Hovav, Y., et al., *The electron depolarization during dynamic nuclear polarization: measurements and simulations.* Phys Chem Chem Phys, 2015. **17**(1): p. 226-44.
125. Mentink-Vigier, F., et al., *Nuclear depolarization and absolute sensitivity in magic-angle spinning cross effect dynamic nuclear polarization.* Phys Chem Chem Phys, 2015. **17**(34): p. 21824-36.
126. Maly, T., A.F. Miller, and R.G. Griffin, *In situ high-field dynamic nuclear polarization--direct and indirect polarization of 13C nuclei.* Chemphyschem, 2010. **11**(5): p. 999-1001.
127. Shimon, D., et al., *Simultaneous DNP enhancements of (1)H and (13)C nuclei: theory and experiments.* Phys Chem Chem Phys, 2015. **17**(17): p. 11868-83.
128. Daube, D., et al., *Heteronuclear Cross-Relaxation under Solid-State Dynamic Nuclear Polarization.* J Am Chem Soc, 2016.
129. Jakeman, D.L., et al., *Effects of sample preparation conditions on biomolecular solid-state NMR lineshapes.* J Biomol NMR, 1998. **12**(3): p. 417-21.
130. Siemer, A.B., K.Y. Huang, and A.E. McDermott, *Protein linewidth and solvent dynamics in frozen solution NMR.* PLoS One, 2012. **7**(10): p. e47242.
131. Lelli, M., et al., *Solid-State Dynamic Nuclear Polarization at 9.4 and 18.8 T from 100 K to Room Temperature.* J Am Chem Soc, 2015. **137**(46): p. 14558-61.
132. Geiger, M.A., et al., *Temperature dependence of cross-effect dynamic nuclear polarization in rotating solids: advantages of elevated temperatures.* Phys Chem Chem Phys, 2016. **18**(44): p. 30696-30704.
133. Fernandez-de-Alba, C., et al., *Matrix-free DNP-enhanced NMR spectroscopy of liposomes using a lipid-anchored biradical.* Chemistry, 2015. **21**(12): p. 4512-7.
134. Maly, T., et al., *1H dynamic nuclear polarization based on an endogenous radical.* J Phys Chem B, 2012. **116**(24): p. 7055-65.
135. Smith, A.N., et al., *A method for dynamic nuclear polarization enhancement of membrane proteins.* Angew Chem Int Ed Engl, 2015. **54**(5): p. 1542-6.
136. Takahashi, H., et al., *Solid-state NMR on bacterial cells: selective cell wall signal enhancement and resolution improvement using dynamic nuclear polarization.* J Am Chem Soc, 2013. **135**(13): p. 5105-10.
137. van der Cruijsen, E.A., et al., *Biomolecular DNP-Supported NMR Spectroscopy using Site-Directed Spin Labeling.* Chemistry, 2015. **21**(37): p. 12971-7.
138. Vitzthum, V., et al., *Fractional spin-labeling of polymers for enhancing NMR sensitivity by solvent-free dynamic nuclear polarization.* Chemphyschem, 2011. **12**(16): p. 2929-32.
139. Voinov, M.A., et al., *Cysteine-Specific Labeling of Proteins with a Nitroxide Biradical for Dynamic Nuclear Polarization NMR.* J Phys Chem B, 2015. **119**(32): p. 10180-90.
140. Wylie, B.J., et al., *Dynamic nuclear polarization of membrane proteins: covalently bound spin-labels at protein-protein interfaces.* J Biomol NMR, 2015. **61**(3-4): p. 361-7.
141. Viennet, T., et al., *Selective Protein Hyperpolarization in Cell Lysates Using Targeted Dynamic Nuclear Polarization.* Angew Chem Int Ed Engl, 2016. **55**(36): p. 10746-50.

142. Rogawski, R., et al., *Dynamic Nuclear Polarization Signal Enhancement with High-Affinity Biradical Tags.* J Phys Chem B, 2017.
143. Mathies, G., et al., *Pulsed Dynamic Nuclear Polarization with Trityl Radicals.* J Phys Chem Lett, 2016. **7**(1): p. 111-6.
144. Rossini, A.J., et al., *Dynamic nuclear polarization surface enhanced NMR spectroscopy.* Acc Chem Res, 2013. **46**(9): p. 1942-51.
145. Berruyer, P., et al., *Three-dimensional structure determination of surface sites.* J Am Chem Soc, 2016.
146. Koers, E.J., et al., *NMR-based structural biology enhanced by dynamic nuclear polarization at high magnetic field.* J Biomol NMR, 2014. **60**(2-3): p. 157-68.
147. Su, Y., L. Andreas, and R.G. Griffin, *Magic angle spinning NMR of proteins: high-frequency dynamic nuclear polarization and (1)H detection.* Annu Rev Biochem, 2015. **84**: p. 465-97.
148. Bajaj, V.S., P.C. van der Wel, and R.G. Griffin, *Observation of a low-temperature, dynamically driven structural transition in a polypeptide by solid-state NMR spectroscopy.* J Am Chem Soc, 2009. **131**(1): p. 118-28.
149. Debelouchina, G.T., et al., *Dynamic nuclear polarization-enhanced solid-state NMR spectroscopy of GNNQQNY nanocrystals and amyloid fibrils.* Phys Chem Chem Phys, 2010. **12**(22): p. 5911-9.
150. Bayro, M.J., et al., *Intermolecular structure determination of amyloid fibrils with magic-angle spinning and dynamic nuclear polarization NMR.* J Am Chem Soc, 2011. **133**(35): p. 13967-74.
151. Debelouchina, G.T., et al., *Higher order amyloid fibril structure by MAS NMR and DNP spectroscopy.* J Am Chem Soc, 2013. **135**(51): p. 19237-47.
152. Potapov, A., et al., *Successive Stages of Amyloid-beta Self-Assembly Characterized by Solid-State Nuclear Magnetic Resonance with Dynamic Nuclear Polarization.* J Am Chem Soc, 2015. **137**(25): p. 8294-307.
153. Sergeyev, I.V., et al., *Chemical shifts for the unusual DNA structure in Pf1 bacteriophage from dynamic-nuclear-polarization-enhanced solid-state NMR spectroscopy.* J Am Chem Soc, 2011. **133**(50): p. 20208-17.
154. Wenk, P., et al., *Dynamic nuclear polarization of nucleic acid with endogenously bound manganese.* J Biomol NMR, 2015. **63**(1): p. 97-109.
155. Mak-Jurkauskas, M.L., et al., *Energy transformations early in the bacteriorhodopsin photocycle revealed by DNP-enhanced solid-state NMR.* Proc Natl Acad Sci U S A, 2008. **105**(3): p. 883-8.
156. Bajaj, V.S., et al., *Functional and shunt states of bacteriorhodopsin resolved by 250 GHz dynamic nuclear polarization-enhanced solid-state NMR.* Proc Natl Acad Sci U S A, 2009. **106**(23): p. 9244-9.
157. Mao, J., et al., *Structural basis of the green-blue color switching in proteorhodopsin as determined by NMR spectroscopy.* J Am Chem Soc, 2014. **136**(50): p. 17578-90.
158. Maciejko, J., et al., *Visualizing Specific Cross-Protomer Interactions in the Homo-Oligomeric Membrane Protein Proteorhodopsin by Dynamic-Nuclear-Polarization-Enhanced Solid-State NMR.* J Am Chem Soc, 2015. **137**(28): p. 9032-43.
159. Becker-Baldus, J., et al., *Enlightening the photoactive site of channelrhodopsin-2 by DNP-enhanced solid-state NMR spectroscopy.* Proc Natl Acad Sci U S A, 2015. **112**(32): p. 9896-901.
160. Salnikov, E., et al., *Solid-State NMR Spectroscopy of Oriented Membrane Polypeptides at 100 K with Signal Enhancement by Dynamic Nuclear Polarization.* Journal of the American Chemical Society, 2010. **132**(17): p. 5940-+.
161. Gelis, I., et al., *Solid-state NMR enhanced by dynamic nuclear polarization as a novel tool for ribosome structural biology.* J Biomol NMR, 2013. **56**(2): p. 85-93.
162. Fricke, P., et al., *Studies on the MxiH protein in T3SS needles using DNP-enhanced ssNMR spectroscopy.* Chemphyschem, 2014. **15**(1): p. 57-60.
163. Kaplan, M., et al., *Probing a cell-embedded megadalton protein complex by DNP-supported solid-state NMR.* Nat Methods, 2015. **12**(7): p. 649-52.
164. Gupta, R., et al., *Dynamic Nuclear Polarization Enhanced MAS NMR Spectroscopy for Structural Analysis of HIV-1 Protein Assemblies.* J Phys Chem B, 2016.
165. Kaplan, M., et al., *EGFR Dynamics Change during Activation in Native Membranes as Revealed by NMR.* Cell, 2016. **167**(5): p. 1241-1251 e11.
166. Linden, A.H., et al., *Neurotoxin II bound to acetylcholine receptors in native membranes studied by dynamic nuclear polarization NMR.* J Am Chem Soc, 2011. **133**(48): p. 19266-9.
167. Reggie, L., et al., *Dynamic nuclear polarization-enhanced solid-state NMR of a 13C-labeled signal peptide bound to lipid-reconstituted Sec translocon.* J Am Chem Soc, 2011. **133**(47): p. 19084-6.
168. Andreas, L.B., et al., *Dynamic nuclear polarization study of inhibitor binding to the M2(18-60) proton transporter from influenza A.* Biochemistry, 2013. **52**(16): p. 2774-82.
169. Ong, Y.S., et al., *Detecting substrates bound to the secondary multidrug efflux pump EmrE by DNP-enhanced solid-state NMR.* J Am Chem Soc, 2013. **135**(42): p. 15754-62.
170. Wang, T., et al., *Sensitivity-enhanced solid-state NMR detection of expansin's target in plant cell walls.* Proc Natl Acad Sci U S A, 2013. **110**(41): p. 16444-9.
171. Jacso, T., et al., *Characterization of membrane proteins in isolated native cellular membranes by dynamic nuclear polarization solid-state NMR spectroscopy without purification and reconstitution.* Angew Chem Int Ed Engl, 2012. **51**(2): p. 432-5.
172. Renault, M., et al., *Solid-state NMR spectroscopy on cellular preparations enhanced by dynamic nuclear polarization.* Angew Chem Int Ed Engl, 2012. **51**(12): p. 2998-3001.
173. Yamamoto, K., et al., *Cellular solid-state NMR investigation of a membrane protein using dynamic nuclear polarization.* Biochim Biophys Acta, 2015. **1848**(1 Pt B): p. 342-9.
174. Frederick, K.K., et al., *Sensitivity-Enhanced NMR Reveals Alterations in Protein Structure by Cellular Milieus.* Cell, 2015. **163**(3): p. 620-8.
175. Graham, F.L., et al., *Characteristics of a human cell line transformed by DNA from human adenovirus type 5.* J Gen Virol, 1977. **36**(1): p. 59-74.

176. Vaughn, J.L., et al., *The establishment of two cell lines from the insectspodoptera frugiperda (lepidoptera; noctuidae).* In Vitro, 1977. **13**(4): p. 213-217.
177. Rosano, G.L. and E.A. Ceccarelli, *Recombinant protein expression in Escherichia coli: advances and challenges.* Front Microbiol, 2014. **5**: p. 172.
178. Studier, F.W. and B.A. Moffatt, *Use of bacteriophage T7 RNA polymerase to direct selective high-level expression of cloned genes.* Journal of Molecular Biology, 1986. **189**(1): p. 113-130.
179. Miroux, B. and J.E. Walker, *Over-production of proteins in Escherichia coli: mutant hosts that allow synthesis of some membrane proteins and globular proteins at high levels.* J Mol Biol, 1996. **260**(3): p. 289-98.
180. Katzen, F., T.C. Peterson, and W. Kudlicki, *Membrane protein expression: no cells required.* Trends Biotechnol, 2009. **27**(8): p. 455-60.
181. Schwarz, D., et al., *Preparative scale expression of membrane proteins in Escherichia coli-based continuous exchange cell-free systems.* Nat Protoc, 2007. **2**(11): p. 2945-57.
182. Takai, K., T. Sawasaki, and Y. Endo, *Practical cell-free protein synthesis system using purified wheat embryos.* Nat Protoc, 2010. **5**(2): p. 227-38.
183. Ding, Y., Y. Yao, and F.M. Marassi, *Membrane protein structure determination in membrana.* Acc Chem Res, 2013. **46**(9): p. 2182-90.
184. Popot, J.L., *Amphipols, nanodiscs, and fluorinated surfactants: three nonconventional approaches to studying membrane proteins in aqueous solutions.* Annu Rev Biochem, 2010. **79**: p. 737-75.
185. Warschawski, D.E., et al., *Choosing membrane mimetics for NMR structural studies of transmembrane proteins.* Biochim Biophys Acta, 2011. **1808**(8): p. 1957-74.
186. Liang, B. and L.K. Tamm, *NMR as a tool to investigate the structure, dynamics and function of membrane proteins.* Nat Struct Mol Biol, 2016. **23**(6): p. 468-74.
187. Klammt, C., et al., *Facile backbone structure determination of human membrane proteins by NMR spectroscopy.* Nat Methods, 2012. **9**(8): p. 834-9.
188. Seddon, A.M., P. Curnow, and P.J. Booth, *Membrane proteins, lipids and detergents: not just a soap opera.* Biochim Biophys Acta, 2004. **1666**(1-2): p. 105-17.
189. Zhou, H.X. and T.A. Cross, *Influences of membrane mimetic environments on membrane protein structures.* Annu Rev Biophys, 2013. **42**: p. 361-92.
190. Reynolds, J.A. and C. Tanford, *The gross conformation of protein-sodium dodecyl sulfate complexes.* J Biol Chem, 1970. **245**(19): p. 5161-5.
191. McDonnell, P.A. and S.J. Opella, *Effect of Detergent Concentration on Multidimensional Solution NMR Spectra of Membrane Proteins in Micelles.* Journal of Magnetic Resonance, Series B, 1993. **102**(1): p. 120-125.
192. Laguerre, A., et al., *From Nanodiscs to Isotropic Bicelles: A Procedure for Solution Nuclear Magnetic Resonance Studies of Detergent-Sensitive Integral Membrane Proteins.* Structure, 2016. **24**(10): p. 1830-1841.
193. Tzitzilonis, C., et al., *Detergent/nanodisc screening for high-resolution NMR studies of an integral membrane protein containing a cytoplasmic domain.* PLoS One, 2013. **8**(1): p. e54378.
194. Lazaridis, T., B. Mallik, and Y. Chen, *Implicit solvent simulations of DPC micelle formation.* J Phys Chem B, 2005. **109**(31): p. 15098-106.
195. Thiyagarajan, P. and D.M. Tiede, *Detergent micelle structure and micelle-micelle interactions determined by small-angle neutron scattering under solution conditions used for membrane protein crystallization.* The Journal of Physical Chemistry, 1994. **98**(40): p. 10343-10351.
196. Lee, D., et al., *Bilayer in small bicelles revealed by lipid-protein interactions using NMR spectroscopy.* Journal of the American Chemical Society, 2008. **130**(42): p. 13822-13823.
197. Tribet, C., R. Audebert, and J.L. Popot, *Amphipols: Polymers that keep membrane proteins soluble in aqueous solutions.* Proceedings of the National Academy of Sciences of the United States of America, 1996. **93**(26): p. 15047-15050.
198. Elter, S., et al., *The Use of Amphipols for NMR Structural Characterization of 7-TM Proteins.* The Journal of Membrane Biology, 2014. **247**(9-10): p. 957-964.
199. Hunte, C., *Specific protein–lipid interactions in membrane proteins.* Biochemical Society Transactions, 2005. **33**(5): p. 938-942.
200. Yeh, V., et al., *Lipids influence the proton pump activity of photosynthetic protein embedded in nanodiscs.* RSC Adv., 2016. **6**(91): p. 88300-88305.
201. Lee, A.G., *Lipid–protein interactions in biological membranes: a structural perspective.* Biochimica et Biophysica Acta (BBA) - Biomembranes, 2003. **1612**(1): p. 1-40.
202. Hunte, C. and S. Richers, *Lipids and membrane protein structures.* Curr Opin Struct Biol, 2008. **18**(4): p. 406-11.
203. Lee, A.G., *How lipids affect the activities of integral membrane proteins.* Biochim Biophys Acta, 2004. **1666**(1-2): p. 62-87.
204. Bayburt, T.H., Y.V. Grinkova, and S.G. Sligar, *Self-assembly of discoidal phospholipid bilayer nanoparticles with membrane scaffold proteins.* Nano Letters, 2002. **2**(8): p. 853-856.
205. Denisov, I.G. and S.G. Sligar, *Nanodiscs for structural and functional studies of membrane proteins.* Nat Struct Mol Biol, 2016. **23**(6): p. 481-6.
206. Orwick-Rydmark, M., et al., *Detergent-free incorporation of a seven-transmembrane receptor protein into nanosized bilayer Lipodisq particles for functional and biophysical studies.* Nano Lett, 2012. **12**(9): p. 4687-92.
207. Dorr, J.M., et al., *The styrene-maleic acid copolymer: a versatile tool in membrane research.* Eur Biophys J, 2016. **45**(1): p. 3-21.
208. Nasr, M.L., et al., *Covalently circularized nanodiscs for studying membrane proteins and viral entry.* Nat Methods, 2016.
209. Reed, J.C., *Bcl-2 and the regulation of programmed cell death.* The Journal of Cell Biology, 1994. **124**(1): p. 1-6.
210. Czabotar, P.E., et al., *Control of apoptosis by the BCL-2 protein family: implications for physiology and therapy.* Nat Rev Mol Cell Biol, 2014. **15**(1): p. 49-63.

211. Yin, X.M., Z.N. Oltvai, and S.J. Korsmeyer, *BH1 and BH2 domains of Bcl-2 are required for inhibition of apoptosis and heterodimerization with Bax.* Nature, 1994. **369**(6478): p. 321-3.
212. Chittenden, T., et al., *A conserved domain in Bak, distinct from BH1 and BH2, mediates cell death and protein binding functions.* EMBO J, 1995. **14**(22): p. 5589-96.
213. Chiou, S.K., L. Rao, and E. White, *Bcl-2 blocks p53-dependent apoptosis.* Molecular and Cellular Biology, 1994. **14**(4): p. 2556-2563.
214. Malia, T.J. and G. Wagner, *NMR structural investigation of the mitochondrial outer membrane protein VDAC and its interaction with antiapoptotic Bcl-xL.* Biochemistry, 2007. **46**(2): p. 514-25.
215. Bertini, I., et al., *The anti-apoptotic Bcl-x(L) protein, a new piece in the puzzle of cytochrome c interactome.* PLoS One, 2011. **6**(4): p. e18329.
216. Hu, Y., et al., *Bcl-XL interacts with Apaf-1 and inhibits Apaf-1-dependent caspase-9 activation.* Proc Natl Acad Sci U S A, 1998. **95**(8): p. 4386-91.
217. Muchmore, S.W., et al., *X-ray and NMR structure of human Bcl-xL, an inhibitor of programmed cell death.* Nature, 1996. **381**(6580): p. 335-41.
218. Sattler, M., et al., *Structure of Bcl-xL-Bak Peptide Complex: Recognition Between Regulators of Apoptosis.* Science, 1997. **275**(5302): p. 983-986.
219. Hill, R.B., K.R. MacKenzie, and M.C. Harwig, *The Tail-End Is Only the Beginning: NMR Study Reveals a Membrane-Bound State of BCL-XL.* Journal of Molecular Biology, 2015. **427**(13): p. 2257-2261.
220. Yao, Y., et al., *Conformation of BCL-XL upon Membrane Integration.* J Mol Biol, 2015. **427**(13): p. 2262-70.
221. Fiebig, A.A., et al., *Bcl-XL is qualitatively different from and ten times more effective than Bcl-2 when expressed in a breast cancer cell line.* BMC Cancer, 2006. **6**: p. 213.
222. Dutta, S., et al., *Potent and specific peptide inhibitors of human pro-survival protein Bcl-xL.* J Mol Biol, 2015. **427**(6 Pt B): p. 1241-53.
223. Lessene, G., et al., *Structure-guided design of a selective BCL-X(L) inhibitor.* Nat Chem Biol, 2013. **9**(6): p. 390-7.
224. Walensky, L.D., et al., *Activation of apoptosis in vivo by a hydrocarbon-stapled BH3 helix.* Science, 2004. **305**(5689): p. 1466-70.
225. Wysoczanski, P., et al., *NMR solution structure of a photoswitchable apoptosis activating Bak peptide bound to Bcl-xL.* J Am Chem Soc, 2012. **134**(18): p. 7644-7.
226. Stoorvogel, J., M.J.A.W.M. Vanbussel, and J.A.M. Vandeklundert, *Cloning of a Beta-Lactam Resistance Determinant of Enterobacter-Cloacae Affecting Outer-Membrane Proteins of Enterobacteriaceae.* Fems Microbiology Letters, 1987. **48**(1-2): p. 277-281.
227. Mecsas, J., et al., *Identification and Characterization of an Outer-Membrane Protein, Ompx, in Escherichia-Coli That Is Homologous to a Family of Outer-Membrane Proteins Including Ail of Yersinia-Enterocolitica.* Journal of Bacteriology, 1995. **177**(3): p. 799-804.
228. Stoorvogel, J., M.J. van Bussel, and J.A. van de Klundert, *Biological characterization of an Enterobacter cloacae outer membrane protein (OmpX).* J Bacteriol, 1991. **173**(1): p. 161-7.
229. Stoorvogel, J., et al., *Molecular characterization of an Enterobacter cloacae outer membrane protein (OmpX).* J Bacteriol, 1991. **173**(1): p. 156-60.
230. Heffernan, E.J., et al., *Specificity of the complement resistance and cell association phenotypes encoded by the outer membrane protein genes rck from Salmonella typhimurium and ail from Yersinia enterocolitica.* Infect Immun, 1994. **62**(11): p. 5183-6.
231. de Kort, G., et al., *Invasion of rabbit ileal tissue by Enterobacter cloacae varies with the concentration of OmpX in the outer membrane.* Infect Immun, 1994. **62**(11): p. 4722-6.
232. Dupont, M., et al., *Enterobacter aerogenes OmpX, a cation-selective channel mar- and osmo-regulated.* FEBS Lett, 2004. **569**(1-3): p. 27-30.
233. Prehna, G., et al., *A protein export pathway involving Escherichia coli porins.* Structure, 2012. **20**(7): p. 1154-66.
234. Koebnik, R., K.P. Locher, and P. Van Gelder, *Structure and function of bacterial outer membrane proteins: barrels in a nutshell.* Mol Microbiol, 2000. **37**(2): p. 239-53.
235. Vogt, J. and G.E. Schulz, *The structure of the outer membrane protein OmpX from Escherichia coli reveals possible mechanisms of virulence.* Structure, 1999. **7**(10): p. 1301-9.
236. Fernandez, C., et al., *NMR structure of the integral membrane protein OmpX.* J Mol Biol, 2004. **336**(5): p. 1211-21.
237. Fernandez, C., K. Adeishvili, and K. Wuthrich, *Transverse relaxation-optimized NMR spectroscopy with the outer membrane protein OmpX in dihexanoyl phosphatidylcholine micelles.* Proc Natl Acad Sci U S A, 2001. **98**(5): p. 2358-63.
238. Fernandez, C., et al., *Solution NMR studies of the integral membrane proteins OmpX and OmpA from Escherichia coli.* FEBS Lett, 2001. **504**(3): p. 173-8.
239. Hilty, C., et al., *Side chain NMR assignments in the membrane protein OmpX reconstituted in DHPC micelles.* J Biomol NMR, 2002. **23**(4): p. 289-301.
240. Fernandez, C., et al., *Lipid-protein interactions in DHPC micelles containing the integral membrane protein OmpX investigated by NMR spectroscopy.* Proc Natl Acad Sci U S A, 2002. **99**(21): p. 13533-7.
241. Hiller, S., et al., *Interactions with hydrophobic clusters in the urea-unfolded membrane protein OmpX.* Angew Chem Int Ed Engl, 2008. **47**(5): p. 977-81.
242. Catoire, L.J., et al., *Solution NMR mapping of water-accessible residues in the transmembrane beta-barrel of OmpX.* Eur Biophys J, 2010. **39**(4): p. 623-30.
243. Mahalakshmi, R., et al., *NMR structural studies of the bacterial outer membrane protein OmpX in oriented lipid bilayer membranes.* Biochim Biophys Acta, 2007. **1768**(12): p. 3216-24.
244. Mahalakshmi, R. and F.M. Marassi, *Orientation of the Escherichia coli outer membrane protein OmpX in phospholipid bilayer membranes determined by solid-State NMR.* Biochemistry, 2008. **47**(25): p. 6531-8.

245. Hagn, F., et al., *Optimized phospholipid bilayer nanodiscs facilitate high-resolution structure determination of membrane proteins.* J Am Chem Soc, 2013. **135**(5): p. 1919-25.
246. Bibow, S., et al., *Measuring membrane protein bond orientations in nanodiscs via residual dipolar couplings.* Protein Sci, 2014. **23**(7): p. 851-6.
247. Hagn, F. and G. Wagner, *Structure refinement and membrane positioning of selectively labeled OmpX in phospholipid nanodiscs.* J Biomol NMR, 2015. **61**(3-4): p. 249-60.
248. Marcel, Y.L. and R.S. Kiss, *Structure-function relationships of apolipoprotein A-I: a flexible protein with dynamic lipid associations.* Curr Opin Lipidol, 2003. **14**(2): p. 151-7.
249. Atkinson, D. and D.M. Small, *Recombinant lipoproteins: implications for structure and assembly of native lipoproteins.* Annu Rev Biophys Biophys Chem, 1986. **15**: p. 403-56.
250. Ohashi, R., et al., *Reverse cholesterol transport and cholesterol efflux in atherosclerosis.* QJM, 2005. **98**(12): p. 845-56.
251. Zannis, V.I., A. Chroni, and M. Krieger, *Role of apoA-I, ABCA1, LCAT, and SR-BI in the biogenesis of HDL.* J Mol Med (Berl), 2006. **84**(4): p. 276-94.
252. Segrest, J.P., *Amphipathic helixes and plasma lipoproteins: thermodynamic and geometric considerations.* Chem Phys Lipids, 1977. **18**(1): p. 7-22.
253. Shih, A.Y., et al., *Assembly of lipids and proteins into lipoprotein particles.* Journal of Physical Chemistry B, 2007. **111**(38): p. 11095-11104.
254. Shih, A.Y., et al., *Assembly of lipoprotein particles revealed by coarse-grained molecular dynamics simulations.* J Struct Biol, 2007. **157**(3): p. 579-92.
255. Shih, A.Y., S.G. Sligar, and K. Schulten, *Maturation of high-density lipoproteins.* J R Soc Interface, 2009. **6**(39): p. 863-71.
256. Borhani, D.W., et al., *Crystal structure of truncated human apolipoprotein A-I suggests a lipid-bound conformation.* Proc Natl Acad Sci U S A, 1997. **94**(23): p. 12291-6.
257. Ajees, A.A., et al., *Crystal structure of human apolipoprotein A-I: Insights into its protective effect against cardiovascular diseases.* Proceedings of the National Academy of Sciences of the United States of America, 2006. **103**(7): p. 2126-2131.
258. Brouillette, C.G. and G.M. Anantharamaiah, *Structural models of human apolipoprotein A-I.* Biochimica et Biophysica Acta (BBA) - Lipids and Lipid Metabolism, 1995. **1256**(2): p. 103-129.
259. Brouillette, C.G., et al., *Structural models of human apolipoprotein A-I: a critical analysis and review.* Biochim Biophys Acta, 2001. **1531**(1-2): p. 4-46.
260. Koppaka, V., *Structural studies of discoidal lipoprotein A-I.* Cell Mol Life Sci, 2001. **58**(7): p. 885-93.
261. Segrest, J.P., et al., *A detailed molecular belt model for apolipoprotein A-I in discoidal high density lipoprotein.* J Biol Chem, 1999. **274**(45): p. 31755-8.
262. Phillips, J.C., et al., *Predicting the structure of apolipoprotein A-I in reconstituted high-density lipoprotein disks.* Biophys J, 1997. **73**(5): p. 2337-46.
263. Wu, Z., et al., *Double superhelix model of high density lipoprotein.* J Biol Chem, 2009. **284**(52): p. 36605-19.
264. Thomas, M.J., S. Bhat, and M.G. Sorci-Thomas, *Three-dimensional models of HDL apoA-I: implications for its assembly and function.* The Journal of Lipid Research, 2008. **49**(9): p. 1875-1883.
265. Davidson, W.S. and R.A. Silva, *Apolipoprotein structural organization in high density lipoproteins: belts, bundles, hinges and hairpins.* Curr Opin Lipidol, 2005. **16**(3): p. 295-300.
266. Rogers, D.P., et al., *Structural analysis of apolipoprotein A-I: effects of amino- and carboxy-terminal deletions on the lipid-free structure.* Biochemistry, 1998. **37**(3): p. 945-55.
267. Catte, A., et al., *Novel changes in discoidal high density lipoprotein morphology: a molecular dynamics study.* Biophys J, 2006. **90**(12): p. 4345-60.
268. Martin, D.D., et al., *Apolipoprotein A-I assumes a "looped belt" conformation on reconstituted high density lipoprotein.* J Biol Chem, 2006. **281**(29): p. 20418-26.
269. Bhat, S., et al., *Conformational adaptation of apolipoprotein A-I to discretely sized phospholipid complexes.* Biochemistry, 2007. **46**(26): p. 7811-21.
270. Wu, Z., et al., *The refined structure of nascent HDL reveals a key functional domain for particle maturation and dysfunction.* Nat Struct Mol Biol, 2007. **14**(9): p. 861-8.
271. Li, Y., et al., *Structural analysis of nanoscale self-assembled discoidal lipid bilayers by solid-state NMR spectroscopy.* Biophys J, 2006. **91**(10): p. 3819-28.
272. Kijac, A., et al., *Lipid-protein correlations in nanoscale phospholipid bilayers determined by solid-state nuclear magnetic resonance.* Biochemistry, 2010. **49**(43): p. 9190-8.
273. Bayburt, T.H., J.W. Carlson, and S.G. Sligar, *Reconstitution and imaging of a membrane protein in a nanometer-size phospholipid bilayer.* J Struct Biol, 1998. **123**(1): p. 37-44.
274. Denisov, I.G., et al., *Directed self-assembly of monodisperse phospholipid bilayer Nanodiscs with controlled size.* J Am Chem Soc, 2004. **126**(11): p. 3477-87.
275. Grinkova, Y.V., I.G. Denisov, and S.G. Sligar, *Engineering extended membrane scaffold proteins for self-assembly of soluble nanoscale lipid bilayers.* Protein Eng Des Sel, 2010. **23**(11): p. 843-8.
276. Bibow, S., et al., *Solution structure of discoidal high-density lipoprotein particles with a shortened apolipoprotein A-I.* Nat Struct Mol Biol, 2016.
277. Spillantini, M.G., et al., *Alpha-synuclein in Lewy bodies.* Nature, 1997. **388**(6645): p. 839-40.
278. Luk, K.C., et al., *Pathological alpha-synuclein transmission initiates Parkinson-like neurodegeneration in nontransgenic mice.* Science, 2012. **338**(6109): p. 949-53.
279. Jucker, M. and L.C. Walker, *Self-propagation of pathogenic protein aggregates in neurodegenerative diseases.* Nature, 2013. **501**(7465): p. 45-51.
280. Vacha, R., S. Linse, and M. Lund, *Surface effects on aggregation kinetics of amyloidogenic peptides.* J Am Chem Soc, 2014. **136**(33): p. 11776-82.

281. Buell, A.K., et al., *Solution conditions determine the relative importance of nucleation and growth processes in alpha-synuclein aggregation.* Proc Natl Acad Sci U S A, 2014. **111**(21): p. 7671-6.
282. Galvagnion, C., et al., *Lipid vesicles trigger alpha-synuclein aggregation by stimulating primary nucleation.* Nat Chem Biol, 2015. **11**(3): p. 229-34.
283. Tuttle, M.D., et al., *Solid-state NMR structure of a pathogenic fibril of full-length human alpha-synuclein.* Nat Struct Mol Biol, 2016. **23**(5): p. 409-15.
284. Davidson, W.S., et al., *Stabilization of alpha-synuclein secondary structure upon binding to synthetic membranes.* Journal of Biological Chemistry, 1998. **273**(16): p. 9443-9449.
285. Jo, E., et al., *alpha-Synuclein membrane interactions and lipid specificity.* J Biol Chem, 2000. **275**(44): p. 34328-34.
286. Gitler, A.D., et al., *The Parkinson's disease protein alpha-synuclein disrupts cellular Rab homeostasis.* Proc Natl Acad Sci U S A, 2008. **105**(1): p. 145-50.
287. Bellani, S., et al., *The regulation of synaptic function by alpha-synuclein.* Commun Integr Biol, 2010. **3**(2): p. 106-9.
288. Bonini, N.M. and B.I. Giasson, *Snaring the function of alpha-synuclein.* Cell, 2005. **123**(3): p. 359-61.
289. Diao, J., et al., *Native alpha-synuclein induces clustering of synaptic-vesicle mimics via binding to phospholipids and synaptobrevin-2/VAMP2.* Elife, 2013. **2**: p. e00592.
290. Fusco, G., et al., *Structural basis of synaptic vesicle assembly promoted by alpha-synuclein.* Nat Commun, 2016. **7**: p. 12563.
291. Landau, D., et al., *Infantile variant of Bartter syndrome and sensorineural deafness: a new autosomal recessive disorder.* Am J Med Genet, 1995. **59**(4): p. 454-9.
292. Rickheit, G., et al., *Endocochlear potential depends on Cl- channels: mechanism underlying deafness in Bartter syndrome IV.* EMBO J, 2008. **27**(21): p. 2907-17.
293. Estevez, R., et al., *Barttin is a Cl- channel beta-subunit crucial for renal Cl- reabsorption and inner ear K+ secretion.* Nature, 2001. **414**(6863): p. 558-61.
294. Kramer, B.K., et al., *Mechanisms of Disease: the kidney-specific chloride channels ClCKA and ClCKB, the Barttin subunit, and their clinical relevance.* Nat Clin Pract Nephrol, 2008. **4**(1): p. 38-46.
295. Fahlke, C. and M. Fischer, *Physiology and pathophysiology of ClC-K/barttin channels.* Front Physiol, 2010. **1**: p. 155.
296. Dutzler, R., E.B. Campbell, and R. MacKinnon, *Gating the selectivity filter in ClC chloride channels.* Science, 2003. **300**(5616): p. 108-12.
297. Dutzler, R., et al., *X-ray structure of a ClC chloride channel at 3.0 A reveals the molecular basis of anion selectivity.* Nature, 2002. **415**(6869): p. 287-94.
298. Scholl, U., et al., *Barttin modulates trafficking and function of ClC-K channels.* Proc Natl Acad Sci U S A, 2006. **103**(30): p. 11411-6.
299. Janssen, A.G., et al., *Disease-causing dysfunctions of barttin in Bartter syndrome type IV.* J Am Soc Nephrol, 2009. **20**(1): p. 145-53.
300. Fischer, M., A.G. Janssen, and C. Fahlke, *Barttin activates ClC-K channel function by modulating gating.* J Am Soc Nephrol, 2010. **21**(8): p. 1281-9.
301. L'Hoste, S., et al., *Characterization of the mouse ClC-K1/Barttin chloride channel.* Biochim Biophys Acta, 2013. **1828**(11): p. 2399-409.
302. Tajima, M., et al., *Barttin binds to the outer lateral surface of the ClC-K2 chloride channel.* Biochem Biophys Res Commun, 2007. **362**(4): p. 858-64.
303. Steinke, K.V., et al., *Human CLC-K Channels Require Palmitoylation of Their Accessory Subunit Barttin to Be Functional.* Journal of Biological Chemistry, 2015. **290**(28): p. 17390-17400.
304. Popot, J.L., *Amphipols, nanodiscs, and fluorinated surfactants: three nonconventional approaches to studying membrane proteins in aqueous solutions.* Annu. Rev. Biochem., 2010. **79**: p. 737-75.
305. Ding, Y., Y. Yao, and F.M. Marassi, *Membrane protein structure determination in membrana.* Acc. Chem. Res., 2013. **46**(9): p. 2182-90.
306. Raschle, T., et al., *Nonmicellar systems for solution NMR spectroscopy of membrane proteins.* Curr. Opin. Struct. Biol., 2010. **20**(4): p. 471-9.
307. Catoire, L.J., X.L. Warnet, and D.E. Warschawski, *Micelles, Bicelles, Amphipols, Nanodiscs, Liposomes, or Intact Cells: The Hitchhiker's Guide to the Study of Membrane Proteins by NMR.* 2014: p. 315-345.
308. Gao, Y., et al., *TRPV1 structures in nanodiscs reveal mechanisms of ligand and lipid action.* Nature, 2016. **534**(7607): p. 347-51.
309. Bayburt, T.H., J.W. Carlson, and S.G. Sligar, *Reconstitution and imaging of a membrane protein in a nanometer-size phospholipid bilayer.* J. Struct. Biol., 1998. **123**(1): p. 37-44.
310. Bayburt, T.H., Y.V. Grinkova, and S.G. Sligar, *Self-assembly of discoidal phospholipid bilayer nanoparticles with membrane scaffold proteins.* Nano Lett., 2002. **2**(8): p. 853-856.
311. Bayburt, T.H. and S.G. Sligar, *Membrane protein assembly into Nanodiscs.* FEBS Lett., 2010. **584**(9): p. 1721-7.
312. Borch, J. and T. Hamann, *The nanodisc: a novel tool for membrane protein studies.* Biol. Chem., 2009. **390**(8): p. 805-14.
313. Hiller, S. and G. Wagner, *Solution NMR Spectroscopy of Integral Membrane Proteins*, in *Comprehensive Biophysics*, E.H. Egelman and Lukas K. Tamm, Editors. 2012, Elsevier Inc.: Burlington. p. 120-138.
314. Hagn, F., et al., *Optimized phospholipid bilayer nanodiscs facilitate high-resolution structure determination of membrane proteins.* J. Am. Chem. Soc., 2013. **135**(5): p. 1919-25.
315. Chromy, B.A., et al., *Different apolipoproteins impact nanolipoprotein particle formation.* J. Am. Chem. Soc., 2007. **129**(46): p. 14348-54.
316. Wang, X., et al., *Smaller Nanodiscs are Suitable for Studying Protein Lipid Interactions by Solution NMR.* Protein J., 2015. **34**(3): p. 205-211.
317. Grinkova, Y.V., I.G. Denisov, and S.G. Sligar, *Engineering extended membrane scaffold proteins for self-assembly of soluble nanoscale lipid bilayers.* Protein Eng. Des. Sel., 2010. **23**(11): p. 843-8.

318. Kucharska, I., et al., *Optimizing nanodiscs and bicelles for solution NMR studies of two beta-barrel membrane proteins.* J. Biomol. NMR, 2015. **61**(3-4): p. 261-74.
319. Opella, S.J., *Structure determination of membrane proteins by nuclear magnetic resonance spectroscopy.* Annu. Rev. Anal. Chem., 2013. **6**: p. 305-28.
320. Shenkarev, Z.O., et al., *Lipid-protein nanodiscs as reference medium in detergent screening for high-resolution NMR studies of integral membrane proteins.* J. Am. Chem. Soc., 2010. **132**(16): p. 5628-9.
321. Klammt, C., et al., *Facile backbone structure determination of human membrane proteins by NMR spectroscopy.* Nat. Methods, 2012. **9**(8): p. 834-9.
322. Shih, A.Y., S.G. Sligar, and K. Schulten, *Maturation of high-density lipoproteins.* J. R. Soc. Interface, 2009. **6**(39): p. 863-71.
323. Thomas, M.J., S. Bhat, and M.G. Sorci-Thomas, *Three-dimensional models of HDL apoA-I: implications for its assembly and function.* J. Lipid Res., 2008. **49**(9): p. 1875-83.
324. Phillips, J.C., et al., *Predicting the structure of apolipoprotein A-I in reconstituted high-density lipoprotein disks.* Biophys. J . 1997. **73**(5): p. 2337-46.
325. Segrest, J.P., *Amphipathic helixes and plasma lipoproteins: thermodynamic and geometric considerations.* Chem. Phys. Lipids, 1977. **18**(1): p. 7-22.
326. Wu, Z., et al., *Double superhelix model of high density lipoprotein.* J. Biol. Chem., 2009. **284**(52): p. 36605-19.
327. Wu, Z., et al., *The refined structure of nascent HDL reveals a key functional domain for particle maturation and dysfunction.* Nat. Struct. Mol. Biol., 2007. **14**(9): p. 861-8.
328. Brouillette, C.G. and G.M. Anantharamaiah, *Structural models of human apolipoprotein A-I.* Biochim. Biophys. Acta, 1995. **1256**(2): p. 103-29.
329. Brouillette, C.G., et al., *Structural models of human apolipoprotein A-I: a critical analysis and review.* Biochim. Biophys. Acta, 2001. **1531**(1-2): p. 4-46.
330. Segrest, J.P., et al., *A detailed molecular belt model for apolipoprotein A-I in discoidal high density lipoprotein.* J. Biol. Chem., 1999. **274**(45): p. 31755-8.
331. Borhani, D.W., et al., *Crystal structure of truncated human apolipoprotein A-I suggests a lipid-bound conformation.* Proc. Natl. Acad. Sci. USA, 1997. **94**(23): p. 12291-6.
332. Ajees, A.A., et al., *Crystal structure of human apolipoprotein A-I: insights into its protective effect against cardiovascular diseases.* Proc. Natl. Acad. Sci. USA, 2006. **103**(7): p. 2126-31.
333. Skar-Gislinge, N., et al., *Elliptical structure of phospholipid bilayer nanodiscs encapsulated by scaffold proteins: casting the roles of the lipids and the protein.* J. Am. Chem. Soc., 2010. **132**(39): p. 13713-22.
334. Shih, A.Y., et al., *Molecular dynamics simulations of discoidal bilayers assembled from truncated human lipoproteins.* Biophys. J . 2005. **88**(1): p. 548-56.
335. Li, Y., et al., *Structural analysis of nanoscale self-assembled discoidal lipid bilayers by solid-state NMR spectroscopy.* Biophys. J . 2006. **91**(10): p. 3819-28.
336. Shih, A.Y., et al., *Assembly of lipids and proteins into lipoprotein particles.* J. Phys. Chem. B, 2007. **111**(38): p. 11095-11104.
337. Shih, A.Y., et al., *Assembly of lipoprotein particles revealed by coarse-grained molecular dynamics simulations.* J. Struct. Biol., 2007. **157**(3): p. 579-92.
338. Denisov, I.G., et al., *Directed self-assembly of monodisperse phospholipid bilayer Nanodiscs with controlled size.* J. Am. Chem. Soc., 2004. **126**(11): p. 3477-87.
339. Puthenveetil, R. and O. Vinogradova, *Optimization of the design and preparation of nanoscale phospholipid bilayers for its application to solution NMR.* Proteins: Struct. Funct. Bioinf., 2013. **81**(7): p. 1222-1231.
340. Civjan, N.R., et al., *Direct solubilization of heterologously expressed membrane proteins by incorporation into nanoscale lipid bilayers.* Biotechniques, 2003. **35**(3): p. 556-+.
341. Duan, H., et al., *Co-incorporation of heterologously expressed Arabidopsis cytochrome P450 and P450 reductase into soluble nanoscale lipid bilayers.* Arch. Biochem. Biophys., 2004. **424**(2): p. 141-53.
342. Shaw, A.W., et al., *The local phospholipid environment modulates the activation of blood clotting.* J. Biol. Chem., 2007. **282**(9): p. 6556-63.
343. Borch, J., et al., *Nanodiscs for immobilization of lipid bilayers and membrane receptors: kinetic analysis of cholera toxin binding to a glycolipid receptor.* Anal. Chem., 2008. **80**(16): p. 6245-52.
344. Kawai, T., et al., *Catalytic activity of MsbA reconstituted in nanodisc particles is modulated by remote interactions with the bilayer.* FEBS Lett., 2011. **585**(22): p. 3533-7.
345. Bocquet, N., et al., *Real-time monitoring of binding events on a thermostabilized human A2A receptor embedded in a lipid bilayer by surface plasmon resonance.* Biochim. Biophys. Acta, 2015. **1848**(5): p. 1224-33.
346. Ritchie, T.K., et al., *Reconstitution of Membrane Proteins in Phospholipid Bilayer Nanodiscs*, in *Methods Enzymol.*, D. Nejat, Editor. 2009, Elsevier Inc. p. 211-231.
347. Bayburt, T.H., Y.V. Grinkova, and S.G. Sligar, *Assembly of single bacteriorhodopsin trimers in bilayer nanodiscs.* Arch. Biochem. Biophys., 2006. **450**(2): p. 215-22.
348. Kijac, A.Z., et al., *Magic-angle spinning solid-state NMR spectroscopy of nanodisc-embedded human CYP3A4.* Biochemistry, 2007. **46**(48): p. 13696-703.
349. Park, S.H., et al., *Nanodiscs versus macrodiscs for NMR of membrane proteins.* Biochemistry, 2011. **50**(42): p. 8983-5.
350. Ding, Y., et al., *Solid-state NMR of the Yersinia pestis outer membrane protein Ail in lipid bilayer nanodiscs sedimented by ultracentrifugation.* J. Biomol. NMR, 2015. **61**(3-4): p. 275-86.
351. Roos, C., et al., *Characterization of co-translationally formed nanodisc complexes with small multidrug transporters, proteorhodopsin and with the E. coli MraY translocase.* Biochim. Biophys. Acta, 2012. **1818**(12): p. 3098-106.
352. Shi, L., et al., *SNARE proteins: one to fuse and three to keep the nascent fusion pore open.* Science, 2012. **335**(6074): p. 1355-9.

353. Bao, H., et al., *Exocytotic fusion pores are composed of both lipids and proteins.* Nat. Struct. Mol. Biol., 2016. **23**(1): p. 67-73.
354. Rues, R.-B., V. Dötsch, and F. Bernhard, *Co-translational formation and pharmacological characterization of beta1-adrenergic receptor/nanodisc complexes with different lipid environments.* Biochim. Biophys. Acta, 2016.
355. Dalal, K., et al., *Structure, binding, and activity of Syd, a SecY-interacting protein.* J. Biol. Chem., 2009. **284**(12): p. 7897-902.
356. Hartley, M.D., P.E. Schneggenburger, and B. Imperiali, *Lipid bilayer nanodisc platform for investigating polyprenol-dependent enzyme interactions and activities.* Proc. Natl. Acad. Sci. USA, 2013. **110**(52): p. 20863-70.
357. Leney, A.C., et al., *Nanodiscs and electrospray ionization mass spectrometry: a tool for screening glycolipids against proteins.* Anal. Chem., 2014. **86**(11): p. 5271-7.
358. Roy, J., et al., *Direct Capture of Functional Proteins from Mammalian Plasma Membranes into Nanodiscs.* Biochemistry, 2015. **54**(41): p. 6299-302.
359. Proverbio, D., et al., *Functional properties of cell-free expressed human endothelin A and endothelin B receptors in artificial membrane environments.* Biochim. Biophys. Acta, 2013. **1828**(9): p. 2182-92.
360. Inagaki, S., et al., *Modulation of the interaction between neurotensin receptor NTS1 and Gq protein by lipid.* J. Mol. Biol., 2012. **417**(1-2): p. 95-111.
361. Inagaki, S., R. Ghirlando, and R. Grisshammer, *Biophysical characterization of membrane proteins in nanodiscs.* Methods, 2013. **59**(3): p. 287-300.
362. Lee, T.Y., et al., *Tuning the Photocycle Kinetics of Bacteriorhodopsin in Lipid Nanodiscs.* Biophys. J . 2015. **109**(9): p. 1899-906.
363. Boldog, T., M. Li, and G.L. Hazelbauer, *Using Nanodiscs to Create Water-Soluble Transmembrane Chemoreceptors Inserted in Lipid Bilayers*, in *Methods Enzymol.*, Melvin I. Simon, B.R. Crane, and C. Alexandrine, Editors. 2007, Elsevier Inc. p. 317-335.
364. Tsukamoto, H., et al., *Monomeric rhodopsin is the minimal functional unit required for arrestin binding.* J. Mol. Biol., 2010. **399**(3): p. 501-11.
365. Ding, Y., et al., *Influence of the lipid membrane environment on structure and activity of the outer membrane protein Ail from Yersinia pestis.* Biochim. Biophys. Acta, 2015. **1848**(2): p. 712-20.
366. Alami, M., et al., *Nanodiscs unravel the interaction between the SecYEG channel and its cytosolic partner SecA.* EMBO J., 2007. **26**(8): p. 1995-2004.
367. Frauenfeld, J., et al., *Cryo-EM structure of the ribosome-SecYE complex in the membrane environment.* Nat. Struct. Mol. Biol., 2011. **18**(5): p. 614-21.
368. Eggensperger, S., et al., *An annular lipid belt is essential for allosteric coupling and viral inhibition of the antigen translocation complex TAP (transporter associated with antigen processing).* J. Biol. Chem., 2014. **289**(48): p. 33098-108.
369. Shi, L., et al., *Preparation and characterization of SNARE-containing nanodiscs and direct study of cargo release through fusion pores.* Nat. Protoc., 2013. **8**(5): p. 935-48.
370. Leitz, A., et al., *Functional reconstitution of β2-adrenergic receptors utilizing self-assembling Nanodisc technology.* BioTechniques, 2006. **40**(5): p. 601-612.
371. Bayburt, T.H., et al., *Transducin activation by nanoscale lipid bilayers containing one and two rhodopsins.* J. Biol. Chem., 2007. **282**(20): p. 14875-81.
372. Bayburt, T.H. and S.G. Sligar, *Self-assembly of single integral membrane proteins into soluble nanoscale phospholipid bilayers.* Protein Sci., 2003. **12**(11): p. 2476-81.
373. Baas, B.J., I.G. Denisov, and S.G. Sligar, *Homotropic cooperativity of monomeric cytochrome P450 3A4 in a nanoscale native bilayer environment.* Arch. Biochem. Biophys., 2004. **430**(2): p. 218-28.
374. Whorton, M.R., et al., *A monomeric G protein-coupled receptor isolated in a high-density lipoprotein particle efficiently activates its G protein.* Proc. Natl. Acad. Sci. USA, 2007. **104**(18): p. 7682-7.
375. Mi, L.Z., et al., *Functional and structural stability of the epidermal growth factor receptor in detergent micelles and phospholipid nanodiscs.* Biochemistry, 2008. **47**(39): p. 10314-23.
376. Kedrov, A., et al., *Elucidating the native architecture of the YidC: ribosome complex.* J. Mol. Biol., 2013. **425**(22): p. 4112-24.
377. Banerjee, S., T. Huber, and T.P. Sakmar, *Rapid incorporation of functional rhodopsin into nanoscale apolipoprotein bound bilayer (NABB) particles.* J. Mol. Biol., 2008. **377**(4): p. 1067-81.
378. Raschle, T., et al., *Controlled Co-reconstitution of Multiple Membrane Proteins in Lipid Bilayer Nanodiscs Using DNA as a Scaffold.* ACS Chem. Biol., 2015. **10**(11): p. 2448-54.
379. Etzkorn, M., et al., *Cell-free expressed bacteriorhodopsin in different soluble membrane mimetics: biophysical properties and NMR accessibility.* Structure, 2013. **21**(3): p. 394-401.
380. D'Antona, A.M., et al., *Assembly of an activated rhodopsin-transducin complex in nanoscale lipid bilayers.* Biochemistry, 2014. **53**(1): p. 127-34.
381. Reichart, T.M., et al., *Trimerization of the HIV Transmembrane Domain in Lipid Bilayers Modulates Broadly Neutralizing Antibody Binding.* Angew. Chem. Int. Ed., 2016. **55**(8): p. 2688-92.
382. Mitra, N., et al., *Calcium-dependent ligand binding and G-protein signaling of family B GPCR parathyroid hormone 1 receptor purified in nanodiscs.* ACS Chem. Biol., 2013. **8**(3): p. 617-25.
383. Katayama, H., et al., *Three-dimensional structure of the anthrax toxin pore inserted into lipid nanodiscs and lipid vesicles.* Proc. Natl. Acad. Sci. USA, 2010. **107**(8): p. 3453-7.
384. Nasvik Ojemyr, L., et al., *Reconstitution of respiratory oxidases in membrane nanodiscs for investigation of proton-coupled electron transfer.* FEBS Lett., 2012. **586**(5): p. 640-5.
385. Denisov, I.G., et al., *Thermotropic phase transition in soluble nanoscale lipid bilayers.* J. Phys. Chem. B, 2005. **109**(32): p. 15580-8.

386. Shaw, A.W., M.A. McLean, and S.G. Sligar, *Phospholipid phase transitions in homogeneous nanometer scale bilayer discs.* FEBS Lett., 2004. **556**(1-3): p. 260-264.
387. Yang, J.P., et al., *Cell-free synthesis of a functional G protein-coupled receptor complexed with nanometer scale bilayer discs.* BMC Biotechnol., 2011. **11**: p. 57.
388. Schwarz, D., et al., *Preparative scale expression of membrane proteins in Escherichia coli-based continuous exchange cell-free systems.* Nat. Protoc., 2007. **2**(11): p. 2945-57.
389. Katzen, F., et al., *Insertion of membrane proteins into discoidal membranes using a cell-free protein expression approach.* J. Proteome Res., 2008. **7**(8): p. 3535-3542.
390. Rajesh, S., T. Knowles, and M. Overduin, *Production of membrane proteins without cells or detergents.* N. Biotechnol., 2011. **28**(3): p. 250-4.
391. Roos, C., et al., *Co-translational association of cell-free expressed membrane proteins with supplied lipid bilayers.* Mol. Membr. Biol., 2013. **30**(1): p. 75-89.
392. Lyukmanova, E.N., et al., *Lipid-protein nanodiscs for cell-free production of integral membrane proteins in a soluble and folded state: comparison with detergent micelles, bicelles and liposomes.* Biochim. Biophys. Acta, 2012. **1818**(3): p. 349-58.
393. Cappuccio, J.A., et al., *Cell-free co-expression of functional membrane proteins and apolipoprotein, forming soluble nanolipoprotein particles.* Mol. Cell. Proteomics, 2008. **7**(11): p. 2246-53.
394. Gao, T., et al., *Characterization of de novo synthesized GPCRs supported in nanolipoprotein discs.* PLoS One, 2012. **7**(9): p. e44911.
395. Cappuccio, J.A., et al., *Cell-free co-expression of functional membrane proteins and apolipoprotein, forming soluble nanolipoprotein particles.* Mol Cell Proteomics, 2008. **7**(11): p. 2246-53.
396. Roos, C., et al., *Characterization of co-translationally formed nanodisc complexes with small multidrug transporters, proteorhodopsin and with the E. coli MraY translocase.* Biochim Biophys Acta, 2012. **1818**(12): p. 3098-106.
397. Lyukmanova, E.N., et al., *Lipid-protein nanodiscs for cell-free production of integral membrane proteins in a soluble and folded state: comparison with detergent micelles, bicelles and liposomes.* Biochim Biophys Acta, 2012. **1818**(3): p. 349-58.
398. Baker, S.E., et al., *Hydrogen production by a hyperthermophilic membrane-bound hydrogenase in water-soluble nanolipoprotein particles.* J. Am. Chem. Soc., 2009. **131**(22): p. 7508-9.
399. Frauenfeld, J., et al., *A saposin-lipoprotein nanoparticle system for membrane proteins.* Nat. Methods, 2016. **13**(4): p. 345-51.
400. Anantharamaiah, G.M., et al., *Studies of synthetic peptide analogs of the amphipathic helix. Structure of complexes with dimyristoyl phosphatidylcholine.* J. Biol. Chem., 1985. **260**(18): p. 10248-55.
401. Zhang, M., et al., *Reconstitution of the Cytb5 -CytP450 Complex in Nanodiscs for Structural Studies using NMR Spectroscopy.* Angew. Chem. Int. Ed., 2016. **55**(14): p. 4497-9.
402. Knowles, T.J., et al., *Membrane proteins solubilized intact in lipid containing nanoparticles bounded by styrene maleic acid copolymer.* J. Am. Chem. Soc., 2009. **131**(22): p. 7484-5.
403. Orwick, M.C., et al., *Detergent-free formation and physicochemical characterization of nanosized lipid-polymer complexes: Lipodisq.* Angew. Chem. Int. Ed., 2012. **51**(19): p. 4653-7.
404. Dorr, J.M., et al., *The styrene-maleic acid copolymer: a versatile tool in membrane research.* Eur. Biophys. J., 2016. **45**(1): p. 3-21.
405. Lee, S.C., et al., *A method for detergent-free isolation of membrane proteins in their local lipid environment.* Nat. Protoc., 2016. **11**(7): p. 1149-62.
406. Orwick-Rydmark, M., et al., *Detergent-free incorporation of a seven-transmembrane receptor protein into nanosized bilayer Lipodisq particles for functional and biophysical studies.* Nano Lett., 2012. **12**(9): p. 4687-92.
407. Long, A.R., et al., *A detergent-free strategy for the reconstitution of active enzyme complexes from native biological membranes into nanoscale discs.* BMC Biotechnol., 2013. **13**.
408. Dorr, J.M., et al., *Detergent-free isolation, characterization, and functional reconstitution of a tetrameric K+ channel: the power of native nanodiscs.* Proc. Natl. Acad. Sci. USA, 2014. **111**(52): p. 18607-12.
409. Postis, V., et al., *The use of SMALPs as a novel membrane protein scaffold for structure study by negative stain electron microscopy.* Biochim Biophys Acta, 2015. **1848**(2): p. 496-501.
410. Lyukmanova, E.N., et al., *Lipid-protein nanoscale bilayers: a versatile medium for NMR investigations of membrane proteins and membrane-active peptides.* J. Am. Chem. Soc., 2008. **130**(7): p. 2140-1.
411. Gluck, J.M., et al., *Integral membrane proteins in nanodiscs can be studied by solution NMR spectroscopy.* J. Am. Chem. Soc., 2009. **131**(34): p. 12060-1.
412. Shenkarev, Z.O., et al., *Lipid-protein nanodiscs: Possible application in high-resolution NMR investigations of membrane proteins and membrane-active peptides.* Biochemistry (Moscow), 2009. **74**(7): p. 756-765.
413. Imai, S., et al., *Functional equilibrium of the KcsA structure revealed by NMR.* J. Biol. Chem., 2012. **287**(47): p. 39634-41.
414. Raschle, T., et al., *Structural and functional characterization of the integral membrane protein VDAC-1 in lipid bilayer nanodiscs.* J. Am. Chem. Soc., 2009. **131**(49): p. 17777-9.
415. Shenkarev, Z.O., et al., *NMR structural and dynamical investigation of the isolated voltage-sensing domain of the potassium channel KvAP: implications for voltage gating.* J. Am. Chem. Soc., 2010. **132**(16): p. 5630-7.
416. Yu, T.Y., et al., *Solution NMR spectroscopic characterization of human VDAC-2 in detergent micelles and lipid bilayer nanodiscs.* Biochim. Biophys. Acta, 2012. **1818**(6): p. 1562-9.
417. Bibow, S., et al., *Measuring membrane protein bond orientations in nanodiscs via residual dipolar couplings.* Protein Sci., 2014. **23**(7): p. 851-6.
418. Susac, L., R. Horst, and K. Wuthrich, *Solution-NMR characterization of outer-membrane protein A from E. coli in lipid bilayer nanodiscs and detergent micelles.* Chembiochem, 2014. **15**(7): p. 995-1000.

419. Fox, D.A., et al., *Structure of the Neisserial outer membrane protein Opa(6)(0): loop flexibility essential to receptor recognition and bacterial engulfment.* J. Am. Chem. Soc., 2014. **136**(28): p. 9938-46.
420. Okude, J., et al., *Identification of a Conformational Equilibrium That Determines the Efficacy and Functional Selectivity of the mu-Opioid Receptor.* Angew. Chem. Int. Ed., 2015. **54**(52): p. 15771-6.
421. Morgado, L., et al., *Characterization of the insertase BamA in three different membrane mimetics by solution NMR spectroscopy.* J. Biomol. NMR, 2015. **61**(3-4): p. 333-45.
422. Mors, K., et al., *Modified lipid and protein dynamics in nanodiscs.* Biochim. Biophys. Acta, 2013. **1828**(4): p. 1222-9.
423. Salzmann, M., et al., *TROSY in triple-resonance experiments: new perspectives for sequential NMR assignment of large proteins.* Proc. Natl. Acad. Sci. USA, 1998. **95**(23): p. 13585-90.
424. Guo, C., D. Zhang, and V. Tugarinov, *An NMR experiment for simultaneous TROSY-based detection of amide and methyl groups in large proteins.* J. Am. Chem. Soc., 2008. **130**(33): p. 10872-3.
425. Kofuku, Y., et al., *Functional Dynamics of Deuterated beta2 -Adrenergic Receptor in Lipid Bilayers Revealed by NMR Spectroscopy.* Angew. Chem. Int. Ed., 2014. **53**(49): p. 13376-9.
426. Viegas, A., et al., *UTOPIA NMR: activating unexploited magnetization using interleaved low-gamma detection.* J. Biomol. NMR, 2016. **64**(1): p. 9-15.
427. Fernandez, C., et al., *NMR structure of the integral membrane protein OmpX.* J. Mol. Biol., 2004. **336**(5): p. 1211-21.
428. Hagn, F. and G. Wagner, *Structure refinement and membrane positioning of selectively labeled OmpX in phospholipid nanodiscs.* J. Biomol. NMR, 2015. **61**(3-4): p. 249-60.
429. Mazhab-Jafari, M.T., et al., *Membrane-dependent modulation of the mTOR activator Rheb: NMR observations of a GTPase tethered to a lipid-bilayer nanodisc.* J. Am. Chem. Soc., 2013. **135**(9): p. 3367-70.
430. Yao, Y., et al., *Conformation of BCL-XL upon Membrane Integration.* J. Mol. Biol., 2015. **427**(13): p. 2262-70.
431. Yao, Y., et al., *Characterization of the membrane-inserted C-terminus of cytoprotective BCL-XL.* Protein Expr. Purif., 2016. **122**: p. 56-63.
432. Ni, D., et al., *Structural and functional analysis of the beta-barrel domain of BamA from Escherichia coli.* FASEB J., 2014. **28**(6): p. 2677-85.
433. Mineev, K.S., et al., *NMR Dynamics of Transmembrane and Intracellular Domains of p75NTR in Lipid-Protein Nanodiscs.* Biophys. J . 2015. **109**(4): p. 772-82.
434. Vilar, M., et al., *Activation of the p75 neurotrophin receptor through conformational rearrangement of disulphide-linked receptor dimers.* Neuron, 2009. **62**(1): p. 72-83.
435. Brewer, K.D., et al., *Reluctance to membrane binding enables accessibility of the synaptobrevin SNARE motif for SNARE complex formation.* Proc. Natl. Acad. Sci. USA, 2011. **108**(31): p. 12723-8.
436. Schuler, M.A., I.G. Denisov, and S.G. Sligar, *Nanodiscs as a new tool to examine lipid-protein interactions*, in *Lipid-Protein Interactions*, J.H. Kleinschmidt, Editor. 2013, Spinger. p. 415-33.
437. Yokogawa, M., et al., *NMR analyses of the interaction between the FYVE domain of early endosome antigen 1 (EEA1) and phosphoinositide embedded in a lipid bilayer.* J. Biol. Chem., 2012. **287**(42): p. 34936-45.
438. Kobashigawa, Y., et al., *Phosphoinositide-incorporated lipid-protein nanodiscs: A tool for studying protein-lipid interactions.* Anal. Biochem., 2011. **410**(1): p. 77-83.
439. Mazhab-Jafari, M.T., et al., *Oncogenic and RASopathy-associated K-RAS mutations relieve membrane-dependent occlusion of the effector-binding site.* Proc Natl Acad Sci U S A, 2015. **112**(21): p. 6625-30.
440. Yoshiura, C., et al., *NMR analyses of the interaction between CCR5 and its ligand using functional reconstitution of CCR5 in lipid bilayers.* J. Am. Chem. Soc., 2010. **132**(19): p. 6768-77.
441. Wan, C., et al., *Insights into the molecular recognition of the granuphilin C2A domain with PI(4,5)P2.* Chem. Phys. Lipids, 2015. **186**: p. 61-7.
442. Boettcher, J.M., et al., *Atomic view of calcium-induced clustering of phosphatidylserine in mixed lipid bilayers.* Biochemistry, 2011. **50**(12): p. 2264-73.
443. Zhang, Z., et al., *Ca(2+) modulating alpha-synuclein membrane transient interactions revealed by solution NMR spectroscopy.* Biochim. Biophys. Acta, 2014. **1838**(3): p. 853-8.
444. Shenkarev, Z.O., et al., *Lipid-protein nanodiscs offer new perspectives for structural and functional studies of water-soluble membrane-active peptides.* Acta Naturae, 2014. **6**(2): p. 84-94.
445. Freedberg, D.I. and P. Selenko, *Live cell NMR.* Annu Rev Biophys, 2014. **43**: p. 171-92.
446. Lundstrom, P., A. Ahlner, and A.T. Blissing, *Isotope labeling methods for large systems.* Adv Exp Med Biol, 2012. **992**: p. 3-15.
447. Kay, L.E., et al., *Four-dimensional heteronuclear triple-resonance NMR spectroscopy of interleukin-1 beta in solution.* Science, 1990. **249**(4967): p. 411-4.
448. Perez-Trujillo, M., et al., *Optimizing sensitivity and resolution in time-shared NMR experiments.* Magn Reson Chem, 2007. **45**(4): p. 325-9.
449. Parella, T. and P. Nolis, *Time-Shared NMR Experiments.* Concept Magn Reson A, 2010. **36A**(1): p. 1-23.
450. Lescop, E., P. Schanda, and B. Brutscher, *A set of BEST triple-resonance experiments for time-optimized protein resonance assignment.* J Magn Reson, 2007. **187**(1): p. 163-9.
451. Schanda, P. and B. Brutscher, *Very fast two-dimensional NMR spectroscopy for real-time investigation of dynamic events in proteins on the time scale of seconds.* J Am Chem Soc, 2005. **127**(22): p. 8014-5.
452. Schanda, P., V. Forge, and B. Brutscher, *Protein folding and unfolding studied at atomic resolution by fast two-dimensional NMR spectroscopy.* Proc Natl Acad Sci U S A, 2007. **104**(27): p. 11257-62.
453. Kern, T., P. Schanda, and B. Brutscher, *Sensitivity-enhanced IPAP-SOFAST-HMQC for fast-pulsing 2D NMR with reduced radiofrequency load.* J Magn Reson, 2008. **190**(2): p. 333-8.
454. Diercks, T. and V.Y. Orekhov, *qTROSY--a novel scheme for recovery of the anti-TROSY magnetisation.* J Biomol NMR, 2005. **32**(2): p. 113-27.
455. Farmer, B.T., *Simultaneous [13C,15N]-HMQC, a pseudo-triple-resonance experiment.* Journal of Magnetic Resonance (1969), 1991. **93**(3): p. 635-641.

456. Kay, L.E., et al., *4d Nmr Triple-Resonance Experiments for Assignment of Protein Backbone Nuclei Using Shared Constant-Time Evolution Periods.* Journal of Magnetic Resonance, 1992. **98**(2): p. 443-450.
457. Sattler, M., et al., *A simultaneous (15)N, (1)H- and (13)C, (1)H-HSQC with sensitivity enhancement and a heteronuclear gradient echo.* J Biomol NMR, 1995. **5**(1): p. 97-102.
458. Frueh, D.P., et al., *Time-shared HSQC-NOESY for accurate distance constraints measured at high-field in (15)N-(13)C-ILV methyl labeled proteins.* J Biomol NMR, 2009. **45**(3): p. 311-8.
459. Szyperski, T., et al., *Useful Information from Axial Peak Magnetization in Projected NMR Experiments.* Journal of the American Chemical Society, 1996. **118**(34): p. 8146-8147.
460. Kupce, E., R. Freeman, and B.K. John, *Parallel acquisition of two-dimensional NMR spectra of several nuclear species.* J Am Chem Soc, 2006. **128**(30): p. 9606-7.
461. Kupce, E., L.E. Kay, and R. Freeman, *Detecting the "afterglow" of 13C NMR in proteins using multiple receivers.* J Am Chem Soc, 2010. **132**(51): p. 18008-11.
462. Reddy, J.G. and R.V. Hosur, *Parallel acquisition of 3D-HA(CA)NH and 3D-HACACO spectra.* J Biomol NMR, 2013. **56**(2): p. 77-84.
463. Chakraborty, S., S. Paul, and R.V. Hosur, *Simultaneous acquisition of 13Calpha-15N and 1H-15N-15N sequential correlations in proteins: application of dual receivers in 3D HNN.* J Biomol NMR, 2012. **52**(1): p. 5-10.
464. Kupce, E. and L.E. Kay, *Parallel acquisition of multi-dimensional spectra in protein NMR.* J Biomol NMR, 2012. **54**(1): p. 1-7.
465. Moore, G.J., M.I. Hrovat, and R.G. Gonzalez, *Simultaneous multinuclear magnetic resonance imaging and spectroscopy.* Magn Reson Med, 1991. **19**(1): p. 105-12.
466. Sambrook, J. and D.W. Russell, *Molecular cloning : a laboratory manual*. 3rd ed. 2001, Cold Spring Harbor, N.Y.: Cold Spring Harbor Laboratory Press.
467. Ritchie, T.K., et al., *Chapter Eleven - Reconstitution of Membrane Proteins in Phospholipid Bilayer Nanodiscs*, in *Methods in Enzymology*, D. Nejat, Editor. 2009, Academic Press. p. 211-231.
468. Keller, R.L.J., *The Computer Aided Assignment Tutorial*. 2004: CANTINA Verlag.
469. Vranken, W.F., et al., *The CCPN data model for NMR spectroscopy: development of a software pipeline.* Proteins, 2005. **59**(4): p. 687-96.
470. Follis, A.V., et al., *PUMA binding induces partial unfolding within BCL-xL to disrupt p53 binding and promote apoptosis.* Nat Chem Biol, 2013. **9**(3): p. 163-8.
471. Hwang, T.L. and A.J. Shaka, *Water Suppression That Works - Excitation Sculpting Using Arbitrary Wave-Forms and Pulsed-Field Gradients.* Journal of Magnetic Resonance Series A, 1995. **112**(2): p. 275-279.
472. Salzmann, M., et al., *Sensitivity gain by simultaneous acquisition of two coherence pathways: the HNCA(+) experiment.* J Magn Reson, 2000. **143**(1): p. 223-8.
473. Wiedemann, C., et al., *Sequential protein NMR assignments in the liquid state via sequential data acquisition.* J Magn Reson, 2014. **239**: p. 23-8.
474. Kupce, E., *NMR with Multiple Receivers.* Modern Nmr Methodology, 2013. **335**: p. 71-96.
475. Zhu, G., X.M. Kong, and K.H. Sze, *Gradient and sensitivity enhancement of 2D TROSY with water flip-back, 3D NOESY-TROSY and TOCSY-TROSY experiments.* J Biomol NMR, 1999. **13**(1): p. 77-81.
476. Eletsky, A., et al., *A novel strategy for the assignment of side-chain resonances in completely deuterated large proteins using 13C spectroscopy.* Journal of Biomolecular NMR, 2003. **26**(2): p. 167-179.
477. Eletsky, A., et al., *A novel strategy for the assignment of side-chain resonances in completely deuterated large proteins using 13C spectroscopy.* J Biomol NMR, 2003. **26**(2): p. 167-179.
478. Salzmann, M., et al., *TROSY in triple-resonance experiments: new perspectives for sequential NMR assignment of large proteins.* Proc Natl Acad Sci U S A, 1998. **95**(23): p. 13585-90.
479. Bermel, W., et al., *13C-detected protonless NMR spectroscopy of proteins in solution.* Prog Nuc Magn Reson, 2006. **48**(1): p. 25-45.
480. Hoch, J.C., A.S. Stern, and M. Mobli, *Maximum Entropy Reconstruction*, in *eMagRes*. 2007, John Wiley & Sons, Ltd.
481. Delaglio, F., et al., *NMRPipe: a multidimensional spectral processing system based on UNIX pipes.* J Biomol NMR, 1995. **6**(3): p. 277-93.
482. Theillet, F.X., et al., *Paramagnetic relaxation enhancement to improve sensitivity of fast NMR methods: application to intrinsically disordered proteins.* J Biomol NMR, 2011. **51**(4): p. 487-95.
483. Frueh, D.P., et al., *NMR methods for structural studies of large monomeric and multimeric proteins.* Curr Opin Struct Biol, 2013. **23**(5): p. 734-9.
484. Theillet, F.X., et al., *Structural disorder of monomeric alpha-synuclein persists in mammalian cells.* Nature, 2016. **530**(7588): p. 45-50.
485. Kim, Y.W., T.N. Grossmann, and G.L. Verdine, *Synthesis of all-hydrocarbon stapled alpha-helical peptides by ring-closing olefin metathesis.* Nat Protoc, 2011. **6**(6): p. 761-71.
486. Glazyrina, J., et al., *High cell density cultivation and recombinant protein production with Escherichia coli in a rocking-motion-type bioreactor.* Microb Cell Fact, 2010. **9**: p. 42.
487. http://bionumbers.hms.harvard.edu/. Available from: http://bionumbers.hms.harvard.edu/.
488. Kubitschek, H.E. and J.A. Friske, *Determination of bacterial cell volume with the Coulter Counter.* J Bacteriol, 1986. **168**(3): p. 1466-7.
489. Rosay, M., et al., *Solid-state dynamic nuclear polarization at 263 GHz: spectrometer design and experimental results.* Phys Chem Chem Phys, 2010. **12**(22): p. 5850-60.
490. Wang, Y. and O. Jardetzky, *Probability-based protein secondary structure identification using combined NMR chemical-shift data.* Protein Sci, 2002. **11**(4): p. 852-61.
491. Zhu, M., J. Li, and A.L. Fink, *The association of alpha-synuclein with membranes affects bilayer structure, stability, and fibril formation.* J Biol Chem, 2003. **278**(41): p. 40186-97.

492. Dikiy, I. and D. Eliezer, *Folding and misfolding of alpha-synuclein on membranes.* Biochim Biophys Acta, 2012. **1818**(4): p. 1013-8.
493. Butterfield, S.M. and H.A. Lashuel, *Amyloidogenic protein-membrane interactions: mechanistic insight from model systems.* Angew Chem Int Ed Engl, 2010. **49**(33): p. 5628-54.
494. Auluck, P.K., G. Caraveo, and S. Lindquist, *alpha-Synuclein: membrane interactions and toxicity in Parkinson's disease.* Annu Rev Cell Dev Biol, 2010. **26**: p. 211-33.
495. Nemani, V.M., et al., *Increased expression of alpha-synuclein reduces neurotransmitter release by inhibiting synaptic vesicle reclustering after endocytosis.* Neuron, 2010. **65**(1): p. 66-79.
496. Dikiy, I. and D. Eliezer, *N-terminal acetylation stabilizes N-terminal helicity in lipid- and micelle-bound alpha-synuclein and increases its affinity for physiological membranes.* J Biol Chem, 2014. **289**(6): p. 3652-65.
497. Rhoades, E., et al., *Quantification of α-Synuclein Binding to Lipid Vesicles Using Fluorescence Correlation Spectroscopy.* Biophysical Journal, 2006. **90**(12): p. 4692-4700.
498. Bodner, C.R., C.M. Dobson, and A. Bax, *Multiple tight phospholipid-binding modes of alpha-synuclein revealed by solution NMR spectroscopy.* J Mol Biol, 2009. **390**(4): p. 775-90.
499. Bodner, C.R., et al., *Differential phospholipid binding of alpha-synuclein variants implicated in Parkinson's disease revealed by solution NMR spectroscopy.* Biochemistry, 2010. **49**(5): p. 862-71.
500. Ulmer, T.S., et al., *Structure and dynamics of micelle-bound human alpha-synuclein.* J Biol Chem, 2005. **280**(10): p. 9595-603.
501. Jao, C.C., et al., *Structure of membrane-bound alpha-synuclein from site-directed spin labeling and computational refinement.* Proc Natl Acad Sci U S A, 2008. **105**(50): p. 19666-71.
502. Drescher, M., et al., *Antiparallel arrangement of the helices of vesicle-bound alpha-synuclein.* J Am Chem Soc, 2008. **130**(25): p. 7796-7.
503. Fusco, G., et al., *Direct observation of the three regions in alpha-synuclein that determine its membrane-bound behaviour.* Nat Commun, 2014. **5**: p. 3827.
504. Eliezer, D., et al., *Conformational properties of alpha-synuclein in its free and lipid-associated states.* J Mol Biol, 2001. **307**(4): p. 1061-73.
505. Fusco, G., et al., *Structural Ensembles of Membrane-bound alpha-Synuclein Reveal the Molecular Determinants of Synaptic Vesicle Affinity.* Sci Rep, 2016. **6**: p. 27125.
506. Georgieva, E.R., et al., *Membrane-bound alpha-synuclein forms an extended helix: Long-distance pulsed ESR measurements using vesicles, bicelles, and rodlike micelles.* Journal of the American Chemical Society, 2008. **130**(39): p. 12856-+.
507. Drescher, M., et al., *Spin-label EPR on alpha-synuclein reveals differences in the membrane binding affinity of the two antiparallel helices.* Chembiochem, 2008. **9**(15): p. 2411-6.
508. Zhu, M. and A.L. Fink, *Lipid binding inhibits alpha-synuclein fibril formation.* J Biol Chem, 2003. **278**(19): p. 16873-7.
509. Zhao, H., E.K. Tuominen, and P.K. Kinnunen, *Formation of amyloid fibers triggered by phosphatidylserine-containing membranes.* Biochemistry, 2004. **43**(32): p. 10302-7.
510. Galvagnion, C., et al., *Chemical properties of lipids strongly affect the kinetics of the membrane-induced aggregation of alpha-synuclein.* Proc Natl Acad Sci U S A, 2016. **113**(26): p. 7065-70.
511. Zhang, Z., et al., *Ca(2+) modulating alpha-synuclein membrane transient interactions revealed by solution NMR spectroscopy.* Biochim Biophys Acta, 2014. **1838**(3): p. 853-8.
512. Viegas, A., T. Viennet, and M. Etzkorn, *The power, pitfalls and potential of the nanodisc system for NMR-based studies.* Biol Chem, 2016. **397**(12): p. 1335-1354.
513. Bayburt, T.H. and S.G. Sligar, *Self-assembly of single integral membrane proteins into soluble nanoscale phospholipid bilayers.* Protein Sci, 2003. **12**(11): p. 2476-81.
514. Lee, T.Y., et al., *Tuning the Photocycle Kinetics of Bacteriorhodopsin in Lipid Nanodiscs.* Biophys J, 2015. **109**(9): p. 1899-906.
515. Inagaki, S., et al., *Modulation of the interaction between neurotensin receptor NTS1 and Gq protein by lipid.* J Mol Biol, 2012. **417**(1-2): p. 95-111.
516. Ouberai, M.M., et al., *alpha-Synuclein senses lipid packing defects and induces lateral expansion of lipids leading to membrane remodeling.* J Biol Chem, 2013. **288**(29): p. 20883-95.
517. Eichmann, C., et al., *Preparation and Characterization of Stable alpha-Synuclein Lipoprotein Particles.* J Biol Chem, 2016. **291**(16): p. 8516-27.
518. Viegas, A., et al., *UTOPIA NMR: activating unexploited magnetization using interleaved low-gamma detection.* J Biomol NMR, 2016.
519. Johnson, M., et al., *Targeted amino-terminal acetylation of recombinant proteins in E. coli.* PLoS One, 2010. **5**(12): p. e15801.
520. Hong, M. and K. Jakes, Journal of Biomolecular NMR, 1999. **14**(1): p. 71-74.
521. Hoyer, W., et al., *Dependence of α-Synuclein Aggregate Morphology on Solution Conditions.* Journal of Molecular Biology, 2002. **322**(2): p. 383-393.
522. Ritchie, T.K., et al., *Reconstitution of membrane proteins in phospholipid bilayer nanodiscs.* Methods Enzymol, 2009. **464**: p. 211-31.
523. Iyer, A., et al., *The Impact of N-terminal Acetylation of alpha-Synuclein on Phospholipid Membrane Binding and Fibril Structure.* J Biol Chem, 2016. **291**(40): p. 21110-21122.
524. Campioni, S., et al., *The presence of an air-water interface affects formation and elongation of alpha-Synuclein fibrils.* J Am Chem Soc, 2014. **136**(7): p. 2866-75.
525. Jo, S., et al., *CHARMM-GUI: a web-based graphical user interface for CHARMM.* J Comput Chem, 2008. **29**(11): p. 1859-65.
526. Lee, J., et al., *CHARMM-GUI Input Generator for NAMD, GROMACS, AMBER, OpenMM, and CHARMM/OpenMM Simulations Using the CHARMM36 Additive Force Field.* J Chem Theory Comput, 2016. **12**(1): p. 405-13.

527. Baldwin, A.J., et al., *Metastability of native proteins and the phenomenon of amyloid formation.* J Am Chem Soc, 2011. **133**(36): p. 14160-3.
528. Maltsev, A.S., J. Ying, and A. Bax, *Impact of N-terminal acetylation of alpha-synuclein on its random coil and lipid binding properties.* Biochemistry, 2012. **51**(25): p. 5004-13.
529. Bartels, T., et al., *N-Alpha-Acetylation of α-Synuclein Increases Its Helical Folding Propensity, GM1 Binding Specificity and Resistance to Aggregation.* PLoS ONE, 2014. **9**(7): p. e103727.
530. Kang, L., et al., *Mechanistic Insight into the Relationship between N-Terminal Acetylation of α-Synuclein and Fibril Formation Rates by NMR and Fluorescence.* PLoS ONE, 2013. **8**(9): p. e75018.
531. Perni, M., et al., *A natural product inhibits the initiation of alpha-synuclein aggregation and suppresses its toxicity.* Proc Natl Acad Sci U S A, 2017.
532. Birkenhager, R., et al., *Mutation of BSND causes Bartter syndrome with sensorineural deafness and kidney failure.* Nat Genet, 2001. **29**(3): p. 310-4.
533. Picollo, A., et al., *Molecular determinants of differential pore blocking of kidney CLC-K chloride channels.* EMBO Rep, 2004. **5**(6): p. 584-9.
534. Fox, D.A., et al., *Structure of the Neisserial outer membrane protein Opa(6)(0): loop flexibility essential to receptor recognition and bacterial engulfment.* J Am Chem Soc, 2014. **136**(28): p. 9938-46.
535. Mineev, K.S., et al., *NMR Dynamics of Transmembrane and Intracellular Domains of p75NTR in Lipid-Protein Nanodiscs.* Biophys J, 2015. **109**(4): p. 772-82.
536. Mitchell, T.W., et al., *Differences in membrane acyl phospholipid composition between an endothermic mammal and an ectothermic reptile are not limited to any phospholipid class.* J Exp Biol, 2007. **210**(Pt 19): p. 3440-50.
537. Kim, O.Y., et al., *Altered heart and kidney phospholipid fatty acid composition are associated with cardiac hypertrophy in hypertensive rats.* Clin Biochem, 2013. **46**(12): p. 1111-7.
538. Schägger, H. and G. von Jagow, *Tricine-sodium dodecyl sulfate-polyacrylamide gel electrophoresis for the separation of proteins in the range from 1 to 100 kDa.* Analytical Biochemistry, 1987. **166**(2): p. 368-379.
539. Maldonado, A.Y., D.S. Burz, and A. Shekhtman, *In-cell NMR spectroscopy.* Prog Nucl Magn Reson Spectrosc, 2011. **59**(3): p. 197-212.
540. Katayama, H., et al., *Three-dimensional structure of the anthrax toxin pore inserted into lipid nanodiscs and lipid vesicles.* Proc Natl Acad Sci U S A, 2010. **107**(8): p. 3453-7.
541. Tsukamoto, H., et al., *Monomeric rhodopsin is the minimal functional unit required for arrestin binding.* J Mol Biol, 2010. **399**(3): p. 501-11.
542. Rues, R.B., V. Dotsch, and F. Bernhard, *Co-translational formation and pharmacological characterization of beta1-adrenergic receptor/nanodisc complexes with different lipid environments.* Biochim Biophys Acta, 2016.
543. Raschle, T., et al., *Structural and functional characterization of the integral membrane protein VDAC-1 in lipid bilayer nanodiscs.* J Am Chem Soc, 2009. **131**(49): p. 17777-9.
544. Parker, M.J., et al., *A combinatorial selective labeling method for the assignment of backbone amide NMR resonances.* J Am Chem Soc, 2004. **126**(16): p. 5020-1.
545. Lohr, F., et al., *Combinatorial triple-selective labeling as a tool to assist membrane protein backbone resonance assignment.* J Biomol NMR, 2012. **52**(3): p. 197-210.
546. Lohr, F., et al., *An extended combinatorial 15N, 13Calpha, and 13C' labeling approach to protein backbone resonance assignment.* J Biomol NMR, 2015. **62**(3): p. 263-79.
547. Schumann, F.H., et al., *Combined chemical shift changes and amino acid specific chemical shift mapping of protein-protein interactions.* J Biomol NMR, 2007. **39**(4): p. 275-89.
548. Shaw, A.W., M.A. McLean, and S.G. Sligar, *Phospholipid phase transitions in homogeneous nanometer scale bilayer discs.* FEBS Lett, 2004. **556**(1-3): p. 260-4.
549. Grzesiek, S. and A. Bax, *Correlating Backbone Amide and Side-Chain Resonances in Larger Proteins by Multiple Relayed Triple Resonance Nmr.* Journal of the American Chemical Society, 1992. **114**(16): p. 6291-6293.
550. Bermel, W., et al., *Speeding up sequence specific assignment of IDPs.* J Biomol NMR, 2012. **53**(4): p. 293-301.